Performance and Survivability of Offshore Oscillating Water Column Wave Energy Converters

by

Ahmed Elhanafi, MSc (Naval Architecture)

National Centre for Maritime Engineering and Hydrodynamics

Australian Maritime College

Submitted in fulfilment of the requirements for the Degree of Doctor of Philosophy

University of Tasmania

July 2017

Declarations

Declaration of Originality

I declare that this thesis contains no material which has been accepted for a degree or diploma by the University or any other institution, except by way of background information and duly acknowledged in the thesis, and that, to the best of my knowledge and belief, this thesis contains no material previously published or written by another person, except where due acknowledgement is made in the text of the thesis.

This thesis may be made available for loan and limited copying in accordance with the Copyright Act 1968.

Authority of Access

The publishers of the papers in Appendices A–K hold the copyright for that content, and access to the material should be sought from the respective journals and conference proceedings. The remaining non–published content of the thesis and Appendix L are submitted and under review, and may be made available for loan and limited copying and communication in accordance with the Copyright Act 1968.

Signed:

Ahmed Elhanafi

Date: 19/07/2017

Statement of Co–Authorship

Paper 1 (Appendix A): Elhanafi A, Fleming A, Macfarlane G, Leong Z. Numerical energy balance analysis for an onshore oscillating water column–wave energy converter. *Energy. 2016;116(1):539-557.*

Percentage of Contribution: Elhanafi A 85%, Fleming A 7%, Macfarlane G 5%, Leong Z 3%.

Paper 2 (Appendix B): Elhanafi A, Fleming A, Macfarlane G, Leong Z. Numerical hydrodynamic analysis of an offshore stationary–floating oscillating water column–wave energy converter using CFD. *International Journal of Naval Architecture and Ocean Engineering. 2017;9(1):77-99*.

Percentage of Contribution: Elhanafi A 85%, Fleming A 7%, Macfarlane G 5%, Leong Z 3%.

Paper 3 (Appendix C): Elhanafi A, Fleming A, Macfarlane G, Leong Z. Underwater geometrical impact on the hydrodynamic performance of an offshore oscillating water column–wave energy converter. *Renewable Energy. 2017;105:209-231*.

Percentage of Contribution: Elhanafi A 85%, Fleming A 5%, Macfarlane G 7%, Leong Z 3%.

Paper 4 (Appendix D): Elhanafi A, Macfarlane G, Fleming A, Leong Z. Investigations on 3D effects and correlation between wave height and lip submergence of an offshore stationary OWC wave energy converter. *Applied Ocean Research. 2017;64:203-216*.

Percentage of Contribution: Elhanafi A 85%, Macfarlane G 7%, Fleming A 5%, Leong Z 3%.

Paper 5 (Appendix E): Elhanafi A, Macfarlane G, Fleming A, Leong Z. Scaling and air compressibility effects on a three–dimensional offshore stationary OWC wave energy converter. *Applied Energy. 2017;189:1-20*.

Percentage of Contribution: Elhanafi A 85%, Macfarlane G 7%, Fleming A 5%, Leong Z 3%.

Paper 6 (Appendix F): Elhanafi A, Macfarlane G, Fleming A, Leong Z. Experimental and numerical investigations on the hydrodynamic performance of a floating–moored oscillating water column wave energy converter. *Applied Energy. 2017;205:369-390*.

Percentage of Contribution: Elhanafi A 85%, Macfarlane G 7%, Fleming A 5%, Leong Z 3%.

Paper 7 (Appendix G): Elhanafi A, Macfarlane G, Fleming A, Leong Z. Experimental and numerical measurements of wave forces on a 3D offshore stationary OWC wave energy converter. *Ocean Engineering*. *2017;144:98-117*.

Percentage of Contribution: Elhanafi A 85%, Macfarlane G 7%, Fleming A 5%, Leong Z 3%.

Paper 8 (Appendix H): Elhanafi A, Macfarlane G, Fleming A, Leong Z. Intact and damaged survivability of an offshore floating–moored OWC device. *In: Proceedings of 27th International Society of Offshore and Polar Engineers (ISOPE), June 25–30, 2017, San Francisco, California, USA*.

Percentage of Contribution: Elhanafi A 85%, Macfarlane G 6%, Fleming A 6%, Leong Z 3%.

Paper 9 (Appendix I): Elhanafi A, Macfarlane G, Fleming A, Leong Z. Experimental and numerical investigations on the intact and damage survivability of a floating–moored oscillating water column device. *Applied Ocean Research. 2017;68:276-292.*

Percentage of Contribution: Elhanafi A 85%, Macfarlane G 6%, Fleming A 6%, Leong Z 3%.

Paper 10 (Appendix J): Elhanafi A, Fleming A, Leong Z, Macfarlane G. Effect of RANS–based turbulence models on nonlinear wave generation in a two–phase numerical wave tank. *Progress in Computational Fluid Dynamics. 2017;17(3):141-158.*

Percentage of Contribution: Elhanafi A 85%, Fleming A 4%, Leong Z 7%, Macfarlane G 4%.

We the undersigned agree with the above–stated proportion of work undertaken for each of the published (or submitted) peer–reviewed manuscripts contributing to this thesis

Signed:

Doctor Alan Fleming
Primary Supervisor
National Centre for Maritime Engineering and Hydrodynamics
Australian Maritime College
University of Tasmania

Associate Professor Gregor Macfarlane
Co–Supervisor
National Centre for Maritime Engineering and Hydrodynamics
Australian Maritime College
University of Tasmania

Doctor Zhi Leong
Co–Supervisor
National Centre for Maritime Engineering and Hydrodynamics
Australian Maritime College
University of Tasmania

Papers related to the thesis

Paper 11 (Appendix K): Elhanafi A. Prediction of regular wave loads on a fixed offshore oscillating water column–wave energy converter using CFD. *Journal of Ocean Engineering and Science. 2016;1(4):268-283*.

Paper 12 (Appendix L): Elhanafi A., Kim C.J. Experimental and numerical investigation on wave height and power take–off damping effects on the hydrodynamic performance of an offshore–stationary OWC wave energy converter. *Renewable Energy. Provisionally accepted, revised manuscript (2nd revision) submitted August 21, 2017*.

Acknowledgements

First and foremost, I thank Allah for giving me time, strength and ability to complete this research.

I sincerely thank my supervisory team Alan Fleming, Gregor Macfarlane and Zhi Leong for the support, guidance, encouragement and motivation provided during the three–years of my PhD candidature that have made working on this research project a great experience. The development and achievements of this research would not have been possible without your help. In particular, I am grateful to Gregor Macfarlane for the financial support of the experiments performed during my study as well as for continuously supporting me in academia and personal life.

I acknowledge the technical support during the experiments provided by AMC towing tank staff, particularly Mr Tim Lilienthal, Mr Liam Honeychurch, Mr Kirk Meyer and Mr Adam Rolls.

I thank all my colleagues at AMC, particularly Dr Nagi Abdussamie and Dr T M Rabiul Islam for the valuable discussions during my study. I also thank my best friend Mr Hossam Salah (a PhD candidate at CENTEC, Instituto Superior Técnico, Universidade de Lisboa) for his continuous support and motivation.

Last but not least, I must thank My father Shawki, my mother (may Allah have mercy on her), my brothers Mourad and Mohamed, my sister Shimaa, my brother–in–law Yasser and my sons Amr and Abdelrahman. Completing this journey would not have been possible without your encouragement and love.

Abstract

This research was performed with a focus on two key aspects of energy cost–reduction for offshore OWC devices; improving the power extraction efficiency and reducing the excess margin in structural safety factors by a better understanding of wave–induced loads on these devices. This study utilised information from three different resources. First, 2D and 3D numerical results from fully nonlinear Computational Fluid Dynamics (CFD) simulations performed using the commercial code STAR–CCM+ that was validated in good agreement with physical scale model measurements at each stage of increasing complexity during this research. Second, published experiments in the literature for 2D OWC devices subjected to unidirectional regular waves to validate the 2D CFD models of this study. Third, experiments conducted in the towing tank of the Australian Maritime College (AMC) for 3D offshore stationary and floating–moored OWC devices (at a model–scale of 1:50) subjected to unidirectional regular and irregular waves. These experiments were designed to (1) compare the hydrodynamic performance of both devices, (2) estimate wave–induced loads on the fixed device during operating conditions, (3) investigate the survivability of the floating–moored device with intact and damaged mooring systems and (4) validate the 3D CFD models of this study.

Using the combined CFD and experimental approach, it was found that optimizing the underwater geometry of an offshore stationary OWC device could significantly improve the power extraction efficiency up to 0.97. However, this efficiency could be reduced due to air compressibility effects at full–scale. The surge motion of the floating–moored device improved device efficiency in regular and irregular waves. Furthermore, the effectiveness of deploying offshore OWC devices in deep–water where waves are more energetic was proven by increasing the extracted pneumatic energy by a maximum of about 7.7 times when wave height was doubled (incident wave energy increased four times). The instantaneous position of the floating–moored OWC device and its interactions with a certain wave train was more important than the maximum wave height in an irregular sea state when assessing device survivability. Survivability with a damaged mooring system was the key analysis for mooring design. For this analysis, using an equivalent design regular wave condition along with the current safety factors recommended for offshore oil and gas platforms was found to over–design the mooring system of the floating OWC device. The good agreement between CFD experiments for survivability analysis with intact and damaged mooring systems in regular waves highlighted that CFD is a very promising tool a designer can employ to investigate and assess device survivability under different conditions upon further validations in irregular waves.

Table of Contents

Declarations ..... **ii**
Declaration of Originality ii
Authority of Access ii
Statement of Co–Authorship ..... **iii**
Acknowledgements ..... **vii**
Abstract ..... **viii**
Table of Contents ..... **ix**
List of Figures ..... **xi**
Nomenclature ..... **xiii**
Abbreviations ..... **xiv**
1. Introduction **1**
1.1. Background 1
1.2. Motivation and Objectives 2
1.3. Research Novelty 4
1.4. Thesis Outline 5
2. Summary of Major Results **6**
2.1. Paper 1: Numerical energy balance analysis for an onshore oscillating water column–wave energy converter 7
2.2. Paper 2: Numerical hydrodynamic analysis of an offshore stationary–floating oscillating water column–wave energy converter using CFD 11
2.3. Paper 3: Underwater geometrical impact on the hydrodynamic performance of an offshore oscillating water column–wave energy converter 14
2.4. Paper 4: Investigations on 3D effects and correlation between wave height and lip submergence of an offshore stationary OWC wave energy converter 15
2.5. Paper 5: Scaling and air compressibility effects on a three–dimensional offshore stationary OWC wave energy converter 16
2.6. Paper 6: Experimental and numerical investigations on the hydrodynamic performance of a floating–moored oscillating water column–wave energy converter 19
2.7. Paper 7: Experimental and numerical measurements of wave forces on a 3D offshore stationary OWC wave energy converter 20
2.8. Paper 8: Intact and damaged survivability of an offshore floating–moored OWC device 22
2.9. Paper 9: Experimental and numerical investigations on the intact and damage survivability of a floating–moored oscillating water column device 24

3. Conclusions and Future Work 29
3.1. Conclusions 29
3.2. Future Work 31
References 33
Appendix A: Paper 1 ..... A1
Appendix B: Paper 2 ..... B1
Appendix C: Paper 3 ..... C1
Appendix D: Paper 4 ..... D1
Appendix E: Paper 5 ..... E1
Appendix F: Paper 6 ..... F1
Appendix G: Paper 7 ..... G1
Appendix H: Paper 8 ..... H1
Appendix I: Paper 9 ..... I1
Appendix J: Paper 10 ..... J1
Appendix K: Paper 11 ..... K1
Appendix L: Paper 12 ..... L1

List of Figures

Fig. 1.1. OWC device scheme. Left: onshore device and right: offshore device 2

Fig. 2.1. Comparison between PIV experimental (EXP) velocity and vorticity fields [27] (left) and CFD results (right) 8

Fig. 2.2. Wave energy balance chart for onshore OWC devices 9

Fig. 2.3. Velocity and vorticity fields for different wave heights and PTO damping conditions during one wave cycle. (a): water entering the chamber and (b) water leaving the chamber . 10

Fig. 2.4. Wave energy balance chart for offshore stationary OWC devices 11

Fig. 2.5. Energy balance comparison between two wave heights H = 50 mm and 100 mm at a wave period T = 1.6 s and a damping factor of C = 60 12

Fig. 2.6. Wave height effect on vortex generation for a wave period T = 1.6 s and PTO damping factor C = 60 under two wave height (a) H = 50 mm and (b) H = 100 mm 13

Fig. 2.7. AMC towing tank. Left: a general view showing the OWC model, looking towards the beach end, right: a closer view of the offshore stationary OWC model 15

Fig. 2.8. 2D, wave flumes (A and B) and 3D CFD modelling effects vs. 3D experiments (EXP) for a wave height H = 0.05 m 15

Fig. 2.9. Scale and air compressibility effects on the efficiency for a regular wave condition (at full–scale) of H = 2.5 m and period T = 9.9 s (resonance) at different PTO damping factors 17

Fig. 2.10. Effect of air chamber height on power extraction efficiency (ζ) for a regular wave condition (at full–scale) of H = 2.5 m and period T = 9.9 s (resonance) at a PTO damping factor C = 60 17

Fig. 2.11. Effect of air compressibility with enlarged air chamber height on the extracted pneumatic power (PE) at full–scale for H = 2.5 m, T = 9.9 s and PTO damping factor C = 60 18

Fig. 2.12. Scaling effect on power extraction efficiency (ζ) with compressible and incompressible air for a wave height H = 2.5 m (at full–scale) and different periods (T) under a PTO damping factor C = 60 18

Fig. 2.13. AMC towing tank. Left: a general view showing the OWC model, looking towards the wavemaker, right: a closer view of the floating–moored OWC model 19

Fig. 2.14. Comparison between floating–moored and fixed OWC models for power extraction efficiency over a range of wave frequency (Kb) under a constant PTO damping and regular wave height H = 0.05 m 20

Fig. 2.15. CFD results showing the impact of the floating OWC device motions on the extracted pneumatic power (P_E) for H = 0.05 m and T = 1.2 s (scale 1:50) 20

Fig. 2.16. Green water and splashing events on the 1:50 scale model offshore stationary OWC device under a regular wave condition of H = 100 mm and T = 0.9 s 21

Fig. 2.17. Vertical wave force on the forward ($F_{Z\text{-}FWD}$) and aft ($F_{Z\text{-}AFT}$) load cells vs. the total vertical force (F_Z) for a regular wave condition of height H = 0.10 m and period T = 1.1 s with a closed orifice 22

Fig. 2.18. Comparison between CFD and experiments (EXP) in predicting the total horizontal (F_X) and vertical (F_Z) wave forces on the offshore stationary OWC device under a constant wave height H = 0.05 m and closed orifice for two periods T = 0.9 s (left) and 2.0 s (right) .22

Fig. 2.19. Schematic diagram of test rig (not to scale) 23

Fig. 2.20. Impact of mooring redundancy on line tension and transient effects. Left y–axis (black): line tension for the four–line arrangement (100 % loss) and right y–axis (red): line tension for the eight–line arrangement (50 % loss) 24

Fig. 2.21. Experimental time–series results for wave elevation approaching the OWC device, mooring tension in the forward (T-FWD) and aft (T-AFT) lines and OWC device motions during two different realisations (a) Re–1 and (b) Re–11 of sea state SS6 (significant height Hs = 220 mm and peak period Tp = 2.0 s) with pre–tension T_{pre}–1 (72 % of OWC device buoyancy) 25

Fig. 2.22. Photographs taken during the experiments showing the OWC device position at four instants during realisations (a) Re–1 and (b) Re–11 of sea state SS6 with T_{pre}–1. The red vertical line provides a reference frame to track the longitudinal position of the model 26

Fig. 2.23. Experimental time–series results showing the effect of breaking the forward starboard line at different instants (T–Irr–1, T–Irr–2, T–Irr–3) on the tension in the remaining intact lines under irregular sea state SS6 (realisation Re–1) and pre–tension T_{pre}–1 27

Fig. 2.24. Comparison between CFD and experiments (EXP) for mooring line tension and OWC device motions with a damaged mooring system under regular waves of H = 250 mm and T = 2.0 s.....28

Fig. 2.25. Experimental time–series results showing the effect of breaking the forward starboard line on the tension in the remaining intact lines under regular wave conditions of the same period T = 1.45 s and different heights.....28

Nomenclature

b	OWC chamber length wave propagation direction
C	PTO damping factor. Defined in 3D as the ratio between the OWC chamber waterplane area and the orifice cross–sectional area or $C = b/e$ for 2D simulations
C_{Abs}	Energy absorption coefficient
$C_{Internal}$	Internal energy extraction coefficient
C_L	Energy losses coefficient
$C_{Overall}$	Overall energy extraction coefficient
C_R	Reflection coefficient
C_S	Stored energy coefficient
C_T	Transmission coefficient
e	Size of slot opening used to simulate nonlinear PTO damping in 2D
E_A	Absorbed wave energy
E_E	Extracted pneumatic energy
E_I	Incoming wave energy
E_L	Energy losses
E_R	Reflected wave energy
E_S	Stored energy as a potential energy in chamber free surface heave motion
E_T	Transmitted wave energy
g	Gravitational acceleration
H	Incident regular wave height
H_R	Reflected wave height
Hs	Irregular significant wave height
H_T	Transmitted wave height
K	ω^2/g
Kb	Non–dimensional parameter used to refer to the changes in wavelength or wave frequency
L	Regular wavelength
P_E	Extracted pneumatic power
Re	Irregular wave realisation
T	Regular wave period
Tp	Irregular peak period
T–Irr	Mooring line failure instant in irregular waves
T_{pre}	Mooring line pre–tension
ω	Wave angular frequency
ζ	Power extraction efficiency

Abbreviations

2D	Two–dimensional
3D	Three–dimensional
AFT	Aft part of OWC device
CFD	Computational Fluid Dynamics
$CH_{7.5m}$	OWC air chamber height of 7.5 m
Comp	Refers to CFD simulations performed with compressible air
DNV	Det Norske Veritas
EXP	Experimental results
FWD	Forward part of OWC device
Incomp	Refers to CFD simulations performed with incompressible air
ITTC	International Towing Tank Conference
LCOE	Levelised Cost of Energy
NWT	Numerical Wave Tank
OWC	Oscillating Water Column
PIV	Particle Imaging Velocimetry
PTO	Power Take–off
RANS	Reynolds Averaged Navier–Stokes Equations
RSM	Reynolds Stress Models
SS	Sea State
SST	Shear–Stress Transport
T-AFT-P	Tension in aft port mooring line(s)
T-AFT-SB	Tension in aft starboard mooring line(s)
T-FWD-P	Tension in forward port mooring line(s)
T-FWD-SB	Tension in forward starboard mooring line(s)
VOF	Volume of Fluid

Chapter 1

Introduction

1.1. Background

The oil crisis of 1973 and the increasing costs of fossil fuels and the environmental impacts from the excessive use of these fuels induced a significant demand for the development and utilization of the renewable energy technologies [1, 2]. Among the available sources of renewable energy, wave energy combines the following advantages [3, 4]: the highest energy density, low negative environmental impact (especially offshore devices), predictability, natural seasonal variability which follows the changes in electricity demand and energy can be extracted about 90% of the time compared to 20 to 30% for wind and solar. Estimating the global figure of the available wave energy is still a question of debate among scholars. The World Energy Council Report on World Energy Sources [5] based on data from Mork et al. [6] provided an estimate of the total theoretical wave energy potential of 32,000 TWh/year. When considering the direction of the wave energy and the world coastline alignment, Reguero et al. [7] recently estimated the potential wave energy resource in the range of 16,000 to 18,500 TWh/year which is comparable to the global electricity consumption (energy demand) of about 20,500 TWh in year 2015 [8]. As reported in the World Energy Council report [9], the economically exploitable resource could vary to a maximum of 2000 TWh/year if all the potential improvements to existing devices are realised. Wave energy is a strategic power source due to the substantial resource in many countries; for example, Australia has a considerable amount of wave energy that has been estimated to be about 1329 TWh/year [10], which is almost six times the country's electricity consumption of 220 TWh in year 2015 [8].

There are a large number of techniques for wave energy conversion which can be categorised by deployment location (shoreline, nearshore and offshore), type (attenuator, point absorber and terminator) and mode of operation (submerged pressure differential, oscillating wave surge converter, oscillating water column and overtopping device) [4]. Of all proposed and existing Wave Energy Converters (WECs), the Oscillating Water Column (OWC) device, which is the focus of the present research work, is arguably one of the most simple and elegant in design and principle of operation. Fundamentally, an OWC device (see Fig. 1.1) utilizes ocean waves to drive the motion of the water column inside a partially submerged chamber

open below the ocean free surface. The free surface oscillations inside the chamber generate mechanical energy via pushing and sucking airflow between the OWC pneumatic chamber and surrounding atmosphere through an air turbine that is designed to rotate in the same direction regardless of airflow direction. An electric generator can be used to convert the mechanical energy into electrical energy. Having no moving parts underwater, an OWC device provides minimal and easier maintenance works. OWC devices can be deployed as fixed structures at the shoreline or nearshore, integrated into breakwaters, or floating structures [11].

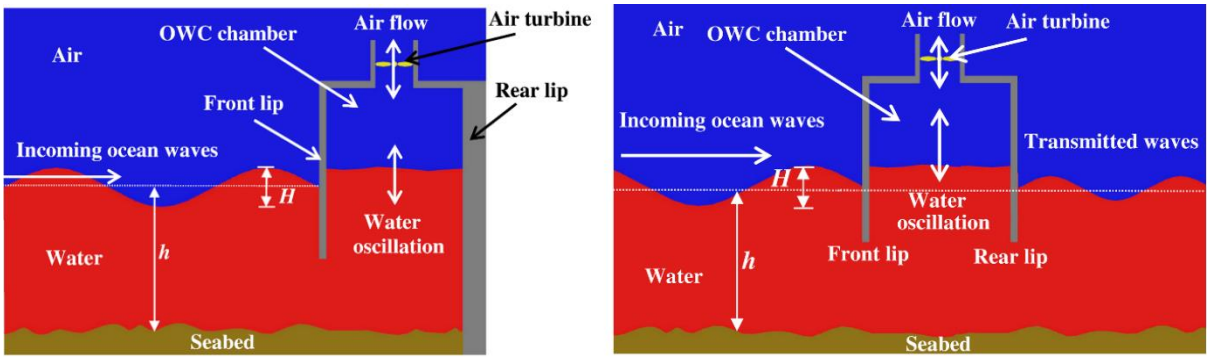

Fig. 1.1. OWC device scheme. Left: onshore device and right: offshore device

1.2. Motivation and Objectives

The operation of OWC devices has been demonstrated by several prototypes of different designs that have been tested worldwide. Examples of onshore devices include Tofteshallen (Norway); Sakata (Japan); Pico (Portugal); Limpet (Scotland); and Mutriku (Spain) [12]. These onshore devices take advantage of easy access and installation as they do not need mooring systems. However, the incident wave energy near the shoreline is smaller compared to offshore locations due to wave breaking and seabed friction [12]. Therefore, offshore OWC devices have been developed by several companies include Mighty Whale (Japan), Oceanlinx Mk3 (Australia), OE Buoy (Ireland) [11]. Even with this number of prototypes, OWC devices have not reached yet a fully commercial stage [13].

Because the technology of WECs is in the early stage of development, the Levelised Cost of Energy (LCOE) is still high [14]. To move WECs from the prototype stage to a more developed and complete technology such as wind and solar, further research effort is still needed [4], particularly to achieve a balance between the power output and the cost to generate that power [14]. Bull and Ochs [15] identified several cost–reduction pathways for offshore OWC devices to be a more economically viable means for converting wave energy into electricity. Among the suggested pathways, optimization of device profile and structural design

was highlighted as important, and therefore this was the focus of this research. The profile of the OWC device affects the energy conversion chain and the natural frequency that can be optimized for a maximum efficiency. WECs are designed not only to harness ocean wave energy efficiently, but they must also withstand extreme wave–induced loads without crashing into other devices or nearby structures [14]. Optimizing the structural design requires a good understanding of the loads acting on the device so that the margin in safety factors can be selected appropriately; however, safety factors are currently very conservative due to the current quite limited understanding of device survivability in extreme events [15].

Applying existing offshore design guidelines or codes to the wave energy sector is not a straightforward process and can lead to conservative designs [16]. This is due to the fundamental differences between typical offshore platforms and WECs including; water depth, designed natural frequencies, structure scale, allowable motion amplitudes, mooring system footprint and number of mooring lines [16, 17]. Although a failure in the mooring system can lead to a catastrophic loss of the WEC (for example, the Wave Dragon prototype [18] and the Oceanlinx MK3PC [19]), the failure consequences are less severe than for offshore platforms (i.e., do not cause fatalities as WECs are usually unmanned, except during installation, maintenance and recovery) [16, 17, 20]. Therefore, directly utilizing the existing offshore standards can potentially lead to an over–designed and expensive WEC mooring system.

The aim of this research was to provide a better understanding of the hydrodynamic performance and survivability of offshore OWC devices. To achieve this aim, physical scale model experiments were performed along with fully nonlinear Computational Fluid Dynamics (CFD) simulations. With an emphasis on floating–moored OWC devices, a sequential development of CFD modelling was performed and validated against experimental results to assess the accuracy of the numerical model at each stage of increasing complexity (from a 2D fixed device to a 3D floating–moored device with a damaged mooring system). This combined CFD and experimental approach was used to fulfil the following underlying objectives:

- Develop a Numerical Wave Tank (NWT) that can accurately generate nonlinear and extreme regular waves.
- Develop a CFD model which can provide a reliable and detailed understanding of the flow behaviour in OWC devices.

- Investigate the influence of different design parameters such as wave conditions, power take–off (PTO) damping, underwater geometry, air compressibility, scaling and 3D effects on the hydrodynamic performance of offshore OWC devices.
- Compare the hydrodynamic performance of offshore fixed and floating–moored OWC devices, and discuss the relevance of the floating device dynamics to its efficiency.
- Study wave forces on offshore OWC devices during the operating conditions.
- Investigate the intact and damage survivability of offshore floating–moored OWC devices by studying mooring line tension in extreme irregular and regular wave conditions.

1.3. Research Novelty

This study contributes to the existing knowledge of OWC–WEC by the following novel aspects:

- The validation and application of CFD with PIV (Particle Imaging Velocimetry) measurements to capture detailed flow field in OWC devices in regular waves.
- Identifying the effect the chamber front and rear lip draughts and thicknesses have on the power extraction efficiency of offshore OWC devices.
- Highlighting the importance of testing offshore OWC devices in 3D domain.
- Assisting the full–scale development of OWC devices by better understanding the differences from small physical model–scales due to air compressibility and scaling effects.
- The measurement and publication of wave forces on 3D offshore fixed OWC devices at model–scale.
- The measurement and publication of mooring line tension and OWC device motions in extreme irregular and regular wave conditions at model–scale.
- The validation and application of CFD to assess the survivability of floating–moored OWC devices with intact mooring systems as well as with a single mooring line failure.
- Quantifying the importance of considering the transient effects induced by mooring line failure.

- Discussing the applicability of using the current design codes of offshore oil and gas platforms in designing floating–moored WECs of OWC type.

1.4. Thesis Outline

This thesis is submitted as a collection of related peer–reviewed papers. The structure of the thesis is as follows: an introduction to the subject of interest along with motivation, objectives and novelty of the work are presented in Chapter 1. Chapter 2 summarizes the major results achieved from the research work conducted during the PhD study. This consists of the salient points from each of the peer–reviewed papers. Chapter 3 provides the conclusions from this research along with recommended future work. The complete research papers are provided in Appendices A–L.

Chapter 2

Summary of Major Results

This thesis combines a series of papers published in journals and conference proceedings during the three–year period of the PhD candidature. In each paper, both experiment and CFD techniques were employed to investigate a subject of interest related to OWC wave energy converters to address the research objectives stated in Chapter 1. The CFD simulations in 2D and 3D numerical wave tanks (NWTs) were carried out using the RANS–VOF solver in STAR–CCM+ code [21] that uses a finite volume method to discretise the integral formulation of the Navier–Stokes equations and uses a predictor–corrector approach to link the continuity and momentum equations. The two–equation shear stress transport (SST) $k-\omega$ turbulence model was implemented to model the Reynolds stresses in RANS equations [21]. Justifications of selecting the (SST) $k-\omega$ turbulence model for both wave generation and capturing detailed flow field in OWC devices were discussed in Papers 10 (Appendix J) and 1 (Appendix A), respectively. In each paper, the criteria for selecting the turbulence model was to find an eddy–viscosity turbulence model that can provide good results compared to the Reynolds Stress Models (RSM), also known as the Reynolds Stress Transport Models, but with less computational cost. It is expected that the RSM provide better results than eddy–viscosity models (such as $k-\omega$ and $k-\varepsilon$) because the RSM models directly calculate the components of the specific Reynolds stress tensor by solving their governing transport equations. Therefore, these models have the potential to predict complex flows more accurately than eddy–viscosity models because the transport equations for the Reynolds stresses naturally account for the effects of turbulence anisotropy, streamline curvature, swirl rotation and high strain rates, but RSM models are more computationally expensive than eddy–viscosity models. The advantage of the $k-\omega$ model over the $k-\varepsilon$ model is its improved performance for boundary layers under adverse pressure gradients, which explains the superior results of (SST) $k-\omega$ to $k-\varepsilon$ for capturing detailed flow field in OWC devices where flow separation and strong eddies are generated at chamber lip. The constructed CFD models were validated against a series of physical tank measurements from either 2D experiments available in the literature or from experiments performed in this thesis at the towing tank of the Australian Maritime College (AMC) for 3D offshore fixed and floating–moored OWC devices.

Experimental uncertainty analysis is very important to ensure high quality and reliable measurements. The uncertainty analysis for the experiments performed in this study was in accordance with the method adopted by the International Towing Tank Conference (ITTC) [22-24]. In general, experimental uncertainties are categorized in two groups, Type A (Random) which is estimated from repeated measurements, and Type B (Systematic), estimated based on the available information such as the calibration procedure and data provided by the manufacture of each instrument. All measurements included in the uncertainty analysis have been repeated several times including non–sequentially repeated runs as recommended by ITTC [22] to demonstrate experiment repeatability. Overall, the uncertainties in these experiments were in the order of ± 6 % considering a level of confidence of approximately 95 %. Further details on the experiment uncertainty analysis are provided in Appendices E and G.

The following sections provide a summary of each paper appended to the thesis.

2.1. Paper 1: Numerical energy balance analysis for an onshore oscillating water column–wave energy converter

In this paper, the effect of wave height and power take–off (PTO) damping on the hydrodynamic performance of an onshore OWC device was investigated through a series of wave energy balance analyses using a 2D CFD model. The CFD model was validated in good agreement with previously published experiments [25] for incident wave propagation along the tank, chamber differential air pressure and chamber free surface elevation. For physical scale model tests, it is possible to use PIV (Particle Imaging Velocimetry) technique to gain a detailed insight into the flow behaviour in OWC devices [26-28]. However, applications of PIV are mostly limited to single plane measurements (2D PIV) due to the increased complexity of Stereo 3D PIV, where it can be extremely difficult to obtain appropriate optical access. This requires collecting data at different 2D planes to have a full understanding of the flow field in 3D domain [29]. Furthermore, PIV is an expensive technique and utilizes a high–intensity laser (class 4) that can easily cause permanent blindness. On the other hand, an experimentally–validated CFD model does not have the above–mentioned experimental issues and can be an efficient tool for engineers to visualize the flow field inside and around the OWC chamber for further applications in optimizing the underwater geometry of OWC devices for a maximum power extraction efficiency by identifying areas of high energy losses.

The capability of CFD modelling in capturing such detailed information has not been performed in previous research, but this has been proven in this paper as demonstrated by the good agreement against PIV measurements [27] for the velocity and vorticity fields during one wave cycle (see Fig. 2.1) in a 1:25 scale model of a shore–based OWC device. In addition to the good qualitative agreement, the average turbulent kinetic energy coefficient over one wave cycle (i.e., the ratio between the turbulent kinetic energy and the flow kinetic energy) estimated using the CFD model was in good agreement with the experimental results.

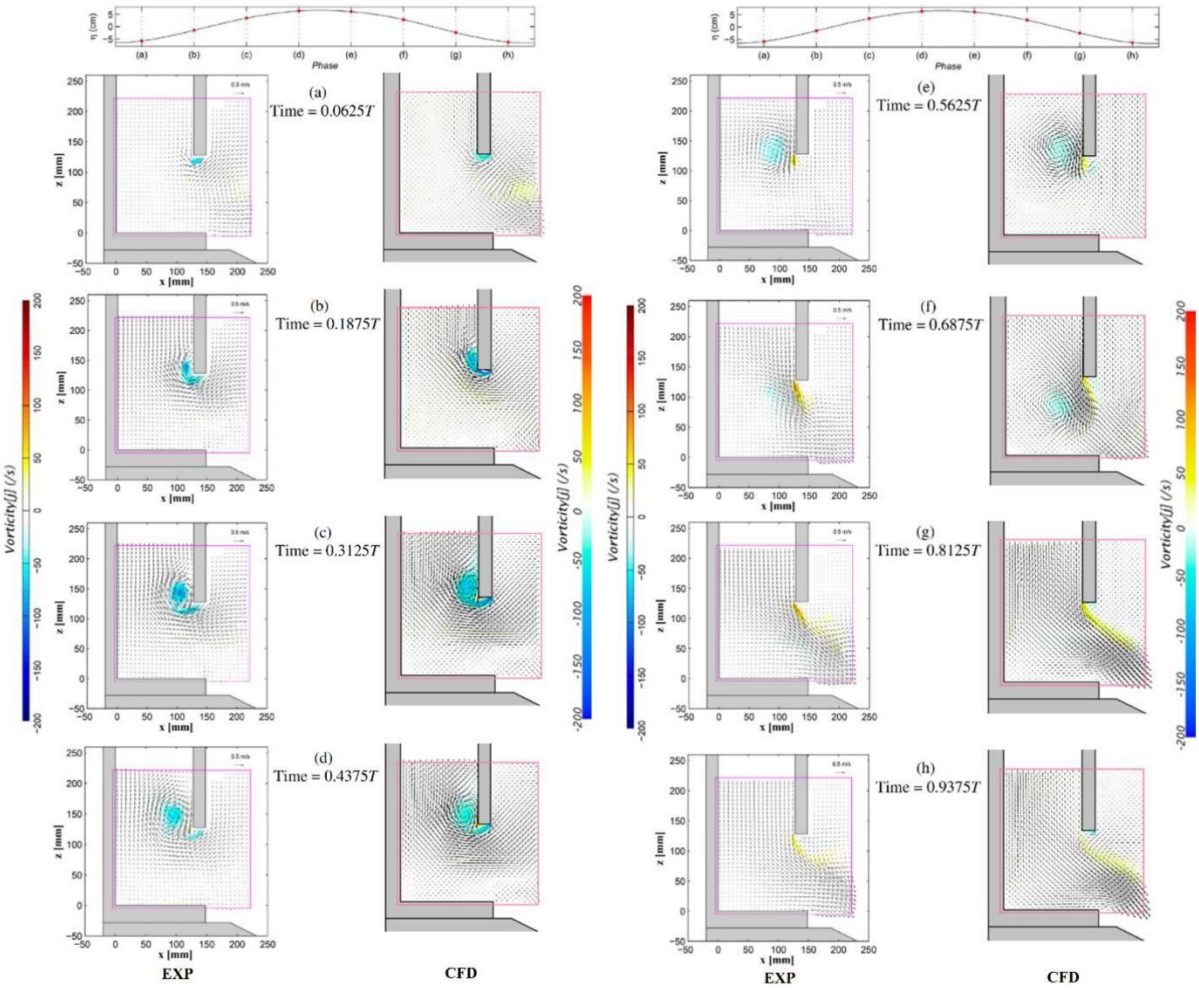

Fig. 2.1. Comparison between PIV experimental (EXP) velocity and vorticity fields [27] (left) and CFD results (right)

From an extensive campaign of 40 wave energy balance analyses (see Fig. 2.2 for the energy balance chart) including five regular wave heights and eight PTO damping values simulated by a slot opening of different sizes (e), it was observed that there was an optimum PTO damping value that maximized the overall ($C_{Overall}$) and internal ($C_{Internal}$) energy extraction coefficients. Increasing the incident wave height (H) by about 2.93 times (nominally from H = 40 mm to

120 mm) at the optimum damping (slot opening size of e = 1.5 mm) increased the extracted pneumatic energy by about 6.9 times, but with the higher incident energy in the larger wave that increased by 8.6 times, the overall energy extraction coefficient reduced by 0.075 (i.e., from $C_{Overall}$ = 0.394 to 0.319). Also, increasing the incident wave height or reducing the PTO damping increased the energy losses. For example, increasing the wave height (H) by about 2.93 times (nominally from H = 40 mm to 120 mm) at the optimum damping increased the energy losses 7.08 times (from 0.61 J/m to 4.32 J/m), and increasing the slot opening size from e = 1 mm to 5 mm (i.e., decreasing the PTO damping) increased the energy losses from 0.55 J/m to 0.63 J/m (1.15 times) at H = 40 mm and from 2.66 J/m to 13.26 J/m (4.98 times) at H = 120 mm. The higher energy losses were demonstrated by a larger and higher strength vortex generation, especially around the upper lip (see Fig. 2.3).

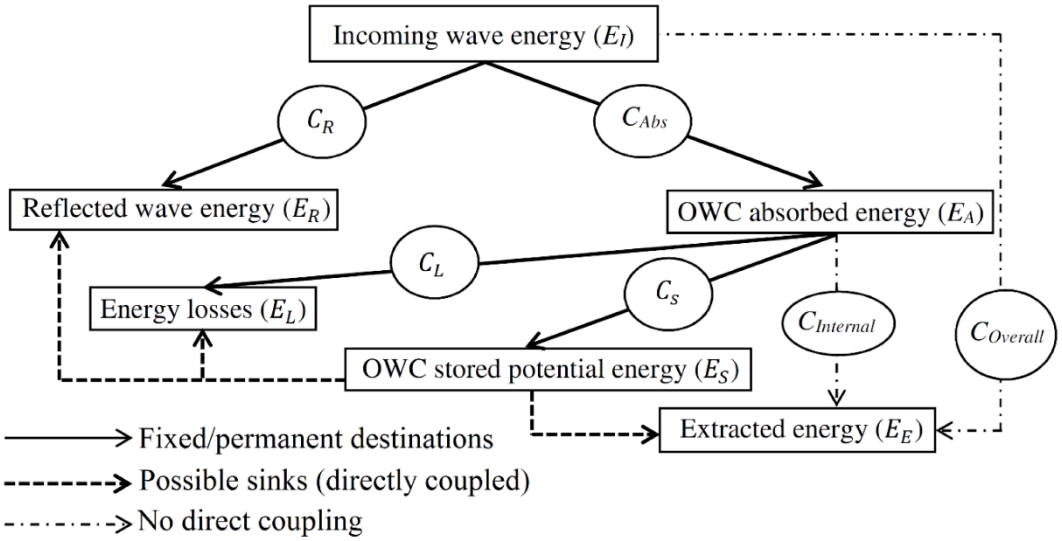

Overall pneumatic energy extraction ($C_{Overall}$)	E_E/E_I
Reflected coefficient (C_R)	H_R/H
OWC energy absorption (C_{Abs})	E_A/E_I
OWC internal energy extraction ($C_{Internal}$)	E_E/E_A
Energy losses (C_L)	E_L/E_A
OWC stored energy (C_S)	E_s/E_A

Fig. 2.2. Wave energy balance chart for onshore OWC devices

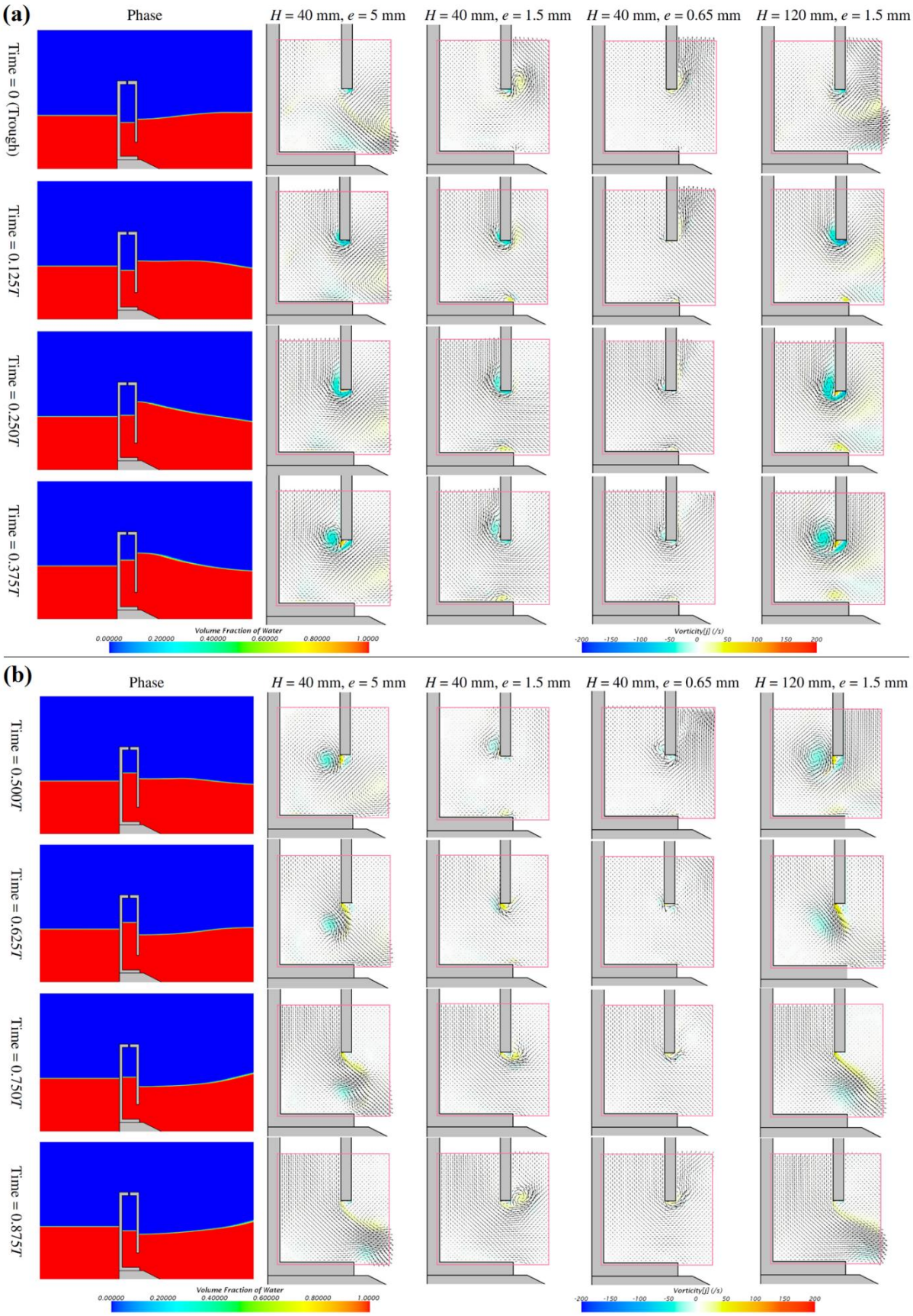

Fig. 2.3. Velocity and vorticity fields for different wave heights and PTO damping conditions during one wave cycle. (a): water entering the chamber and (b) water leaving the chamber

2.2. Paper 2: Numerical hydrodynamic analysis of an offshore stationary–floating oscillating water column–wave energy converter using CFD

In this paper, the CFD model developed and validated in Paper 1 was modified to consider wave transmission underneath the 1:50 scale model offshore OWC device investigated in this paper. Further validation was performed to ensure the accuracy of the CFD model in estimating the transmission coefficient (C_T, the ratio between the transmitted wave height H_T and the incident wave height H), which is a fundamental difference from onshore OWC devices. The model was validated in good agreement with experiments of a pile supported breakwater–OWC model [30], and then the energy balance model used in Paper 1 was extended to consider an additional sink for the energy transmitted underneath the device (see Fig. 2.4).

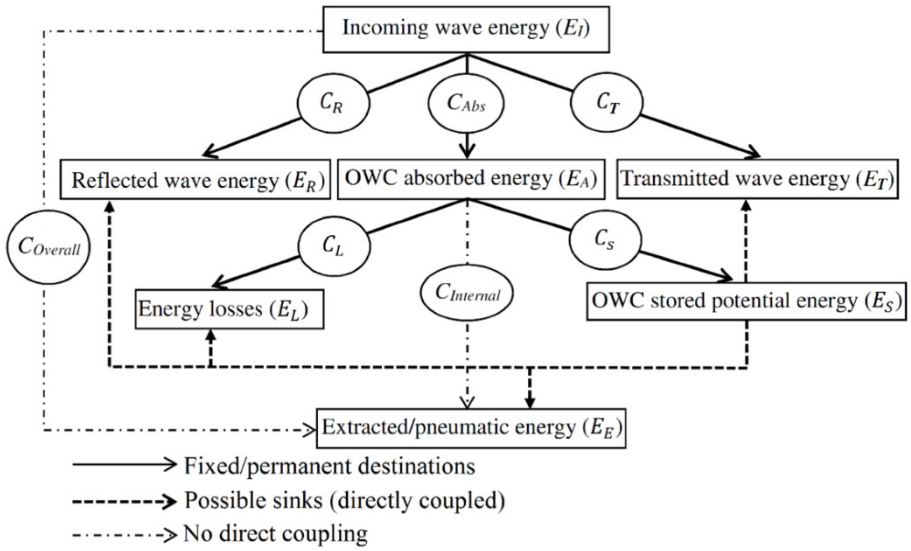

Overall pneumatic energy extraction ($C_{Overall}$)	E_E/E_I
Reflected coefficient (C_R)	H_R/H
Transmitted coefficient (C_T)	H_T/H
OWC energy absorption (C_{Abs})	E_A/E_I
OWC internal energy extraction ($C_{Internal}$)	E_E/E_A
Energy losses (C_L)	E_L/E_A
OWC stored energy (C_S)	E_s/E_A

Fig. 2.4. Wave energy balance chart for offshore stationary OWC devices

The energy balance model and the validated CFD model were employed to perform a benchmark study of 102 numerical tests investigating the effect of incoming wavelength, wave height and PTO damping on the hydrodynamic performance and wave energy conversion process in offshore fixed OWC devices. Fig. 2.4 illustrates that the absorbed energy is the remainder of the incoming energy that was not reflected or transmitted, and this energy represents the maximum available energy to be extracted by the PTO after subtracting the

energy stored and energy losses. It was found that as wave frequency increased the reflection coefficient increased, whereas the transmission coefficient decreased. These contrary trends resulted in a larger energy absorption coefficient (C_{Abs}) over the intermediate–frequency range. Variations in the internal energy extraction coefficient over this frequency range was found to be negligible; therefore, the overall energy extraction coefficient ($C_{Overall}$) and the overall hydrodynamic efficiency ($\zeta_{Overall}$, the ratio between the extracted pneumatic power and incident wave power) peaked at a certain frequency within this intermediate–frequency range.

The PTO damping provided an important control parameter for extracting more energy over a broader frequency band. This required adjusting the PTO damping to tune the device to a given wavelength. However, this depends on the constraints of regulating the turbine rotational speed (assuming a constant turbine diameter is selected)[31]. The overall hydrodynamic efficiency decreased as wave height increased, especially for large PTO damping. However, for the low–frequency waves under small and intermediate PTO damping, a higher efficiency was observed as wave height increased. Similar to the results of Paper 1, increasing the wave height not only increased the energy losses, but also the extracted pneumatic energy increased due to the larger differential air pressure and airflow rate. For instance, increasing the incident wave height twofold (i.e., increasing the incoming wave energy four times), increased the energy losses and the extracted pneumatic energy in the range of 3.0–4.4 times and 2.9–8.6 times, respectively. This effect was influenced by the wave frequency and the PTO damping such that the maximum increase in extracted pneumatic energy (8.6 times) was found for the longest wavelength tested under the lowest PTO damping. Fig. 2.5 compares each energy component in the energy chart of Fig. 2.4 at two different wave heights H = 50 mm and 100 mm.

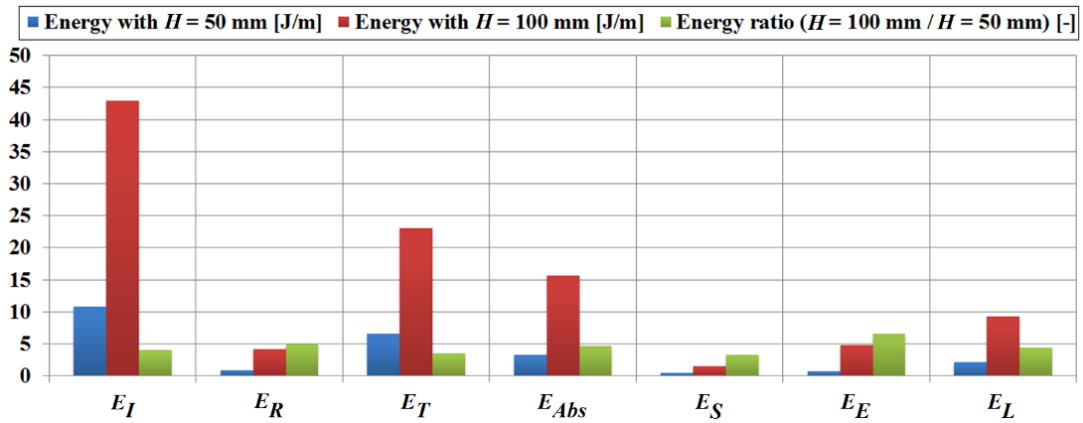

Fig. 2.5. Energy balance comparison between two wave heights H = 50 mm and 100 mm at a wave period T = 1.6 s and a damping factor of C = 60

The strength and size of the generated vortices significantly increased as wave height increased. This is demonstrated by the flow field results in Fig.2.6 at three instants during one wave cycle, which also explains the increase in energy losses shown in Fig. 2.5 under the larger wave height (H = 100 mm). The vortices generated at the rear lip almost disappeared under high–frequency waves due to the very small transmission coefficient.

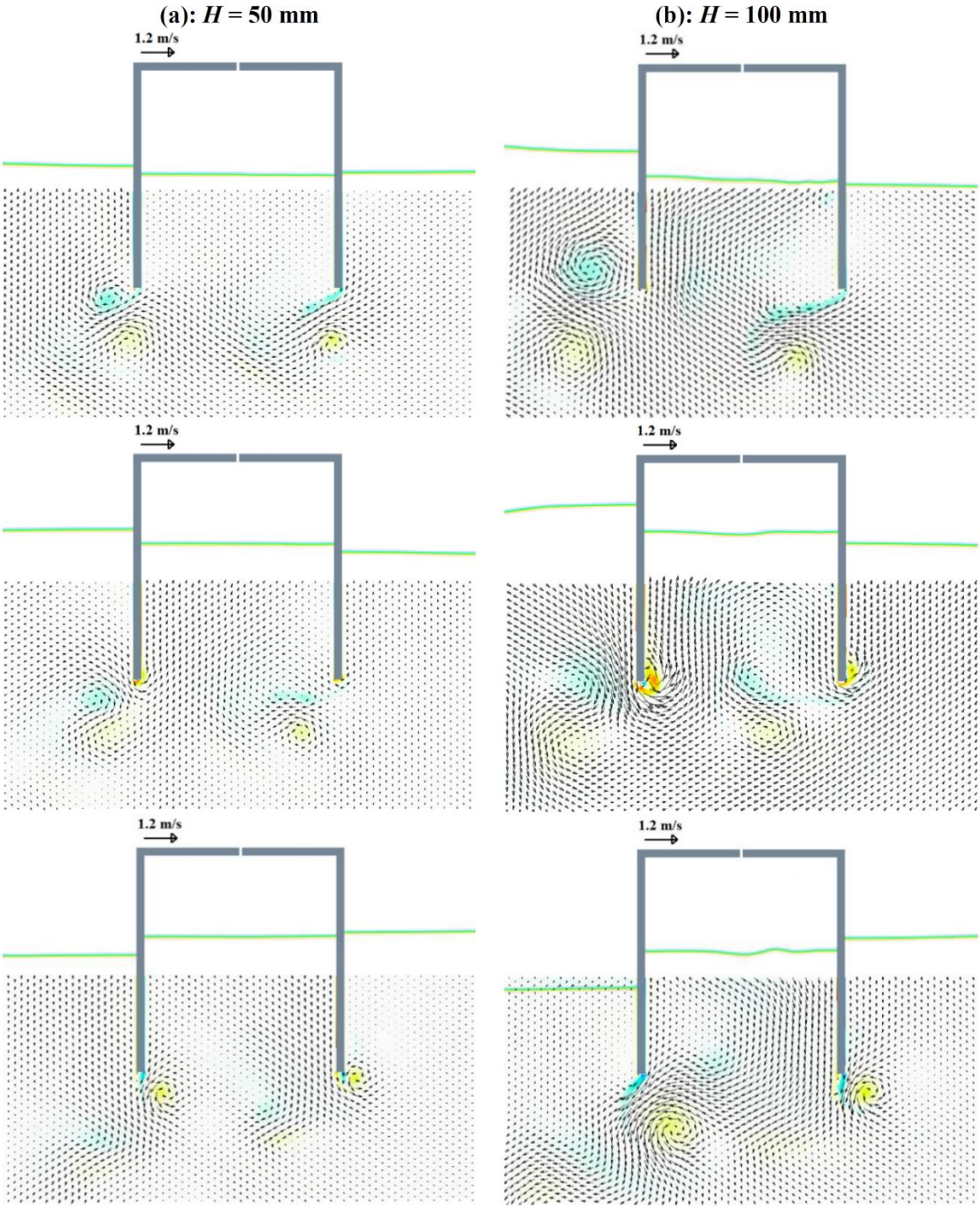

Fig. 2.6. Wave height effect on vortex generation for a wave period T = 1.6 s and PTO damping factor C = 60 under two wave height (a) H = 50 mm and (b) H = 100 mm

2.3. Paper 3: Underwater geometrical impact on the hydrodynamic performance of an offshore oscillating water column–wave energy converter

In this paper, the 2D CFD model of Paper 2 was used to investigate how the underwater geometry of an offshore OWC device can influence the power extraction efficiency. The CFD model was also validated in good agreement with model–scale experimental results for predicting the power extraction efficiency of a pile supported breakwater–OWC device [32] under a constant regular wave height for a range of wave periods and two different slot opening sizes simulating different PTO damping values. An extensive campaign consisting of 320 numerical simulations was performed to study the relevance of the front and rear lip submergence and thickness to the performance of offshore fixed OWC devices over a wide range of wave periods under a constant wave height and PTO damping. In addition, numerical decay tests were conducted to estimate the resonant frequency of each OWC geometry tested.

Changing lip draught altered the device resonant frequency so that it could be tuned to a certain wave frequency range. However, tuning the device to a wide frequency range by symmetrically changing the front and rear lip draughts was found to be impractical as it required decreasing and increasing the draught for high– and low– frequency regions, respectively. In contrast, for a certain front lip draught that provided an efficient path for water particles to enter and leave the chamber over a certain frequency range, asymmetrically increasing the rear lip draught shifted the resonant frequency to a lower value and improved the device efficiency over a broader frequency bandwidth without detracting the efficiency at the high–frequency region.

Changing lip thickness had a negligible influence on the device resonant frequency. Solely increasing the thickness of the front and rear lips reduced and increased the efficiency, respectively. Hence, symmetrically increasing the thickness of both lips increased the efficiency up to an optimum thickness value that was found in this study to be 12% of the chamber length (b) in the wave propagation direction. However, the improvement achieved in efficiency was quite small relative to asymmetrically changing lip draught.

The optimal combination (the front lip draught was two times the wave height and the rear lip draught was three times the front lip draught with symmetrical lip thickness of 0.12b) achieved a peak efficiency exceeding 0.79, which represented a massive enhancement over more simplistic geometries that returned peak efficiencies of approximately 0.30. With this combination, the peak efficiency (0.3) of the parent OWC geometry tested in this study could be obtained almost over the entire frequency range without changing the PTO damping.

2.4. Paper 4: Investigations on 3D effects and correlation between wave height and lip submergence of an offshore stationary OWC wave energy converter

Papers 1–3 utilized 2D CFD models. Therefore, 3D effects were discussed in this paper. A 3D CFD model was constructed and validated in good agreement with experiments of a 3D 1:50 scale model of the offshore stationary OWC device shown in Fig. 2.7. Following the validation stage, an extensive campaign consisting of 190 computational tests was performed with two primary objectives (1) investigate the effect of testing offshore OWC devices in 2D domain or narrow wave flumes on device efficiency, and (2) find the relationship between the incoming wave height and the chamber front lip draught for a maximum efficiency.

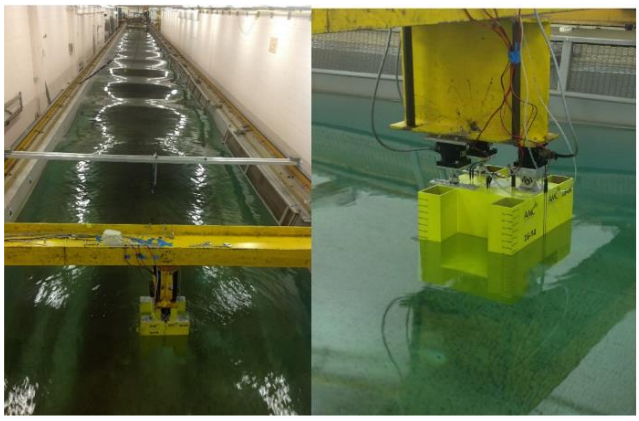

Fig. 2.7. AMC towing tank. Left: a general view showing the OWC model, looking towards the beach end, right: a closer view of the offshore stationary OWC model

Results in Fig. 2.8 revealed that testing offshore OWC devices in 3D tanks is paramount to avoid overestimating the power extraction efficiency (ζ), especially for wave frequencies higher than the chamber resonant frequency. This frequency was equivalent to a wavelength L = 2.63 m, which was almost the minimum wavelength (2.51 m) after which the effect of wave diffraction becomes noticeable [33].

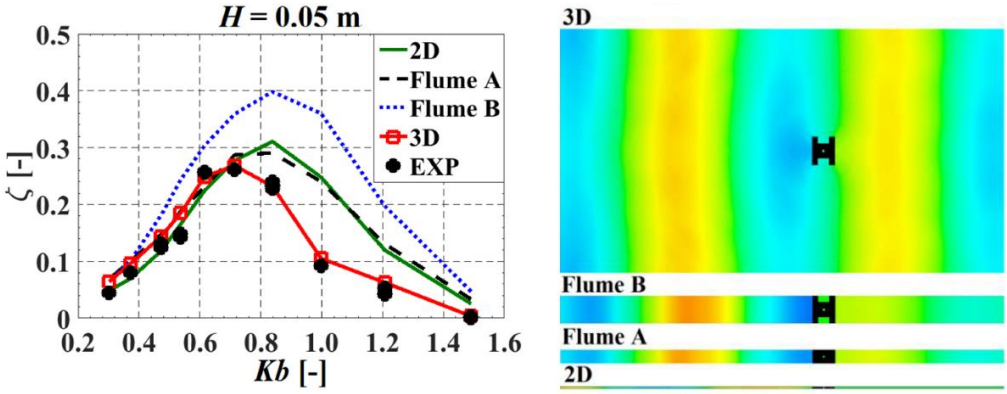

Fig. 2.8. 2D, wave flumes (A and B) and 3D CFD modelling effects vs. 3D experiments (EXP) for a wave height H = 0.05 m

The relevance of asymmetrically changing the front and rear lips draught to device efficiency as discussed in Paper 3 (using 2D CFD) was also verified in this paper using the validated 3D CFD model. But, again the 2D model utilized in Paper 3 overestimated the device performance. This indicated that a 2D model (low computation cost) can only be used to preliminary understand the effect of different design parameters such as wave conditions and underwater geometries on device efficiency, but using a more computationally expensive 3D CFD model is important to accurately predict the efficiency.

Furthermore, a front lip submergence equal to the incident wave amplitude afforded maximum efficiency whilst preventing air leakage, hence it was recommended that the front lip draught be minimized. For example, a maximum efficiency of 0.97 was achieved for a device with a front lip draught equal to the wave amplitude and a rear lip draught of 23 % of the water depth. This significant improvement was comparable to other onshore and nearshore OWC devices where the rear lip of these devices extends to the seabed.

2.5. Paper 5: Scaling and air compressibility effects on a three–dimensional offshore stationary OWC wave energy converter

Air compressibility has usually been neglected in small scale model experiments and numerical simulations similar to those discussed in Papers 1–4. However, at full–scale, air compressibility becomes more important and may affect the predicted performance. Therefore, this paper was designed to contribute to the full–scale development of OWC devices by better understanding the differences from small physical model–scales. The validated 3D CFD model of Paper 4 was employed in this paper to investigate the importance of air compressibility at different scales from 1:50 (physical model experiments) up to full–scale for different design parameters including wave height, wave period, PTO damping, pneumatic chamber height and underwater geometry.

Results revealed that air compressibility at full–scale resulted in about 12 % reduction in the maximum efficiency predicted at (1:50) model–scale under regular waves at the resonant frequency and the optimum PTO damping as shown in Fig. 2.9. This error (over–estimation) increased as PTO damping increased. Also, air compressibility at full–scale slightly reduced the optimum PTO damping at the resonant period.

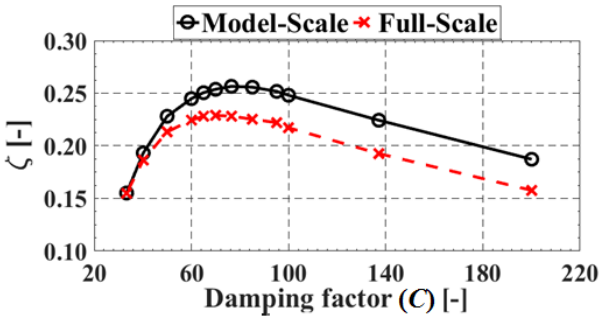

Fig. 2.9. Scale and air compressibility effects on the efficiency for a regular wave condition (at full–scale) of H = 2.5 m and period T = 9.9 s (resonance) at different PTO damping factors

For small OWC models scaled with Froude's similitude law up to scale 1:10, it was found that air compressibility effects can be neglected without significant differences in the device performance obtained with compressible air at these small scales. Therefore, compensation for full–scale air compressibility effects is paramount when testing devices at such small scales. This can be performed by increasing the air chamber height or attaching the air chamber to an external air reservoir. The error in the estimated efficiency (in comparison to the full–scale efficiency) when enlarging the air chamber of a small OWC model–scale was investigated (see Fig. 2.10), and it was found that this error could be minimized to less than 1.2 % with an air chamber height equal to the full–scale height (i.e., the air chamber volume is scaled using squared (rather than cubed) the scale factor based on Froude's similitude law).

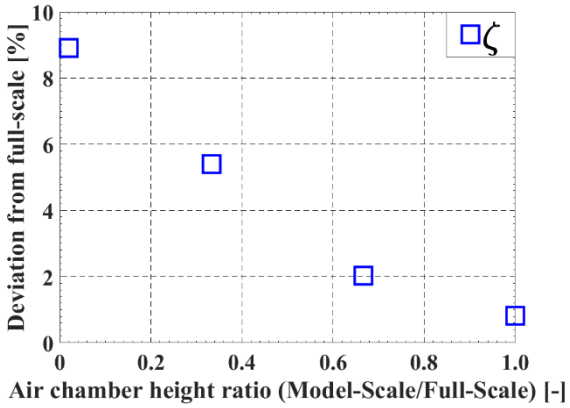

Fig. 2.10. Effect of air chamber height on power extraction efficiency (ζ) for a regular wave condition (at full–scale) of H = 2.5 m and period T = 9.9 s (resonance) at a PTO damping factor C = 60

When using CFD for the above–mentioned procedure, it was found that (see Fig 2.11) air must be modelled as a compressible fluid otherwise no impact of air compressibility will be considered even with an air chamber height equal to the full–scale height of 7.5 m (referred to

as $CH_{7.5m}$). In this figure, $CH_{7.5m}$–Comp and $CH_{7.5m}$–Incomp refer to the results (scaled to full–scale using Froude's similitude law) from a 1:50 model–scale with an enlarged air chamber when air was modeled as a compressible and incompressible fluid, respectively. Also shown in this figure results when the full–scale model was simulated in CFD with compressible air (referred to as Full–scale–Comp).

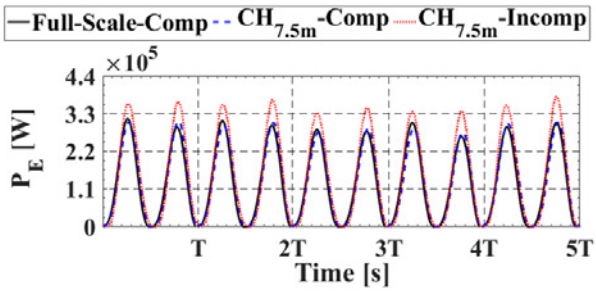

Fig. 2.11. Effect of air compressibility with enlarged air chamber height on the extracted pneumatic power (P_E) at full–scale for H = 2.5 m, T = 9.9 s and PTO damping factor C = 60

It was also expected that other scaling effects from vortex shedding, viscous effects and other physical phenomena that do not typically scale with Froude's similitude law would exist. However, results in this study (see Fig. 2.12) did not show strong evidence of scaling effects with incompressible air. This indicates that results from small scale model experiments with compensation of full–scale air compressibility effects can be used to represent the performance of the full–scale prototype.

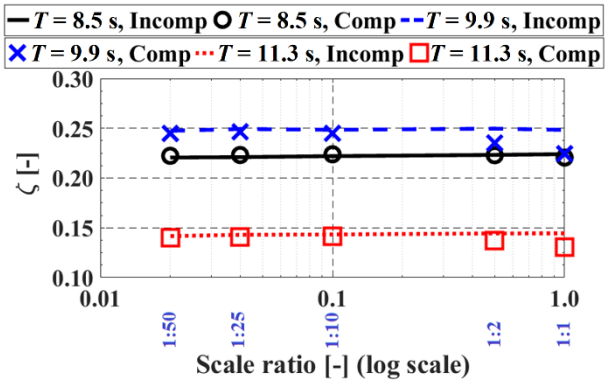

Fig. 2.12. Scaling effect on power extraction efficiency (ζ) with compressible and incompressible air for a wave height H = 2.5 m (at full–scale) and different periods (T) under a PTO damping factor C = 60

2.6. Paper 6: Experimental and numerical investigations on the hydrodynamic performance of a floating–moored oscillating water column–wave energy converter

Deployment of offshore OWC devices in deep water where waves are more energetic may require the device to be moored to the seabed. Therefore, this paper investigated the hydrodynamic performance of the offshore floating–moored OWC device shown in Fig. 2.13 using both physical scale model experiments and CFD simulations. The device performance was assessed for different design parameters include unidirectional regular and irregular waves of different heights and periods, PTO damping and mooring line pre–tension. The results were also compared with those for the stationary device of the same geometry tested in Papers 4 and 5.

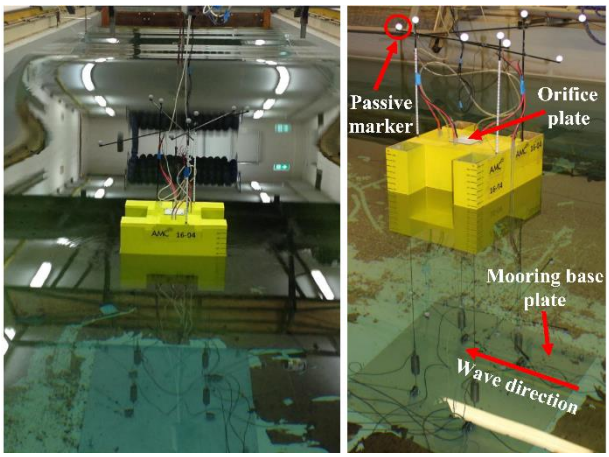

Fig. 2.13. AMC towing tank. Left: a general view showing the OWC model, looking towards the wavemaker, right: a closer view of the floating–moored OWC model

Results in Fig. 2.14 show that the hydrodynamic efficiency of the floating–moored OWC device followed the same general trend as the fully–constrained (fixed) device, but the floating device exhibited improved the power extraction efficiency (ζ) over a broader bandwidth around the chamber resonant frequency. Similar results were observed for (1) a larger regular wave height (H = 0.10 m), (2) higher and lower PTO damping factors, and (3) more realistic irregular wave conditions. Furthermore, for both fixed and floating–moored devices, increasing the incoming wave height resulted in a higher efficiency for low–frequency waves. Also, doubling the wave height increased the extracted pneumatic energy for the entire frequency range by about 2.5–7.7 times; the largest ratios were observed at the low–frequency zone.

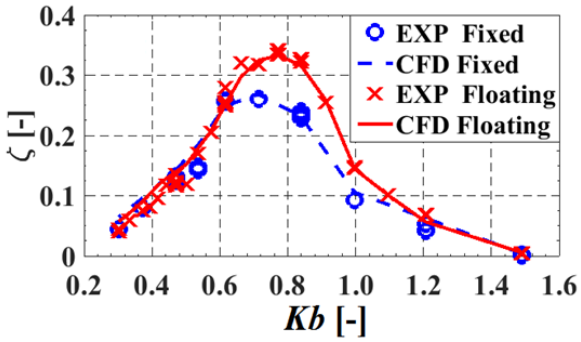

Fig. 2.14. Comparison between floating–moored and fixed OWC models for power extraction efficiency over a range of wave frequency (*Kb*) under a constant PTO damping and regular wave height $H = 0.05$ m

By investigating the relevance of each permitted degree of freedom of the floating device, CFD results in Fig. 2.15 demonstrated that among the three motion combinations (surge, heave and pitch), the improvement in the efficiency of the floating OWC device could be primarily attributed to the surge motion.

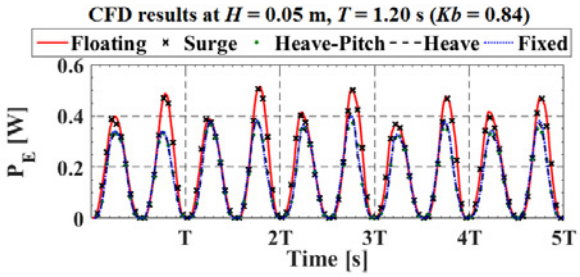

Fig. 2.15. CFD results showing the impact of the floating OWC device motions on the extracted pneumatic power (P_E) for $H = 0.05$ m and $T = 1.2$ s (scale 1:50)

Mooring line pre–tension did not have a significant effect on device efficiency, but a slight increase in the efficiency over the intermediate–frequency zone was found by reducing mooring line pre–tension. Overall, this study highlighted the possibility of harnessing a large amount of ocean wave energy using an OWC device that can be deployed in deep water where waves are more energetic.

2.7. Paper 7: Experimental and numerical measurements of wave forces on a 3D offshore stationary OWC wave energy converter

After assessing the hydrodynamic performance of offshore fixed and floating–moored OWC devices in Paper 2–6, wave forces on these devices were studies in this Paper and the next two Papers. In this paper, wave forces on the 1:50 scale model offshore stationary OWC device shown in Fig. 2.16 were studied in 3D physical and numerical wave tanks. 120 test conditions

systematically investigated two different incident wave heights H = 50 and 100 mm for a range of wave periods T = 0.9–2.0 s and six PTO damping conditions simulated by an orifice of different sizes. During the experiments, green water and water splashing were observed for wave conditions of H = 100 mm at high–frequencies (T = 0.9 and 1.0 s) (see Fig. 2.16 for green water and splashing events circled in red). Although the tested conditions did not include extreme waves, this was an important stage to understand the relevance of the different parameters tested and to validate the 3D CFD model before increasing the complexity of the hydrodynamic interactions between ocean waves and floating–moored OWC devices.

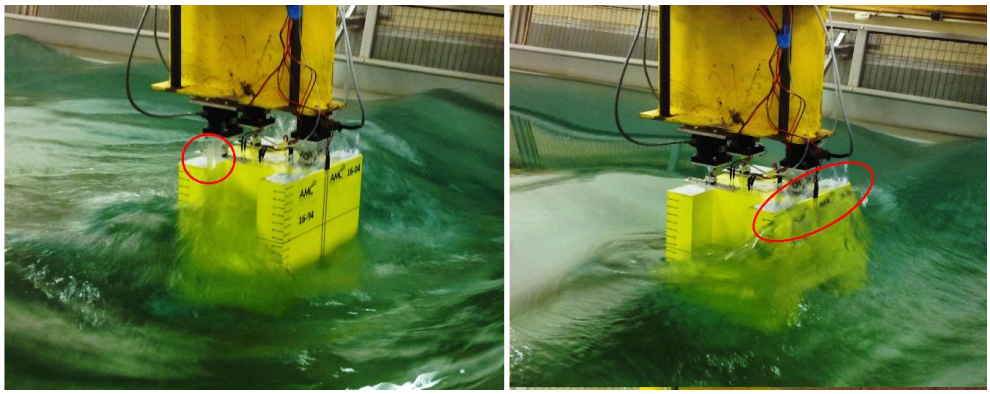

Fig. 2.16. Green water and splashing events on the 1:50 scale model offshore stationary OWC device under a regular wave condition of H = 100 mm and T = 0.9 s

It was found that the horizontal wave force acting on the OWC device was always larger than the vertical force up to a maximum of 12 times. The total horizontal and vertical forces had contrary trends over the entire frequency range such that the maximum horizontal and minimum vertical forces occurred almost at the same frequency at the intermediate–frequency zone. Furthermore, the PTO damping did not show a significant effect on the horizontal force, but the vertical force increased as PTO damping increased due to the increased chamber differential air pressure. This experimental finding supported the 2D CFD results of Elhanafi [34] (see Appendix K) who also found that the total vertical force was linearly proportional to the pneumatic force induced by the chamber differential air pressure on the chamber's top plate.

Results in Fig. 2.17 show that the forward (FWD) and aft (AFT) regions of the OWC device exhibited vertical forces larger than the total vertical force measured on the whole structure. Forces on both regions were different in magnitude and phase, which indicated a turning moment that needs to be considered in designing for station keeping (such as piles). This also highlighted that using the total vertical force to estimate the maximum vertical force on the structure can be misleading.

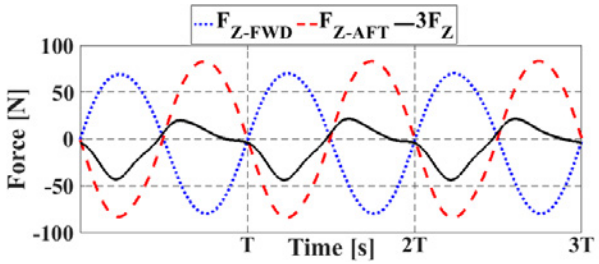

Fig. 2.17. Vertical wave force on the forward ($F_{Z\text{-}FWD}$) and aft ($F_{Z\text{-}AFT}$) load cells vs. the total vertical force (Fz) for a regular wave condition of height $H = 0.10$ m and period $T = 1.1$ s with a closed orifice

The CFD model was validated in good agreement with the physical measurements as shown in Fig. 2.18. The CFD was also utilized to investigate the effect of tank sidewalls on the predicted wave forces, and it was found that use of a tank width less than five times the breadth of the OWC device will likely provide misleading wave forces due to blockage effects.

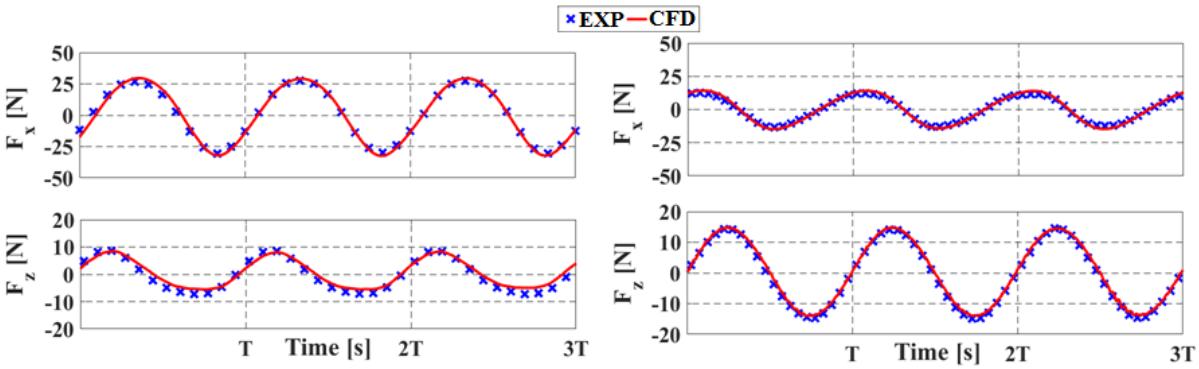

Fig. 2.18. Comparison between CFD and experiments (EXP) in predicting the total horizontal (F_X) and vertical (F_Z) wave forces on the offshore stationary OWC device under a constant wave height $H = 0.05$ m and closed orifice for two periods $T = 0.9$ s (left) and 2.0 s (right)

2.8. Paper 8: Intact and damaged survivability of an offshore floating–moored OWC device

This paper discussed the influence of mooring line failure for the floating–moored OWC device tested in Paper 6 when subjected to unidirectional regular waves. Refer the schematic diagram of the test rig shown in Fig. 2.19. A 3D CFD model was constructed and validated in good agreement against experiments for the floating–moored OWC device with a mooring line failure at different instants. The CFD model was then used to investigate mooring failure transient effects on maximum line tension. Two different mooring arrangements were studied; four–line arrangement: single line at each leg and eight–line arrangement: two lines at each leg (which represented a mooring system with redundancy). For each mooring arrangement,

different failure scenarios were investigated by breaking one mooring line at the forward starboard leg at several failure instants at and around the peak tension in that line. This single line failure represented 100 % and 50 % loss of mooring in one leg in case of four–line and eight–line arrangement, respectively. The transient overshooting in line tension was quantified for each failure scenario by comparing the maximum line tension in the damaged mooring system to the maximum tension achieved from the case when the damaged line was initially disconnected prior to running the experiment or the simulation.

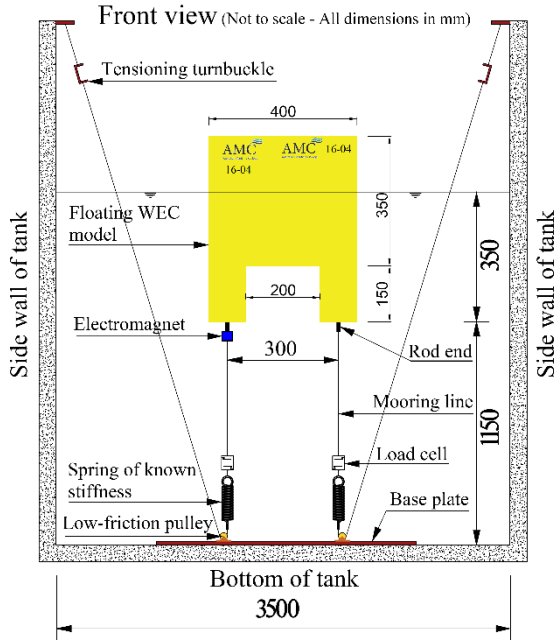

Fig. 2.19. Schematic diagram of test rig (not to scale)

It was found that (see Fig. 2.20) the forward port line in the four–line arrangement experienced the maximum tension with about 19 % transient overshooting effect due to breaking the forward starboard line at a certain instant before its peak tension. In case of having redundant mooring lines in the eight–line arrangement, transient effects in the forward port line reduced to 11 %, but the redundant line at the failure leg exhibited the maximum tension with 23 % transient overshooting effect. Although transient effects were higher in the case of the eight–line arrangement, the redundancy of this system relatively reduced the possibility of having a successive mooring line failure scenario by decreasing the maximum line tension of the remaining undamaged lines compared to the non–redundant mooring line failure scenario (four–line arrangement).

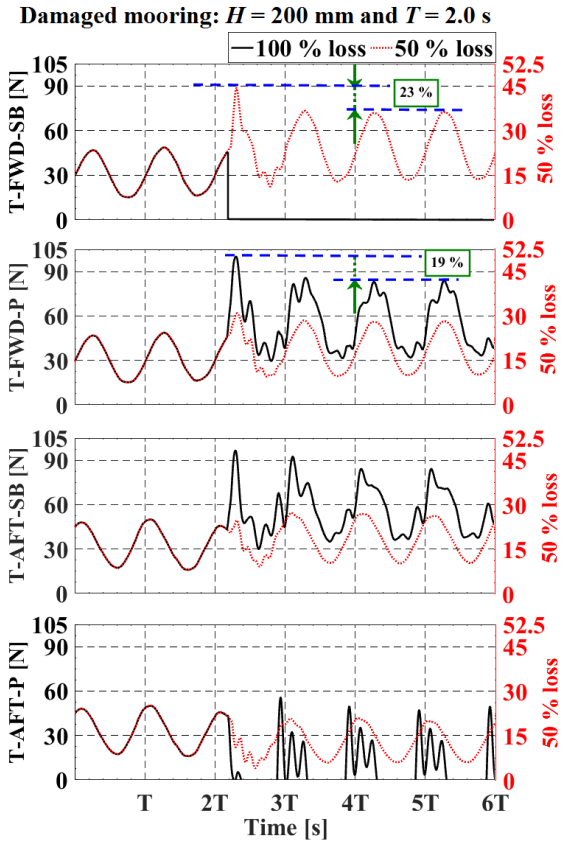

Fig. 2.20. Impact of mooring redundancy on line tension and transient effects. Left y–axis (black): line tension for the four–line arrangement (100 % loss) and right y–axis (red): line tension for the eight–line arrangement (50 % loss)

2.9. Paper 9: Experimental and numerical investigations on the intact and damage survivability of a floating–moored oscillating water column device

This paper investigated in detail the intact and damaged survivability of the floating–moored OWC device (which was preliminarily studied in Paper 8) using physical scale model experiments and CFD simulations. Different extreme wave conditions have been tested using unidirectional irregular and regular wave conditions, also the effect of mooring line pre–tension on the device response was tested. The survival conditions have been identified experimentally from seven different irregular sea states each lasted for a full–scale equivalent duration of 3–hours (consisting of sixteen random realisations) with an intact mooring system. It was found that (see Fig. 2.21) it is not always the largest wave height (see Figs. 2.21–b and 2.22–b) in an irregular sea state that causes the largest mooring line tension and surge, but it is the instantaneous position of the floating device that interacts with a series of waves and results in the extreme response (see Fig. 2.21–a and 2.22–a).

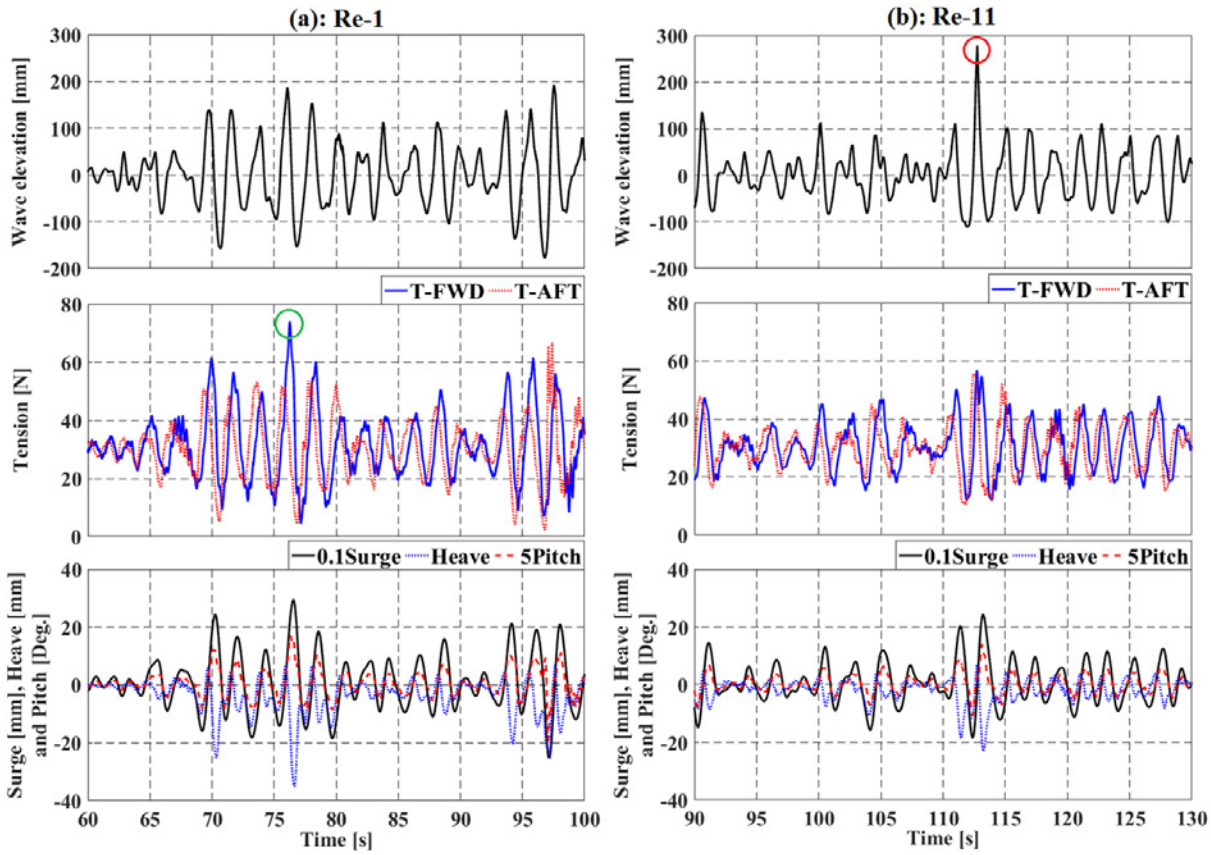

Fig. 2.21. Experimental time–series results for wave elevation approaching the OWC device, mooring tension in the forward (T-FWD) and aft (T-AFT) lines and OWC device motions during two different realisations (a) Re–1 and (b) Re–11 of sea state SS6 (significant height Hs = 220 mm and peak period Tp = 2.0 s) with pre–tension T_{pre}–1 (72 % of OWC device buoyancy)

Fig. 2.21 shows that the forward mooring lines exhibited the maximum tension. However, for the survival condition (SS6 Re–1 and T_{pre}–1), reducing the pre–tension from T_{pre}–1 (72 % of OWC device buoyancy) to T_{pre}–3 (36 % of OWC device buoyancy) significantly increased the maximum tension by about 1.57 times (from 74 N to 116 N) due to mooring slack events causing snatch loads in the aft lines.

It was also found that an equivalent design regular wave condition of a period (T) equal to the peak period (Tp) and a height (H) of 1.9–2.0 times the significant wave height (Hs) as recommended by DNV [35] for oil and gas offshore platforms could reasonably estimate the maximum line tension as the irregular sea state, but a smaller wave height of about $H = 1.75H$s was required to achieve the maximum surge and avoid overestimation the surge motion by 13 % when using $H = 1.9H$s.

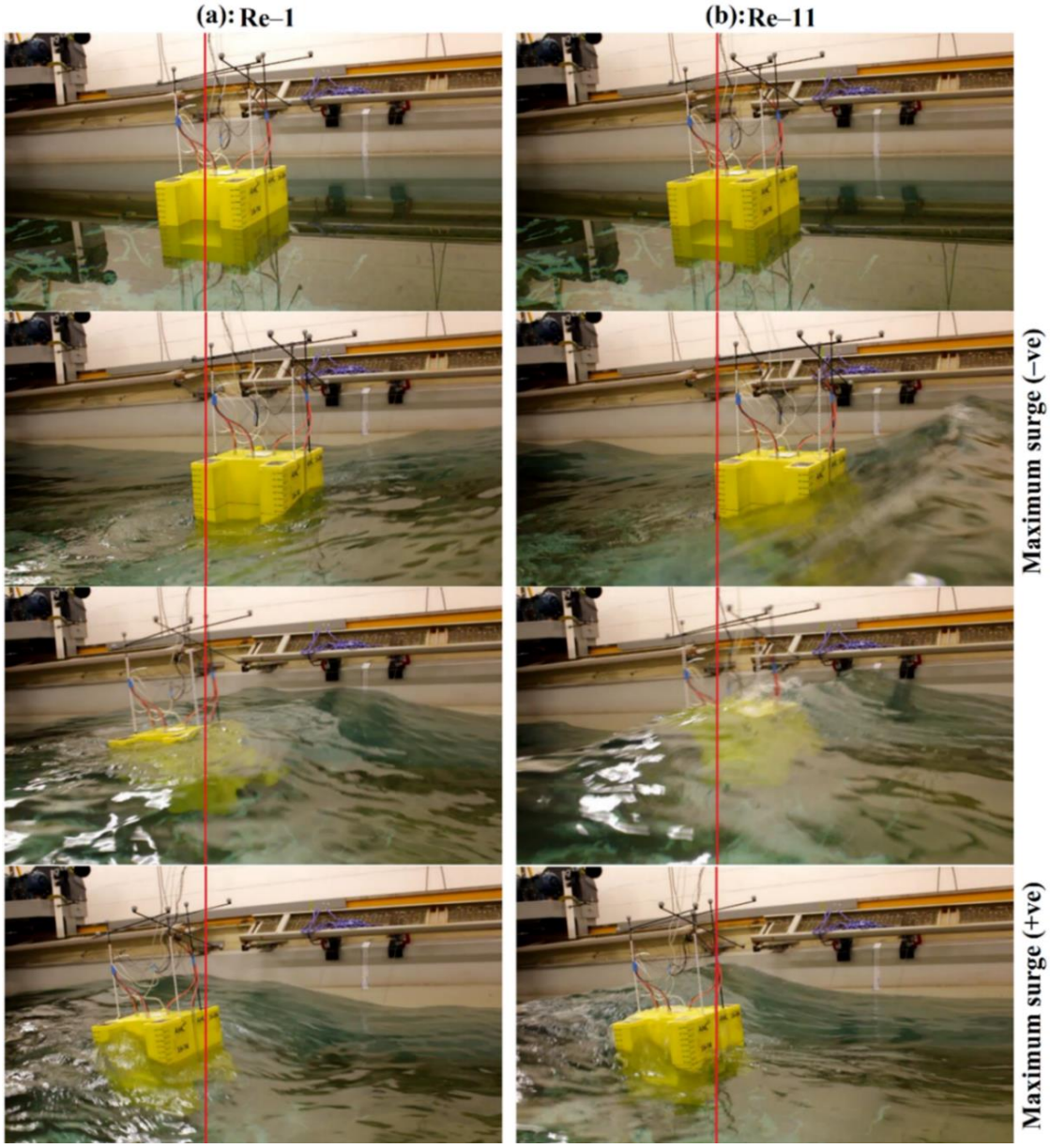

Fig. 2.22. Photographs taken during the experiments showing the OWC device position at four instants during realisations (a) Re–1 and (b) Re–11 of sea state SS6 with T_{pre}–1. The red vertical line provides a reference frame to track the longitudinal position of the model

For the survival condition of SS6 Re–1 and T_{pre}–1, a single failure in the mooring system (in the forward starboard line) increased the maximum tension by 1.55 times the intact tension (i.e., from 74 N to 115 N, see Fig. 2.23). By applying the same safety factors recommended by DNV [36] for offshore oil and gas platforms to the intact and damaged mooring systems tested in this study, it was found that the survivability analysis with the damaged mooring system resulted in a higher minimum breaking load requirements, which in turn indicated that this analysis was the key analysis in designing the mooring system of the floating–moored OWC device.

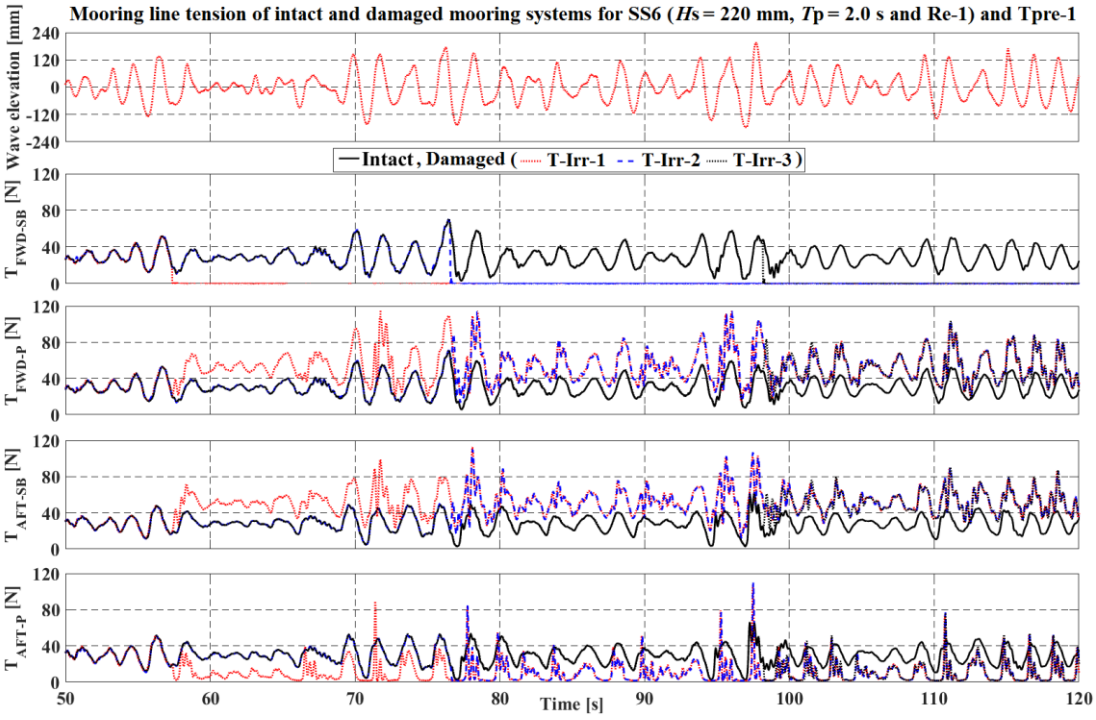

Fig. 2.23. Experimental time–series results showing the effect of breaking the forward starboard line at different instants (T–Irr–1, T–Irr–2, T–Irr–3) on the tension in the remaining intact lines under irregular sea state SS6 (realisation Re–1) and pre–tension T_{pre}–1

For the damaged mooring system, using the same design regular wave condition (H = 1.9–2.0Hs and T = Tp) derived from the survivability analysis with an intact mooring system resulted in overestimating the maximum tension by more than 20 % in comparison to the tension obtained from the irregular sea state. To avoid increasing the cost of the mooring system due to overprediction of mooring maximum tension, smaller regular wave heights H = 1.14–1.36 Hs and H = 1.64 Hs could be used and lead to the same maximum tension of the irregular sea state (about 115 N) and the maximum surge respectively, especially when considering the transient effects discussed in Paper 8 with the CFD model that was validated in good agreement with experiments as shown in Fig. 2.24.

Also, a different regular wave condition (for example, H = 2.03 Hs and T = Tp = 1.45 s) representing another sea state (SS3: Hs = 160 mm and Tp = 1.45 s) that might not be considered as a survival condition in the case of intact mooring system (resulted in a maximum intact tension of only 58 N compared to 74 N for SS6) could result in a maximum line tension of 117 N in the case of a damaged mooring system (see Fig. 2.25). This maximum tension was slightly higher than that for SS6 with a damaged mooring system (115 N), which in turn highlighted the importance of researching for the survival conditions with a damaged mooring system instead of simply using the same conditions derived for the intact mooring system.

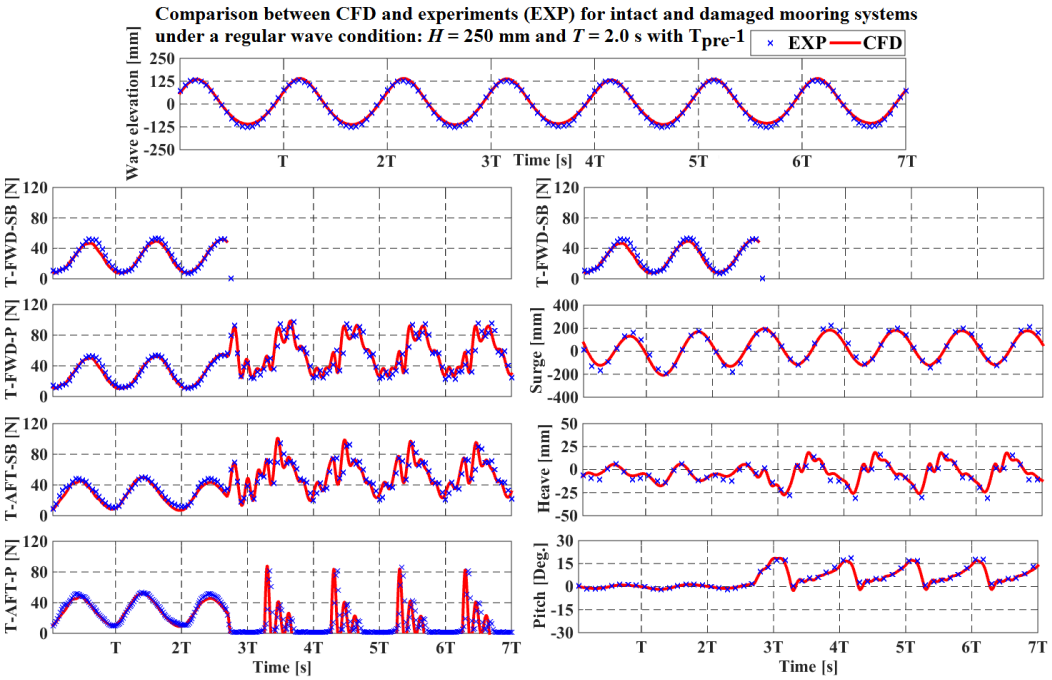

Fig. 2.24. Comparison between CFD and experiments (EXP) for mooring line tension and OWC device motions with a damaged mooring system under regular waves of H = 250 mm and T = 2.0 s

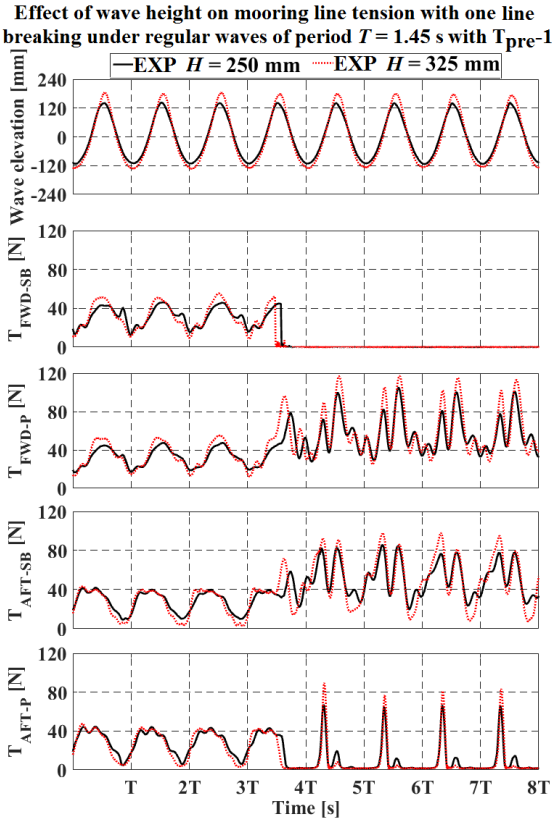

Fig. 2.25. Experimental time–series results showing the effect of breaking the forward starboard line on the tension in the remaining intact lines under regular wave conditions of the same period T = 1.45 s and different heights

Chapter 3

Conclusions and Future Work

3.1. Conclusions

In this thesis, the hydrodynamic performance and survivability of OWC devices were investigated using physical scale model experiments and Computational Fluid Dynamic (CFD) simulations. During the operating conditions the following main aspects were studied (1) regular and irregular wave conditions, (2) PTO damping, (3) underwater geometry, (4) 3D effects, (5) air compressibility and scaling effects and (6) wave forces. A CFD model based on RANS–VOF approach was developed in this study not only to monitor the basic parameters required to predict the efficiency of an OWC device such as chamber free surface elevation and differential air pressure, but also to capture detailed flow field (velocity and vorticity) measurements. The model was validated in good agreement with different model–scale tests for 2D OWC devices from previously published research and experiments performed in this study for 3D offshore stationary and floating–moored OWC devices. In particular, the good agreement against 2D PIV (Particle Imaging Velocimetry) measurements for an onshore OWC device demonstrates the CFD capability of capturing more detailed information and providing a better understanding of the flow behaviour inside and around the OWC chamber as well as identifying areas of high energy losses that need further modifications for maximizing the efficiency. For example, the developed CFD model was successfully employed to (1) perform energy balance analysis for onshore and offshore–stationary OWC devices and (2) improve the device efficiency by optimising the underwater geometry and relate the front lip draft to the incoming wave height.

Under extreme wave conditions, the survivability of a floating–moored OWC device subjected to irregular waves of different sea states was assessed experimentally with a focus on the maximum surge and mooring line tension. The applicability of using the safety factors and the design regular wave conditions recommended for offshore oil and gas structures was discussed using CFD and experiments with an intact mooring system as well as with a single mooring line failure.

The following main conclusions can be drawn from the studies performed in this thesis:

- Although increasing the incoming wave height increased the energy losses, more wave energy could still be extracted such that doubling the regular and irregular wave heights increased the extracted pneumatic energy in the range of 2.5–7.7 times depending on the wave frequency and the applied PTO damping [Papers 1, 2, 6 and 12].

- To improve the power extraction efficiency of an offshore OWC device, it is important to select the lip submergence and thickness that provide an efficient path for the water particles to enter and leave the chamber without obstructing the flow field. In particular, the immersed depth of both front and rear lips represents a crucial design parameter in optimizing offshore OWC devices for a higher efficiency [Paper 3]. For regular waves, to avoid air leakage underneath the chamber lip while maintaining a high efficiency, a front lip draught equal to the amplitude of the maximum expected wave height during the operational conditions is recommended. For example, a significant improvement in the efficiency up to 0.97 was achieved when shortening the front lip to be equal to the incident wave amplitude and extending the rear lip to 23 % of the water depth [Paper 4].

- Modelling offshore OWC devices in a 2D domain or a narrow wave flume should only be used to provide a general insight into the effect of different design parameters such as wave conditions and underwater geometries on device efficiency, but 3D modelling is required to accurately predict the device efficiency, especially when wave diffraction is important for the high–frequency waves where 2D and narrow wave flumes significantly overestimate the efficiency [Paper 4].

- Neglecting air compressibility effects at full–scale could result in about 12 % over–estimation in the device maximum efficiency at its resonant period and optimum damping. To account for this effect with errors not exceeding 1.2 % while physically testing a small–scale OWC model, the air chamber volume must be scaled using squared (rather than cubed) scale factor (based on Froude's similitude law), and air must be modelled as a compressible fluid in case of using CFD [Paper 5].

- When estimating wave forces on a fixed offshore OWC device it is essential to consider the phase–shift between the measured vertical forces on the forward and aft regions of the device rather than using the total vertical force to design the foundations. Also, the PTO damping was found to only affect the vertical forces, which increased with

increasing PTO damping. Wave forces must be measured in a tank of a width not less than five times the OWC model breadth to avoid blockage effects [Paper 7].

- In comparison to a fixed (fully–constrained) offshore OWC device, the surge motion of the floating–moored OWC model enables the device to absorb more incoming wave energy, which in turn improves the device efficiency in regular and irregular waves. This highlights the possibility of harnessing a large amount of ocean wave energy using an OWC device that could be deployed in deep water where waves are more energetic [Paper 6].
- It is paramount to assess the survivability of floating–moored OWC devices, but this is challenging due to the random nature of the survival wave conditions and their interactions with the device dynamics. A survival wave condition could be a series of waves that do not include the largest wave of a given irregular sea state, but their interactions with the instantaneous position of the floating device could result in the extreme response. Investigating the device survivability with a damaged mooring system highlighted the importance of testing several survival conditions that might be different from those used with an intact mooring system. Using a single design regular wave condition equivalent to the survival sea state along with the current safety factors (that are recommended for offshore oil and gas platforms) when assessing the device survivability with a damaged mooring system can result in over–designing the mooring system [Paper 9].
- A mooring system with redundancy (eight–line arrangement) may experience a higher tension overshooting due to the transient effects induced by a single mooring line failure. This was pronounced at the redundant line in the failure leg. However, the maximum tension in the redundant system with a single mooring line failure was smaller than that for a mooring system with a single mooring line failure without redundancy (four–line arrangement). This highlights the advantage of using a redundant system to reduce the possibility of a successive mooring line failure scenario [Paper 8].

3.2. Future Work

The relationship between the incoming wave height and front lip draught was discussed in this study for maximizing the device efficiency without causing air leakage events. However, the conclusion drawn from this study was based on deterministic regular wave conditions of a

certain wave height. Therefore, it is necessary to investigate how the front lip draught can be correlated to more realistic irregular wave conditions. This can be carried out using the CFD model developed in this study upon validation with irregular wave conditions. Although results in this study did not show strong evidence of scaling effects with incompressible air, one might expect to have scaling effects from vortex shedding, viscous effects and other physical phenomena that do not typically scale with Froude's similitude law. Accordingly, further analyses including detailed flow field (velocity and vorticity) as performed in Papers 1–3 are considered as a future work together with additional experimental measurements at different scales as applicable.

Using only unidirectional waves, the dynamics of the floating–moored OWC device were proven to be vital in the survivability analysis and in improving the power harnessing efficiency through the surge motion. Therefore, further studies can still be performed to investigate the effect the direction of the incident waves has on device performance and survivability. In that case, several mooring line failure scenarios can be tested including failures in the aft mooring lines. Although there was a very good agreement between CFD and experiments in capturing the device response in extreme regular wave conditions with intact and damaged mooring systems, further validations are still required against experiments of more realistic sea states. This can be performed by utilizing the methodology provided in Gao et al. [37] to model and predict the device response under the action of an irregular time–series window such as that from sea state SS6 (realisation Re–1) tested in this study.

The higher air pressure developed inside the OWC chamber under the extreme wave conditions tested in this study highlights the importance of investigating air compressibility and scaling effects under such survival conditions in order to accurately predict the extreme response. For the vertical taut mooring system and the water depth tested in this study, neglecting mooring line dynamics in CFD modelling was found to be acceptable even when stanch loads occur with a damaged mooring system. However, for a catenary mooring system, this assumption needs to be verified. This verification requires a fully coupled CFD–mooring analysis with a finite element solver for the mooring cables rather than using a simplified spring. At the submission time of this thesis, this coupling still does not exist in any commercial CFD codes, and very limited research has been performed on this subject, mostly restricted to intact mooring systems [38, 39].

References

[1] Veigas M, López M, Iglesias G. Assessing the optimal location for a shoreline wave energy converter. Applied Energy. 2014;132:404-11.

[2] Falcão AFdeO. Wave energy utilization: A review of the technologies. Renewable and sustainable energy reviews. 2010;14:899-918.

[3] Fadaeenejad M, Shamsipour R, Rokni SD, Gomes C. New approaches in harnessing wave energy: With special attention to small islands. Renewable and Sustainable Energy Reviews. 2014;29:345-54.

[4] Drew B, Plummer AR, Sahinkaya MN. A review of wave energy converter technology. Proceedings of the Institution of Mechanical Engineers, Part A: Journal of Power and Energy. 2009;223:887-902.

[5] The World Energy Council. World Energy Resources.

https://www.worldenergy.org/wp-content/uploads/2016/10/World-Energy-Resources-Full-report-2016.10.03.pdf [last accessed April 19, 2017].

[6] Mork G, Barstow S, Kabuth A, Pontes MT. Assessing the global wave energy potential. In: Proceedings of 29th International Conference on Ocean, Offshore and Arctic Engineering, American Society of Mechanical Engineers (ASME), June 6-11, Shanghai, China 2010.

[7] Reguero BG, Losada IJ, Méndez FJ. A global wave power resource and its seasonal, interannual and long-term variability. Applied Energy. 2015;148:366-80.

[8] Enerdata. Global Energy Statistical Yearbook 2016.

https://yearbook.enerdata.net/#electricity-domestic-consumption-data-by-region.html [Last accessed April 19. 2017].

[9] The World Energy Council. 2010 Survey of Energy Resources.

https://www.worldenergy.org/wp-content/uploads/2012/09/ser_2010_report_1.pdf [Last accessed April 19, 2017].

[10] Hemer MA, Griffin DA. The wave energy resource along Australia's southern margin. Journal of Renewable and Sustainable Energy. 2010;2:043108.

[11] Falcão AFO, Henriques JCC. Oscillating-water-column wave energy converters and air turbines: A review. Renewable Energy. 2015;85:1391-424.

[12] Teixeira PRF, Davyt DP, Didier E, Ramalhais R. Numerical simulation of an oscillating water column device using a code based on Navier–Stokes equations. Energy. 2013;61:513-30.

[13] Iturrioz A, Guanche R, Armesto JA, Alves MA, Vidal C, Losada IJ. Time-domain modeling of a fixed detached oscillating water column towards a floating multi-chamber device. Ocean engineering. 2014;76:65-74.

[14] Yu Y-H, Van Rij J, Coe R, Lawson M. Preliminary wave energy converters extreme load analysis. In: Proceedings of 34th International Conference on Ocean, Offshore and Arctic Engineering, American Society of Mechanical Engineers (ASME), May 31–June 5, St. John's, Newfoundland, Canada, 2015.

[15] Bull D, Ochs ME. Technological cost-reduction pathways for oscillating water column wave energy converters in the marine hydrokinetic environment. Published by Sandia National Laboratories, Report: SAND2013-7205, September, 2013.

[16] Weller S, Johanning L, Davies P. Best practice report–mooring of floating marine renewable energy devices. Deliverable 3.5.3 from the MERiFIC Project. 2013.

[17] Coe RG, Neary VS, Lawson M, Yu Y, Weber J. Extreme conditions modeling workshop report. National Renewable Energy Laboratory and Sandia National Laboratories, Technical Report: NREL/ TP-5000-62305 - SNL/ SAND2014-16384R, July, 2014.

http://www.nrel.gov/docs/fy14osti/62305.pdf [Last accessed April 23, 2017].

[18] Christensen L, Friis-Madsen E, Kofoed JP. The wave energy challenge: the wave dragon case. In: Proceedings of PowerGen 2005 Europe conference, June 28-30, Milan, Italy, 2005.

[19] ABC-News. Huge swell sinks wave energy generator, May 2010. ABC-News.

http://www.abc.net.au/news/2010-05-17/huge-swell-sinks-wave-energy-generator/829282. [Last accessed April 23, 2017].

[20] Zanuttigh B, Martinelli L, Castagnetti M. Screening of suitable mooring systems. Structural Design of Wave Energy Devices (SDWED), Derivable D21, Department of Civil Engineering, Aalborg University, Denmark 2012.

[21] CD-Adapco. User Guide STAR-CCM+ Version 10.02. 2015.

[22] ITTC. Testing and extrapolation methods loads and responses, ocean engineering, floating offshore platform experiments , ITTC Report: 7.5-02 07-03.1. 2002.

[23] ITTC. Recommended procedures and guidelines: guide to the expression of uncertainty in experimental hydrodynamics, ITTC Report: 7.5-02-01-01. 2008.

[24] ITTC. Recommended procedures and guidelines: seakeeping experiments, ITTC Report: 7.5-02 07-02.1. 2011.

[25] López I, Pereiras B, Castro F, Iglesias G. Performance of OWC wave energy converters: influence of turbine damping and tidal variability. International Journal of Energy Research. 2015;39:472-83.

[26] Graw K-U, Schimmels S, Lengricht J. Quantifying losses around the lip of an OWC by use of particle image velocimetry (PIV). LACER-Leipzig Annual Civil Engineering Report, Aalborg, Denmark. 2000.

[27] López I, Castro A, Iglesias G. Hydrodynamic performance of an oscillating water column wave energy converter by means of particle imaging velocimetry. Energy. 2015;83:89-103.

[28] Fleming AN, Macfarlane GJ. Experimental flow field comparison for a series of scale model oscillating water column wave energy converters. Marine Structures. 2017;52:108-25.

[29] Ferguson TM, MacFarlane G, Fleming A, Penesis I. PIV investigation of 3-dimensional flow within an oscillating water column. International Journal of Marine Energy. 2015;11:120-31.

[30] He F, Huang Z. Hydrodynamic performance of pile-supported OWC-type structures as breakwaters: An experimental study. Ocean Engineering. 2014;88:618-26.

[31] Pereiras B, López I, Castro F, Iglesias G. Non-dimensional analysis for matching an impulse turbine to an OWC (oscillating water column) with an optimum energy transfer. Energy. 2015;87:481-9.

[32] He F, Li M, Huang Z. An experimental study of pile-supported OWC-type breakwaters: energy extraction and vortex-induced energy loss. Energies. 2016;9:540.

[33] Chakrabarti SK. Hydrodynamics of Offshore Structures: Springer Verlag.; 1987.

[34] Elhanafi A. Prediction of regular wave loads on a fixed offshore oscillating water column-wave energy converter using CFD. Journal of Ocean Engineering and Science. 2016;1:268-83.

[35] DNV. Environmental Conditions and Environmental Loads. DNV-RP-C205. 2014.

[36] DNV. Position Mooring. DNV-OS-E301. 2010.

[37] Gao N, Yang J, Zhao W, Li X. Numerical simulation of deterministic freak wave sequences and wave-structure interaction. Ships and Offshore Structures. 2016;11:802-17.

[38] Palm J, Eskilsson C, Paredes GM, Bergdahl L. Coupled mooring analysis for floating wave energy converters using CFD: Formulation and validation. International Journal of Marine Energy. 2016;16:83-99.

[39] Nicholls-Lee R, Walker A, Hindley S, Argall R. Coupled multi-phase CFD and transient mooring analysis of the floating wave energy converter OWEL. In: Proceedings of 32nd International Conference on Ocean, Offshore and Arctic Engineering, American Society of Mechanical Engineers (ASME), June 9-14, Nantes, France, 2013.

Appendix A

Paper 1: Elhanafi A, Fleming A, Macfarlane G, Leong Z. Numerical energy balance analysis for an onshore oscillating water column–wave energy converter. *Energy. 2016;116(1):539-557.*

Appendix B

Paper 2: Elhanafi A, Fleming A, Macfarlane G, Leong Z. Numerical hydrodynamic analysis of an offshore stationary–floating oscillating water column–wave energy converter using CFD. *International Journal of Naval Architecture and Ocean Engineering. 2017;9(1):77–99*.

Available online at www.sciencedirect.com

ScienceDirect

Publishing Services by Elsevier

International Journal of Naval Architecture and Ocean Engineering 9 (2017) 77–99

http://www.journals.elsevier.com/international-journal-of-naval-architecture-and-ocean-engineering/

Numerical hydrodynamic analysis of an offshore stationary–floating oscillating water column–wave energy converter using CFD

Ahmed Elhanafi*, Alan Fleming, Gregor Macfarlane, Zhi Leong

National Centre for Maritime Engineering and Hydrodynamics, Australian Maritime College, University of Tasmania, Launceston, Tasmania 7250, Australia

Received 21 March 2016; revised 9 July 2016; accepted 9 August 2016

Available online 1 October 2016

Abstract

Offshore oscillating water columns (OWC) represent one of the most promising forms of wave energy converters. The hydrodynamic performance of such converters heavily depends on their interactions with ocean waves; therefore, understanding these interactions is essential. In this paper, a fully nonlinear 2D computational fluid dynamics (CFD) model based on RANS equations and VOF surface capturing scheme is implemented to carry out wave energy balance analyses for an offshore OWC. The numerical model is well validated against published physical measurements including; chamber differential air pressure, chamber water level oscillation and vertical velocity, overall wave energy extraction efficiency, reflected and transmitted waves, velocity and vorticity fields (PIV measurements). Following the successful validation work, an extensive campaign of numerical tests is performed to quantify the relevance of three design parameters, namely incoming wavelength, wave height and turbine damping to the device hydrodynamic performance and wave energy conversion process. All of the three investigated parameters show important effects on the wave–pneumatic energy conversion chain. In addition, the flow field around the chamber's front wall indicates areas of energy losses by stronger vortices generation than the rear wall.

Keywords: Offshore oscillating water column; OWC; Wave energy; Energy balance; Numerical wave tank

1. Introduction

Wave energy is one of the most promising renewable energy resources and research is being conducted worldwide. There is a large number of invented techniques for wave energy conversion which can be categorised by deployment location (shoreline, nearshore and offshore), type (attenuator, point absorber and terminator) and mode of operation (submerged pressure differential, oscillating wave surge converter, oscillating water column and overtopping device) (Drew et al., 2009).

The Oscillating Water Column (OWC) is a wave energy extraction device that is based on wave to air energy conversion by driving an oscillating column in a chamber open to the sea. The air energy is extracted by means of a bi–directional air turbine connected to the chamber. As the water level oscillates up and down inside the chamber, the air inside it is compressed and decompressed, respectively. In turn, this process generates mechanical energy through a reversible flow between the atmosphere and the chamber utilizing an air turbine that rotates in the same direction regardless of the airflow direction. Different from other Wave Energy Converters (WEC), OWCs are not only one of the simplest devices from an operational point of view, but also having no moving parts underwater provides lesser and easier maintenance works. OWCs can be deployed as fixed structures at the shoreline or nearshore, or integrated in breakwaters and floating structures (Falcão and Henriques, 2015).

Investigating the hydrodynamic performance of OWCs has been studied analytically, experimentally, numerically or a combination of the aforementioned. A theoretical model of the

* Corresponding author.
E-mail address: Ahmed.Elhanafi@utas.edu.au (A. Elhanafi).

Peer review under responsibility of Society of Naval Architects of Korea.

http://dx.doi.org/10.1016/j.ijnaoe.2016.08.002

hydrodynamics for a fixed OWC device was developed by Evans (1978). Ignoring the spatial variation, Evans assumed a rigid weightless piston motion for the chamber's internal free surface of a small width relative to the incident wavelength, which allowed the application of the oscillating body theory. Falcão and Sarmento (1980), Evans (1982) and Falnes and McIver (1985) improved the rigid–body approach of an OWC via allowing the increase in pressure at the free surface as well as providing the possibility of a non–plane surface.

With the aim of validating the oscillating surface pressure theory proposed by Sarmento and Falcão (1985) in OWCs, Sarmento (1992) conducted a set of wave flume experiments with regular waves of very small steepness under linear, as well as quadratic, power take–off (PTO) simulated by either filters or orifice plate, accordingly. Hong Hong et al. (2007) performed a 2D experiment concentrating on the effects of several shape parameters of OWC chamber in wave energy absorbing capability. Morris-Thomas et al. (2007) performed experiments in a wave flume to investigate the influence of the chamber's front wall thickness, shape and draught under various wave parameters on the hydrodynamic efficiency of a shore–based OWC device.

Generally, numerical models can be divided into two categories; the first category is based on applying potential flow theory, which is usually solved with a boundary element method (BEM). Extensive review of potential flow models can be found in Baudry et al. (2013). The second category, which is applied in the present study, is based on Reynolds–averaged Navier–Stokes (RANS) equations, which provides more advantages in overcoming the potential flow weaknesses in handling problems that involve strong nonlinearity, dispersion, wave breaking, complex viscous, turbulence and vortex shedding. This method is widely used by several researchers; examples that are most relevant to the present study include Zhang et al. (2012) who developed, validated and studied the impact the geometrical parameters have on a shore–based OWC efficiency curve using a 2D two–phase numerical wave tank based on a level–set immersed boundary method. They reported a reasonable agreement with experimental data measured by Morris-Thomas et al. (2007) for the device hydrodynamic efficiency with a slight over–prediction attributed to the complex pressure changes in the chamber around resonance. Additional parameters such as pressure variation, free surface elevation inside the chamber and flow field were presented and discussed, but without comparison to experimental data. Teixeira et al. (2013) implemented a numerical model (Fluinco) based on the two–step semi–implicit Taylor–Galerkin method to simulate a fixed OWC device subjected to regular waves. After validating their model against numerical results from the commercial CFD code Fluent, they investigated the effects of the chamber geometry including the front wall depth, chamber length, chamber height and the turbine characteristic relation that provide the best device performance. Luo et al. (2014) implemented a 2D numerical model using a commercial CFD code (Fluent) to investigate the effect of wave nonlinearity on the capture efficiency of an onshore OWC device. López et al. (2014, 2016) studied the importance of different turbine damping coefficients on the performance of an onshore OWC device under regular and irregular waves to determine the optimum turbine–induced damping on an OWC device using a 2D commercial CFD model (Star–CCM+). Kamath et al. (2015a, 2015b) utilized a 2D open–source CFD model (REEF3D) to simulate and study the interaction of a fixed shore–based OWC with regular waves of different wavelengths and steepness, and also investigated the response of the OWC under different damping values from the PTO device.

Quantifying the energy losses inside OWCs has not been studied extensively in comparison with the considerable research effort focused on the overall hydrodynamic performance and geometry optimization of onshore OWCs. Always in such research, there is a part of the incoming wave energy that is assumed to be lost inside the OWC system; however, only a few researchers have paid more attention to either visualizing and/or quantifying such losses. Only via visualizing the flow behaviour in a shoreline OWC, Müller and Whittaker (1995) highlighted different energy loss mechanisms. Tseng et al. (2000) experimentally estimated about 33%–68% energy losses throughout the energy conversion chain for a multi–resonant cylindrical caisson. Similarly, Mendes and Monteiro (2007) carried out a series of wave tank experiments on a shoreline OWC under regular waves. In addition to studying the energy conversion chain and estimating the energy losses, they visualized the flow inside the OWC using a sequence of video–frames to discover the energy dissipation physics.

Furthermore, by utilizing advanced measurement techniques such as particle imaging velocimetry (PIV), a detailed flow field picture can be obtained. For instance, using PIV, Morrison (1995) calculated the kinetic energy and viscous dissipation rates in a shore–based OWC. Graw et al. (2000) studied the impact of an onshore OWC underwater geometry such as the front lip shape and its inclination on the energy losses in the vicinity of the lip over four wave frequencies. They concluded that at low frequencies with the cornered lip shape, the mean energy losses over one cycle (mean dissipation divided by the mean power) may be as much as 15%. Within the wave energy balance framework, Fleming et al. (2011, 2012a, 2012b and 2013) utilized flow field measurements using PIV in a forward facing bent duct OWC with a phase–averaging technique to perform detailed energy balance analyses considering different energy sources, stores and sinks components. López et al. (2015) applied Reynolds decomposition technique to estimate the turbulent kinetic energy in a shore–based OWC by resolving the velocity fluctuations from PIV measurement. Using this methodology, they investigated the relevance of different wave conditions, PTO pneumatic damping and change in tidal level on the OWC hydrodynamic performance. With respect to numerical modelling, Elhanafi et al. (2016b) developed a 2D numerical model based on RANS–VOF with validation against experimental results including PIV data. Building on the achieved good agreement, they applied their model to further investigate the impact of increasing the incident wave amplitude and

turbine damping on the energy conversion process in a fixed bottom–standing OWC device.

All of the abovementioned publications consider the common fixed onshore or nearshore types of OWC devices where the chamber rear wall is resting on the shoreline or extending to the seabed, respectively. Thus, no wave energy can be transmitted behind these OWC structures. In contrast, offshore OWCs are typically floating structures that allow ocean waves to pass around and underneath the device walls; accordingly, the incoming wave energy decomposition will consider an additional sink component for the transmitted wave energy. Subsequently, this will change the wave energy balance model, and affect the absorbed energy, extracted energy and the design parameters. Research on assessing the offshore OWCs performance is limited in comparison with the shore–based OWCs. In this regard, He and Huang (2014) and He et al. (2012, 2013) experimentally studied a pile–supported and a floating rectangular breakwater with pneumatic damping, respectively. In their study, more attention was given for the shore protection objective through quantifying the relevance of different design parameters such as wave frequency, pneumatic damping and the device draught to the transmission, reflection, air pressure and loss coefficients. Energy dissipation was assumed to come from two sources: vortex shedding at the tips of the chamber walls and the pneumatic power. This assumption was properly given due to the high cost and risk associated with required instruments to visualize and evaluate these losses such as using PIV. Although air pressure coefficients describing the pressure fluctuation inside the OWC chamber were measured, no output power measurements were given, and only one wave height representing weakly nonlinear waves with a maximum steepness of 0.029 and 0.023 for the fixed and floating OWC, respectively. Within the potential flow theory and its abovementioned shortcomings, Hong et al. (2004) investigated the motion and the drift force of a free floating OWC in regular waves. Sheng et al. (2014) utilized experimental data to validate a potential flow solver (WAMIT) in simulating a floating cylindrical OWC. Recently, Iturrioz et al. (2014, 2015) developed and validated a CFD model based on RANS–VOF using open source code (IHFOAM) with flume tank experiments to study the hydrodynamics and pneumatics around a fixed detached OWC. Crema et al. (2015) experimentally investigated the pneumatic efficiency of an OWC to be installed on a floating platform. The OWC device has back and side walls extending deeply in the water to increase the water column oscillation by increasing wave reflection, and their study included different geometrical parameters and both regular and irregular waves under different pneumatic damping. Simonetti et al. (2015) presented the numerical settings of an open source CFD code (OpenFOAM) and validation results against physical measurements of a similar OWC device tested by Crema et al. (2015). However, none of these studies investigate the impact of the wave height and the PTO damping on the offshore OWC hydrodynamic efficiency and wave energy conversion process through a detailed wave energy balance analysis, which is a part of the added values of the present work.

Providing a better understanding of the hydrodynamic performance of offshore OWCs through a detailed wave energy balance analysis is the driving force behind the present study. In this way, the present paper utilizes a 2D numerical model based on RANS equations solver with a VOF surface capturing scheme introduced by Hirt and Nichols (1981) to investigate the hydrodynamics of a stationary–floating offshore OWC device. With the CFD model, the OWC hydrodynamic performance is deeply investigated via a series of numerical wave energy balance analyses under different design parameters such as incoming wave height and frequency and PTO damping. The analysis includes the variation of the free surface, air pressure and airflow rate inside the chamber and the incident wave energy decomposition into reflected, transmitted, absorbed, extracted, stored and losses. Additionally, a detailed flow field analysis is conducted to uncover the energy losses mechanism through the vortex generation and dissipation processes.

2. Numerical model

2.1. Governing equations and numerical settings

In the present study, the numerical model assumes incompressible flow in the OWC chamber considering that air compressibility effect is negligible in the small model scale used herein. The flow motion of the incompressible fluid is described by the continuity and RANS equations. In RANS, the instantaneous velocity and pressure fields in the Navier–Stokes equations are decomposed into mean and fluctuating components, and then time–averaged. This process results in additional unknowns called Reynolds stresses that need to be modelled. In this paper, the two–equation Shear Stress Transport (SST) $k-\omega$turbulence model is implemented to model the Reynolds stresses in order to mathematically close the problem. Star–CCM + code is utilised to solve the flow sets of equations. The numerical model settings are as follows, time modelling: implicit unsteady with second–order temporal discretization scheme, flow modelling: segregated flow model with second–order upwind scheme (the segregated flow solver controls the solution update for the segregated flow model according to the SIMPLE algorithm) and multiphase model: VOF with segregated VOF solver that controls the solution update for the phase volume fractions (i.e. solve the discretized volume–fraction conservation equation for each phase present in the flow) with second–-order convection (CD-Adapco, 2015).

2.2. Computational fluid domain

Ocean waves are the primary exciting source acting on offshore structures such as OWCs and therefore, accurate modelling of these waves is crucial for providing a good estimation of the hydrodynamic loads and predict the structure's response and performance (Elhanafi et al., 2016a). The computational domain considered herein is divided into three main regions namely: domain, free surface and OWC, as

illustrated in Fig. 1. Domain lengths with different damping zone lengths are studied in order to properly select the location of the OWC and wave probe array along the tank. This study revealed that an overall domain length of 10 L, where L is the considered wavelength (L) is sufficient for collecting eight wave periods up to a distance of 8 L without getting reflection (negligible) from outlet boundary assigned at the end of the wave–damping zone of 1 L in length. In Star–CCM + code (CD-Adapco, 2015), waves are damped by implementing the method of Choi and Yoon (2009) by adding a resistance term to the equation for the vertical velocity component. The tank width is set to only two cells (2D model), and the OWC model is placed at a distance of 6.5 L from the wave inlet boundary. Considering the water oscillation inside the OWC chamber as well as the partial standing waves envelope generation in front of the chamber, a free surface zone height of 3.0 times the wave height (H) is adapted. Based on the grid and time sensitivity studies carried out it is found that when a base grid cell size of 400 mm is applied for the domain zone and the cell aspect ratio at the free surface zone is kept less than 16 with at least 12 and 36 cells per wave height and wavelength respectively, accurate water waves of less than 1.5% wave height error can be generated. Also, with Second–order temporal discretization scheme with 1200 time steps per wave period (T) is selected, this error becomes less than 1.0% in comparison with the analytical input wave height. Additional surface refinement is applied with 6.25 mm and 0.78125 mm cell surface size for the OWC walls and the PTO slot opening, respectively. For all non–slip walls, a first cell height equivalent to $y+ \cong 1$ ($y+$ is a non-dimensional distance from the wall to the first cell, and obtained by multiplying this distance with the friction/shear velocity divided by the kinematic viscosity) is used with a growth rate of 1.5 and 10 prism layers. The initial conditions implemented in the present CFD model are set as: the water level is defined at the desired level (h), waves are prescribed by the velocity components at the wave velocity inlet boundary and fully generated throughout the whole domain until the OWC's front lip by specifying that point on the water level. The tank two sides are defined as symmetry planes, and atmospheric pressure is defined at the top and end boundaries.

3. OWC energy conversion chain

It is paramount to get a good understanding of the impact of the environmental conditions in terms of incoming wave height and frequency together with the PTO pneumatic damping not only on the extracted energy but also on the different components included in the wave–pneumatic energy conversion chain. Therefore, the energy conversion chain proposed and applied for onshore–based OWCs (Elhanafi et al., 2016b; Mendes and Monteiro, 2007; Tseng et al., 2000) is extended in the present study to consider an additional sink for the energy transmitted underneath the device as given by Eq. (1) and described in Fig. 2 with the different performance assessment parameters/coefficients.

$$E_I = E_R + E_T + E_E + E_S + E_L \tag{1}$$

where E_I is the incident wave energy, E_R is the reflected energy, E_T is the transmitted energy, E_E is the extracted/pneumatic energy, E_S is the energy stored in OWC chamber's internal heave motion and E_L is the energy losses.

Using regular wave theory, the incident wave energy per unit width is defined as the product of the total (potential and kinetic) wave energy per unit ocean's surface area and the incident wavelength (L):

$$E_I = \frac{1}{2}\rho g A^2 L \left[\frac{J}{m}\right] \tag{2}$$

where A is the incoming wave amplitude, ρ is the water density and g is the gravitational acceleration.

Considering that all of the incident, reflected and transmitted energy are proportional to the square of the wave height, the wave reflection coefficient (C_R) is defined as the ratio between the reflected wave height (H_R) and the incident

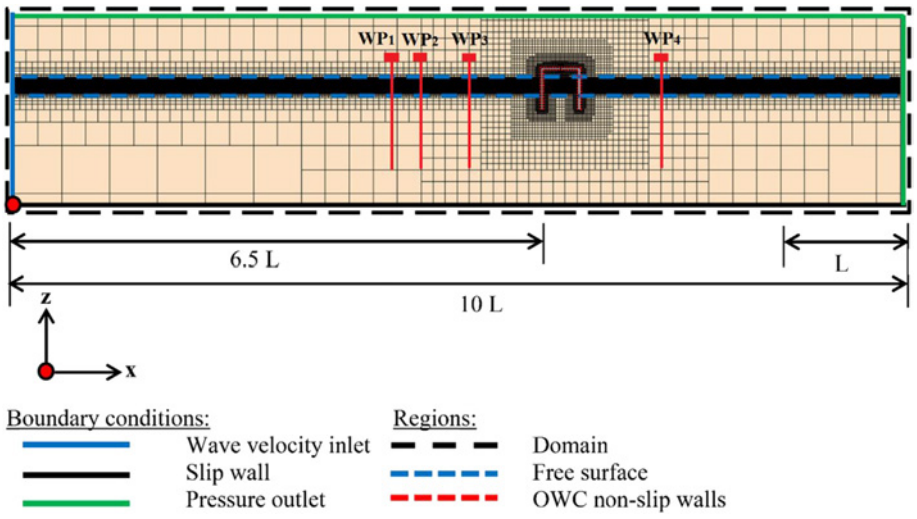

Fig. 1. Computational fluid domain (Not to scale).

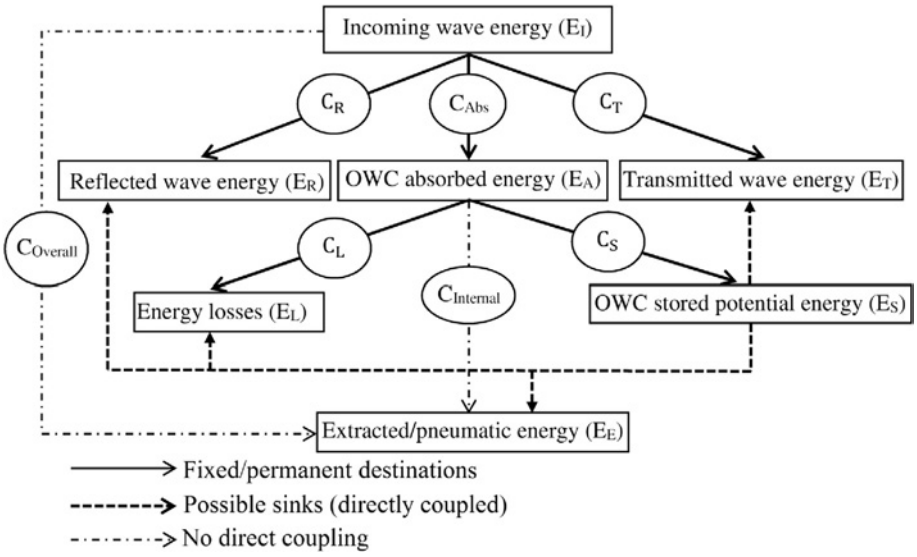

Fig. 2. Offshore stationary–floating OWC wave energy balance chart.

wave height (H), whereas the transmission coefficient (C_T) is given by the ratio of the transmitted wave height (H_T) measured behind the OWC structure to the incident wave height. Three numerical wave probes placed in front of the chamber sea wall are used to resolve the incident and reflected waves based on Mansard and Funke (1980) method. The spacing between the wave probes (shown in Fig. 1) were adjusted for each frequency according to the criteria specified by Mansard and Funke (1980), so that the spacing between WP_1 and WP_2 is L/10 and between WP_1 and WP_3 is L/4. Also, WP_3 is located at 0.75 L from the OWC front wall, which is more that 0.2 L as recommended by Goda and Suzuki (1976) in case of regular wave test. The transmitted wave height is measured at a distance of about one wavelength behind the OWC lee side, which is inside the tank area of free wave reflection (see Section 2.2).

While a part of the incoming wave energy is being reflected and transmitted as a result of the wave–OWC structure interactions, the rest is the energy absorbed by the OWC (E_A), which represents the maximum available energy to be extracted for electricity generation; and is given by:

$$E_A = E_I - E_R - E_T = E_I\left(1 - C_R^2 - C_T^2\right)\left[\frac{J}{m}\right] \tag{3}$$

The energy available at the turbine (extracted energy) (E_E) over one wave period is given by Eq. (4) as the time–integral of product of the instantaneous chamber's differential air pressure ($\Delta P(t)$) between the chamber interior and the exterior atmosphere and the airflow rate across the PTO ($q(t)$) (Elhanafi et al., 2016b; Tseng et al., 2000).

$$E_E = \int_0^T \Delta P(t)\cdot q(t)dt\left[\frac{J}{m}\right] \tag{4}$$

The energy stored in the OWC (E_S)represents the energy contained in the standing wave entrapped inside the chamber. This potential energy depends on the instantaneous oscillation of the chamber free surface (η) from its still water level, and is given by Eq. (5) per chamber's unit width (Elhanafi et al., 2016b). While the average value over a wave period is given by Eq. (6) (Elhanafi et al., 2016b; Mendes and Monteiro, 2007; Tseng et al., 2000) as a result of time–averaging of Eq. (5):

$$\grave{E}_s = \frac{\rho g \eta^2 b}{2}\left[\frac{J}{m}\right] \tag{5}$$

$$E_s = \frac{1}{T}\int_0^T \frac{\rho g \eta^2 b}{2}dt = \frac{\rho g H_w^2 b}{16}\left[\frac{J}{m}\right] \tag{6}$$

where b is the chamber length in the wave propagation direction and H_w is the height of the water column oscillations inside the OWC's chamber.

Considering the energy conservation principle in Eq. (1) and applying the energy balance chain shown in Fig. 2, the total losses in the OWC can be defined as the rest of the absorbed energy that has not been converted into pneumatic energy minus the energy stored in the water column oscillations. These losses (E_L) given in Eq. (7) can be attributed to different sources such as wave breaking, viscous, turbulence and vortex losses at chamber' lips and PTO.

$$E_L = E_A - E_E - E_S\left[\frac{J}{m}\right] \tag{7}$$

With estimating the different wave energy components together with the energy balance chain illustrated in Fig. 2, the OWC hydrodynamic performance is evaluated by analysing the energy balance coefficients summarized in Table 1.

In addition, to assess the OWC's overall power extraction efficiency, it is important to not only consider the incoming

wave height and length as in calculating the incoming energy (Eq. (2)), but also, the group velocity needs to be taken into account. Therefore, using regular wave theory, the incident wave energy flux (power) (P_I) per unit width is defined as the product of the incoming wave energy per unit ocean's surface area and the group velocity (C_g) (Dalrymple and Dean, 1991). Then, the OWC's overall power extraction efficiency ($\zeta_{Overall}$) is defined as in Eq. (10):

$$P_I = \frac{1}{2}\rho g A^2 C_g \left[\frac{W}{m}\right] \tag{8}$$

$$C_g = \begin{cases} \frac{\omega}{2k}\left(1+\frac{2kh}{\sinh(2kh)}\right) & \text{for intermediate water conditions}\left(\frac{L}{20}<h<\frac{L}{2}\right) \\ \frac{1}{2}\frac{L}{T} & \text{for deep water conditions}\left(h>\frac{L}{2}\right) \end{cases} \left[\frac{m}{s}\right] \tag{9}$$

where ω is the wave angular frequency, k is the wave number given by the dispersion relationship $\omega^2/g = k\tanh(kh)$ and h is the still water depth.

$$\zeta_{Overall} = \frac{P_E}{P_I}[-] \tag{10}$$

where P_E is the pneumatic extracted power, and is given by Eq. (11) as the time–average of Eq. (4) (Mendes and Monteiro, 2007):

$$P_E = \frac{1}{T}\int_0^T \Delta P(t)\cdot q(t)dt \left[\frac{W}{m}\right] \tag{11}$$

4. Experiments and validations

The numerical model used in the present study was previously validated in capturing the flow field (velocity and vorticity) inside an onshore OWC as well as monitoring the wave elevation along the numerical wave tank (Elhanafi et al., 2016b). Herein, additional two sets of experiments are used for further validating the numerical model. In the first validation, important parameters including chamber instantaneous differential air pressure (ΔP), chamber free surface elevation (η), chamber free surface vertical velocity (V) and overall system hydrodynamic efficiency ($\zeta_{Overall}$) are considered. The numerical results are compared against experimental measurements conducted by Morris-Thomas et al. (2007) (Case–B) and others numerical model results for the OWC model shown in Fig. 3.

As given in Eq. (11), both chamber's differential air pressure and airflow rate through the PTO are the two parameters required to evaluate the extracted pneumatic power. The differential pressure is numerically monitored by measuring the pressure at two points: one inside the chamber and another outside (on domain top boundary). A numerical array of different points inside the chamber at 1–20 mm from the back wall and 50–125 mm from the top wall have been tested, and there are no differences found for the positive pressure, while little variations are observed for the negative values. Airflow rate can simply be monitored numerically by measuring the air volume flow rate through the PTO via performing surface integral to the air's normal velocity or dividing the monitored

Table 1
Offshore OWC energy balance coefficients.

Wave energy balance coefficient	Description
Overall pneumatic energy extraction ($C_{Overall}$)	E_E/E_I
Reflected energy (C_R^2)	$(H_R/H)^2$
Transmitted energy (C_T^2)	$(H_T/H)^2$
OWC energy absorption (C_{Abs})	E_A/E_I
OWC internal energy extraction ($C_{Internal}$)	E_E/E_A
Energy losses (C_L)	E_L/E_A
OWC stored energy (C_S)	E_s/E_A

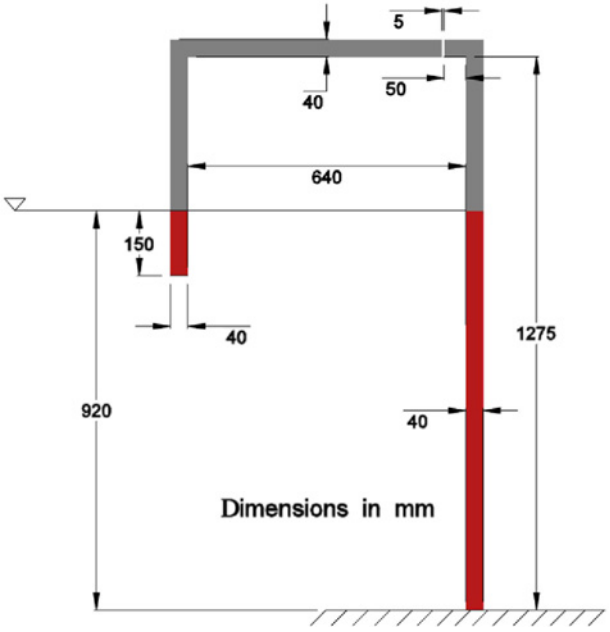

Fig. 3. Schematic of the OWC device (Case–B) tested by Morris-Thomas et al. (2007).

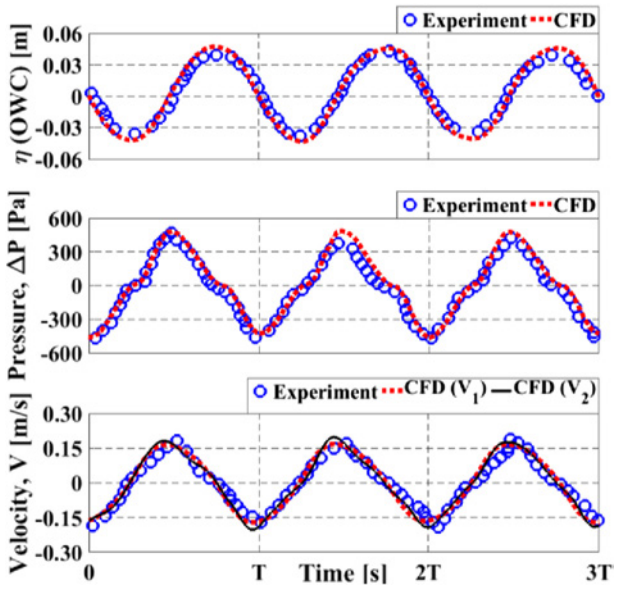

Fig. 4. Comparison between experiment (Kamath et al., 2015b) and CFD results for chamber free surface (water level) oscillation (η), chamber differential air pressure (ΔP) and chamber free surface velocity (V) under a wave condition of H = 120 mm and Kh = 1.26.

air mass flow rate by air density. However, experimentally it is usually defined as the product of the chamber's free surface velocity (rate of change of the wave level displacement, dη/dt) and the chamber's horizontal cross−sectional area (or the chamber's length in case of 2D model) assuming incompressible air. Although the first procedure for measuring the airflow rate is used in this paper, the free surface vertical velocity calculated from both procedures are compared against the experimental measurements. Fig. 4 compares the numerically measured time series data for free surface elevation inside the chamber (η) at chamber's centreline (b/2), differential air pressure (ΔP), free surface vertical velocity calculated from the air velocity measured through the PTO slot opening (1st procedure, V_1) together with applying the continuity equation and chamber's free surface vertical velocity (2nd procedure, V_2) calculated from its oscillation against the experimental data extracted from Kamath et al. (2015b). The experimental data uses a regular wave height of H = 120 mm and a wavelength that excites the device natural frequency presented by the dimensionless parameter Kh = 1.26, where K is defined as $K = \omega^2/g$. From this comparison, it can be noted that the experimental results have some uncertainties that can be clearly seen in variations between the subsequent peak and/or trough values, especially for the measured pressure and free surface oscillations, whereas CFD results seem to be more consistent/repeatable with standard deviations less than 2.5%. Qualitatively, the numerical model agrees well with the experimental data. Also, there is no significant difference between the two procedures used for measuring the air velocity (i.e., airflow rate), which is experimentally highlighted by Thiebaut et al. (2015) who found no significant differences in measuring the flow rate either by orifice pre−calibration and pressure measurement or by measuring the water column

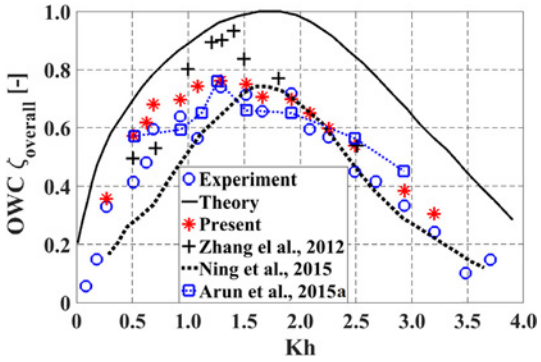

Fig. 5. OWC hydrodynamic efficiency comparison between experimental results (Morris-Thomas et al., 2007), analytical theory, others numerical models and present CFD results.

elevation inside the chamber. Additionally, the normalized root mean square deviation/error (López et al., 2014) of CFD results is within two standard deviations of the experimental data (calculated based on the available experimental time−series data).

In addition to validating the present model at the OWC natural frequency, simulating the device interactions with different wavelengths (steepness) are performed; the device overall hydrodynamic efficiency ($\zeta_{Overall}$) is illustrated in Fig. 5 in comparison with the analytical linear theory results (Evans and Porter, 1995), experimental measurements (Morris-Thomas et al., 2007) and others numerical results based on the Navier−Stokes equations (Ning et al., 2015; Zhang et al., 2012; Kamath et al., 2015a) over a range of Kh. Neglecting the wave nonlinearity as well as energy losses by viscous dissipation, the efficiency predicted by the linear wave theory represents the upper bound (extreme) with a peak value of $\zeta_{Overall\text{-}max}$ = 1.0 at the theoretical resonance frequency. On the other hand, the present CFD model agrees well with the experimental data even at the experimental resonance frequency (Kh = 1.26), where the experimental and CFD maximum efficiency is 0.74 and 0.76, respectively, which is less than 3% overestimation by CFD.

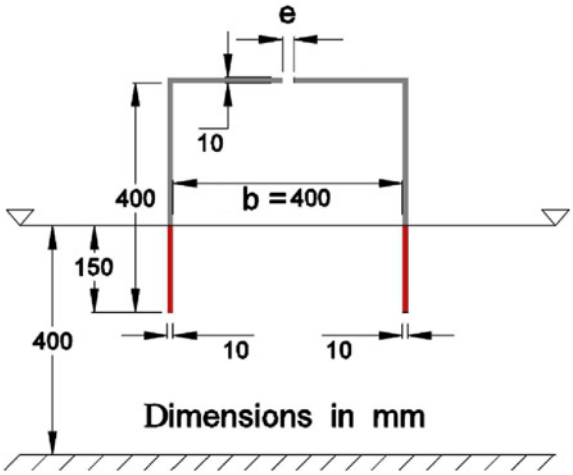

Fig. 6. Schematic of the stationary floating pile supported breakwater−OWC model tested by He and Huang (2014).

The second set of experiments used in the validation stage focuses on estimating the reflection (C_R), transmission (C_T), dissipation ($C_d = 1 - C_R^2 - C_T^2$) and pressure ($C_P = \Delta P / 0.5\rho g H$) coefficients resulting from regular waves interaction with a pile supported breakwater–OWC model (shown in Fig. 6) performed by He and Huang (2014). The validation uses a wave height of 35 mm over a range of wave periods represented by a non–dimensional ratio of the chamber length (b) to the incoming wavelength (L). The PTO damping is simulated by three slot opening ratios (defined as the slot opening size (e) divided by the chamber length) of 0.625%, 1.25% and zero (closed). The comparison of results illustrated in Fig. 7 shows that both the pressure and transmitted energy coefficients are captured well, whereas a little discrepancy found in the reflected energy coefficient, and as a result, the dissipation coefficient shows a slight deviation from the experimental data. These differences can be related to the methodology used in the experiment to resolve the incident and reflected waves, which is based on a two–point measurement procedure proposed by Goda and Suzuki (1976), while the present paper uses a three–point method proposed by Mansard and Funke (1980).

5. Stationary floating OWC model

The 1:50 floating–stationary OWC model shown in Fig. 8 is considered in the present study (with the same numerical wave tank dimensions and settings described in Section 2) to perform a series of numerical wave energy balance analysis. Considering the wave climate at the proposed deployment location of Bass Strait in southern Australia, a total of 102 numerical tests were performed under the following conditions at model scale: wave height, H = 50 mm and 100 mm, wave period (T) ranges from 0.8 s to 2.2 s with 0.1 s increment (corresponding to Kb = 1.8864–0.2494) and 11 slot opening (e = 1.5–9.0 mm) at a constant water depth, h = 1.5 m.

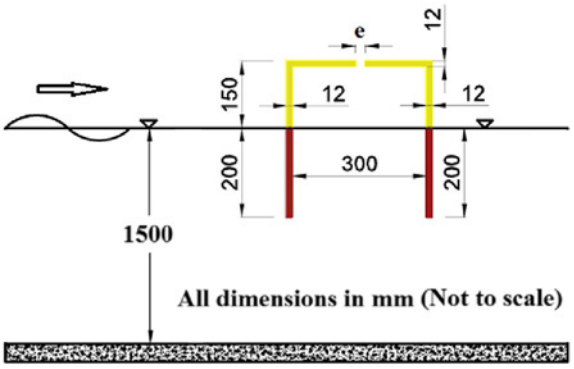

Fig. 8. Schematic of the 1:50 offshore stationary–floating OWC model considered in the present study.

6. Results and discussions

6.1. Overall OWC hydrodynamic performance

The device performance is initially investigated under a constant wave height of H = 50 mm for the whole Kb range with three different PTO damping values simulated by slot opening percentages (slot size/chamber length × 100) of 0.5, 1.0 and 2.0%, which are corresponding to a slot size (e) of 1.5, 3.0 and 6.0 mm, respectively. Generally, it is found that as the pneumatic damping increases, the pressure oscillation amplitudes (ΔP) increase (Fig. 9–a), while the airflow rate (q) (Fig. 9–b), as well as the chamber's free surface oscillation amplitude relative to the incident wave amplitude (amplification factor, η_{max}/A) (Fig. 9–c), decreases. This is in agreement with the experimental observations performed by Ning et al. (2016) for an onshore OWC. With the largest imposed damping (e = 1.5 mm or 0.5% opening slot), the pressure and the airflow rate have their maximum values of 117 Pa and 0.014 m^3/ms, accordingly when the device interacts with almost the lowest steepness (longest) waves

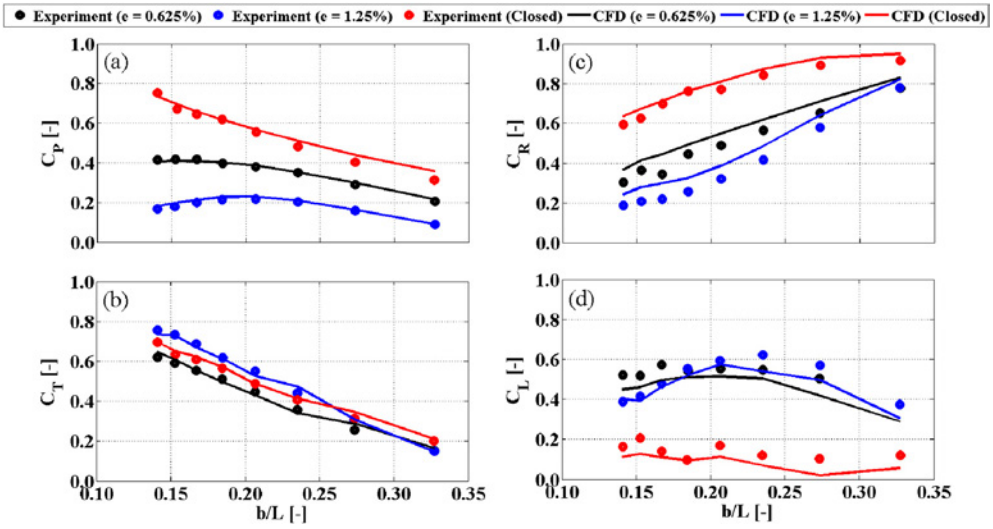

Fig. 7. Comparison between experimental (He and Huang, 2014) and CFD results for variations in (a): pressure coefficient (C_P), (b): transmission coefficient (C_T), (c): reflection coefficient (C_R) and (d): dissipation coefficient (C_d) versus b/L under a regular wave height of H = 35 mm.

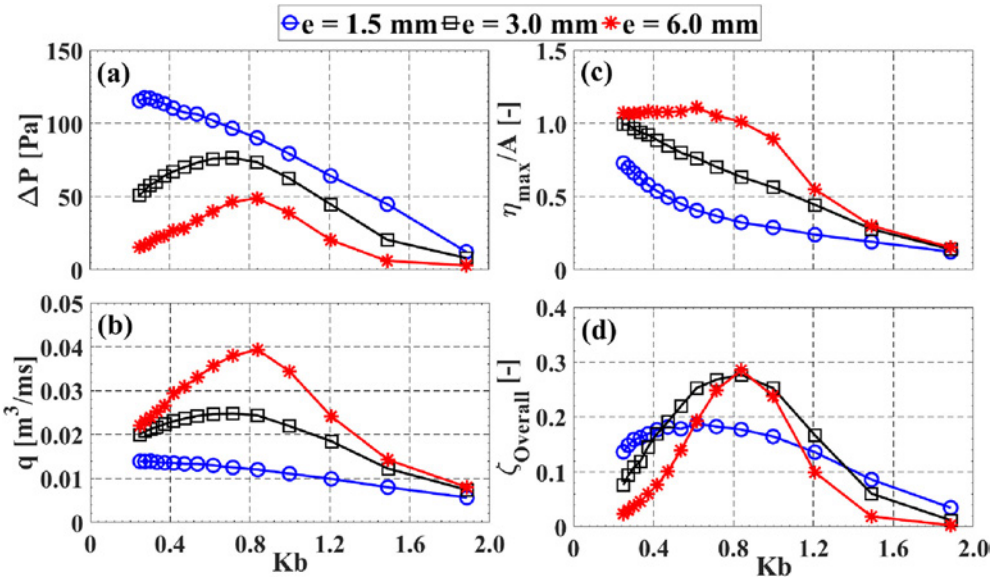

Fig. 9. Impact of the incoming wavelength on (a): chamber's differential air pressure (ΔP), (b): airflow rate (q), (c): chamber's free surface amplification factor (η_{max}/A) and (d): overall hydrodynamic efficiency ($\zeta_{Overall}$) over a range of Kb under three PTO damping values (e) and a wave height H = 50 mm.

(Kb = 0.2494–0.2738), which is the same pressure trend experimentally observed by He and Huang (2014) for a chamber with 0.625% slot opening; however, as Kb increases both quantities almost linearly reduce. It also worth mentioning that the corresponding pressure coefficient (C_P=ΔP/0.5ρgH) for ΔP = 117 Pa is 0.50, which is close to the value obtained by He and Huang (2014) and presented in Fig. 7 of the present paper, but this is smaller than a value of about 0.56 and 0.82 for onshore OWCs with 0.66% and 0.78% opening as presented in Ning et al. (2016) and Kamath et al. (2015b), respectively. This lower pressure coefficient can be assigned to the difference in hydrodynamic interactions with the offshore OWC that allows water waves to pass underneath the device, which in turn reduces the reflected waves and changes the wave envelope developed in front of device as will be discussed further in Section 6.2. On the other hand, both of the intermediate (e = 3.0 mm) and the lower (e = 6.0 mm) damping values result in nearly the same trends for the chamber differential air pressure and the airflow rate, which increase as the wavelength becomes shorter till peaked with ΔP = 76, 49 Pa and q = 0.025 and 0.039 m^3/ms at Kb = 0.616–0.714 and 0.8384 for the intermediate and the lower damping values, respectively, which is almost at the device natural frequency as reported in Iturrioz et al. (2015) for pressure measurements. This indicates that as the applied damping decreases the peak frequency of these parameters increases. After hitting these peaks, both variables diminish while Kb is advancing. The higher amplification factors (η_{max}/A) are observed to be 1.11, 1.0 and 0.73 for each damping value (lower–higher) when the device is subjected to the longest waves, and these values are gradually damped as the waves become shorter (i.e., higher steepness), except the case of the large damping (e = 6.0 mm) where a slight increase is observed till Kb = 0.616. For the device overall efficiency ($\zeta_{Overall}$) illustrated in Fig. 9–d, it is found that it initially increases with boosting the Kb until it tunes with maxima of 0.286, 0.277 and 0.187 at the device resonance frequency of Kb = 0.8384, 0.8384 and 0.616 associated with a damping of e = 6.0, 3.0, and 1.5 mm, accordingly, and then the efficiency declines with a further increase in Kb. Although the highest damping factor (e = 1.5 mm) results in a drop of about 0.11 in the maximum overall efficiency, it provides more frequency bandwidth allowing the device to be tuned to a wider wave frequency range. Also, the PTO damping of e = 3.0 mm provides almost the same maximum efficiency as e = 6.0 mm, but allows a broader frequency bandwidth.

Although Iturrioz et al. (2015) reported that the maximum pressure oscillation occurs close to the resonant period (except the case with a closed chamber), and in this case the maximum chamber free surface oscillations reach a maximum, Simonetti et al. (2015) and Ning et al. (2016) found that for a given OWC geometry, the maximum pressure amplitudes occur at higher frequencies than those for the chamber free surface oscillations. In the present study, results from Fig. 9 indicate that Iturrioz et al. (2015) findings are only valid for the case under the largest damping of e = 1.5 mm. Generally, the large pressure and airflow rate oscillations at a given pneumatic damping are not directly related to the chamber free surface oscillation, but rather its instantaneous slope is the important parameter. This importance can be described by considering that increasing the water vertical oscillation inside the chamber in a very short time (high frequency–short waves) results in a rapid change in the internal air pressure and forcing the air to evacuate the chamber through the PTO at high speed before air pressure equilibrium with the surrounding atmosphere occurs. In contrast, the slow change in the chamber's water oscillation associated with long waves, and even with large oscillation amplitudes, will displace a bigger amount of air out of the chamber but in a longer period.

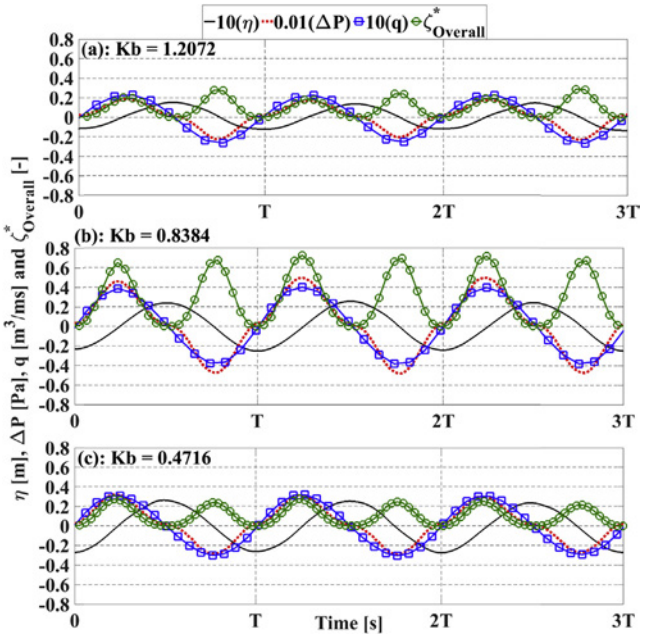

Fig. 10. Instantaneous chamber free surface oscillations (η), air pressure oscillations (ΔP), airflow rate (q) and overall hydrodynamic efficiency ($\zeta^*_{Overall}$) at different wavelengths (Kb) of 1.2072 (short), 0.8384 (intermediate) and 0.4716 (long) with a slot opening e = 6.0 mm and a wave height H = 50 mm.

In supporting the above explanation, Fig. 10 illustrates the instantaneous chamber free surface oscillation, differential air pressure, airflow rate and the overall efficiency (instantaneous overall efficiency, $\zeta^*_{Overall}$, which is defined as the ratio between instantaneous extracted pneumatic power = $\Delta P(t)\cdot q(t)$ and the incoming wave power P_I) for three wavelengths sorted as short (Kb = 1.2072), intermediate (Kb = 0.8384) and long (Kb = 0.4716) under a damping of e = 6.0 mm. It can be seen that the chamber free surface oscillation amplitudes at Kb = 0.4716 and 0.8384 are almost the same (η_{max}/A at Kb = 0.8384 is slightly lower than that at Kb = 0.4716 in Fig. 9–c); however, the shorter wave period with Kb = 0.8384 leads to a higher rate of change in the chamber free surface elevation (higher slope), which in turn produces higher pressure as well as airflow rate oscillation amplitudes. Conversely, for the shorter wave period of Kb = 1.2072, the oscillation amplitudes for both pressure and airflow rate are smaller than those for Kb = 0.8384, and this is due to the lower free surface oscillation inside the chamber with Kb = 1.2072, which causes the slow rate of change in the chamber internal water oscillation. It is also shown that as the wave frequency (Kb) increases, steepness (H/L) magnifies from 0.012 at Kb 0.4716 to 0.030 at Kb = 1.2072, and nonlinearity effects become more pronounced in the low pressure and airflow rate oscillations during the pressurizing stage. For these reasons, an asymmetric power extraction efficiency is observed clearly at Kb = 1.2072 with an inhalation (depressurizing) efficiency peak of almost 1.44 times that during the exhalation (pressurizing) stage.

Additionally, it worth noting that for the largest damping of e = 1.5 mm shown in Fig. 9, the maximum pressure oscillation, as well as the airflow rate, exists almost at Kb = 0.2494 together with the maximum free surface oscillation; however, the device overall efficiency is not at its maxima, which is achieved at a different Kb value of 0.616. According to Kamath et al. (2015a), this low efficiency with high chamber free surface oscillation and air pressure is related to the phase difference between both the pressure and the chamber's free surface vertical velocity (airflow rate). Actually, this phase difference is important to estimate the extracted power, but it cannot be considered as a direct indicator for the device efficiency; this is because the overall efficiency is defined as the ratio between the extracted and incident wave power. By this way, while the extracted power decreases with increasing pressure–airflow phase difference, the incident wave power increases with increasing the wave period (group velocity) (See Eqs. (8)–(11)). In addition, changing the wave period also affects every component in the energy conversion chain, which in turn alters the energy absorbed by the OWC (E_A) to extract from. For instance, time series of the chamber's free surface elevation, air pressure oscillation, airflow rate and the overall power extraction efficiency are presented in Fig. 11 at Kb = 0.2494 in comparison with results for Kb = 0.616. Despite the negligible phase difference between the power extraction parameters (pressure and airflow rate) for both Kb values, the overall efficiency is lower for Kb = 0.2494 than Kb = 0.616. For this reason, understanding the OWC performance in depth through the wave energy conversion chain is required.

6.2. OWC energy conversion chain

The different parameters describing the energy conversion chain (demonstrated in Fig. 2 and summarised in Table 1) are shown in Fig. 12 where it can be seen that the device tends to reflect most of the incoming wave energy as the wavelength becomes shorter (Fig. 12–a). Also, the reflection coefficient (C_R) increases with increasing pneumatic damping, but this effect becomes nil for the shorter waves with Kb almost greater than 1.5. On the other side, the transmitted energy

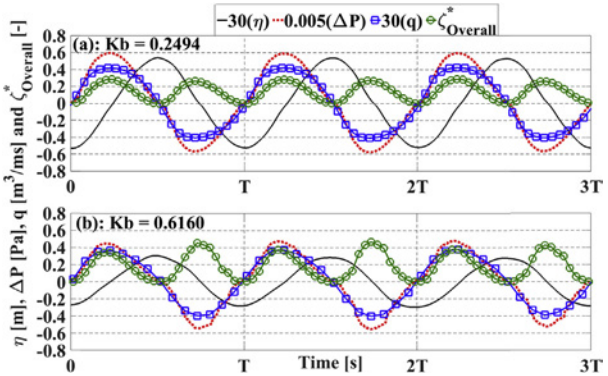

Fig. 11. Instantaneous chamber free surface oscillations (η), air pressure oscillations (ΔP), airflow rate (q) and overall hydrodynamic efficiency ($\zeta^*_{Overall}$) at different wavelengths (Kb) of 0.2494 and 0.616 with a slot opening (e) = 1.5 mm and a wave height H = 50 mm.

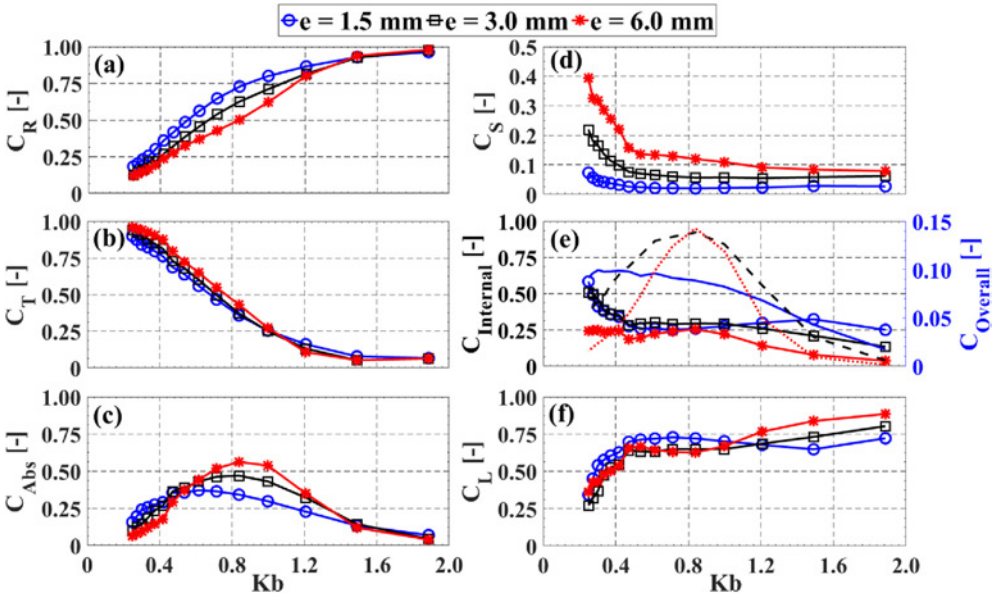

Fig. 12. OWC energy balance coefficients for three PTO damping values over a range of Kb and a wave height H = 50 mm including (a): reflection (C_R), (b): transmission (C_T), (c): energy absorption (C_{Abs}), (d): energy stored (C_S), (e): internal and overall energy extraction ($C_{Internal}$ and $C_{Overall}$) and (f): energy losses (C_L). Solid, dashed and dotted lines in subplot (e) correspond to a slot opening of e = 1.5, 3.0 and 6.0 mm, respectively for $C_{Overall}$.

represented by the transmission coefficient (C_T) in Fig. 12−b has completely an opposite trend to the reflection coefficient. Consequently, for longer waves, most of the incident energy passes underneath the OWC chamber. In addition, the higher PTO damping results in a slight reduction in the transmission coefficient, yet this effect occurs a little after Kb = 1.0. Considering the variation in the reflection and transmission coefficients, it is expected that the maximum energy absorption coefficient (C_{Abs}) is located in a bandwidth away from the Kb extremes as shown in Fig. 12−c. It is also shown that the device has a maximum energy absorption coefficient of 0.56, 0.47 and 0.37 almost at the device resonance of Kb = 0.8384, 0.8384 and 0.616 corresponding to a PTO damping of e = 6.0, 3.0 and 1.5 mm, respectively.

Having the amplification factor trends illustrated in Fig. 9−c, the OWC model seems to have a tendency to store more energy in the chamber's free surface heave motion under longer waves and smaller PTO damping as shown in Fig. 12−d. Furthermore, as Kb develops, the amplification factor lessens, and the energy absorption coefficient increases till peaked, which in turn results in progressively decreasing the energy storage coefficient almost up to Kb = 0.8384. Afterwards, the energy storage coefficient becomes nearly steady as a result of decreasing the absorped energy coefficient, while the amplification factor remains falling.

Regarding the overall energy extraction capability of the device, it can be seen in Fig. 12−e (right axis) that the OWC tends to extract most of the incoming wave energy at the intermediate frequency range with a maximum overall extraction coefficient ($C_{Overall}$) of 0.143 at Kb = 0.8384, 0.138 at Kb = 0.8384 and 0.099 at Kb = 0.3018−0.4716 for slot opening e = 6.0, 3.0 and 1.5 mm, respectively. Similar to the overall efficiency (Fig. 9−d), the intermediate damping of e = 3.0 mm provides more frequency bandwidth. On the other hand, the system ability to extract apart of absorbed energy, which is defined by the internal energy extraction coefficient ($C_{Internal}$) shown in Fig. 12−e (left axis). It is obvious that $C_{Internal}$ has a contrary trend to the energy losses coefficient in Fig. 12−f, but both have almost a steady trend over the intermediate frequencies where $C_{Overall}$ is high. Before discussing the energy losses in the OWC system in more detail, it is worth noting that the possible sources include hydrodynamic losses, which represent the underwater part up to the free surface interface as well as the aerodynamic losses resulting mainly from the airflow into and out of the chamber through the PTO. The hydrodynamic losses involve the friction head losses coming from the chamber free surface interaction with the OWC non−slip walls. These losses heavily depend upon the water amplification (i.e. contact length with OWC walls), free surface vertical velocity and friction coefficient, which is related to the Reynolds number together with the walls roughness. In addition to the friction/viscous losses, the chamber sharp lips enforce the water particles to change their travelling direction, and then accelerate the flow at those regions inducing flow separation and vortex formation. This kind of loss is wave frequency dependent due to its coupling with the water particles orbital motion, which changes under different frequency, and consequently, its interaction with the chamber lips of a given thickness will be different.

As discussed in Section 6.1, throughout the whole tested frequency (Kb) range, the airflow rate (Fig. 9−b), as well as the amplification factor (Fig. 9−c), is inversely proportional to the applied pneumatic damping. This indicates that the viscous losses also follow the same trend. Under the longest wave (Kb = 0.2494), the incoming wave energy is maximum (Eq. (2)), but the energy absorption coefficient (C_{Abs}) is low and diminishes with reducing the PTO damping. Considering the extracted energy' parameters (airflow rate and pressure

amplitudes) in Fig. 9, the device tends to extract most of the absorbed energy (i.e., maximum $C_{Internal}$) at this frequency. However, in comparison with the incoming wave energy, the overall energy extraction coefficient ($C_{Overall}$) is minima at this frequency for damping e = 3.0 and 6.0, which can be assigned to the large difference between this frequency (Kb = 0.2494) and that where both airflow rate and pressure amplitudes are peaked for these damping. This maximum $C_{Internal}$ together with the energy conservation principle in Eq. (7) result in minimum losses coefficients (C_L). Furthermore, as the water particles have longer orbital motion under longer wavelength, which leads to longer particle excursion and lesser vortex formations at the chambers' lips (further flow field results are discussed in Section 6.5). These characteristics contribute to the smaller losses coefficient for the different damping values shown in Fig. 12–f under longer waves.

With a further increase in Kb, the wave steepness magnifies, and nonlinearity arises together with the water particles excursions become shorter leading to stronger vortex generation and breaking the chamber flat (piston–rigid) internal free surface motion. These effects result in increasing the losses coefficient, and eliminate magnifying the extracted energy' parameters significantly, especially for the intermediate and high damping, whereas the energy absorption coefficient increases. Consequently, the internal energy extraction coefficient reduces, except under the lower damping (e = 6.0 mm) that shows a steady trend indicating reasonable improvements in the air pressure and airflow rate as the absorbed energy increases. Moreover, the energy chain in Fig. 2 demonstrates the direct coupling between the stored energy and other possible sinks, which further explains the changes in the internal energy extraction and losses coefficients. For instance, as Kb increases, the energy stored coefficient decreases, and the amount of this decreased energy seems to escalate the energy losses more than be converted to pneumatic energy for damping e = 1.5 and 3.0 mm, but this is not the case for the lower damping of e = 6.0 mm. During the intermediate frequency bandwidth (Kb = 0.4716–0.9978), the changes in the energy stored, energy losses and internal energy extraction coefficients are negligible, while the absorbed energy coefficient increases and the incoming wave energy decreases, which in turn results in the maximum overall energy extraction coefficient almost at the same frequency of the maximum energy absorption coefficient. Out of this frequency range, it is expected that the losses show more reduction as a result of the reduction in the airflow rate and chamber's free surface amplification; however, the losses coefficients show higher values at the maximum tested frequency of Kb = 1.8864. This can be assigned to the further shortening in the wavelength, nonlinearities escalation, the lower energy extraction and absorption coefficients and the steadiness of the stored energy coefficient.

6.3. PTO damping and wave height effects on OWC overall performance

In order to discover the impact of the PTO damping together with the incident wave height on the offshore OWC model performance in more detail, a series of two–dimensional damping factors (C = b/e) defined as the ratio between the chamber length (b) and the slot opening size (e) are studied. Eleven different slot opening sizes (e = 1.5, 2.0, 2.5, 3.0, 3.5, 4.0, 5.0, 6.0, 7.0, 8.0 and 9.0 mm) are applied for three different incident wavelengths corresponding to Kb = 0.4716, 0.8384 and 1.2072 under two wave heights of H = 50 mm and 100 mm.

Starting with the PTO impact, the chamber differential air pressure amplitude (ΔP), the airflow rate amplitude through the PTO (q), the chamber free surface amplification factor (η_{max}/A) and the overall hydrodynamic efficiency ($\zeta_{Overall}$) for the different PTO damping values and wavelengths under a regular wave height of 50 mm are presented in Fig. 13. The chamber differential air pressure is seen to gradually increase with growing the damping factor (C) from 33.33 (e = 9.0 mm) to 200 (e = 1.5 mm) as shown in Fig. 13–a. On the contrary, airflow rate and chamber free surface amplification factor decrease as the pneumatic damping accumulates as illustrated in Fig. 13 b and c, accordingly. Throughout the entire simulated damping factors, always the shorter wavelength (Kb = 1.2072) results in the minimum pressure, airflow rate and amplification factor, whereas the intermediate wavelength (Kb = 0.8384) produces the largest chamber air pressure and airflow rate amplitudes up to a damping factor C = 100 before the longer wavelength (Kb = 0.4716) starts taking place instead. A maximum pressure of 108 Pa is observed at the largest damping of C = 200 with the longer wavelength, while the airflow rate peaks at 0.046 m^3/ms with the intermediate wavelength under the lowest PTO damping of C = 33.33.

Overall, it can be seen that for the entire PTO damping range investigated, the chamber's amplification factor declines with decreasing incoming wavelength. The observed maximum chamber free surface oscillation amplitudes (η_{max}) are about 1.21, 1.14 and 0.61 times the incident wave amplitude under the lowest applied damping for the three simulated wavelengths corresponding to Kb = 0.8384, 0.4716 and 1.2072, accordingly; however, these oscillations are progressively damped to about 0.32, 0.50 and 0.24, respectively as the PTO damping boosts to its maximum (C = 200).

In Fig. 13–d, the device overall efficiency continues rising with increasing PTO damping, then reaches peak values at a specific damping factor over a narrow damping range before declining. Considering the longer wavelength (Kb = 0.4716), the overall efficiency increases from 0.058 at a damping factor of C = 33.33 to about 0.2 at C = 120, and then slightly drops by 0.021 under the maximum damping of C = 200. For the simulated shorter wavelength (Kb = 1.2072), a similar trend as the longer wavelength is observed; however, the maximum efficiency is found to be 0.035 less at the same damping factor of C = 120. On the other side, with the intermediate wavelength (Kb = 0.8384), the maximum efficiency occurs at a low damping factor of C = 60–75, and it is found to be approximately 0.3; however, with either decreasing or increasing the applied damping out of the optimum value, the efficiency moves down to about 0.23 and 0.18 for the minimum and maximum exerted damping factors, respectively. These

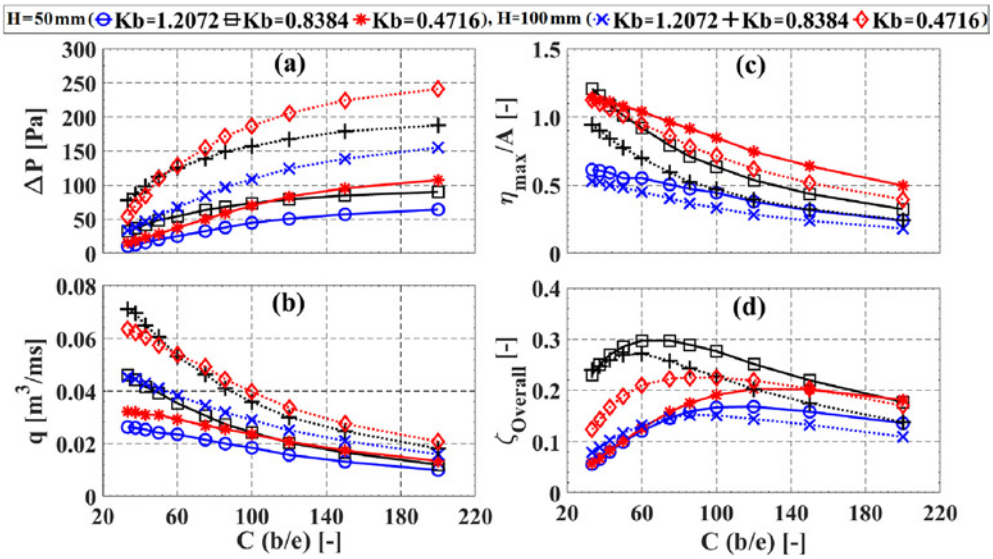

Fig. 13. Impact of PTO damping factor (C) on (a): variation in chamber differential air pressure (ΔP), (b): airflow rate (q), (c): chamber free surface amplification (η_{max}/A) and (d): the overall hydrodynamic efficiency ($\zeta_{Overall}$) under two wave heights H = 50 and 100 mm.

variations highlight the possibility of extracting power out of the designed resonance frequency by altering the PTO damping in order to tune the device to the incoming wavelength. In comparison with onshore OWCs, numerical CFD results from Kamath et al. (2015b) show the same general trends of all measured variables presented in Fig. 13. However, the measured values are larger for onshore OWCs. For instance, considering a wave height of 50 mm, the maximum overall efficiency for the offshore OWC is found to be 0.3 for the intermediate wavelength, where a value of about 0.83 was reported by Kamath et al. (2015b) for a 60 mm wave height under an intermediate wavelength. Again, this may be a consequence of the measured smaller pressure and airflow rate for the offshore OWC.

Although increasing the PTO damping factor (C) leads to increasing air pressure, the chamber free surface oscillation decreases. Consequently, the airflow rate drops down at a given frequency. This can be explained by studying the impact of three PTO damping corresponding to a slot opening e = 9.0, 5.0 and 1.5 mm on the instantaneous chamber free surface elevation, air pressure, airflow rate and the overall hydrodynamic efficiency at a given wavelength of Kb = 0.8384 as shown in Fig. 14. Considering that the chamber free surface vertical velocity is defined as the rate of change in its oscillation ($d\eta/dt$), which simply can be presented by $(\eta_{crest}-\eta_{trough})/T$, it is found that the free surface oscillation decays with enlarging the applied damping while the wave period (T) (wavelength) is fixed; accordingly, this slows down the free surface oscillation rate, and as a consequence, the airflow rate also deteriorates.

In addition, Fig. 14 illustrates that increasing the pneumatic damping also has an impact on the power extraction parameters (pressure and airflow rate) through the whole operation cycle. By escalating the damping from e = 9.0 mm to 1.5 mm, the air pressure and airflow rate change from having higher magnitudes during the pressurizing stage to larger values during the air suction process, respectively. As a consequence, the OWC device tends to extract the incoming wave power with a maximum overall instantaneous efficiency during the exhalation of about 1.16 times that during inhalation stage under a low damping of e = 9.0, while this value drops to 0.81 at e = 1.5 mm.

The relevance of increasing the incoming wave energy to the device performance is investigated by doubling the incident wave height to 100 mm, which escalates the incoming wave energy four times (Eq. (2)). Generally, it can be seen that

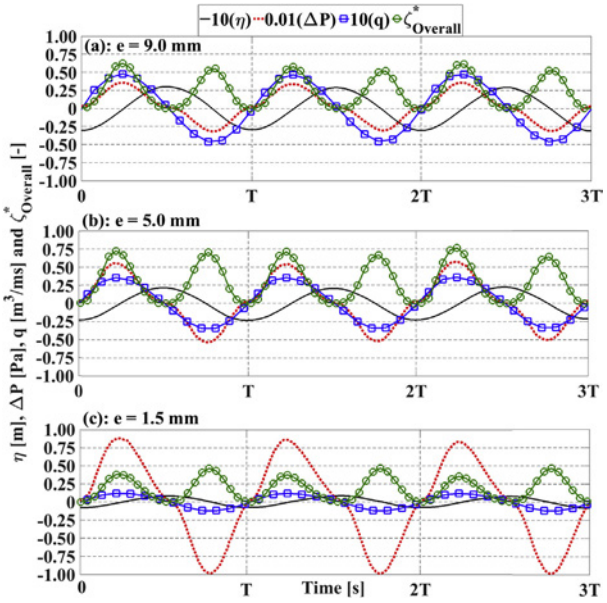

Fig. 14. Instantaneous chamber free surface oscillations (η), air pressure oscillations (ΔP), airflow rate (q) and overall hydrodynamic efficiency ($\zeta^*_{Overall}$) under different PTO of a slot opening e = 9.0, 5.0 and 1.5 mm for a wavelength of Kb = 0.8384 and height H = 50 mm.

the overall trend of the air pressure, airflow rate, amplification factor and the overall efficiency presented in Fig. 13 are similar to those with the lower wave height. The air pressure oscillation amplitudes in Fig. 13–a seems to increase as the wave height increases, and this effect gradually decreases as the damping factor increases with a maximum amplitude of about 3.47, 2.44 and 3.18 times values with the smaller wave height (H = 50 mm) corresponding to a wavelength of Kb = 0.4716, 0.8384 and 1.2072, respectively at C = 33.33 in comparison with almost 2.24, 2.08 and 2.42 at C = 200. Similar to the impact of increasing the wave height on the pressure amplitudes, the airflow rate amplitudes also increase to about 1.5–2.0 times the corresponding values with the 50 mm wave height at the lowest damping, and this impact slowly weakens to 1.5–1.6 as the damping increases to its maximum. In contrast, the amplification factors are inversely proportional to the wave height over the entire tested damping factors. The discrepancy between the impact that the wave height has on reducing the amplification factor and increasing the airflow rate for a given Kb value can also be assigned to the fact that the amplification factor represents the chamber's free surface oscillation amplitude relative to the incident wave amplitude, which increased two times. As a result, decreasing the amplification factor does not mean decreasing the absolute oscillation amplitude (unless for a constant wave height). Also, considering that the airflow rate is coupled with the chamber's free surface slope not its oscillation amplitude, which again is illustrated in Fig. 15–b for a wavelength of Kb = 0.8384, a damping of e = 6.0 mm and wave heights of 50 and 100 mm. Results clarify that although increasing the wave height to 100 mm resulted in a lower amplification factor, the chamber free surface oscillation amplitude is larger than that with 50 mm wave height of the same frequency (Kb = 0.8384); therefore, the free surface slope (with respect to the time axis) is larger with the higher wave, which in turn produces higher free surface velocity and airflow rate.

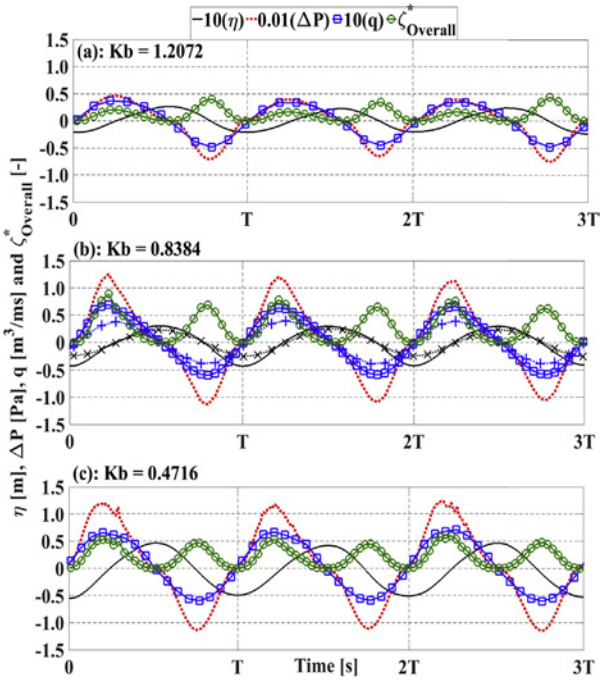

Fig. 15. Instantaneous chamber free surface oscillations (η), air pressure oscillations (ΔP), airflow rate (q) and overall hydrodynamic efficiency ($\zeta^*_{Overall}$) at different wavelengths of Kb 1.2072, 0.8384 and 0.4716 for a wave height H = 100 mm with a slot opening e = 6.0 mm. The dotted line with x markers in subplot (b) refers to η at H = 50 mm.

For the overall hydrodynamic efficiency shown in Fig. 13–d, increasing the incident wave height results in decreasing the device maximum efficiency at Kb = 0.8384 by about 0.025, shifting the optimum damping to lower values and narrowing its range. The reduction in the efficiency is more pronounced under high PTO damping. In contrast, under small and intermediate damping factors, there a little increase in the efficiency for the shorter waves (Kb = 1.2072), and this improvement is more noticeable for the longer wavelength (Kb = 0.4716) where the overall efficiency increases with increasing wave height with a peak efficiency at a damping of C = 75–120 approximately 0.022 higher than that under 50 mm wave height at damping C = 120, which indicates that for higher waves (energetic seas), the offshore OWCs can extract more energy over a wider frequency bandwidth.

In comparison with the results of the smaller wave height (H = 50 mm) shown in Fig. 10, the larger incoming wave height (H = 100 mm) introduces more nonlinear effects throughout the whole frequency range as demonstrated in Fig. 15 for three wavelengths. Moving from longer waves (Kb = 0.4716) with steepness of 0.024 to shorter waves (Kb = 1.2072) with 0.06 steepness, results in changing the air pressure and airflow rate crests and troughs from having higher crests to deeper troughs at steeper waves. Consequently, the OWC overall instantaneous efficiency peak changes from being larger during exhalation with about 1.28 times the inhalation efficiency at Kb = 0.4716 to only 0.45 at Kb = 1.2072, which is smaller than that of 0.7 achieved with a 50 mm wave height at the same frequency (Kb = 1.2072).

6.4. Impact of PTO damping and wave height on OWC energy balance

The results of varying the PTO damping and increasing the wave steepness (wave height) on each component involved in the wave–pneumatic energy conversion process are presented in Fig. 16. Fig. 16–a shows that the reflection coefficient (C_R) increases as the applied damping, as well as the wave height, increases. In addition, over all damping factors investigated, the reflection coefficient increases as the wavelength becomes shorter. On the other side, the transmitted energy coefficient (C_T) in Fig. 16–b shows a contrary trend to the reflection coefficient. Thus, the OWC transmission coefficient tends to slightly decrease with increasing the PTO damping and wave height. An exception found for the shorter wavelength (Kb = 1.2072), which shows a slight increase with increasing the damping and insignificant response to the wave height. For damping factors larger than C = 120, the transmission coefficient becomes insensitive to the applied damping.

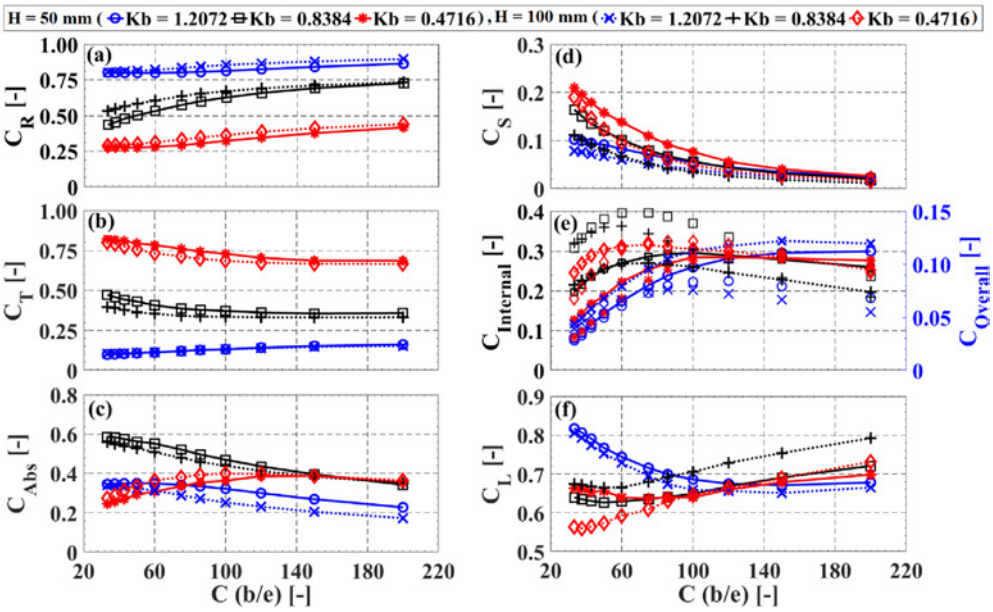

Fig. 16. OWC energy balance coefficients vs. PTO damping factor (C) under two wave heights H = 50 and 100 mm including (a): reflection (C_R), (b): transmission (C_T), (c): energy absorption (C_{Abs}), (d): energy stored (C_S), (e): internal and overall energy extraction ($C_{Internal}$ and $C_{Overall}$) and (f): energy losses (C_L). Markers without lines in subplot (e) refer to $C_{Overall}$.

For the energy absorption coefficient (C_{Abs}) in Fig. 16–c, under the shorter (Kb = 1.2072) and intermediate (Kb = 0.8384) wavelengths, this coefficient falls down with a further increase in the PTO damping as well as the incident wave height. Overall, the shorter wavelength (Kb = 1.2072) provides almost the lowest absorption coefficient, while the device tends to absorb more energy more efficiently as the damping and wave height increase when being subjected to the longer wavelength (Kb = 0.4716).

Similar to the observed impact of increasing the pneumatic damping and the wave height on the amplification factor (Fig. 13–c), the energy stored coefficient shown in Fig. 16–d also follows the same trend of the amplification factor. Regarding the device internal energy extraction coefficient ($C_{Internal}$) illustrated in Fig. 16–e, it seems that as the damping increases, $C_{Internal}$ arising till a certain damping that represents the optimum value for a given wavelength, and then it tends to slightly decrease with further increasing the applied damping. Furthermore, as the wave height increases, the device's $C_{Internal}$ increases except the intermediate wavelength (Kb = 0.8384) that shows a reduction in the internal energy extraction coefficient after a damping factor C = 60. Similar impacts of the applied damping on the overall energy extraction coefficient are observed (Fig. 16–e), but increasing the wave height only improves the overall energy extraction coefficient under the longer wavelength (Kb = 0.4716) as found for the overall efficiency in Fig. 13–d.

In addition to having an opposite trend to the internal energy extraction coefficient, the losses coefficient in Fig. 16–f gradually decreases as the damping increases until achieving a minimum value at almost the same damping corresponds to maximum $C_{Internal}$. Following this minima, the losses coefficient begins to move up following the increase in the PTO damping. Also, the shorter wavelength (Kb = 1.2072) shows lesser sensitivity to the higher damping factors. Except the intermediate wavelength, which produces higher losses coefficient with increasing the wave height especially after the optimum damping of C = 60, increasing the wave height results in further reductions of the losses coefficients for Kb = 1.2072 over all damping and for Kb = 0.4716 when the damping factor (C) is less than 100. It is, however, important to note that this drop in the losses coefficient is a representation for the energy losses relative to the absorbed energy, and this does not mean that the absolute energy losses are reducing with increasing the wave height. As one can expect, increasing the wave height raises the nonlinear effects, which can result in increasing the energy losses. Evidence for supporting and clarifying this argument is given in Fig. 17 for the absolute energy values corresponding to every component in the energy balance model under a wavelength of Kb = 0.4716 and a pneumatic damping of e = 5.0 mm (C = 60) for both wave heights of H = 50 mm and 100 mm. Results show that under the higher wave (H = 100 mm), each energy component in the energy balance model is larger than that for H = 50 mm. Also, the energy losses in the system when being subjected to the 100 mm wave height is about 4.4 times that with 50 mm wave height. More details about the vortex formation in the OWC is discussed in the following section.

6.5. Flow visualization and vortex generation

Flow visualization provides more information about the flow field, which highlights the areas of interest where energy can be dissipated and/or stored such as locations of stronger vortices and chamber free surface sloshing, respectively. The capability of the numerical model used herein for capturing

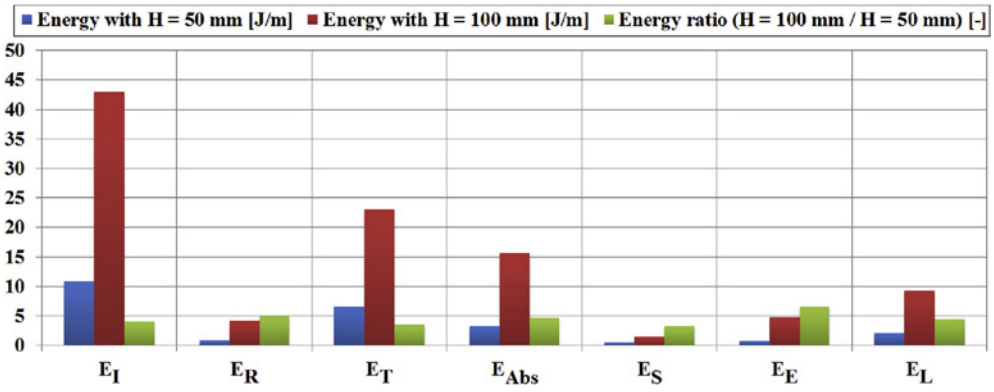

Fig. 17. OWC energy balance comparison between two wave heights of 100 mm and 50 mm at a wavelength of Kb = 0.4716 and a damping factor of C = 60 (e = 5.0 mm).

the flow behaviour, vortex generation and dissipation has previously been validated by the authors (Elhanafi et al., 2016b) against PIV data from model scale experiments for a fixed–bottom standing OWC. In this section, the same settings/meshing required at the virtual field of view implemented by Elhanafi et al. (2016b) are applied on the current model to discover the influence of different design parameters such as the incoming wave frequency, wave height and PTO damping on the flow behaviour inside the considered fixed offshore OWC (Fig. 8). The flow field is discovered

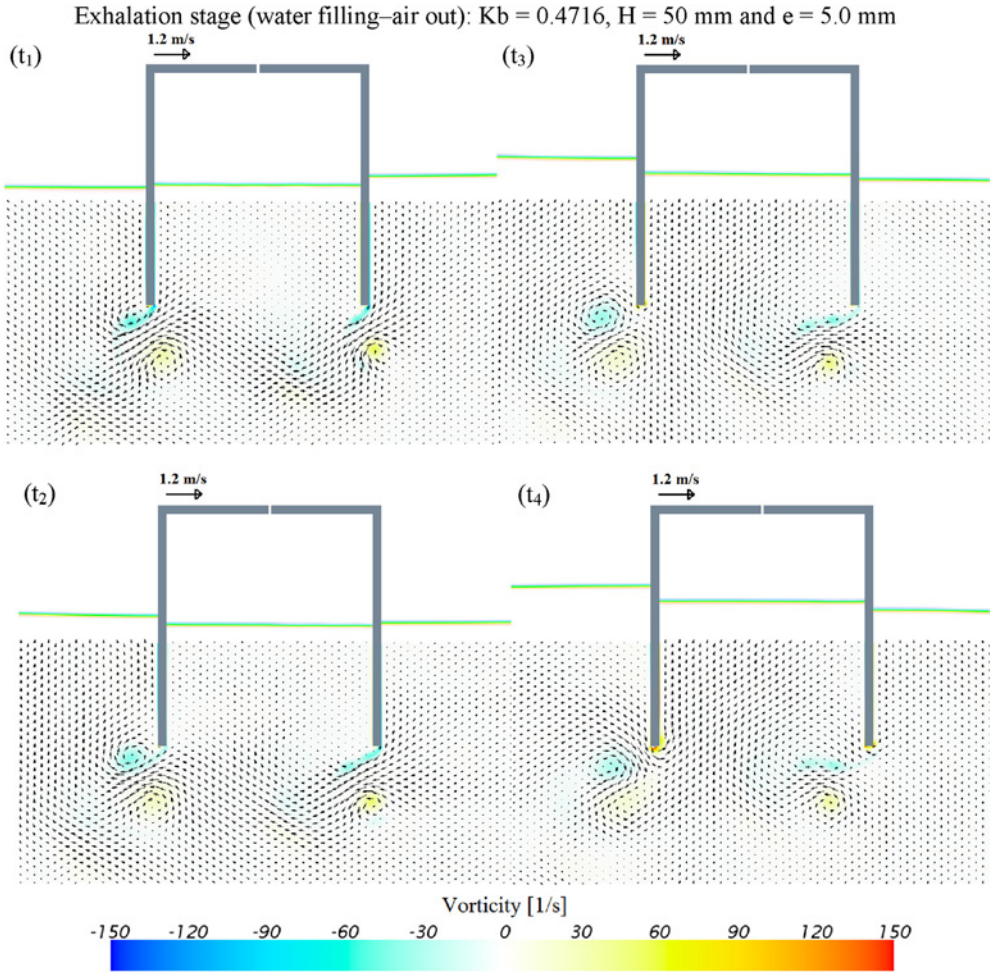

Fig. 18. Flow field during the exhalation stage for a constant 50 mm wave height and a damping of e = 5.0 mm slot opening under a wavelength of Kb = 0.4716. (Wave propagation direction →).

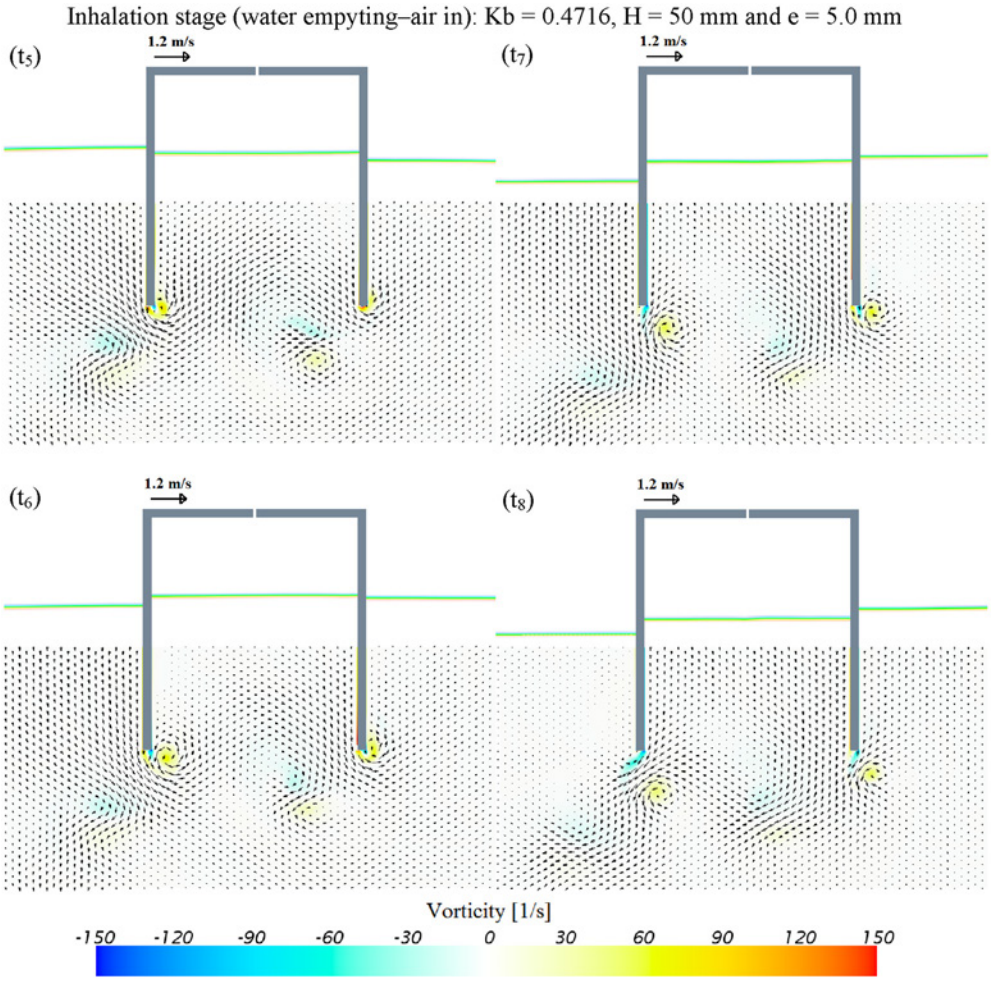

Fig. 19. Flow field during the inhalation stage for a constant 50 mm wave height and a damping of e = 5.0 mm slot opening under a wavelength of Kb = 0.4716.

through eight phases (t_1 – t_8) representing one wave cycle with a T/8 time increment between each phase. The first phase (t_1) starts when the chamber free surface level is minimum (trough).

Figs. 18 and 19 visualize the water flow through the OWC model during the exhalation (inflow–water filling the chamber or pressurizing–pushing air out of the chamber) and inhalation (outflow–water falling/emptying the chamber or depressurizing–air sucking into the chamber) stages, accordingly for a fixed PTO damping represented by e = 5.0 mm, a constant wave height of 50 mm and under a wavelength of Kb = 0.4716. Starting when the water level inside the OWC chamber is at its minima (t_1), the velocity magnitudes inside the chamber are still quite small. In addition, the vortices generated from the passed emptying process are clearly visible and extend towards the incoming ocean waves. These vortices consist of clockwise vortices (negative) positioned underneath the chamber lips, while anti–clockwise vortices (positive) are located under the negative vortices at both of the front and rear lips. Furthermore, as the water level moves upward, the velocity field increases and vortices start to strengthen till the maximum inflow occurs when the chamber free surface restores its initial still water level (mean zero level at t_3). At this instant, the generated clockwise vortices start detaching from the chamber lips, and small counter–clockwise vortices following the wave propagation direction begin taking place just below the submerged walls, which become obvious at t_4. Following this phase, the clockwise vortices begin to dissipate and move towards the seabed, whereas the wall–attached positive vortices initially observed at t_3 keep escalating and travelling upward with higher strength being assigned to the vortices at the ocean side wall. This process continues developing until the exhalation process ends, and the inhalation stage initiates at t_5 when the chamber free surface reaches its peak. When the inhalation stage commences, the velocity field begins to re–increase towards a maximum at the outflow instant (t_7). During this process, the anti–clockwise vortices keep building up with a reversed travelling direction (i.e., following the water level falling direction). In addition to these vortices, clockwise vortices attached to the walls' tips appear while the anti–clockwise vortices begin to separate from the lips. With further downward chamber water level movement towards the end of the emptying stage, the anti–clockwise vortices become weaker, whereas the clockwise vortices grow up till retaining the same characteristics as at t_1.

In order to uncover the impact of the incoming wavelength on the flow field, instantaneous shots are illustrated in Fig. 20 for additional three different Kb values of 0.2494, 0.8384 and

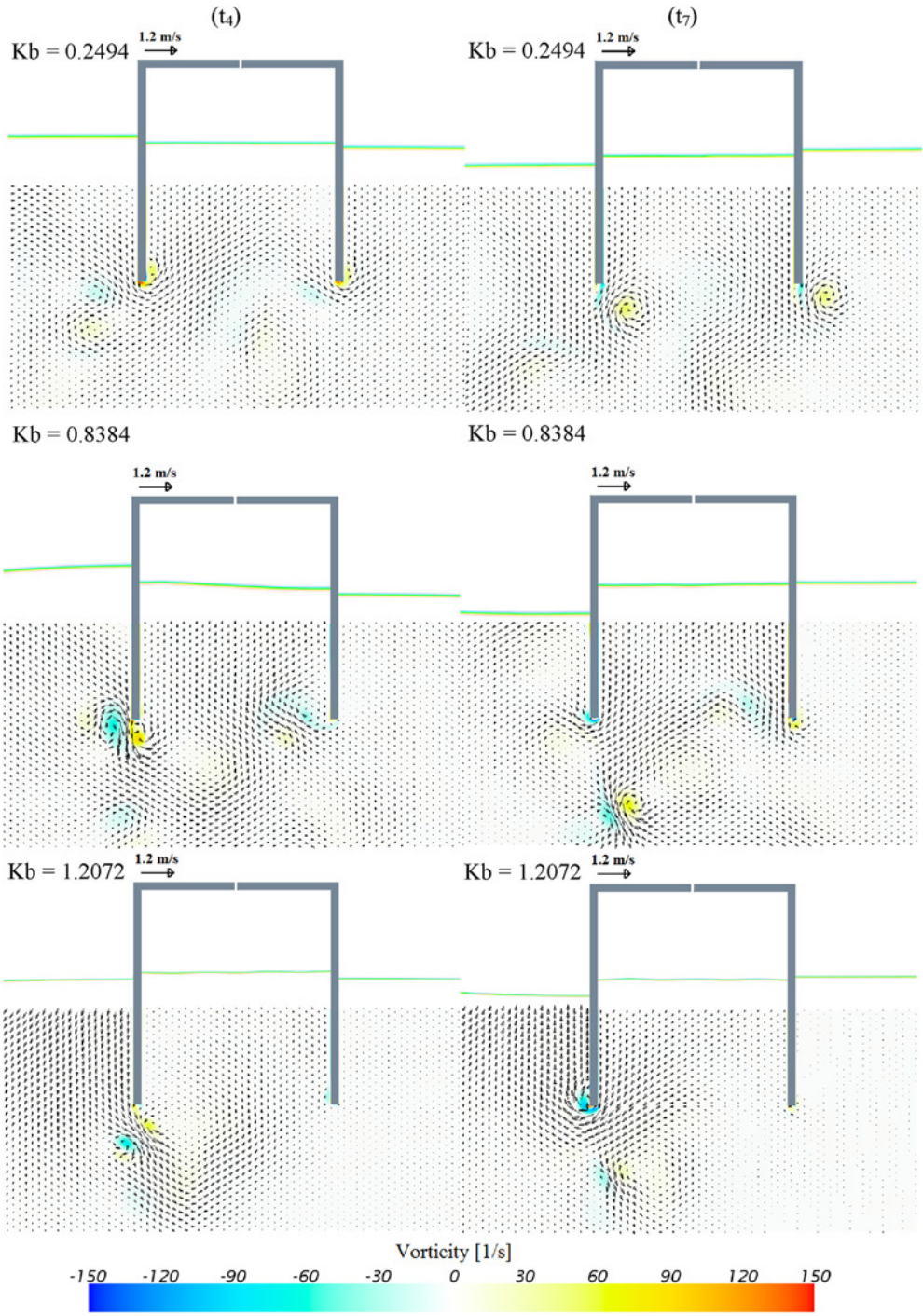

Fig. 20. Wavelength impact on the flow field for a constant 50 mm wave height and a damping of 5.0 mm slot opening.

1.2072. Generally, it is found that as the wavelength decreases, the vortex generation and dissipation processes significantly change. The magnitude and size of the clockwise vortices increase compared with the longest waves (Kb = 0.2494) especially for the resonance wavelength (Kb = 0.8384) during the exhalation stage (t_4). The negative vortices associated with the shorter waves (Kb = 1.2072) are almost of the same magnitudes as those at the resonance wavelength; however, their sizes are smaller and larger during the inflow and outflow, accordingly. In addition, as the waves become shorter, most of the generated vortices at chamber's front lip are located out of the chamber (i.e. no longer behind the front wall). This can be due to the increase in the free surface oscillation frequency associated with the incoming wave frequency, which does not provide enough time for the water particles to completely change their direction towards the chamber's top side.

Furthermore, during the outflow stage, the dominate vortices at the sea wall change from being anti–clockwise to

clockwise as the wavelength shortens. Also, the vortex generation at the lee side diminishes as the wavelength decreases (high steepness), and becomes almost invisible for the shorter wavelength (Kb = 1.2072), which can be attributed to the associated reduction in the energy transmission coefficient with reducing the incoming wavelength (see Fig. 12–b). In addition, increasing the wave steepness by decreasing the wavelength, raising the nonlinearity, which obviously affects the chamber free surface flatness. Accordingly, with the longest wave, the free surface seems to move as a rigid piston, while sloshing and free surface distortion increase as the wavelength decreases.

For the PTO damping effects, Fig. 21 shows the impact of changing the applied PTO damping of e = 1.5, 5.0 and 9.0 mm on the flow behaviour under 50 mm wave height and a constant wavelength of Kb = 0.8384. It is found that during the inflow stage, the clockwise vortices generated around the front wall are almost of the same magnitudes with slightly larger

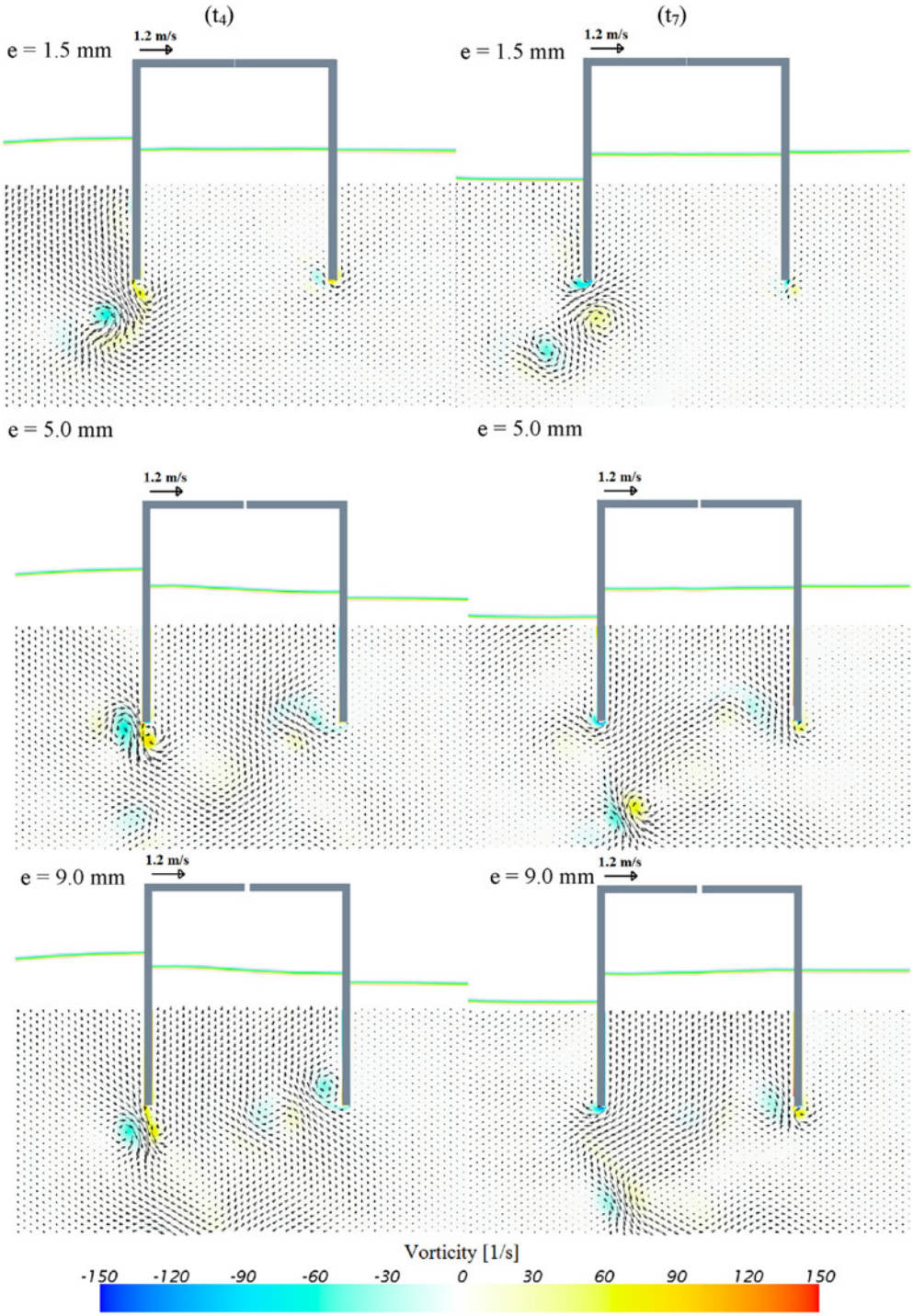

Fig. 21. PTO damping impact on the flow field for a constant 50 mm wave height and a wavelength of Kb = 0.8384.

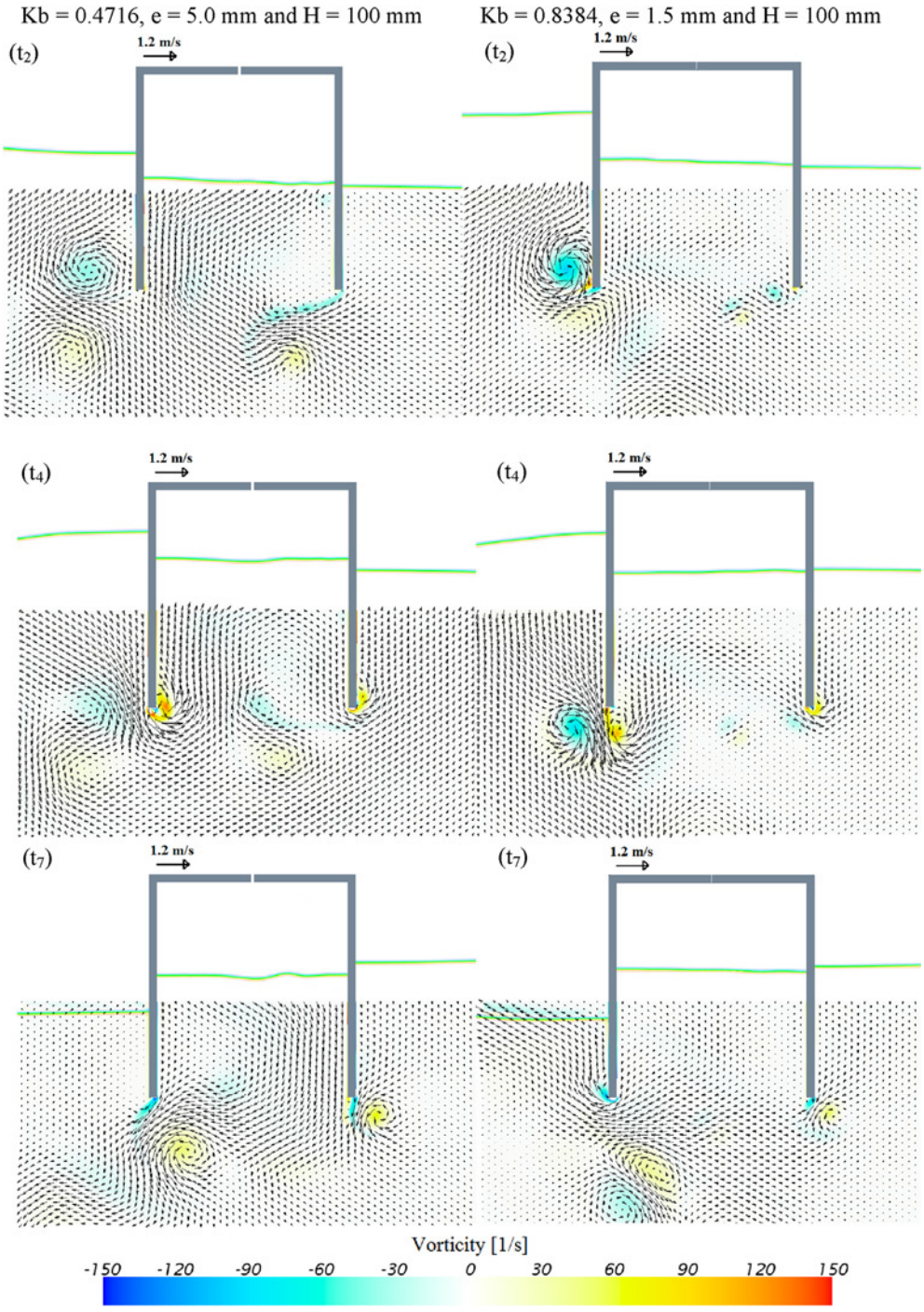

Fig. 22. Wave height (H = 100 mm) impact on the flow field. (left): Kb = 0.4716 and e = 5.0 mm, (right): Kb = 0.8384 and e = 1.5 mm.

sizes observed for the intermediate damping of e = 5.0 mm, whereas, at the rear wall, vortices become stronger as the PTO damping decreases. On the other side, during the outflow process, stronger vortices are observed at the seawall and lee wall under the highest and lowest applied damping, accordingly. Furthermore, decreasing the PTO damping induces more free surface nonlinearity and sloshing phenomena.

Regarding the incoming wave height impact, Fig. 22 discovers the consequences of increasing the wave height during the chamber filling and emptying processes. Two different conditions under a wave height of 100 mm are studied for wavelengths corresponding to Kb = 0.4716 with a damping e = 5.0 mm and Kb = 0.8384 under a damping e = 1.5 mm. In comparison with the results for 50 mm wave height shown in Figs. 18 and 19 for Kb = 0.4716, and e = 5.0 mm and Fig. 21 for Kb = 0.8384 and e = 1.5 mm, it was found that increasing the incoming wave height from 50 mm to 100 mm leads to amplifying the vortices magnitudes and enlarging their sizes throughout the whole operation process. Also, as a result of increasing the incident wave height, nonlinearity in the free

surface was observed especially under the lower pneumatic damping where the free surface looks to be highly distorted. Finally, in comparison with the 50 mm wave height, the significant increase in the vortices strength and size for Kb = 0.4716 and e = 5.0 mm under H = 100 mm, shown in Fig. 22 (left), supports the increase in the energy losses magnitude from doubling the wave height in the energy balance analysis shown in Fig. 17.

7. Conclusions

A 2D CFD model based on RANS–VOF is developed and applied in this paper in order to carry out wave energy balance analysis for an offshore floating–stationary oscillating water column–wave energy converter (OWC–WEC). The model was validated in good agreement with two sets of experimental measurements. The first included the chamber differential air pressure, chamber free surface elevation and device overall hydrodynamic efficiency over a wide range of wave frequencies, whereas the second validation was regarding the reflection, transmitted, losses and pressure coefficients. The comprehensively validated model allowed many parameters affecting the OWC wave energy conversion process such the incident wavelength, wave amplitude and the turbine pneumatic damping to be investigated. From the investigations carried out through a total of 102 numerical tests, the following conclusions are drawn:

7.1. Impact of the incoming wavelength

- The overall hydrodynamic efficiency, energy absorption coefficient, chamber air pressure and airflow rate increase with decreasing incident wavelength, achieve a maximum value at a certain wavelength, and then decline with a further decrease in the wavelength. Exception is found under the largest pneumatic damping where the pressure and airflow rate oscillation amplitudes tend to keep reducing as the wavelength decreases.
- Uneven power extraction between the inhalation and exhalation stages. The shorter the wavelength, the larger overall efficiency during inhalation process and vice versa.
- The reflection coefficient increases as the wavelength decreases, while the transmission coefficient, chamber free surface amplification factor and energy stored coefficient decrease as the wavelength becomes shorter.
- The losses coefficient accumulates with decreasing wavelength, reaches a stable/steady band region with small variations before increasing with a further increase in the wave steepness.
- The internal energy extraction coefficient has an inverse trend to the losses coefficient.
- Changing the incoming wavelength affects not only the vortices magnitude or size but also the rotational direction especially during the outflow stage at the front wall.
- As the wavelength reduces, the vortices generated at the rear wall become weak and almost invisible under high–frequency waves.
- Increasing the wave frequency introduces nonlinearity to the chamber free surface, and water sloshing becomes obvious.

7.2. Impact of the PTO pneumatic damping

- Increasing the PTO damping results in higher chamber differential air pressure, lower airflow rate, lesser chamber's free surface oscillation and smaller energy storage coefficient.
- The overall hydrodynamic efficiency increases as the PTO damping increases till hitting maxima and then drops down with a further increase in the damping.
- Altering the PTO damping can provide a damping value that tunes the device to a given wavelength, which provides an important control parameter for harvesting more energy over a wider frequency band.
- Asymmetric power extraction between the inflow and outflow processes. The larger the PTO damping, the higher overall efficiency during outflow process and vice versa.
- The internal energy extraction coefficient also increases as the damping increase till a certain value, and then a slight reduction is observed at higher damping factors.
- Similar to the wavelength effect, the losses coefficient has a contrary trend to that found for the internal energy extraction coefficient.
- The reflection and transmission coefficients are slightly rising and declining, accordingly when the applied damping increases.
- The more increase in the damping, the less energy stored coefficient with lesser impacts at higher damping values.
- The absorbed energy coefficient falls down with increasing the damping, except for the longer waves where this coefficient gradually increases as damping increases.
- The lower PTO damping applied on the chamber free surface, the stronger vortices generation especially at the rear side, whereas the higher damping leads to stronger vortices at the front walls during outflow.
- Chamber free surface waviness and sloshing are increasing as the adapted damping decreases.

7.3. Impact of the incoming wave height

- Increasing the incident wave height results in accumulating additional differential air pressure, and airflow rate, whereas the chamber's free surface amplification factor, as well as the energy storage coefficient, declines with increasing wave height.
- The unsymmetrical power extraction during the compression and decompression processes increases as the wave height increases.
- The reflection coefficient increases, while transmission coefficient and the energy absorption coefficient degrade with increasing wave height. An exception is found for the longer waves where the absorption coefficient tends to increase as the wave height grows up especially for low damping factors.

- The overall hydrodynamic efficiency is seen to decrease as the wave height increases. This impact becomes obvious when applying larger pneumatic damping. On the other hand, under small damping factors, there is a slight increase in the hydrodynamic efficiency. An exception is observed for the longer waves, which provide higher efficiency when the wave height increases especially under small and intermediate PTO damping; this provides a possibility for extracting more energy over a wider frequency band at more energetic seas.
- As the wave height moves up, the losses coefficient decreases and the internal energy extraction coefficient extends except for the intermediate wavelength.
- The generated vortices significantly strengthen as the incoming wave height arises. Similarly, the chamber free surface deformation and sloshing boost with increasing the wave height.

As a continuation of this research, the CFD model will be employed for further investigating the impact of adjusting the underwater geometry, especially the symmetrical and asymmetrical lips' submergence and its relevance to the incoming wave height. Furthermore, extending the current model to 3D will provide more insight into the device performance considering the impact of disturbing the flow by the chamber' sidewalls as well as the wave diffraction. Additionally, air compressibility may impact device performance, especially for large–scale prototypes (Falcão and Henriques, 2014), thus scaling effects with both incompressible and compressible airflow will be investigated.

References

Baudry, V., Babarit, A., Clement, A., 2013. An overview of analytical, numerical and experimental methods for modelling oscillating water columns. In: 10th European Wave and Tidal Energy Conference (EWTEC), September 2–5, Aalborg, Denmark.

CD-Adapco, 2015. User Guide STAR-CCM+ Version 10.02.

Choi, J., Yoon, S.B., 2009. Numerical simulations using momentum source wavemaker applied to RANS equation model. Coast. Eng. 56 (10), 1043–1060.

Crema, I., Simonetti, I., Cappietti, L., Oumeraci, H., 2015. Laboratory experiments on oscillating water column wave energy converters integrated in a very large floating structure. In: 11th European Wave and Tidal Energy Conference (EWTEC), September 6-11, Nantes, France.

Dalrymple, R.A., Dean, R.G., 1991. Water Wave Mechanics for Engineers and Scientists. World Scientific Publishing Company, New Jersey.

Drew, B., Plummer, A., Sahinkaya, M.N., 2009. A review of wave energy converter technology. Proceedings of the Institution of Mechanical Engineers. Part A J. Power Energy 223 (8), 887–902.

Elhanafi, A., Fleming, A., Leong, Z., Macfarlane, G., 2016a. Effect of RANS-based turbulence models on nonlinear wave generation in a two-phase numerical wave tank. Prog. Comput. Fluid Dyn. (in press).

Elhanafi, A., Fleming, A., MacFarlane, G., Leong, Z., 2016b. Numerical energy balance analysis for an onshore oscillating water column wave energy converter. Energy (provisionally accepted).

Evans, D., 1978. The oscillating water column wave-energy device. IMA J. Appl. Math. 22 (4), 423–433.

Evans, D., 1982. Wave-power absorption by systems of oscillating surface pressure distributions. J. Fluid Mech. 114, 481–499.

Evans, D., Porter, R., 1995. Hydrodynamic characteristics of an oscillating water column device. Appl. Ocean Res. 17 (3), 155–164.

Falcão, A.F., Henriques, J.C., 2014. Model-prototype similarity of oscillating-water-column wave energy converters. Int. J. Mar. Energy 6, 18–34.

Falcão, A.F., Henriques, J.C., 2015. Oscillating-water-column wave energy converters and air turbines: a review. Renew. Energy 85, 1391–1424.

Falcão, A.d.O., Sarmento, A., 1980. Wave generation by a periodic surface pressure and its application in wave-energy extraction. In: 15th International Congress of Theoretical and Applied Mechanics, Toronto, Canada.

Falnes, J., McIver, P., 1985. Surface wave interactions with systems of oscillating bodies and pressure distributions. Appl. Ocean Res. 7 (4), 225–234.

Fleming, A., Penesis, I., Goldsworthy, L., Macfarlane, G., Bose, N., Denniss, T., 2011. Phase averaged flow analysis in an oscillating water column wave energy converter. In: ASME, 30th International Conference on Ocean, Offshore and Arctic Engineering, Rotterdam, The Netherlands, June 19–24, pp. 475–484.

Fleming, A., Penesis, I., Macfarlane, G., Bose, N., Denniss, T., 2012a. Energy balance analysis for an oscillating water column wave energy converter. Ocean. Eng. 54, 26–33.

Fleming, A., Penesis, I., Macfarlane, G., Bose, N., Hunter, S., 2012b. Phase averaging of the velocity fields in an oscillating water column using splines. Proc. Inst. Mech. Eng. Part M J. Eng. Marit. Environ. 226 (4), 335–345, 1475090212439826.

Fleming, A., Penesis, I., Goldsworthy, L., Macfarlane, G., Bose, N., Denniss, T., 2013. Phase averaged flow analysis in an oscillating water column wave energy converter. J. Offshore Mech. Arct. Eng. 135 (2), 021901.

Goda, Y., Suzuki, T., 1976. Estimation of incident and reflected waves in random wave experiments. Coast. Eng. Proc. 1 (15).

Graw, K.-U., Schimmels, S., Lengricht, J., 2000. Quantifying Losses Around the Lip of an OWC by Use of Particle Image Velocimetry (PIV). LACER-Leipzig Annual Civil Engineering Report, Aalborg, Denmark.

He, F., Huang, Z., 2014. Hydrodynamic performance of pile-supported OWC-type structures as breakwaters: an experimental study. Ocean. Eng. 88, 618–626.

He, F., Huang, Z., Law, A.W.-K., 2012. Hydrodynamic performance of a rectangular floating breakwater with and without pneumatic chambers: an experimental study. Ocean. Eng. 51, 16–27.

He, F., Huang, Z., Law, A.W.-K., 2013. An experimental study of a floating breakwater with asymmetric pneumatic chambers for wave energy extraction. Appl. Energy 106, 222–231.

Hirt, C.W., Nichols, B.D., 1981. Volume of fluid (VOF) method for the dynamics of free boundaries. J. Comput. Phys. 39 (1), 201–225.

Hong, D., Hong, S., Hong, S., 2004. Numerical study of the motions and drift force of a floating OWC device. Ocean. Eng. 31 (2), 139–164.

Hong, K., Shin, S.-H., Hong, D.-C., Choi, H.-S., Hong, S.-W., 2007. Effects of shape parameters of OWC chamber in wave energy absorption. In: The Seventeenth International Offshore and Polar Engineering Conference, (ISOPE), Lisbon, Portugal, July 1-6, pp. 428–433.

Iturrioz, A., et al., 2014. Time-domain modeling of a fixed detached oscillating water column towards a floating multi-chamber device. Ocean. Eng. 76, 65–74.

Iturrioz, A., Guanche, R., Lara, J., Vidal, C., Losada, I., 2015. Validation of OpenFOAM® for oscillating water column three-dimensional modeling. Ocean. Eng. 107, 222–236.

Kamath, A., Bihs, H., Arntsen, Ø.A., 2015a. Numerical investigations of the hydrodynamics of an oscillating water column device. Ocean. Eng. 102, 40–50.

Kamath, A., Bihs, H., Arntsen, Ø.A., 2015b. Numerical modeling of power take-off damping in an oscillating water column device. Int. J. Mar. Energy 10, 1–16.

López, I., Pereiras, B., Castro, F., Iglesias, G., 2014. Optimisation of turbine-induced damping for an OWC wave energy converter using a RANS–VOF numerical model. Appl. Energy 127, 105–114.

López, I., Castro, A., Iglesias, G., 2015. Hydrodynamic performance of an oscillating water column wave energy converter by means of particle imaging velocimetry. Energy 83, 89–103.

López, I., Pereiras, B., Castro, F., Iglesias, G., 2016. Holistic performance analysis and turbine-induced damping for an OWC wave energy converter. Renew. Energy 85, 1155–1163.

Luo, Y., Nader, J.-R., Cooper, P., Zhu, S.-P., 2014. Nonlinear 2d analysis of the efficiency of fixed oscillating water column wave energy converters. Renew. Energy 64, 255–265.

Mansard, E.P., Funke, E., 1980. The measurement of incident and reflected spectra using a least squares method. Coast. Eng. Proc. 1 (17).

Mendes, A., Monteiro, W., 2007. Performance analysis of a model of OWC energy converter in non-linear waves. In: 7th European Wave and Tidal Energy Conference (EWTEC), September 11–13, Porto, Portugal.

Morris-Thomas, M.T., Irvin, R.J., Thiagarajan, K.P., 2007. An investigation into the hydrodynamic efficiency of an oscillating water column. J. Offshore Mech. Arct. Eng. 129 (4), 273–278.

Morrison, I.G., 1995. The Hydrodynamic Performance of an Oscillating Water Column Wave Energy Converter.

Müller, G., Whittaker, T.J., 1995. Visualisation of flow conditions inside a shoreline wave power-station. Ocean. Eng. 22 (6), 629–641.

Ning, D.-Z., Shi, J., Zou, Q.-P., Teng, B., 2015. Investigation of hydrodynamic performance of an OWC (oscillating water column) wave energy device using a fully nonlinear HOBEM (higher-order boundary element method). Energy 83, 177–188.

Ning, D.-Z., Wang, R.-Q., Zou, Q.-P., Teng, B., 2016. An experimental investigation of hydrodynamics of a fixed OWC wave energy converter. Appl. Energy 168, 636–648.

Sarmento, A., 1992. Wave flume experiments on two-dimensional oscillating water column wave energy devices. Exp. Fluids 12 (4–5), 286–292.

Sarmento, A.J., Falcão, A.d.O., 1985. Wave generation by an oscillating surface-pressure and its application in wave-energy extraction. J. Fluid Mech. 150, 467–485.

Sheng, W., Alcorn, R., Lewis, T., 2014. Numerical assessment on primary wave energy conversion of oscillating water columns. (OMAE2014–23218). In: ASME 2014 33rd International Conference on Ocean, Offshore and Arctic Engineering, San Francisco, USA, June 8–13.

Simonetti, I., Cappietti, L., El Safti, H., Oumeraci, H., 2015. Numerical modelling of fixed oscillating water column wave energy conversion devices: toward geometry hydraulic optimization. (OMAE2015-42056). In: ASME 2015 34th International Conference on Ocean, Offshore and Arctic Engineering, St. John's, Newfoundland, Canada, May 31–June 5.

Teixeira, P.R., Davyt, D.P., Didier, E., Ramalhais, R., 2013. Numerical simulation of an oscillating water column device using a code based on navier–stokes equations. Energy 61, 513–530.

Thíebaut, F., Pascal, R.e, Andreu, A.G.a., 2015. Investigation into the calibration of orifices used in OWC tank testing. In: 11th European Wave and Tidal Energy Conference (EWTEC), September 6–11, Nantes, France.

Tseng, R.-S., Wu, R.-H., Huang, C.-C., 2000. Model study of a shoreline wave-power system. Ocean. Eng. 27 (8), 801–821.

Zhang, Y., Zou, Q.-P., Greaves, D., 2012. Air–water two-phase flow modelling of hydrodynamic performance of an oscillating water column device. Renew. Energy 41, 159–170.

Appendix C

Paper 3: Elhanafi A, Fleming A, Macfarlane G, Leong Z. Underwater geometrical impact on the hydrodynamic performance of an offshore oscillating water column–wave energy converter. *Renewable Energy. 2017;105:209-231*.

Appendix D

Paper 4: Elhanafi A, Macfarlane G, Fleming A, Leong Z. Investigations on 3D effects and correlation between wave height and lip submergence of an offshore stationary OWC wave energy converter. *Applied Ocean Research. 2017;64:203-216*.

Appendix E

Paper 5: Elhanafi A, Macfarlane G, Fleming A, Leong Z. Scaling and air compressibility effects on a three-dimensional offshore stationary OWC wave energy converter. *Applied Energy. 2017;189:1-20.*

Appendix F

Paper 6: Elhanafi A, Macfarlane G, Fleming A, Leong Z. Experimental and numerical investigations on the hydrodynamic performance of a floating–moored oscillating water column wave energy converter. *Applied Energy. 2017;205:369–390.*

Appendix G

Paper 7: Elhanafi A, Macfarlane G, Fleming A, Leong Z. Experimental and numerical measurements of wave forces on a 3D offshore stationary OWC wave energy converter. *Ocean Engineering*. *2017;144:98-117*.

Appendix H

Paper 8: Elhanafi A, Macfarlane G, Fleming A, Leong Z. Intact and damaged survivability of an offshore floating–moored OWC device. *In: Proceedings of 27th International Society of Offshore and Polar Engineers (ISOPE), June 25–30, 2017, San Francisco, California, USA*.

Appendix I

Paper 9: Elhanafi A, Macfarlane G, Fleming A, Leong Z. Experimental and numerical investigations on the intact and damage survivability of a floating–moored oscillating water column device. *Applied Ocean Research. 2017;68:276-292.*

Appendix J

Paper 10: Elhanafi A, Fleming A, Leong Z, MacFarlane G. Effect of RANS–based turbulence models on nonlinear wave generation in a two–phase numerical wave tank. *Progress in Computational Fluid Dynamics. 2017;17(3):141-158.*

Effect of RANS-based turbulence models on nonlinear wave generation in a two-phase numerical wave tank

Ahmed Elhanafi*, Alan Fleming, Zhi Leong and Gregor Macfarlane

National Centre for Maritime Engineering and Hydrodynamics,
Australian Maritime College,
University of Tasmania,
Launceston, Tasmania 7250, Australia
Email: ahmed.elhanafi@utas.edu.au
Email: alan.fleming@utas.edu.au
Email: zhi.leong@utas.edu.au
Email: gregor.macfarlane@utas.edu.au
*Corresponding author

Abstract: Ocean waves are the most important exciting source acting on marine structures such as ships, offshore platforms and wave energy converters. To efficiently design such structures, accurate modelling of these waves is of importance. This paper utilised a two-dimensional numerical wave tank based on the Reynolds-averaged Navier-Stokes (RANS) equations and volume of fluid (VOF) method and a commercial software code to numerically investigate ocean wave generation. Impact of different turbulence models such as standard k-ε, realisable k-ε, shear stress transport (SST) and Reynolds stress models (RSM) on the generated waves were investigated. Experimental wave measurements have been conducted to validate the numerical results. Excessive generation of eddy viscosity can lead to significant damping. Good numerical agreement with both experimental measurements and analytical wave theory was only successfully achieved either with the RSM or implementing artificial turbulence damping at the air-water interface with the SST model.

Keywords: ANSYS FLUENT; numerical wave tank; NWT; wave generation; free surface turbulence damping; shear stress transport; SST; Reynolds stress models; RSM.

Reference to this paper should be made as follows: Elhanafi, A., Fleming, A., Leong, Z. and Macfarlane, G. (2017) 'Effect of RANS-based turbulence models on nonlinear wave generation in a two-phase numerical wave tank', *Progress in Computational Fluid Dynamics*, Vol. 17, No. 3, pp.141–158.

Biographical notes: Ahmed Elhanafi received his Bachelor of Science (BSc) with distinction in 2009 and Master of Science (MSc) in 2013 from the Department of Naval Architecture and Marine Engineering, Faculty of Engineering, Alexandria University, Egypt. In 2014, he was awarded a PhD scholarship from the National Centre for Maritime Engineering and Hydrodynamics, Australian Maritime College, University of Tasmania. Currently, he is a PhD candidate with a research focus on the hydrodynamic performance of offshore oscillating water column-wave energy converters.

Alan Fleming is a post-doctoral research fellow in Ocean Wave Energy at the Australian Maritime College National Centre for Maritime Engineering and Hydrodynamics. He has an experienced in experimental analysis of wave energy converters and imaging techniques such as particle imaging velocimetry, close range photogrammetry and videogrammetry.

Zhi Leong is an Ocean Engineer and serves as a research fellow at the Australian Maritime College. His research includes varied applications of computational fluid dynamics and experimental methods to investigate hydrodynamic phenomena and related challenges in maritime engineering, with a special interest in underwater vehicles.

Gregor Macfarlane is an Associate Professor in Maritime Hydrodynamics at the Australian Maritime College, a specialist institute of the University of Tasmania. He is a Naval Architect with 20 years experience in experimental techniques applied to engineering hydrodynamic problems. Water waves are a central theme to his work: how they affect the motions and loads of ships and offshore structures, quantifying waves created by moving ships, generating the perfect wave for man-made surfing facilities, and extracting energy from ocean waves.

1 Introduction

Among the different sources of renewable energy, wave energy has attracted more attention over recent years due to its high energy density and wide global availability. For safe and efficient marine structures such as wave energy converters, it is important to develop an efficient and reliable method to simulate ocean waves. Accurate simulation of these waves which represent the primary exciting source can provide a good estimation of the hydrodynamic loads and predict the structure's response and performance.

Increasing computing power in recent years is resulting in the rapid development of capability in computational fluid dynamics (CFD) analysis which is seeing the emergence of new fields such as the numerical wave tank (NWT). The NWT is an attractive tool that can be utilised in the development of marine vehicles and structures, and once validated offers advantages over experiments in physical wave tanks. In particular, various design parameters can be modified and run iteratively and provides an in-depth view of the underlying complex phenomenon of wave structure interaction (Bhinder et al., 2009). In addition, performing physical model scale tests would be expensive, restricted and in some cases, risky. For instance, in order to carry out wave energy balance analysis for an oscillating water column wave energy converter (Fleming et al., 2012), physical water velocity fields were measured using particle image velocimetry (PIV) which involves the use of a high intensity laser (class 4) that can easily cause permanent blindness (Fleming, 2012).

NWTs have been developed to aid investigations in a wide range of maritime engineering applications. Examples that are most relevant to the present study include Horko (2007), Liu et al. (2008, 2010), Bhinder et al. (2009), Şentürk and Özdamar (2011), Hu et al. (2011), Zhang et al. (2012), Gomes et al. (2013), Yu and Li (2013), Bouali and Larbi (2013) and Seibt et al. (2014) who all have applied NWTs to numerical studies related to marine renewable wave energy aspects.

As recommended by Coe and Neary (2014), when a comparison between experimental data and CFD predictions for device response is planned, a separate validation to assess the accuracy of the waves in the numerical simulation can rule out a potentially large source of error. Therefore, the present paper represents the main stage for the upcoming hydrodynamic performance investigation of an offshore forward facing bent duct oscillating water column wave energy converter under various wave conditions.

In developing a NWT, the influence of both grid size and time step on the generated numerical waves are the two most common factors being studied by researchers in order to find the most efficient approach before the validation step against analytical wave theory and/or experimental measurements such as the work done by Joubert (2013), Finnegan and Goggins (2012), Silva et al. (2010), Lal and Elangovan (2008) and Horko (2007). In the present study, in addition to these two factors, impact of other mesh parameters including the growth rate factor for smooth moving between fine and coarse grids and the air column height on the generated waves are considered. Moreover, the compatibility of the proposed model with different solution methods and various turbulence models are also investigated.

Due to the large number of parameters involved in the numerical solver setup, simplifications and assumptions have to be made, thus it is highly recommended that the CFD analysis be validated with experimental data (Havn, 2011) in order to get an accurate indication of how well the NWT can simulate physical conditions (Lambert, 2012). In studies such as this, it is often the case that physical experiments, which have the advantage of integrating the right equations governing the physical phenomena, are designed to provide data that can validate specific aspects of a numerical tool. Following these studies into the various options to be considered when developing a NWT, one-way analysis of variance (ANOVA) technique is used to check the repeatability quality of experimental wave measurements conducted in a wave basin at the Australian Maritime College (AMC) as well as to validate the developed NWT against these measurements. Furthermore, analytical wave theory is used to validate the NWT over a broad range of wave conditions in both intermediate and deep water regimes.

2 NWT generation

The accurate modelling of the behaviour of water waves is an important subject for the field of coastal and ocean engineering. Many NWTs have been developed based on the volume of fluid (VOF) method introduced by Hirt and Nichols (1981) for treating flows with a free surface. The common methods which use VOF technique for wave generation can be classified into two main categories. The first one is named here as the inflow method in which the inlet boundary condition is set based on the free surface elevation and the velocity components calculated according to the desired wave using the corresponding analytical wave theory. Lin and Liu (1998) were the first of several researchers to use this procedure to generate waves in a two dimensional wave flume. The second method is referred to as moving boundary which consists of modelling the prescribed motion of the wave paddle inside the fluid domain. Hence the inlet boundary condition will be an oscillating wall, which will move similarly to a piston or flap-type physical paddles. This technique requires using the dynamic mesh technique that allows employing a variation of the wall motion. The movement control of the moving boundary is made according to the characteristics of the wave that will be generated, providing the period and the height of the desired wave. Then, using the transfer function, which relates the wave height and paddle displacement, it is possible to determine the displacement that is needed to generate the desired wave characteristics. This transfer function is defined by the method described by Dean and Dalrymple (1991). Because this technique requires a solid wall moving inside the fluid domain, a

re-meshing is inevitable in each time step or after a specified distortion of the generated grid occurs. However, re-meshing is seen by most researchers as a process that should be avoided. In the present study, it was decided to investigate the capability of using the built-in function in ANSYS-FLUENT (2014, Release 15.0) to generate regular waves via the velocity inlet's open wave boundary conditions (inlet wave B.C.) to avoid re-meshing at the inlet boundary. This function works simply by specifying certain wave characteristics, including the water depth, wave height, wave length, phase and heading.

2.1 Main characteristics and numerical settings

The schematic diagram of the NWT considered in this study is given in Figure 1. The fluid domain is a rectangle with 40 m overall length divided to 24 m fine mesh for the area of interest (corresponding to approximately six times the maximum wave length being generated), 4 m for the transition zone between the fine mesh at the area of interest and the damping zone of 12 m long (corresponding to about three times the maximum wave length) which has a coarse mesh size and numerical beach treatment to minimise the boundary-reflected waves. The height of the domain, D is 0.7 m, 0.8 m and 1.0 m for the three different water depths considered in the present study of 0.4 m, 0.5 m and 0.7 m respectively. The free surface zone height was kept constant for all conditions at 0.3 m (almost twice the maximum considered wave height).

Figure 1 NWT computational domain (not to scale) (see online version for colours)

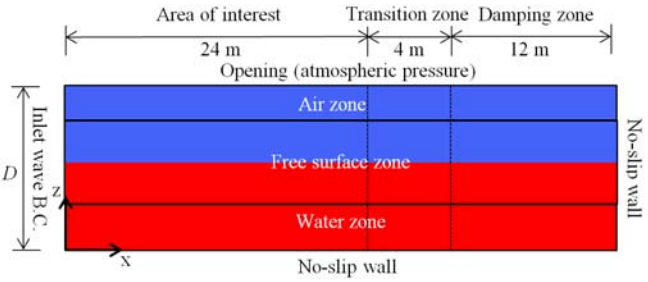

Nonlinear Stokes second-order waves defined in equation (1) (Dean and Dalrymple, 1991) enter the domain from the wave generation boundary on the domain left side (inlet wave B.C.) and propagate along the no-slip wall boundary at the bottom towards the no-slip wall at the far end of the domain. The NWT is open to atmosphere, similar to an open channel flow problem, and a pressure outlet boundary was therefore specified at the top.

$$z = \frac{H}{2}\cos\left(\frac{2\pi}{L}x - 2\pi ft\right) + \frac{\pi H^2}{8L}\frac{\cosh\left(\frac{2\pi}{L}h\right)}{\sinh^3\left(\frac{2\pi}{L}h\right)} \left[2 + \cosh\left(\frac{2\pi}{L}h\right)\right]\cos\left[2\left(\frac{2\pi}{L}x - 2\pi ft\right)\right] \quad (1)$$

where z is the free surface elevation, H the wave height, L the wave length, f the wave frequency, h the water depth, x the longitudinal position along the tank and t is the time. The flow is assumed to be laminar for the simulations in Sections 2 and 3, while the base numerical settings summarised in Table 1 are used for the whole simulations in the present paper except in Section 3.

Table 1 Base numerical settings

Parameter	*Setting*
Solver method	Pressure-based solver
Precision	Single
Multiphase model	Volume of fluid (VOF)
Multiphase scheme	Implicit
Viscous model	Laminar
Pressure-velocity coupling	PISO
Interpolation gradient method	Least squares cell-based
Pressure interpolation method	PRESTO!
Momentum discretisation method	Second-order upwind
VOF interface scheme	Compressive
Transient formulation	Bounded second-order implicit

2.2 Mesh independency study

The computational domain is discretised with a structured grid using ANSYS Workbench mesh (Figure 2). Due to the importance of the free surface zone, a very fine grid is generated in this region which extends to 0.3 m (± 0.15 m around the mean water level). Furthermore, in order to avoid the numerical diffusion or wave damping due to sudden changes in the grid sizes either in the vertical or longitudinal directions of the computation domain, a smooth grid transition was adapted out of the area of interest and the free surface zone with a bias growth rate (BGR) of 1.2.

Figure 2 Typical grid structure in different zones of the domain (see online version for colours)

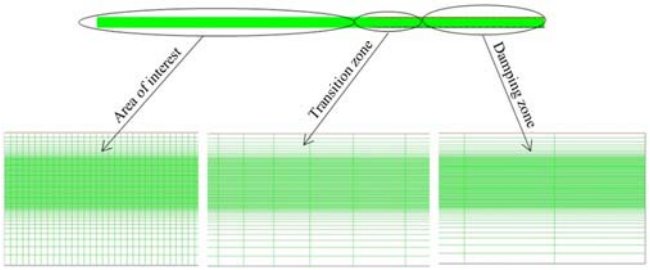

A grid independence study was carried out to evaluate the effects of mesh density on the prediction of the wave profile. Three meshes were studied with different cell sizes in the longitudinal (Δx) and vertical (Δz) directions. The grid's characteristics are summarised in Table 2. The base wave condition considered in this study was a nonlinear Stokes second-order with water depth, h = 500 mm, wave height, H = 80 mm and wave frequency, f = 0.8 Hz

(corresponding wave period, T = 1.25 s and wave length, L = 2,181 mm).

Table 2 Grid independency parameters

Grid	$\frac{H}{\Delta z}$	$\frac{L}{\Delta x}$	Δx *(mm)*	Δz *(mm)*	*Time step,* Δt *(s)*	*No. of cells*	*Courant number*
M1	10	31.16	70	8.0	0.007	21,060	0.17448
M2	20	54.53	40	4.0	0.004	65,508	0.17448
M3	40	109.1	20	2.0	0.002	227,976	0.17448

As the implicit solver is used in ANSYS-FLUENT (2014), keeping the Courant number (defined as the product of the wave celerity and the time step divided by the longitudinal cell size) below 1 to satisfy the Courant-Friedrichs-Lewy (CFL) condition is not of importance, as is the case for an explicit solver in order to have solution stability. This means that a higher Courant number can be used without convergence problems. However, to investigate the grid size effect it was decided to maintain a constant Courant number for the three grids considered in this section.

The generated numerical wave height was monitored at three different distances from the inlet boundary, P_1 (x = 4 m), P_2 (x = 6 m) and P_3 (x = 7.5 m). The time history of the generated waves (only three wave cycles were considered) is shown in Figure 3. Based on the results shown in Figure 3, the discrepancy between the different grids become more visible as the wave propagates through the computational domain from P_1 to P_3; however both M2 and M3 give the same results. As a result, grid M2 (with 3.5 times less cells than M3) will be considered for the time step study.

2.3 *Time independency study*

In this section, the influence of the time step size on the generated waves was studied. Considering the grid M2, four different time steps that result in four different Courant numbers as illustrated in Table 3 have been tested and results are shown in Figure 4. As can be seen, the largest time step (T/100) results in free surface elevation damping as the wave moves through the tank, whereas for other time steps (T/250 to T/1,000) the numerical results are identical. Therefore, a time step size of T/250 (M2-2) is considered for the remaining simulations in this paper. The selected grid with this time step (M2-2) is hereafter referred as the Base mesh.

Table 3 Time step size for time independency study

Grid	*No. of time steps per wave cycle, C*	$\Delta t = T/C$ *[s]*	*Courant number*
M2-1	100	0.0125	0.545
M2-2	250	0.005	0.218
M2-3	500	0.0025	0.109
M2-4	1,000	0.00125	0.054

Figure 3 Wave surface elevation for grid independency study (see online version for colours)

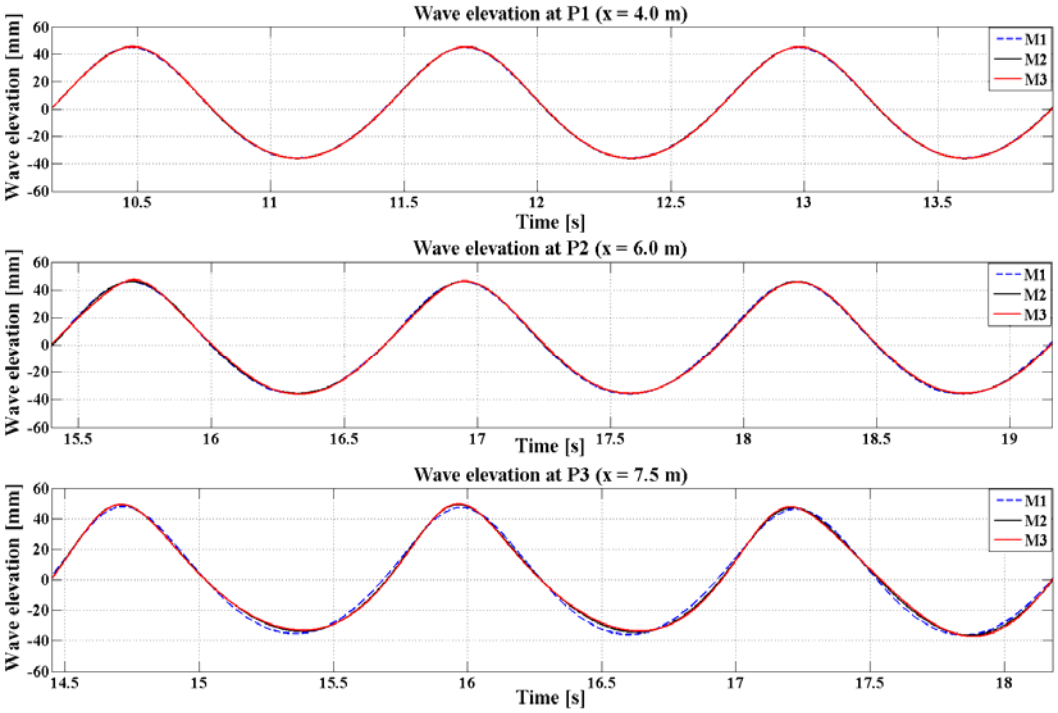

Figure 4 Wave surface elevation for time independency study (see online version for colours)

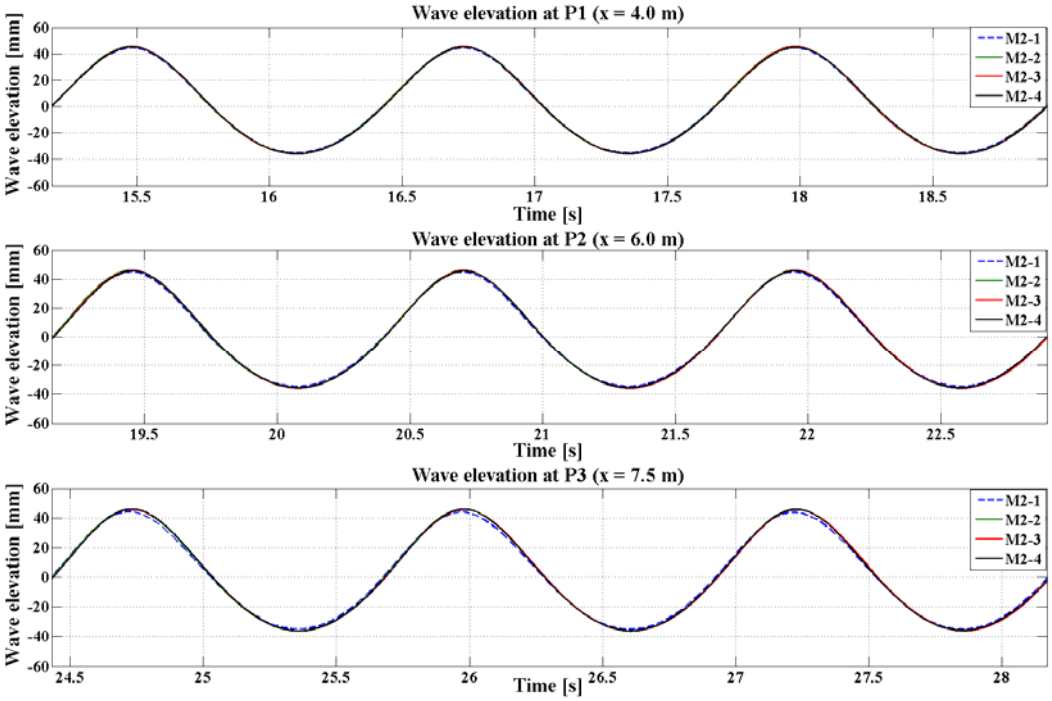

2.4 Growth rate effect

As stated in Section 2.2, the generated mesh has a smooth transition between the fine and coarse mesh zones with a BGR = 1.2. The effect of growth rate is investigated for the same regular waves as in Section 2.2 by comparing two alternative BGR, as listed in Table 4. It was found that these reduced values of BGR have no measurable influence on the generated waves in terms of either wave height or wave frequency. Considering the increase in mesh size and computation time required for the reduction in BGR, it is concluded that the base mesh is sufficient.

Table 4 Bias growth rates

Grid	*BGR*	*No. of cells*
Base	1.2	65,508
B1	1.1	75,440
B2	1.05	90,521

2.5 Air column height effect

Initially the NWT was generated with 0.3 m air column height including 0.15 m in the free surface refine zone. In order to study the influence of this height and the effect of the air column pressure on the generated waves, the air zone above the free surface was increased to 0.35 m (the corresponding mesh containing 68,688 cells). The comparison revealed that this change in air column height has a negligible measurable effect on the generated waves.

3 NWT solution methods

After investigating the mesh generation and time step aspects in the previous section as well as the solution sensitivity to different mesh parameters, in this section different solution methods are studied and their impact on the generated waves highlighted. With pressure-based solver, PISO scheme is considered for pressure-velocity coupling. PISO scheme is recommended by ANSYS-FLUENT (2014) as it provides faster convergence for unsteady flows than the standard SIMPLE approach. The solution methods included in this investigation are listed in Table 5, whereas their influences on the generated waves are discussed in the following sections.

Table 5 Investigated solution methods

Method	*Setting*
Pressure interpolation methods	PRESTO!
	Body force weighted
Interpolation gradient methods	Least squares cell-based
	Green-Gauss node-based
Momentum discretisation methods	Second-order upwind
	MUSCL
	QUICK
VOF interface schemes	Modified-HRIC
	Compressive
Transient formulation	First-order implicit
	Second-order implicit
	Bounded second-order implicit

3.1 Pressure interpolation methods

For VOF schemes, PRESTO! and body force weighted are the two pressure interpolation methods available in FLUENT, however a comparison found no clear difference between the methods. As a result, the base settings with PRESTO! method is considered in the following sections.

3.2 Interpolation gradient and momentum discretisation schemes

A matrix combining different interpolation gradient methods with momentum discretisation schemes is investigated in this section. The base setting through previous sections was set with least-squares cell-based interpolation gradient method and second-order upwind momentum discretisation scheme which is a second-order of accuracy. This is compared against third-order of accuracy schemes such as monotone upstream-centred schemes for conservation laws (MUSCL) and quadratic upwind interpolation (QUICK). Moreover, Green-Gauss node-based is considered as an alternative interpolation gradient method.

Each of the abovementioned schemes/methods provided identical numerical wave profiles, indicating that there is no impact from any combination of the available schemes. Those adopted in the base settings are kept for subsequent sections.

3.3 VOF interface schemes and transient formulation

In order to track/capture the free surface sharp interface, VOF technique is used in the present study. In this section a comparison between two schemes with different accuracy is performed; compressive (high accuracy) and modified-high resolution interface capturing (HRIC) (medium accuracy). For each scheme, first-order implicit, second-order implicit and bounded second-order implicit are the considered transient formulation schemes sorted in ascending order according to their accuracy.

Starting with the influence of the transient formulation schemes, it is clear from Figures 5 and 6 that both second-order implicit and bounded second-order implicit give the same results (with almost the same accuracy), but the first-order implicit scheme results in wave height damping. This damping effect increases as the wave propagates through the numerical tank and becomes very obvious at $x = 7.5$ m (P_3).

For the impact of VOF schemes, the comparison between compressive and modified-HRIC with the investigated transient formulation methods found that using any of the proposed VOF schemes gives the same results. Accordingly, using either compressive or modified-HRIC VOF schemes does not affect the generated waves, provided the first-order implicit transient formulation is not used.

Figure 5 Wave elevation for compressive VOF scheme with different transient formulation schemes (see online version for colours)

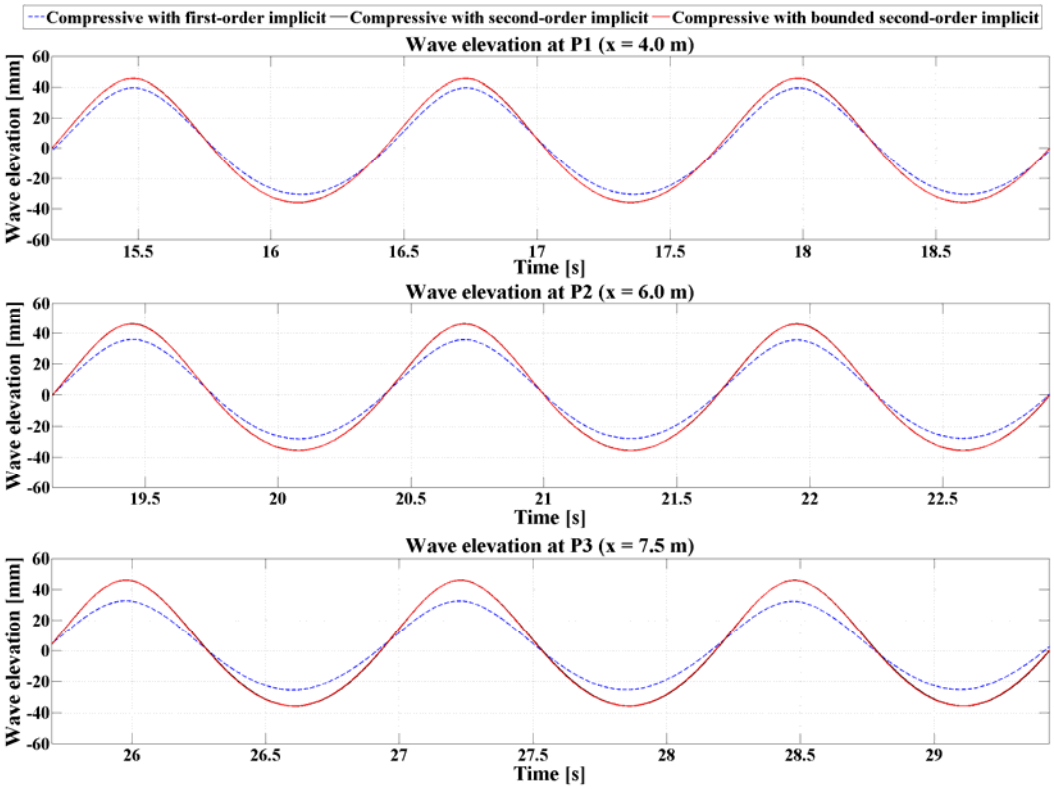

Figure 6 Wave elevation for modified-HRIC VOF scheme with different transient formulation schemes (see online version for colours)

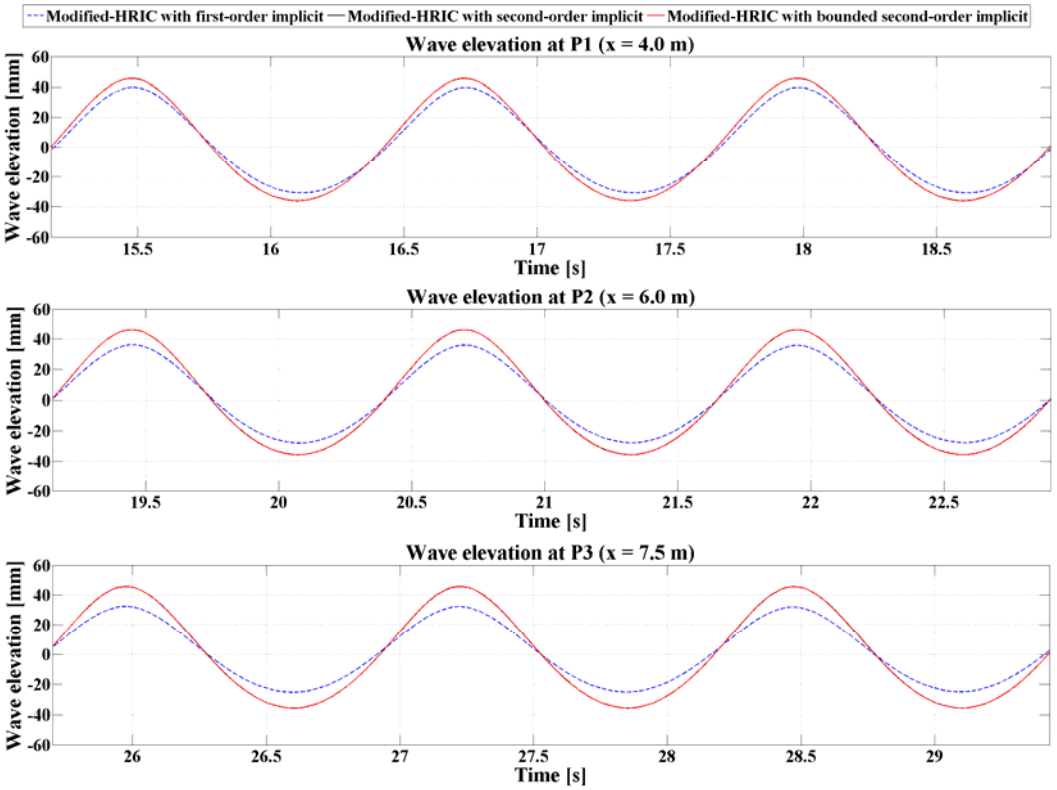

4 Turbulence modelling

Turbulence and eddy generation from wave-structure interaction represent a source of wave energy losses, therefore it is important to ensure the appropriate turbulence model is selected to avoid affecting the wave generation process. From Reynolds decomposition, the velocity can be written as a mean and fluctuation velocity terms. Introducing the mean velocity will define a time averaging velocity. By adding a fluctuation velocity in all three directions and insert it into the Navier-Stokes equations we get Reynolds averaged Navier Stokes (RANS) equations. In RANS equations, the apparent turbulent stresses (called Reynolds stresses) represent an additional unknown, resulting in more unknowns than equations. A turbulence model provides the relationship between extra unknown turbulent stresses and mean flow variables. Turbulence models can be divided into Eddy viscosity models (EVM) and Reynolds stress models (RSM). EVMs use the Boussinesq hypothesis by using an eddy (or turbulence) viscosity, while RSM use transport equations for Reynolds stresses (Woelke, 2007; Rao, 2010).

The most commonly used models among engineers are EVM, especially *k-ε* and shear stress transport (SST) models. The influence of using EVM on free surface modelling is discussed in the following section.

4.1 Free surface turbulence modelling

The VOF method treats the interface as any other point of the domain with the exception of the surface tension model. When shear between phases is negligible (as in free surface flows) no additional treatment is needed at the interface. However, when the flow results in considerable shear between phases, correction to turbulence in the region close to the interface is required to ensure that turbulent viscosity is correctly predicted (Lo and Tomasello, 2010).

According to the investigation by Teixeira and Belcher (2002) to study interaction between initially homogenous shear-free turbulence and a progressive, irrotational surface wave, the turbulence suffers two distortions when interacting with surface water waves. Firstly, vorticity in the turbulence is modulated by the periodic orbital motion of the wave over a wave cycle, which leads to streamwise Reynolds stress attaining maxima at wave crests and minima at wave troughs; the Reynolds stress normal to the free surface develops minima at wave crests and maxima at the troughs. Secondly, over several wave cycles the turbulence is made strongly anisotropic as the Stokes drift associated with the wave tilts the vertical component of the turbulent vorticity into the horizontal direction, and subsequently stretching it into elongated streamwise vortices, which come to dominate the flow. Although shear stress was initially zero since turbulence was initially isotropic, the generation of streamwise vortices by distortion of the turbulence by Stokes drift also generates a negative shear stress in the turbulence.

In order to address free-surface effects, Nakayama and Yokojima (2003) summarised the options that need to be considered in computing turbulent flows in open channels using Reynolds-averaged equations of motion:

1 turbulent kinetic energy (k) is damped

2 energy dissipation rate (ε) is increased

3 length scale is decreased

4 eddy viscosity is markedly decreased near the free surface compared with that at the centre of a closed duct.

There have been considerable efforts to develop models which can reflect free-surface effects, most of which are modifications of bounded flows. Naot and Rodi (1982) used a two-equation model that prescribes the free-surface boundary value of the dissipation to be larger than in a closed duct by setting a smaller dissipation length scale. Celik and Rodi (1984) noted that not only should the dissipation be increased, the eddy viscosity must be reduced near the free surface where the normal to free surface fluctuation decreases. Akai et al. (1981) imposed interface conditions modelled on those used in the wall treatment of turbulence, accounting empirically for turbulence production in the liquid due to the wavy interface. Lorencez et al. (1997) prescribed a zero gradient for k and enforce the dissipation rate to follow an ad hoc correlation to match their experimental data at the free surface in open channel flow.

Nakayama and Yokojima (2003) proposed an approach to model free-surface effects based on a critical examination of the direct numerical simulation results on fully-developed open-channel flows as well as existing experimental data. This indicates that turbulent kinetic energy and its dissipation rate do not vary much from the closed-duct-flow counterparts, therefore there is no need to alter the scheme significantly from the closed duct cases and the gradients may be set to zero, but that the eddy viscosity near the free surface drops sharply. They also relate this reduction in the eddy viscosity to eddy-free-surface interaction as when the free surface can move, large eddies push it up and the reflection is not perfect and there is some energy reduction. This means that the best way of treating free-surface effects within the two-equation modelling is to introduce a damping function for eddy viscosity near the free surface, and to leave the transport equations and the boundary conditions for the turbulent kinetic energy and dissipation rate unaltered.

This brief review of techniques highlights that particular attention is required for shear stress at the interface between phases, which leads to the need for treatment of turbulent quantities in the free surface region. Without any special treatment of the free surface, a spurious amount of eddy viscosity is generated at the interface, which tends to smear high frequency surface instabilities, and introduce strong errors in estimating the interfacial shear, which is the most important ingredient for mass transfer modelling. Moreover, without this treatment, the high velocity gradients at the free surface, especially in the gaseous phase, generate excessive turbulence throughout the two-phase flow when using differential EVMs like the k-ε or k-ω models. Therefore, certain damping of turbulence is necessary in the interfacial area because the mesh is too coarse to resolve the velocity gradient in the gas at the interface (Höhne and Mehlhoop, 2014). On the gas side of the smooth free surface, this damping should be similar to that used near a solid wall. Moreover, on the liquid side the advanced model should take the anisotropy between the normal and the tangential Reynolds stresses into account. The interface treatment implemented in ANSYS-FLUENT (2014) is based on a simple symmetric damping procedure proposed by Egorov (2004). This procedure provides for the solid wall-like damping of turbulence in both gas and liquid phases. It is based on the standard ω-equation, formulated by Wilcox (1998).

The base conditions for mesh resolution and numerical settings summarised in Table 1 (and adopted for the investigations covered in Sections 2 and 3) proved to be accurate in the case of laminar flow. Different turbulence models including standard k-ε, realisable k-ε, SST (with and without turbulence damping option) and RSM are investigated in this section in order to determine the applicability of using these models to capture the free surface profile when generating non-breaking regular waves.

4.2 Turbulence initial values and boundary conditions

While the initial condition of the mean flow field is specified with the zero mean velocities and hydrostatic pressure, physically, the turbulence field should also be zero since nothing has happened at this stage. However, because the production term in the turbulence kinetic energy equation is proportional to k per set value, the turbulence will remain zero if it is zero initially (Wu, 2004). In order to prevent this, an 'initial seeding' method is imposed to this study. The initial seeding means that we impose a very small value on k as the initial condition. The initial values for k and ε were set according to Lin and Liu (1998) as expressed in equations (2) and (3):

$$k = \frac{1}{2}u_t^2, \;\; u_t = \delta C_w, \;\; \delta = 0.0025 \tag{2}$$

$$\varepsilon = C_d \frac{k^2}{v_t}, \;\; v_t = \alpha v \tag{3}$$

where C_w is the wave celerity at the inflow boundary, C_d is an empirical coefficient taken to be 0.09 (Rodi, 1980), v and v_t are respectively the fluid and eddy viscosities and α is the eddy viscosity ratio and was chosen by Lin and Liu (1998) to be 0.1 (in the present study, another higher value of 10 is also tested which reflects the influence of the initial eddy viscosity value on the simulated waves), while the specific dissipation rate (ω) is defined as $\omega = \frac{k}{v_t}$.

Figure 7 Wave elevation with different turbulence models ($\alpha = 0.1$) (see online version for colours)

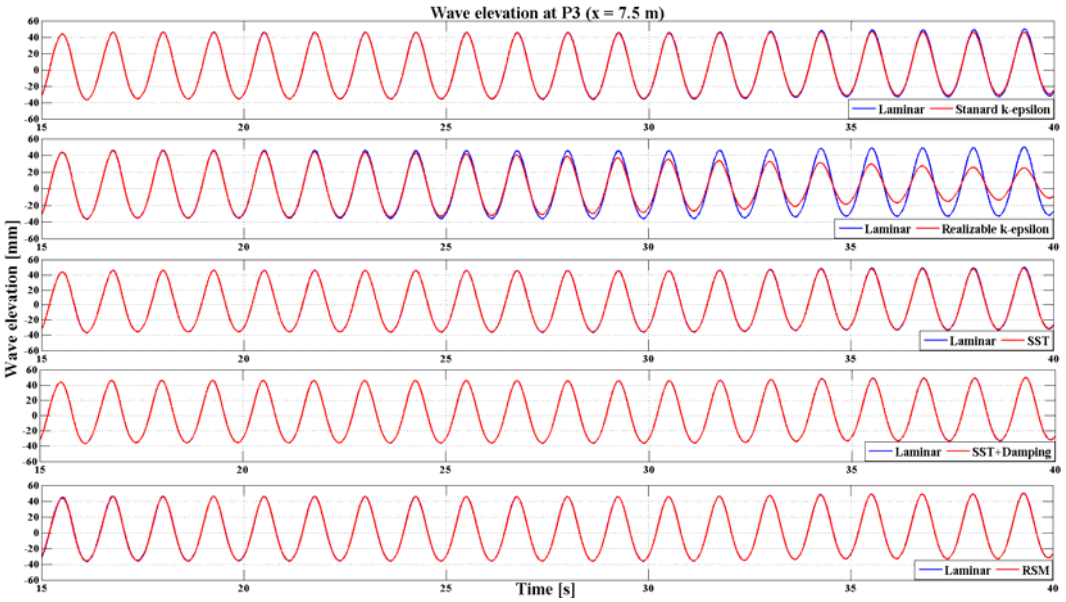

There are different ways to specify the turbulence characteristics at the inlet and outlet boundary conditions in FLUENT such as explicitly input k, ε and ω, or alternatively define the turbulence intensity and the eddy viscosity ratio (ANSYS-FLUENT, 2014). In the present work, the initial seeding values are also used at the inlet boundary, whereas the default values of 5% turbulent intensity and turbulent viscosity ratio of 10 are assigned for the outlet boundary conditions. Another set of these parameters (2% and 2) was tested and no influence on the results was observed (results are not presented). Table 6 summarises the different turbulence models considered in the present analysis.

Table 6 Turbulence models

Model	*Standard k-ε*	*Realisable k-ε*	*SST*	*SST + Damping*	*RSM*
$\alpha = \frac{\nu_t}{\nu}$	0.1, 10	0.1, 10	0.1, 10	0.1, 10	0.1, 10

4.3 Turbulent wave results

In this section, the generated numerical waves with each of the considered turbulence models are investigated against laminar results. As there is no structure disturbing the fluid flow, no separation or turbulence is expected. As a result, generating non-breaking regular waves can be assumed to be laminar in which the flow follows the orbital motion and implementing a turbulence model should not change the characteristics of the generated waves.

For the case with initial eddy viscosity ratio, α = 0.1, Figure 7 shows that there is a perfect match between laminar flow and the turbulent case with RSM and SST with turbulence damping models. In contrast, other EVMs such as standard k-ε, realisable k-ε and SST show good agreement at the beginning of the simulation, however after running for several cycles, discrepancies start appearing which are more clearly illustrated for a single wave cycle in Figure 8. It is worth noting that the simulation results using applied turbulence models should be independent of the initial seeding values after a sufficiently long simulation time (ANSYS-FLUENT, 2014).

Figure 8 Single wave cycle with different turbulence models ($\alpha = 0.1$) (see online version for colours)

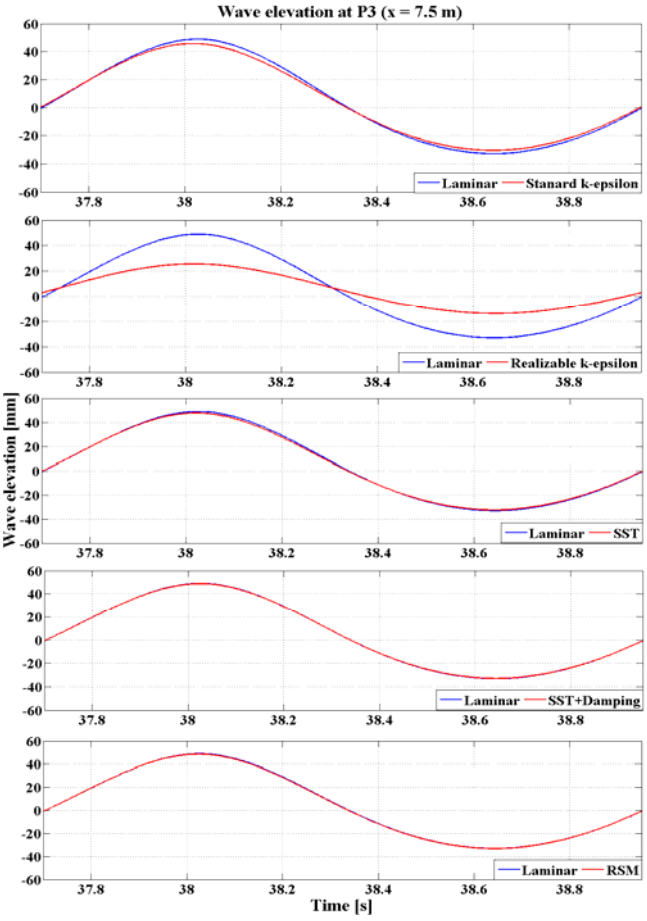

Figure 9 Wave elevation with different turbulence models ($\alpha = 10$) (see online version for colours)

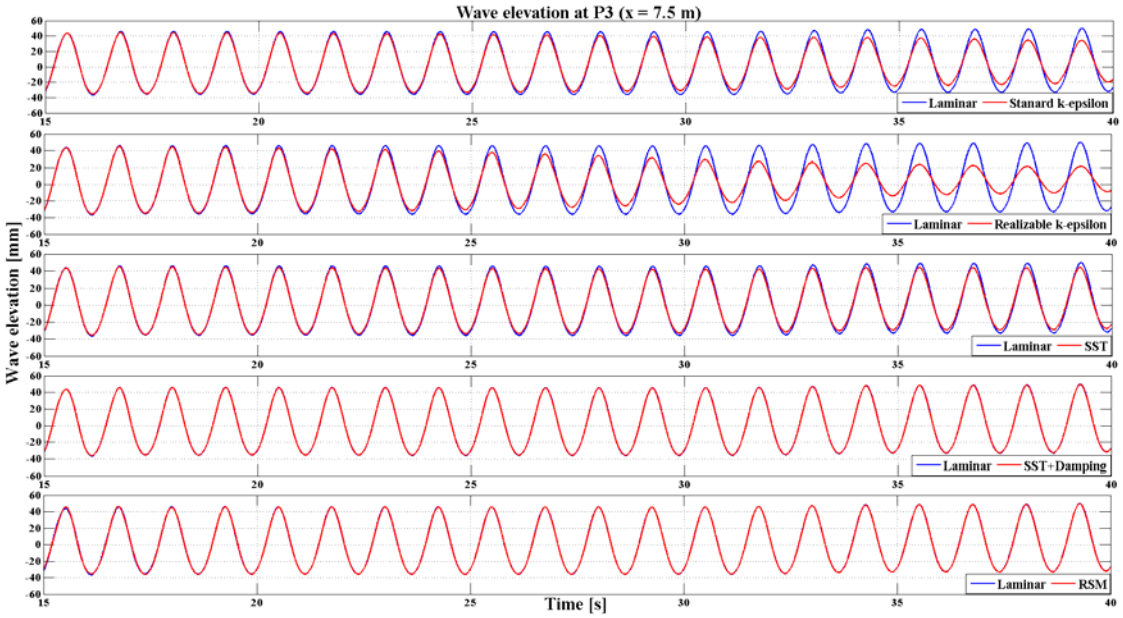

The discrepancies between laminar and turbulence models after a certain period of time can be related to the increase in the generated eddy viscosity with time. To illustrate how the generated waves rely on the initial seeding value, simulation cases with the investigated turbulence models were repeated with a higher initial eddy viscosity ratio of 10, with results shown in Figures 9 and 10. In comparison with the results where $\alpha = 0.1$, increasing the initial eddy viscosity ratio to 10 resulted in earlier damping in the generated waves with EVMs. On the other hand, both RSM and SST with turbulence damping models still give good agreement with the laminar case.

Figure 11 shows a comparison between the generated eddy viscosity ratio contours from the different turbulence models through the fluid domain at $t = 5$ s and at the end of the simulation (t = 40 s) with 0.1 and 10 initial eddy viscosity ratios. The values of the eddy viscosity ratio at the free surface interface through the area of interest ($x = 4$ m to $x = 7.5$ m) are compared in Figure 12.

The results presented in Figures 11 and 12 highlight that increasing the initial eddy viscosity ratio results in higher eddy viscosity through the fluid domain. However, for cases with realisable k-ε and SST with turbulence damping, the influence of the initial seeding values becomes smaller with time, which can be seen in the close matching between results for $\alpha = 0.1$ and 10 after 40 s simulation time in Figure 12 for these two models. Furthermore, the generated eddy viscosity grows as the simulation time increases, with excessive production at the free surface interface within the area of interest found for the EVMs such as realisable k-ε, standard k-ε and SST. Thus, the massive eddy viscosity at the free surface essentially takes away wave energy, resulting in the wave height damping seen in Figures 7 to 10. Moreover, the eddy viscosity contours in Figure 11 illustrate the special treatment of the free surface interface in which the interface area appears as an isolated region due to activating the turbulence damping with SST turbulence model.

Figure 10 Single wave cycle with different turbulence models ($\alpha = 10$) (see online version for colours)

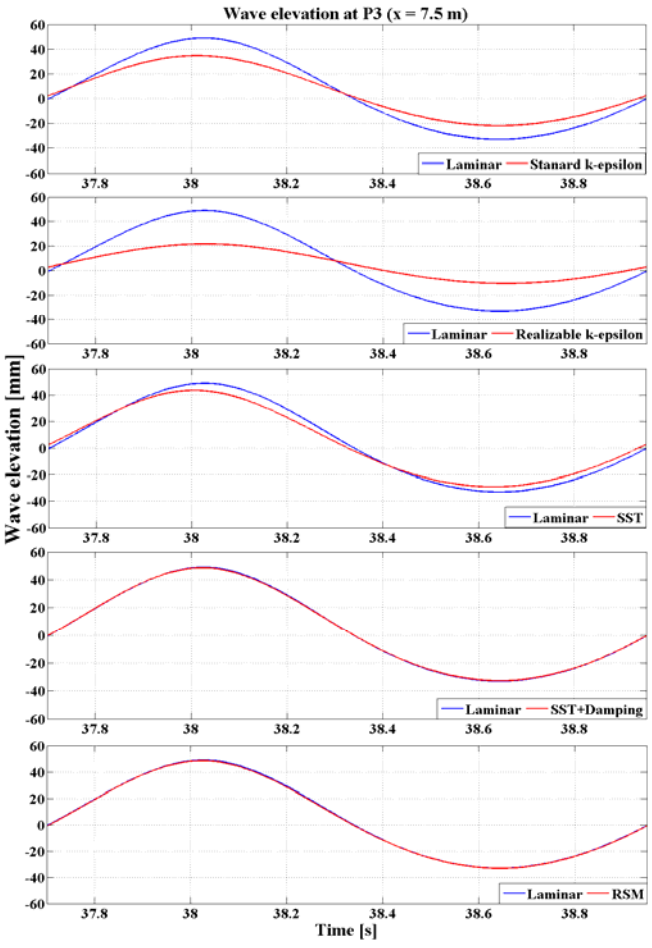

Figure 11 Eddy viscosity ratio contours for different turbulence models (see online version for colours)

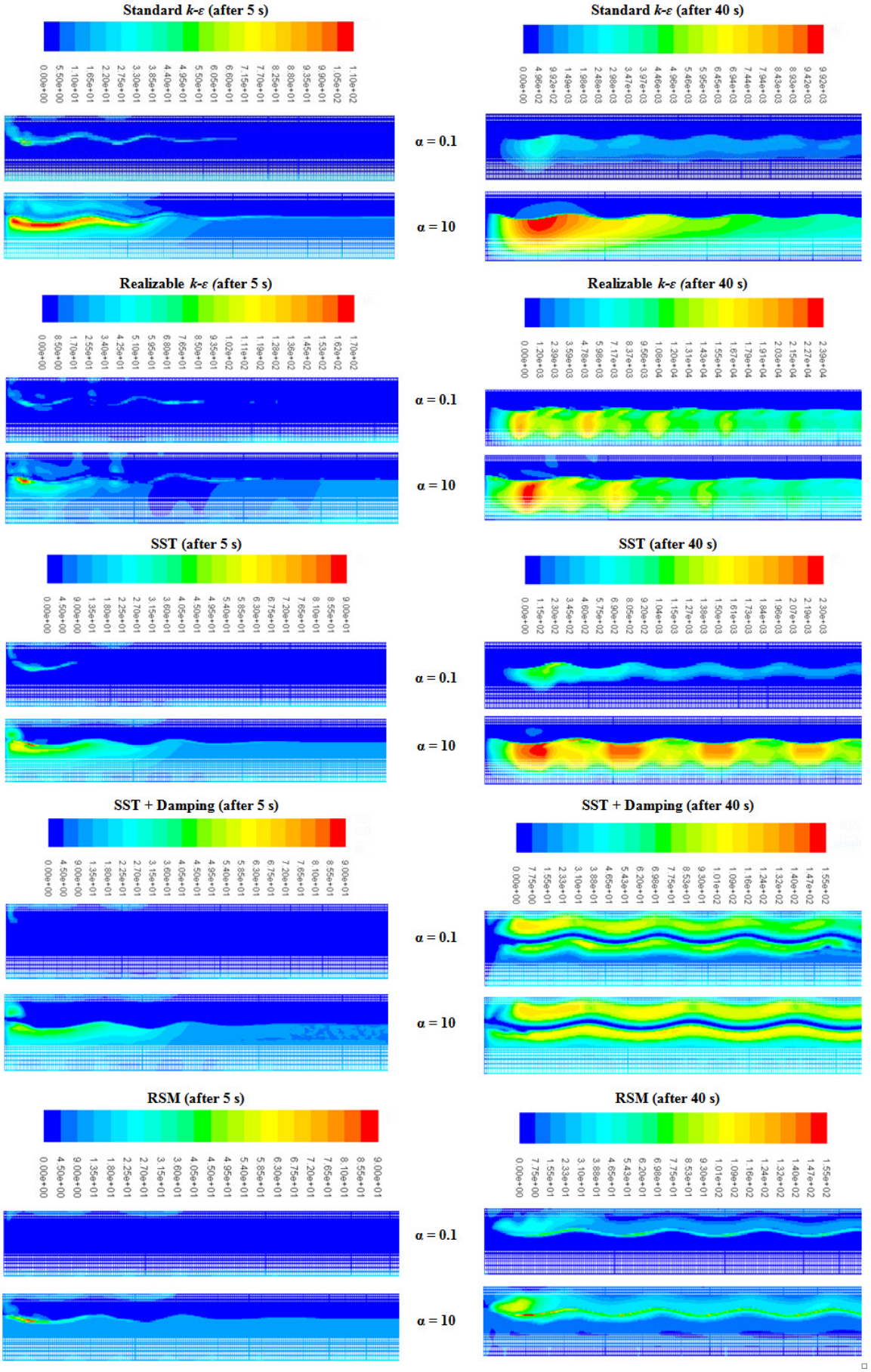

Figure 12 Eddy viscosity ratio at the free surface interface (see online version for colours)

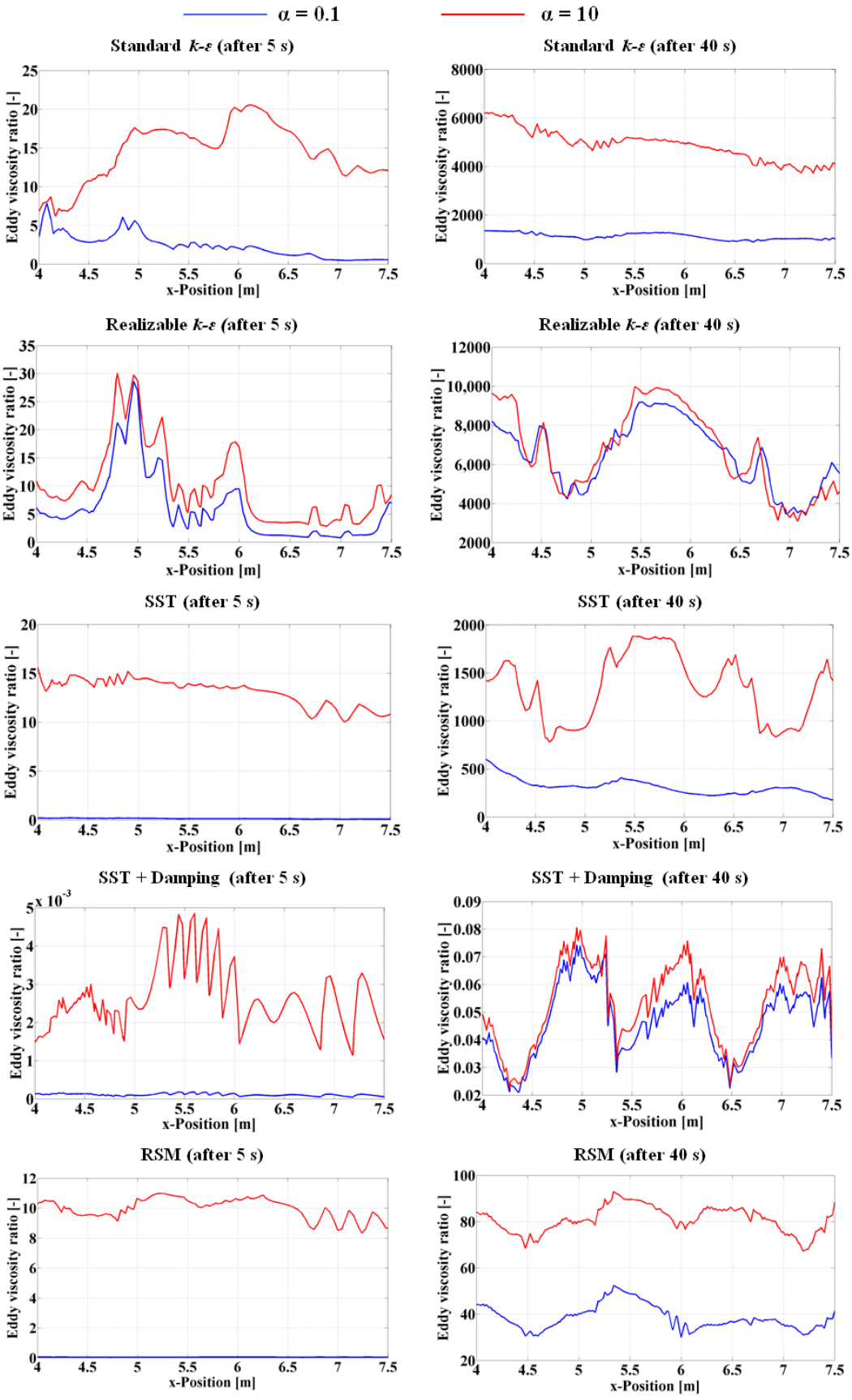

5 Experimental set-up and NWT validation

5.1 Experimental wave measurements

Physical wave measurements were performed in a 35 m long and 12 m wide wave basin at the AMC. Both regular and irregular waves can be generated by 16 piston-type wave paddles driven by servo-motors. Using capacitance-type wave probes, the wave elevation was measured at four points as shown in Figures 13 and 14 with 200 Hz sampling frequency. P_0 was used to measure the incident waves that represent the input for the NWT, where P_1, P_2 and P_3 were used to validate the numerical waves.

A wide range of nonlinear wave conditions covering both intermediate and deep water regimes in three water depths 400, 500 and 700 mm have been generated in the wave basin. For verification of experiment repeatability, measurements were repeated two times. An example of the result of three repeated physical wave measurements is shown in Figure 15 (five wave cycles were considered) for wave condition of H = 80 mm, f = 0.8 Hz and h = 500 mm. EFD refers to experimental fluid dynamics (wave measurement); EFD-R1 and EFD-R2 refer to the first and second repeated experimental measurements, accordingly. No numerical waves were monitored at the inlet boundary condition that is corresponding to P_0 in the physical measurements. Therefore, validation is limited to the area of interest (i.e., at P_1, P_2 and P_3).

Figure 13 Experimental wave measurements layout (not to scale)

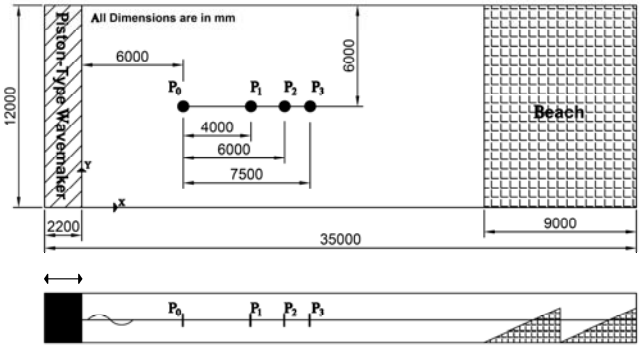

Figure 14 Experimental wave measurements set-up at AMC model test basin (see online version for colours)

Figure 15 Experimental wave measurements with repeatability check (see online version for colours)

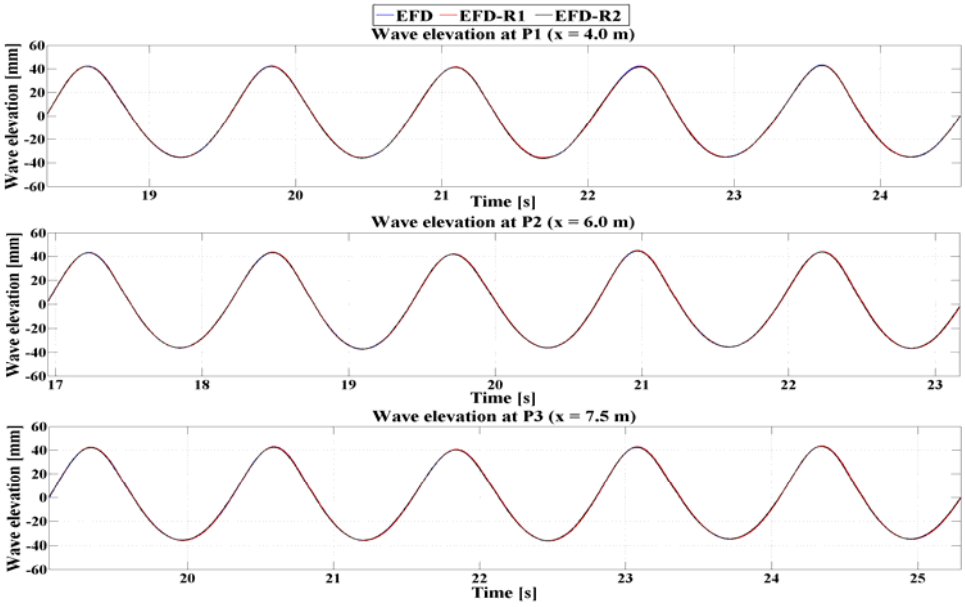

In addition to the good repeatability illustrated in the qualitative comparison in Figure 15, one-way ANOVA was used to check the validity of the null hypothesis for the experimental measurements. The overall null hypothesis for one-way ANOVA with q groups is $\mu_1 = \ldots = \mu_q$, where μ is the population mean for each group. The alternative hypothesis is that the population means are not all equal. Using the F-critical value found from the F-distribution for a given alpha (significance level, 0.05 is a common value that was used in the present study and corresponding to 95% confidence level), the null hypothesis is rejected with 95% confidence if the observed F-statistic (from the ANOVA test) is larger than the critical value, otherwise we retain the null hypothesis with indication that there are no statistically significant differences found. For more details about ANOVA test, the reader is referred to Seltman (2014).

For each wave probe (P_1, P_2 and P_3), there were five wave heights (observations) measured from five wave cycles and three groups (runs) (EFD, EFD1 and EFD2). Final ANOVA test results are summarised in Table 7. As the calculated F-statistic ratio for the analysed data found to be less than the F-critical values, hence the null hypothesis is retained. This proves that the experimental wave measurements are highly repeatable, therefore can be used for the validation process of the generated numerical waves.

5.2 *NWT validation*

The numerical waves generated in the previous sections were validated against both experimental measurements and Stokes nonlinear second-order wave theory. For instance, a comparison between the numerical results (with SST + Damping turbulence model and other numerical settings listed in Table 1) for the same base wave condition used in Sections 2 to 4, experimental measurements and Stokes nonlinear second-order waves is shown in Figure 16. While adopting ANOVA test in the validation process of the developed NWT, CFD results were considered as an additional group to the experimental measurements; therefore the total number of groups will be four. Based on this statistical analysis, F-statistic values were found to be less than F-critical (for example, F-statistic = 0.262 and F-critical = 3.24 at P_2), as a result there are no significant statistical differences found, which provides that the developed NWT is in good quantitative agreement with the physical wave measurements.

In addition to the base wave condition considered in the present study, a wide range of wave conditions in terms of wave height, frequency and water depth were also tested with the same base mesh, time step and numerical settings. Table 8, summarises the range of the whole tested conditions. Considering the regions of validity for various wave theories (Le Mehaute, 1976), all waves investigated in this section have $0.0147 \le \frac{h}{gT^2} \le 0.1028$ and $0.0011 \le \frac{H}{gT^2} \le 0.0132$ that are classified either as second-order Stokes waves or weakly third-order Stokes waves.

Table 7 ANOVA test results for experiment repeatability check

	Experiment repeatability		
	P_1	P_2	P_3
F-statistic	1.200	0.095	0.969
F-critical	3.89	3.89	3.89
Null hypothesis	Retained	Retained	Retained

Figure 16 NWT validation: CFD results (with SST + turbulence damping) versus experimental measurements (EFD) and Stokes second-order waves (see online version for colours)

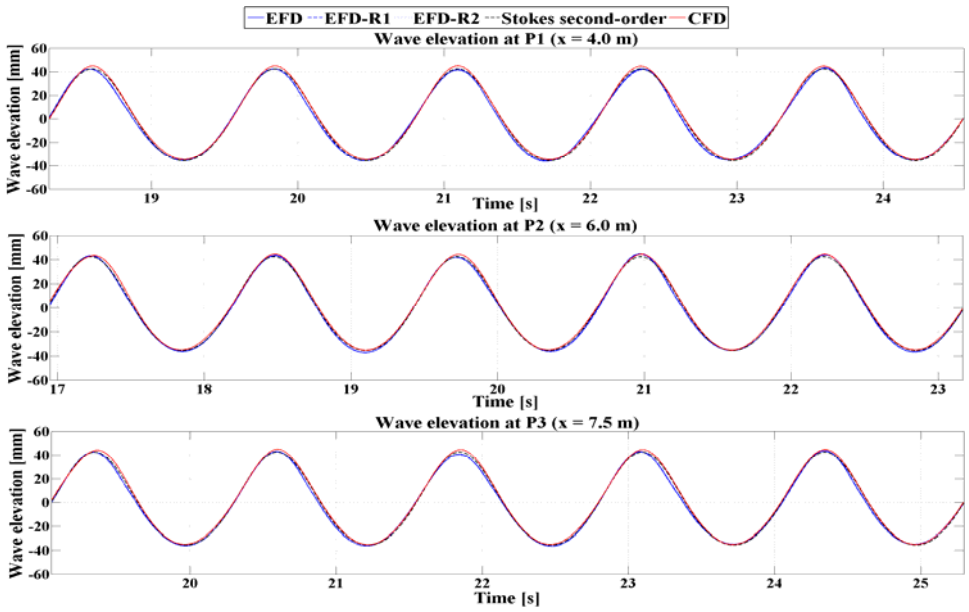

Table 8 Tested wave conditions

h (mm)	*f* (Hz)	*H* (mm)	*Wave steepness* (H/L)	$\frac{H}{\Delta z}$	$\frac{L}{\Delta x}$	$C=\frac{T}{\Delta t}$
400	0.6–1.0	30–100	0.010–0.075	7.5–25	74.5–26.6	333.3–166.7
	1.1	30–90				
	1.2	30–80				
500	0.6–0.9	30–120	0.009–0.084	7.5–30	81.1–26.9	333.3–166.7
	1.0, 1.1	30–100				
	1.2	30–90				
700	0.6–0.8	30 –160	0.008–0.085	7.5–40	90.8–27.1	333.3–166.7
	0.9	30–140				
	1.0	30–120				
	1.1	30–110				
	1.2	30–90				

Table 9 Base numerical settings

Parameter	*Setting*
Solver method	Pressure-based solver
Precision	Single
Multiphase model	Volume of fluid (VOF)
Multiphase scheme	Implicit
Viscous model	Laminar
Pressure-velocity coupling	PISO
Interpolation gradient method	Least squares cell-based
Pressure interpolation method	PRESTO!
Momentum discretisation method	Second-order upwind
VOF interface scheme	Compressive
Transient formulation	Bounded second-order implicit

Table 10 Grid independency parameters

Grid	$\frac{H}{\Delta z}$	$\frac{L}{\Delta x}$	*Δx (mm)*	*Δz (mm)*	*Time step, Δt (s)*	*No. of cells*	*Courant number*
M1	10	31.16‡	70	8.0	0.007	21,060	0.17448
M2	20	54.53‡	40	4.0	0.004	65,508	0.17448
M3	40	109.1‡	20	2.0	0.002	227,976	0.17448

Table 11 Time step size for time independency study

Grid	*No. of time steps per wave cycle, C*	*Δt = T/C (s)*	*Courant number*
M2-1	100	0.0125	0.545
M2-2	250	0.005	0.218
M2-3	500	0.0025	0.109
M2-4	1,000	0.00125	0.054

Table 12 Bias growth rates

Grid	*BGR*	*No. of cells*
Base	1.2	65,508
B1	1.1	75,440
B2	1.05	90,521

Table 13 Investigated solution methods

Method	*Setting*
Pressure interpolation methods	PRESTO!
	Body force weighted
Interpolation gradient methods	Least squares cell-based
	Green-Gauss node-based
Momentum discretisation methods	Second-order upwind
	MUSCL
	QUICK
VOF interface schemes	Modified-HRIC
	Compressive
Transient formulation	First-order implicit
	Second-order implicit
	Bounded second-order implicit

Table 14 Turbulence models

Model	*Standard k-ε*	*Realisable k-ε*	*SST*	*SST + damping*	*RSM*
$\alpha=\frac{v_t}{v}$	0.1, 10	0.1, 10	0.1, 10	0.1, 10	0.1, 10

Table 15 ANOVA test results for experiment repeatability check

	Experiment repeatability		
	P_1	P_2	P_3
F-statistic	1.200	0.095	0.969
F-critical	3.89	3.89	3.89
Null hypothesis	Retained	Retained	Retained

Table 16 Tested wave conditions

h (mm)	f (Hz)	H (mm)	Wave steepness (H/L)	$\frac{H}{\Delta z}$	$\frac{L}{\Delta x}$	$C=\frac{T}{\Delta t}$
400	0.6–1.0	30–100	0.010–0.075	7.5–25	74.5–26.6	333.3–166.7
	1.1	30–90				
	1.2	30–80				
500	0.6–0.9	30–120	0.009–0.084	7.5–30	81.1–26.9	333.3–166.7
	1.0, 1.1	30–100				
	1.2	30–90				
700	0.6–0.8	30 –160	0.008–0.085	7.5–40	90.8–27.1	333.3–166.7
	0.9	30–140				
	1.0	30–120				
	1.1	30–110				
	1.2	30–90				

Figure 17 Wave height comparison between CFD and wave theory (see online version for colours)

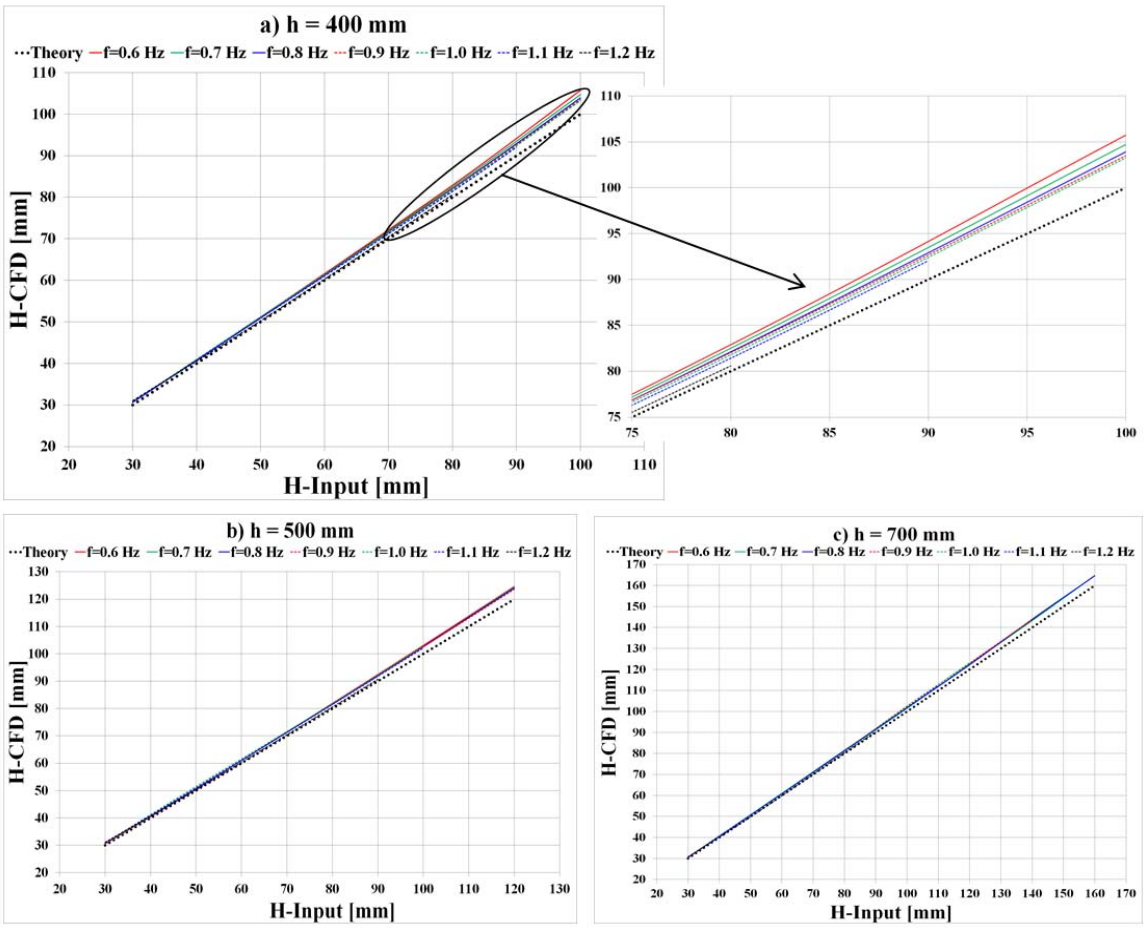

A comparison between generated numerical wave height (H-CFD) and analytical wave theory (H-Input) results for the different wave conditions in Table 8 is shown in Figure 17. Results show good agreement, even for the cases where the number of elements per wave height and wave length are lower than those of the base case. In addition, as the wave height increases (wave nonlinearity develops) the deviation from theory broadens with a maximum of 5.7% in the case of 400 mm water depth with 0.6 Hz wave frequency. Furthermore, moving from low frequency to higher wave frequency results in reducing the numerical deviation (3.62% at 0.6 Hz to 0.73% at 1.2 Hz for H = 80 mm and h = 400 mm), which can be assigned to the reduction in shallowing effect as the wavelength decreases in comparison with the water depth (i.e., increasing $\frac{h}{gT^2}$).

6 Conclusions

A guide to designing a NWT using a CFD model that can accurately be used to generate nonlinear regular water waves in intermediate and deep water regimes is presented. In particular, the effects of meshing parameters, time step interval, solution methods and turbulence models on the generated numerical wave profile are explored.

Except the grid size and time step effects, a negligible influence was found for reducing the BGR lower than 1.2 to improve the smooth transition between the fine and coarse mesh zones as well as increasing the air column height. Furthermore, among the studies carried out on the influence of different solver settings and discretisation schemes, the appropriate selection of the transient formulation scheme has a direct impact on the generated waves. It is recommended to use either the second-order implicit or bounded second-order implicit methods to avoid significant damping of the generated waves when using the first-order implicit transient formulation scheme.

Different turbulence models were investigated to illustrate their ability to address the free-surface effect when generating non-breaking regular water waves. All of the tested EVMs such as standard k-ε, realisable k-ε and SST were found to be unsuitable due to massive eddy viscosity generation at the free surface interface, resulting in considerable damping of the generated waves. However, activating the free surface treatment option available in FLUENT to damp the excessive turbulence generation at the free surface interface improved the generated waves with SST model. Results were in good agreement with both the laminar flow and RSM.

Based on the conducted one-way ANOVA, there are no statistical significant differences found either between the subsequent experimental runs (repeated measurements) or between the experimental and CFD results. Furthermore, the developed NWT was validated against analytical wave theory for three different water depths and an extensive range of wave steepness with good agreement, even for wave conditions with 7.5 and 26.6 elements per wave height and wave length, accordingly. In addition to the regular waves investigated in this paper, studying actual wave spectra will be considered in future work.

References

Akai, M., Inoue, A. and Aoki, S. (1981) 'The prediction of stratified two-phase flow with a two-equation model of turbulence', *International Journal of Multiphase Flow*, Vol. 7, No. 1, pp.21–39.

ANSYS-FLUENT (2014) *User's Guide*, Release 15.0. ANSYS Inc., USA.

Bhinder, M., Mingham, C., Causon, D., Rahmati, M., Aggidis, G., Chaplin, R. (2009) 'Numerical and experimental study of a surging point absorber wave energy converter. *Proceedings of the 8th European Wave and Tidal Energy Conference*.

Bouali, B. and Larbi, S. (2013) 'Contribution to the geometry optimization of an oscillating water column wave energy converter', *Energy Procedia*, Vol. 36, pp.565–573.

Celik, I. and Rodi, W. (1984) 'Simulation of free-surface effects in turbulent channel flows', *Physicochemical Hydrodynamics*, Vol. 5, Nos. 3–4, pp.217–227.

Coe, R.G. and Neary, V.S. (2014) 'Review of methods for modeling wave energy converter survival in extreme sea states', *Proceedings of the 2nd Marine Energy Technology Symposium (METS)*, Seattle, WA, USA.

Dean, R.G. and Dalrymple, R.A. (1991) *Water Wave Mechanics for Engineers and Scientists*, World Scientific Publishing Company, Singapore.

Egorov, Y. (2004) 'Contact condensation in stratified steam-water flow. Validation of CFD codes with PTS-relevant test cases', *5th Euratom Framework Programme*, ECORA Project (Technical Report EVOL–ECORA–D 07).

Finnegan, W. and Goggins, J. (2012) 'Numerical simulation of linear water waves and wave-structure interaction', *Ocean Engineering*, Vol. 43, pp.23–31.

Fleming, A., Penesis, I., Macfarlane, G., Bose, N. and Denniss, T. (2012) 'Energy balance analysis for an oscillating water column wave energy converter', *Ocean Engineering*, Vol. 54, pp.26–33.

Fleming, A.N. (2012) *Phase-averaged Analysis of an Oscillating Water Column Wave Energy Converter*, PhD thesis, University of Tasmania.

Gomes, M.D.N., Dos Santos, E.D., Isoldi, L.A. and Rocha, L.A.O. (2013) 'Two-dimensional geometric optimization of an oscillating water column converter of real scale', *22nd International Congress of Mechanical Engineering (COBEM)*.

Havn, J. (2011) *Wave Loads on Underwater Protection Covers*. Master thesis, Department of Marine Technology, Norwegian University of Science and Technology (NTNU), Norway.

Hirt, C.W. and Nichols, B.D. (1981) 'Volume of fluid (VOF) method for the dynamics of free boundaries', *Journal of Computational Physics*, Vol. 39, No. 1, pp.201–225.

Höhne, T. and Mehlhoop, J-P. (2014) Validation of closure models for interfacial drag and turbulence in numerical simulations of horizontal stratified gas-liquid flows', *International Journal of Multiphase Flow*, Vol. 62, pp.1–16.

Horko, M. (2007) *CFD Optimisation of an Oscillating Water Column Energy Converter,* Thesis of Master of Engineering Science, School of Mechanical Engineering, The University of Western Australia.

Hu, Z.Z., Causon, D., Mingham, C. and Qian, L. (2011) 'Numerical simulation of floating bodies in extreme free surface waves', *Natural Hazards and Earth System Science*, Vol. 11, No. 2, pp.519–527.

Joubert, J.R. (2013) *Design and Development of a Novel Wave Energy Converter*, PhD thesis, Stellenbosch University.

Lal, A. and Elangovan, M. (2008) 'CFD simulation and validation of flap type wave-maker', *World Academy of Sciences, Engng. Tech.*, Vol. 46, pp.76–82.

Lambert, R.J. (2012) *Development of a Numerical Wave Tank using OpenFoam*, Thesis of Master in Energy Sustainable, Universidade De Coimbra.

Le Mehaute, B. (1976) *An Introduction to Hydrodynamics and Water Waves*, Springer-Verlag, New York.

Lin, P. and Liu, P.L-F. (1998) 'A numerical study of breaking waves in the surf zone', *Journal of Fluid Mechanics*, Vol. 359, pp.239–264.

Liu, Z., Hyun, B-S. and Hong, K-Y. (2008) 'Application of numerical wave tank to OWC air chamber for wave energy conversion', *International Offshore and Polar Engineering Conference*, pp.350–356.

Liu, Z., Hyun, B-S., Shi, H. and Hong, K. (2010) 'Practical simulation of oscillating water column chamber for wave energy conversion', *International Journal of Green Energy*, Vol. 7, No. 3, pp.337–346.

Lo, S. and Tomasello, A. (2010) *Recent Progress in CFD Modelling of Multiphase Flow in Horizontal and Near-Horizontal Pipes*, CD-adapco.

Lorencez, C., Nasr-Esfahany, M., Kawaji, M. and Ojha, M. (1997) 'Liquid turbulence structure at a sheared and wavy gas-liquid interface', *International Journal of Multiphase Flow*, Vol. 23, No. 2, pp.205–226.

Nakayama, A. and Yokojima, S. (2003) 'Modeling free-surface fluctuation effects for calculation of turbulent open-channel flows', *Environmental Fluid Mechanics*, Vol. 3, No. 1, pp.1–21.

Naot, D. and Rodi, W. (1982) 'Calculation of secondary currents in channel flow', *Journal of the Hydraulics Division*, Vol. 108, No. 8, pp.948–968.

Rao, P.S. (2010) 'Modeling of turbulent flows and boundary layer', in Houng Woo Oh (Ed.): Computational *Fluid Dynamics*, In Tech.

Rodi, W. (1980) *Turbulent Models and Their Application in Hydraulics – A State of the Art Review*, International Association for Hydraulics Research, Delft.

Seibt, F.M., Couto, E.C., Santos, E.D.d., Isoldi, L.A., Rocha, L.A.O. and Teixeira, P.R.d.F. (2014) 'Numerical study on the effect of submerged depth on horizontal plate wave energy converter', *China Ocean Engineering*, Vol. 28, No. 5, pp.687–700.

Seltman, H.J. (2014) 'Experimental design and analysis' [online] http://www.stat.cmu.edu/~hseltman/309/Book/Book.pdf. (accessed 6 April 2015).

Şentürk, U. and Özdamar, A. (2011) 'Modelling the interaction between water waves and the oscillating water column wave energy device', *Mathematical and Computational Applications*, Vol. 16, No. 3, pp.630–640.

Silva, M., Vitola, M.d.A., Pinto, W. and Levi, C. (2010) *Numerical Simulation of Monochromatic Wave Generated in Laboratory: Validation of a CFD Code*, 23o Congresso Nacional de Transporte Aquaviário, Construção Naval e Offshore, SOBENA, Rio de Janeiro.

Teixeira, M. and Belcher, S. (2002) 'On the distortion of turbulence by a progressive surface wave', *Journal of Fluid Mechanics*, Vol. 458, pp.229–267.

Wilcox, D.C. (1998) *Turbulence Modeling for CFD*, DCW industries La Canada, CA.

Woelke, M. (2007) 'Eddy viscosity turbulence models employed by computational fluid dynamic', *Transactions of the Institute of Aviation*, Vol. 191, No. 4, pp.92–113.

Wu, T.R. (2004) *A Numerical Study of Three-Dimensional Breaking Waves and Turbulence Effects*, PhD thesis, Faculty of the Graduate School of Cornell University.

Yu, Y-H. and Li, Y. (2013) 'Reynolds-averaged Navier-Stokes simulation of the heave performance of a two-body floating-point absorber wave energy system', *Computers & Fluids*, Vol. 73, pp.104–114.

Zhang, Y., Zou, Q-P. and Greaves, D. (2012) 'Air-water two-phase flow modelling of hydrodynamic performance of an oscillating water column device', *Renewable Energy*, Vol. 41, pp.159–170.

Appendix K

Paper 11: Elhanafi A. Prediction of regular wave loads on a fixed offshore oscillating water column–wave energy converter using CFD. *Journal of Ocean Engineering and Science. 2016;1(4):268-283*.

Available online at www.sciencedirect.com

ScienceDirect

Journal of Ocean Engineering and Science 1 (2016) 268–283

www.elsevier.com/locate/joes

Prediction of regular wave loads on a fixed offshore oscillating water column-wave energy converter using CFD

Ahmed Elhanafi [a,b,*]

[a] *National Centre for Maritime Engineering and Hydrodynamics, Australian Maritime College, University of Tasmania, Launceston, Tasmania 7250, Australia*
[b] *Department of Naval Architecture and Marine Engineering, Alexandria University, Alexandria, Egypt*

Received 24 June 2016; received in revised form 29 July 2016; accepted 2 August 2016
Available online 23 September 2016

Abstract

In this paper, hydrodynamic wave loads on an offshore stationary–floating oscillating water column (OWC) are investigated via a 2D and 3D computational fluid dynamics (CFD) modeling based on the RANS equations and the VOF surface capturing scheme. The CFD model is validated against previous experiments for nonlinear regular wave interactions with a surface-piercing stationary barge. Following the validation stage, the numerical model is modified to consider the pneumatic damping effect, and an extensive campaign of numerical tests is carried out to study the wave–OWC interactions for different wave periods, wave heights and pneumatic damping factors. It is found that the horizontal wave force is usually larger than the vertical one. Also, there a direct relationship between the pneumatic and hydrodynamic vertical forces with a maximum vertical force almost at the device natural frequency, whereas the pneumatic damping has a little effect on the horizontal force. Additionally, simulating the turbine damping with an orifice plate induces higher vertical loads than utilizing a slot opening. Furthermore, 3D modeling significantly escalates and declines the predicted hydrodynamic vertical and horizontal wave loads, respectively.

Keywords: Offshore oscillating water column; OWC; Hydrodynamic wave loads; Numerical wave tank; CFD; 3D effects.

1. Introduction

Nowadays, wave energy is one of the greatest future renewable energy resources, and research is being conducted worldwide. Oscillating water column (OWC) is a wave energy extraction device that uses the incoming ocean wave' oscillations to drive an oscillating column in a pneumatic chamber that has an opening to the sea. As the water level inside the OWC chamber moves up and down, it compresses and decompresses the air, respectively. Air energy is then converted into mechanical energy by means of a bi-directional air turbine connected to the pneumatic chamber. Electricity can then be generated by utilizing an electric generator that converts the mechanical energy to useful electricity. For its simplicity from operation point of view and having no moving parts underwater that provides lesser and easier maintenance works, OWC has drawn attention of many researchers as one of the most promising wave energy converters.

A theoretical model of the hydrodynamics for a fixed OWC device was developed by Evans [1] who ignored the spatial variation and assumed a rigid weightless piston motion for the chamber's internal free surface of a small width relative to the incident wavelength. These assumptions allowed the application of the oscillating body theory. The rigid-body approach was then improved by Falcão and Sarmento [2], Evans [3] and Falnes and McIver [4] by allowing the increase in pressure at the free surface as well as providing the possibility of a non-plane free surface. To validate the oscillating surface pressure theory proposed by Sarmento and Falcão [5] in OWCs, Sarmento [6] carried out a set of wave flume experiments utilizing very small steepness regular waves with linear and quadratic power take-off (PTO) represented by filters and orifice plate, accordingly. Morris-Thomas et al. [7] and Ning

* Correspondence to: National Centre for Maritime Engineering and Hydrodynamics, Australian Maritime College, University of Tasmania, Launceston, Tasmania 7250, Australia.
E-mail address: Ahmed.Elhanafi@utas.edu.au.

http://dx.doi.org/10.1016/j.joes.2016.08.001

et al. [8] experimentally investigated the impacts the underwater chamber's geometry has on onshore OWCs performance.

Adding to the analytical and experimental studies, Numerical Wave Tank (NWT) based on potential flow solver or solving the Reynolds–averaged Navier–Stokes (RANS) equations are also being used. In contrast to potential flow models, RANS models do not have the shortcomings of handling problems with strong nonlinearity, dispersion, wave breaking, complex viscous, turbulence and vortex shedding. On the other hand, with potential flow solvers, the solution can be obtained in a reasonable time on standard computers. Usually, potential flow models are solved using Boundary Element Method (BEM). Studies on OWCs that implement potential flow solvers are for instance, Brito-Melo et al. [9], Delauré and Lewis [10], Josset and Clément [11], Lopes et al. [12], Sykes et al. [13, 14] and Gomes et al. [15].

With increasing the computation power, RANS models became more attractive for researchers to study the OWC hydrodynamic performance. Examples that implemented CFD models for investigating the impacts the environmental conditions (wave height and period), the chamber underwater geometry and PTO damping have on the hydrodynamic performance of onshore OWC devices include Zhang et al. [16], Teixeira et al. [17], López et al. [18], Kamath et al. [19, 20], Luo et al. [21], Anbarsooz et al. [22], Şentürk and Özdamar [23] and Elhanafi et al. [24].

In contrast to onshore OWCs, offshore OWCs do not have the chamber rear wall extending to the seabed. As a result, offshore OWCs allow the ocean waves to pass around and underneath the device walls. Recently, Iturrioz et al. [25, 26] developed and validated a CFD model based on RANS–VOF using open source code (IHFOAM) with tank flume experiments to study the hydrodynamics and pneumatics of a fixed detached OWC. Crema et al. [27] studied experimentally the efficiency of an OWC designed for installation on a floating structure. The study included different geometrical parameters and both regular and irregular waves under different pneumatic damping. Simonetti et al. [28] presented the numerical settings of an open source CFD code (OpenFOAM) and validation results against physical measurements of a similar OWC device tested by Crema et al. [27]. Elhanafi et al. [29] utilized a 2D validated numerical model based on (RANS–VOF) using a commercial CFD code (Star–CCM+) with experimental results to uncover the impact of increasing the incident wave amplitude, frequency and turbine damping on the energy balance of an offshore stationary-floating OWC through detailed energy balance analyses. Using a 2D CFD model, Elhanafi et al. [30] studied the impact of the underwater chamber' lips thickness and submergence on the hydrodynamic performance of an offshore OWC under a constant wave height and PTO damping. They observed that with increasing the asymmetric lips submergence ratio (rear wall draught to front wall draught), the rear wall thickness or an appropriate combination between the asymmetric lips submergence and thickness, the overall hydrodynamic efficiency can considerably be escalated over a broad frequency bandwidth.

Providing a better understanding of the offshore OWCs hydrodynamic performance is important; however studying the hydrodynamic loads on these devices is essential for their stability and continuation in operation safely. There is a limited research focusing on studying these loads such as Jayakumar [31] who experimentally found that the wave forces on OWC caisson breakwater when air damping inside the OWC model is less were smaller than the traditional rectangular caisson. Ashlin et al. [32] experimentally quantified the horizontal and vertical wave forces on an onshore OWC model scale with constant pneumatic damping in a 2D wave flume. They studied, the effect of wave steepness and relative water depth on the measured wave forces, and observed that at natural frequency of system, the force on the structure is less.

The present paper aims to develop and validate a CFD model based on RANS equations solver with a VOF surface capturing scheme introduced by Hirt and Nichols [33] (RANS–VOF) to preliminary investigate the hydrodynamic wave loads acting on an offshore OWC model scale. The study includes a validation against existing experiments and then discovering the relevance of the incoming wave period, wave height, PTO damping, PTO and 3D modeling to the horizontal and vertical wave forces and their nonlinearity.

2. Numerical wave tank (NWT)

2.1. Governing equations

The Computational Fluid Dynamics (CFD) model utilized in the present study is a fully nonlinear model that is based on the RANS equations together with VOF surface capturing scheme introduced by Hirt and Nichols [33]. For the small OWC model scale considered in this investigation, air compressibility inside the OWC chamber has a negligible effect. Accordingly, the NWT used in the present study assumes incompressible flow, and the continuity and RANS equations are used to describe the flow motion via using a commercial CFD code (Star–CCM+). In order to mathematically close the flow sets of equations, the two-equation Shear Stress Transport (SST) k—ω turbulence model is implemented to model the Reynolds Stresses in RANS equations.

2.2. Computational fluid domain

In this section, only settings for 2D CFD model is presented. A 10 wavelengths (L) NWT with 2 cells in width is used in the present study with boundary conditions defined as in Fig. 1a. To reduce the unwanted reflected waves from the NWT downstream outlet boundary, one wavelength at the end of the fluid domain is assigned for damping the transmitted waves underneath the structure. The hydrodynamic wave interaction with a bluff body such as an OWC will produce a partial standing wave envelope in front of the OWC structure; therefore, a sufficient refined free surface zone of three times the incoming wave height (H) is used. Considering that ocean waves are the main exciting source acting on offshore structures like OWCs, proper modeling of these waves is

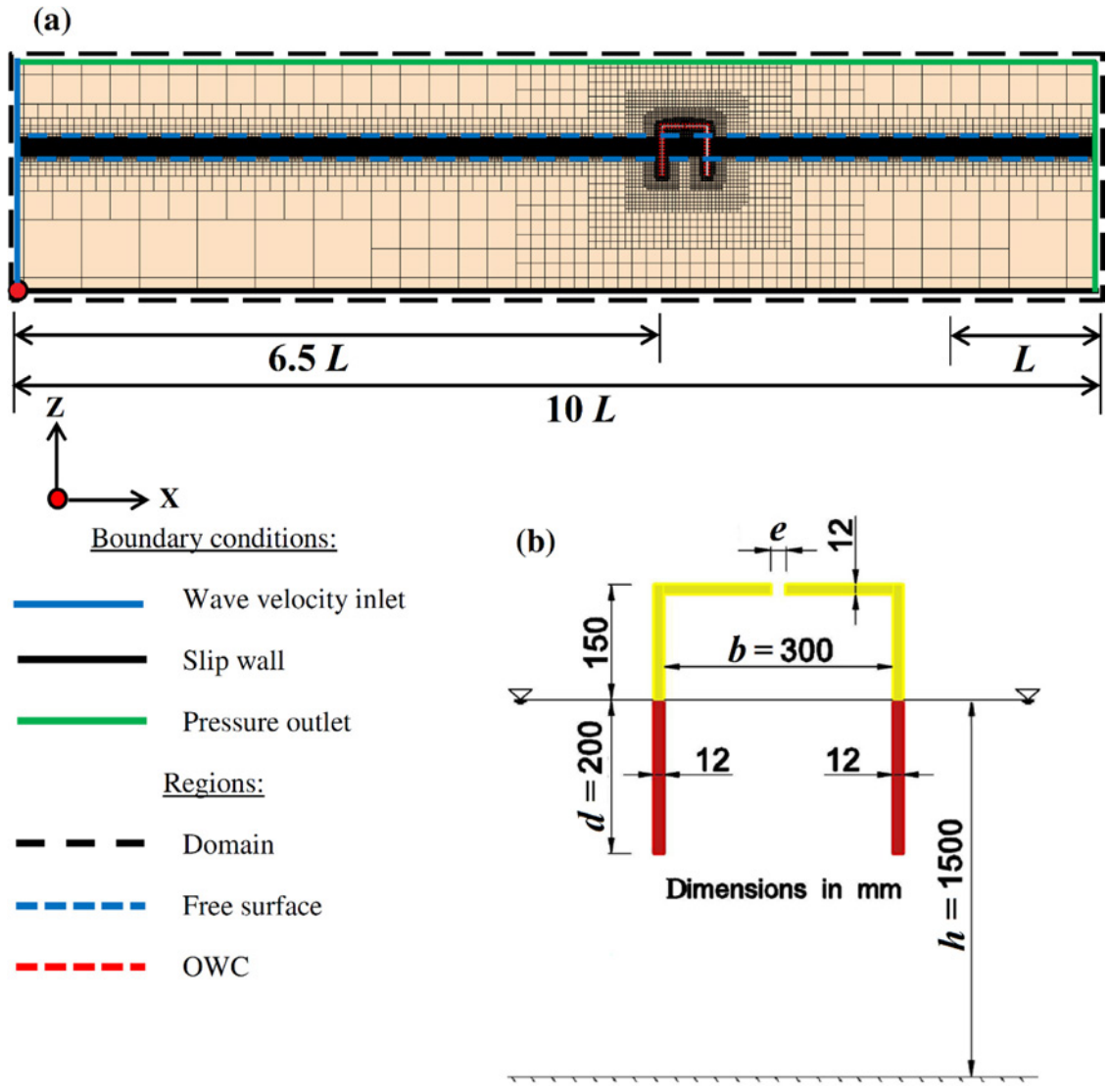

Fig. 1. (a) Computational fluid domain and (b) offshore OWC 1:50 model scale.

paramount for accurate prediction of the hydrodynamic loads, structure's response and performance [34]. Accordingly, the gird and time step recommended by Elhanafi et al. [24] are implemented in the present study. Elhanafi et al. [24] found that a domain base cell size of 400 mm with free surface grid size of at least 12 and 36 cells per wave height and wavelength while maintaining a maximum cell aspect ratio of 16 are recommended for accurately generate waves with less than 1.0% deviation from the analytical input wave height when using a second-order temporal discretization scheme with 1200 time steps per wave period (T).

A mesh convergence study was performed considering five different surface mesh sizes for the OWC' walls (Fig. 1b) under a wave height of H=50 mm, wave period T=1.2 s and PTO slot opening of e=5.0 mm. The cell surface size of the coarser mesh (Mesh1) was 25 mm, and the total cells count 170,000. More refinement was applied with 12.5 mm (Mesh2), 6.25 mm (Mesh3), 3.125 mm (Mesh4) and the most refine mesh of 1.5625 mm (Mesh5) surface size that counts 540,000 cells. A further refinement of 0.78125 mm was given to the power take-off (PTO) slot opening walls for all of the five mesh sizes (Mesh1–5). For all non-slip walls of the considered OWC, a first cell height equivalent to $y+\cong 1$ is used with a growth rate of 1.5 and 10 prism layers. Results in Fig. 2a show that the horizontal wave force (F_X) is almost identical for all considered mesh sizes, whereas the vertical force (F_Z) in Fig. 2b seems to be independent of the mesh size starting from Mesh3. Considering the computational time, Mesh3 is selected for the rest of the simulations performed in the present study.

2.3. CFD model validation

The considered CFD model was previously validated with experimental results for overall and detailed performance parameters of OWCs including chamber differential air pressure, chamber water level elevation, overall hydrodynamic efficiency and detailed flow fields (velocity and vorticity)

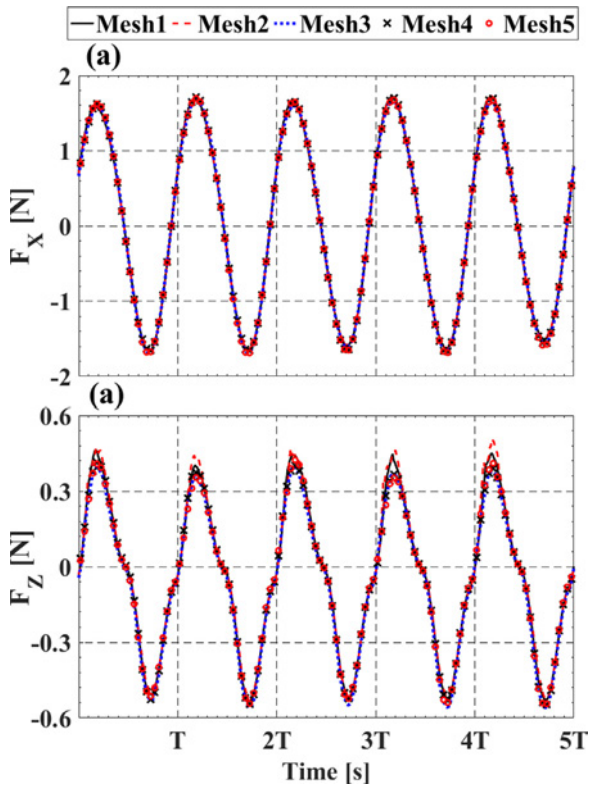

Fig. 2. Mesh convergence study. (a) Horizontal wave force (F_X) and (b) Vertical wave force (F_Z). $H = 50$ mm, $T = 1.2$ s and $e = 5.0$ mm.

[24,29]. Building on these validations, and considering the very limited reliable experimental data for hydrodynamic wave loads on OWCs in public literature under the action of nonlinear regular waves, the author decided to further validate the fully nonlinear CFD model utilized in this study against physical measurements including the reflection coefficient, transmission coefficient and wave loads acting on a 2D stationary-floating surface-piercing barge shown in Fig. 3 that is subjected to nonlinear regular waves [35]. The experimental results for this validation use a constant wave height $H = 70$ mm, water depth $h = L$, where L is the incident wavelength and a range of wave periods represented by a non-dimensional wavenumber (ζ) given by Eq. (1). The experimental results were also represented in non-dimensional forms for different parameters given in Eqs. (2)–(5) including: reflection coefficient (C_R), transmission coefficient (C_T), normalized horizontal force (F_X^*) and normalized vertical force (F_Z^*). The above-mentioned parameters are numerically calculated with the CFD model and compared against the experimental results conducted by Nojiri and Murayama [35] and others numerical results such as Tanizawa et al. [36]. Incident and reflected waves are resolved via utilizing three numerical wave probes (WPs) placed in front of the OWC at spacing as proposed by Mansard and Funke [37]. The spacing between wave probes were adjusted based on the incoming wavelength, so that the first WP is always located at a distance equal to one wavelength (L) from the OWC's front lip, the second WP at $0.9L$ and the third WP

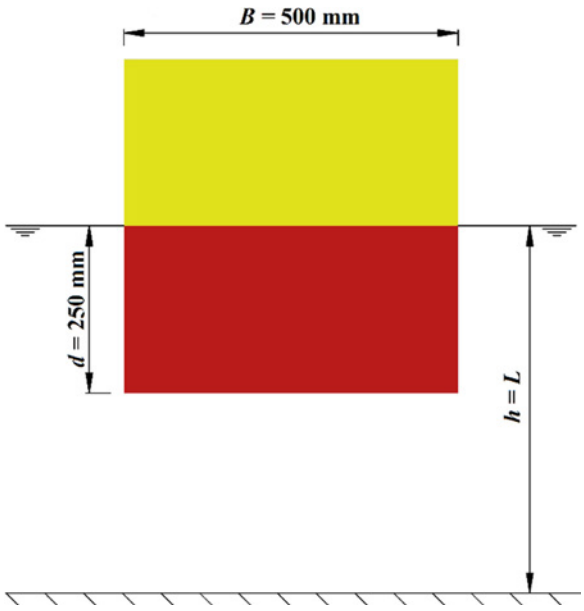

Fig. 3. Stationary-floating surface-piercing barge.

at $0.75L$, which is more that $0.2L$ as recommended by Goda and Suzuki [38] in case of regular wave tests. The transmitted wave height is monitored at a distance of about one wavelength behind the OWC's leeward lip. A mesh convergence study consisting of five mesh sizes ranging from 75,000 cells to 340,000 cells was also performed for this model (full results are not presented), and the selected mesh size was 12.5 mm (140,000 cells). The comparison results illustrated in Fig. 4 revealed that the present CFD model results are in good agreement with both experimental and others numerical results, which provides reasonable confidence in the capability of the utilized CFD model for accurately simulating the nonlinear waves interacting with a fixed bluff body such as a stationary-floating OWC.

$$\zeta = \frac{\omega^2 B}{2g} \tag{1}$$

where ω is the wave angular frequency, B is the barge length in the wave propagation direction and g is the gravitational acceleration.

$$C_R = \frac{H_R}{H} \tag{2}$$

$$C_T = \frac{H_T}{H} \tag{3}$$

where H, H_R and H_T are the incident, reflected and transmitted wave heights, respectively.

$$F_X{}^* = \frac{F_X}{\rho g W d A} \tag{4}$$

$$F_Z{}^* = \frac{F_Z}{\rho g W B A} \tag{5}$$

where F_X and F_Z are the measured horizontal and vertical wave loads, ρ is the water density (fresh water), d is the

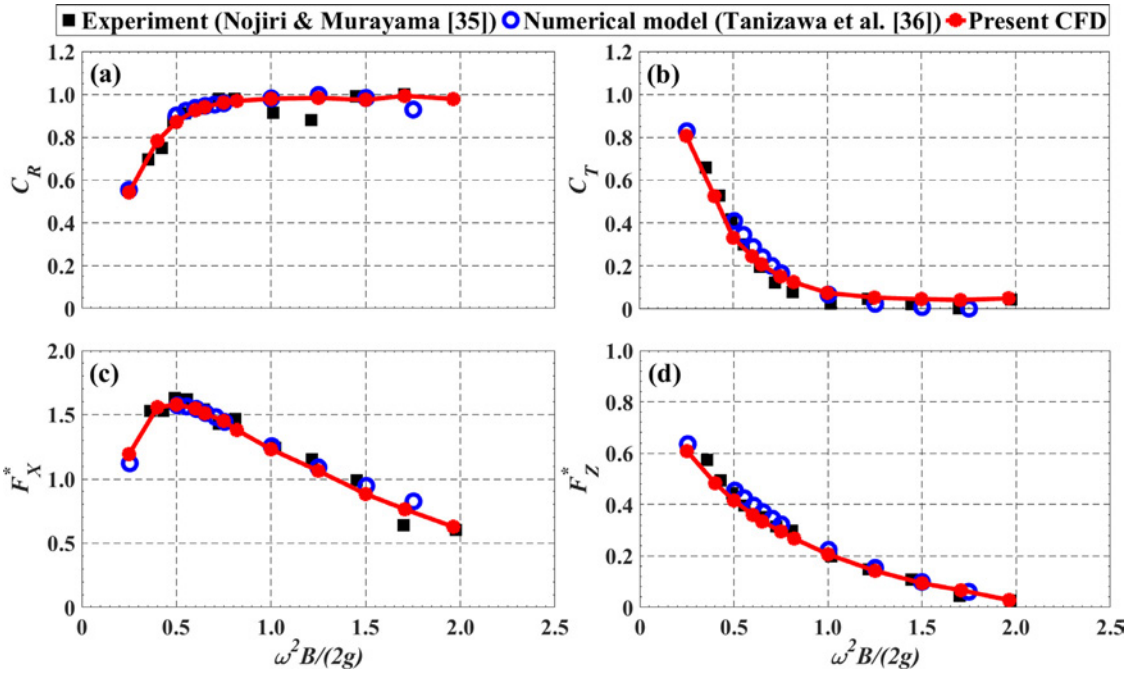

Fig. 4. CFD validation of regular wave interactions with a surface-piercing fixed barge. (a) reflection coefficient (C_R), (b) transmission coefficient (C_T), (c) normalized horizontal force (F_X^*) and (d) normalized vertical force (F_Z^*) versus nondimensional wavenumber $\zeta = \omega^2 B/2g$ under a regular wave height of $H = 70$ mm.

barge draft (250 mm), W is the barge breadth (not shown in Fig. 3) and A is the incident wave amplitude.

3. Wave loads on OWC

To investigate the hydrodynamic wave loads on an offshore-stationary OWC, the above well validated CFD model is utilized after replacing the surface-piercing barge in Fig. 3 with a 1:50 OWC model scale shown in Fig. 1b. The CFD model is then used to further study the wave–OWC interactions under fifteen wave periods (T) ranging from 0.8 to 2.2 s with 0.1 s increment that are represented by a dimensionless parameter Kb =1.8864–0.2494, where K is defined as $K=\omega^2/g$ and b is the chamber length in the wave propagation direction (see Fig. 1b), two wave heights (H) of 50 and 100 mm, eleven PTO damping simulated via different slot opening sizes (e)=1.5–9.0 mm and a constant water depth (h) of 1500 mm.

3.1. Wavelength effect

OWC interactions with a constant incoming wave height of 50 mm are studied in this section for the whole considered wave periods under three different PTO damping corresponding to a top slot size (e) of 6.0 mm (low damping), 3.0 mm (intermediate damping) and 1.5 mm (large damping). Starting with the horizontal wave force, considering that the surging force mainly results from the wave loads on the OWC's front and rear lips, the amplitude and phase shift between the two wave envelopes developed in front and behind the OWC structure are controlling the resultant force's amplitudes presented in Fig. 5c. The reflection and transmission coefficients, which are a function of the structural geometry and incoming waves can provide an indication of these envelopes. In addition, the radiated waves from the OWC chamber's internal free surface oscillation that depends on many factors such as wave characteristic and PTO damping may influence these wave envelopes. As seen in Fig. 5a, the reflection and transmission coefficients have fully opposite trends. Under low-frequency waves, the reflection and transmission coefficients are minimum and maximum, respectively. As the wavelength shortens, the reflection coefficient increases whereas transmission coefficient declines.

Considering the variations of these coefficients together with the trend of the horizontal wave force in Fig. 5c, it can be seen that under long waves, the amplitude and phase of forces acting on both lips are close to each other, which leads to a minimum resultant force. With increasing the wave frequency (Kb), the transmitted wave amplitude reduces; and therefore, the force amplitude on the aft wall decreases. On the other hand, increasing the reflection coefficient with Kb does not necessarily means enlarging the forces on the front wall. This is because the wave envelope in front of the OWC can be seen as a partial standing wave consisting of nodes and antinodes, and changing the phase between the incident, reflected and radiated waves will alter the position of these nodes and antinodes. However, considering that the resultant force increases with Kb, this explains the higher wave oscillations (antinodes) developed on or close to the front lip, which in turn improves the resultant force until getting its maximum at a certain Kb value. It is also interesting to see the horizontal force's peak occurs over a frequency (Kb) bandwidth

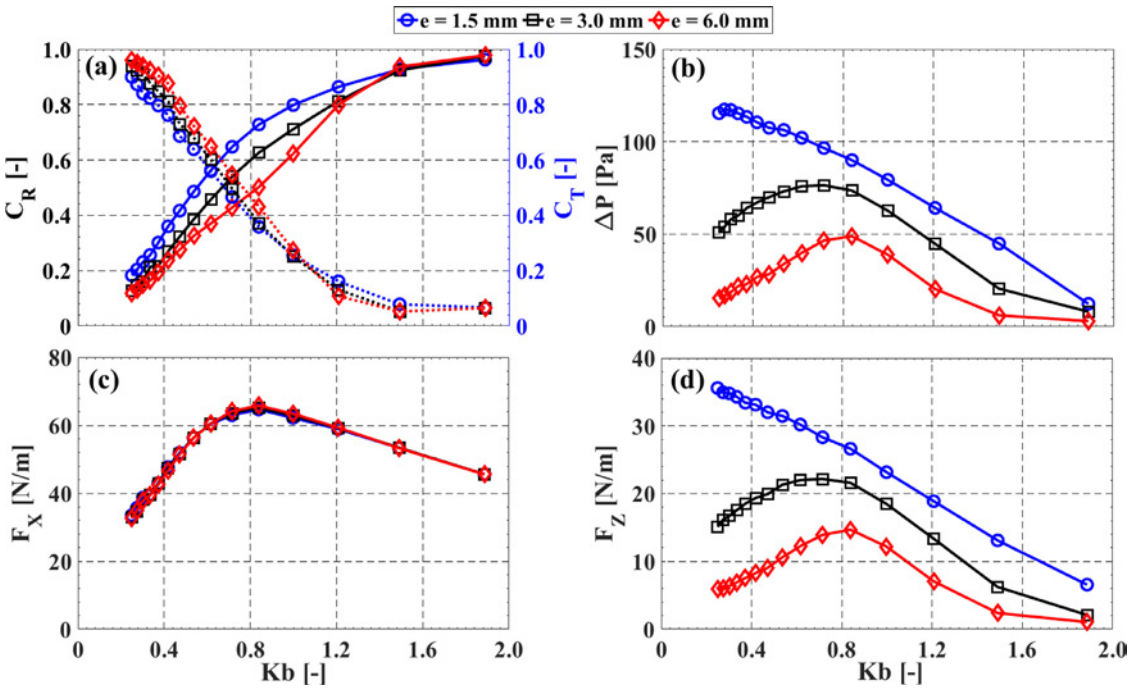

Fig. 5. OWC interactions with regular waves (H = 50 mm) versus nondimensional parameter (Kb) under different PTO slot opening size (e). (a) reflection (C_R) and transmission (C_T, dotted lines with markers) coefficients, (b) chamber's differential air pressure (ΔP), (c) horizontal wave force (F_X) and (d) vertical wave force (F_Z).

corresponds to the same frequency zone where both reflection and transmission coefficients are roughly equal, which is the same region of the maximum energy absorbed by the OWC structure [29]. Following this peak, while loads on the real lip keep decreasing due to the reduction in transmission coefficient with a further increase in Kb, forces on seaward wall seems to start declining, and the phase shift between both forces increases. Consequently, the total horizontal force declines. Additionally, under high–frequency waves, the chamber's free surface motion is no longer flat, and nonlinear effects as well as water sloshing increase, which are expected to influence the resultant force. For instance, the horizontal wave load per chamber's unit width (F_X) acting on the OWC and presented in Fig. 5c is seen to gradually increases from 33 N/m at Kb =0.2494 as the incoming wavelength decreases (i.e., Kb increases) till peaked with 66 N/m at a certain wavelength corresponding to a Kb = 0.8384. Following its maximum value, the horizontal force tends to linearly decrease with further shortening the wavelength up to 45 N/m at Kb = 1.886. Although, changing the PTO damping impacts the reflected and transmitted waves (Fig. 5a), it is observed that the predicted horizontal force is almost identical for the three simulated PTO damping, which again can be assigned to the change in phase shift on the measured forces considering that the applied damping significantly influences the chamber's free surface oscillation as well as the radiated waves. Further discussion is provided in Section 3.5.

Before discussing the hydrodynamic vertical wave loads, the chamber's differential air pressure is investigated. Results in Fig. 5b demonstrate that as the incoming wave becomes shorter (Kb increases), the differential air pressure amplitude (ΔP) increases before hitting its maxima at a given Kb value that represents the device natural frequency (resonance) or closer to that frequency [39]. Following the achieved peak value, the pressure amplitude progressively drops down. Changing the PTO damping affects the pressure amplitude and the device natural frequency, which in turn alters the Kb value at which the maximum pressure occurs. For instance, increasing the applied damping from e = 6.0 to 3.0 mm pushes the pressure peak from 49 Pa at Kb = 0.8384 to 76 Pa at a smaller Kb = 0.7144. This effect is also more obvious for the largest damping of e = 1.5 mm where the pressure peak of 117 Pa occurs almost under the longest wavelength (Kb = 0.2738). In addition to changing the resonance frequency (Kb value) and the corresponding peak pressure amplitude, increasing the PTO damping by reducing the slot opening (e) results in increasing the chamber pressure amplitude throughout the entire frequency range. Based on the differential air pressure results and the vertical wave loads presented in Fig. 5d, it is clear that the vertical wave force per chamber's unit width (F_Z) is following the same trend of the chamber's differential air pressure (ΔP) (Fig. 5b) for the whole tested frequencies (Kb) and PTO damping.

3.2. Wave height and PTO damping effects

Uncovering the impacts of increasing the incoming wave height two fold (i.e., H = 100 mm) on the predicted hydrodynamic loads are discussed in this section versus a 50 mm wave height over a series of PTO damping factors ($C = b/e$) and under three selected wave periods represented

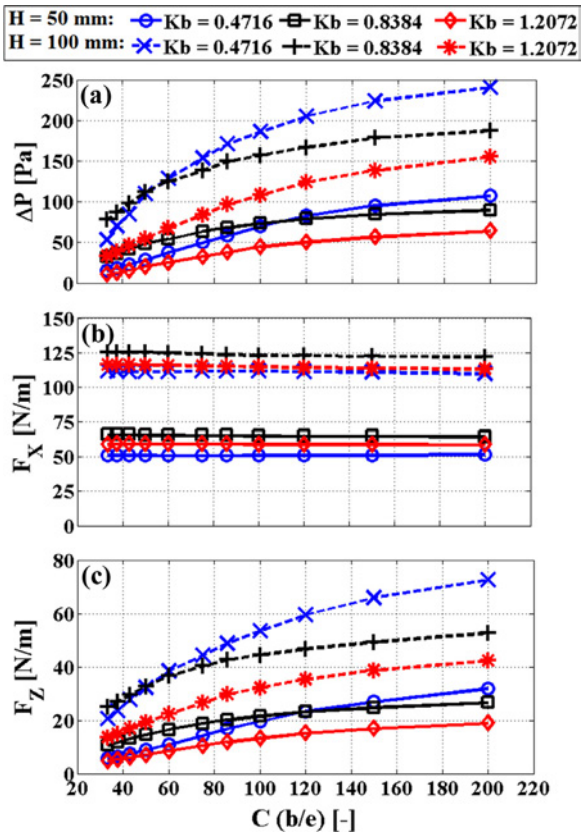

Fig. 6. Wave height impact on the OWC interactions with regular waves versus PTO damping factor (C) under different wavelengths (Kb). (a) chamber differential air pressure (ΔP), (b) horizontal force (F_X) and (c) vertical force (F_Z).

by $Kb = 0.4716$ (long wave, low steepness $H/L = 0.025$), 0.8384 (intermediate wavelength, $H/L = 0.044$) and 1.2072 (short wave, high-frequency and steepness of 0.064). Fig. 6a illustrates that air pressure amplitude (ΔP) increases with either increasing the PTO damping factor (C) or escalating the incident wave height for the three simulated wavelengths ($Kb = 0.4716$, 0.8384 and 1.2072). The higher wave frequency ($Kb = 1.2072$) provides the lower pressure amplitude over the 11 tested PTO damping and wave heights ($H = 50$ and 100 mm). The large PTO damping factors (C higher than 110) induce the higher pressure amplitudes when the OWC interacts with low frequency (long) waves ($Kb = 0.4716$) and height of 50 mm, whereas doubling the wave height shifts this damping factor limit ($C = 110$) to a lower value of $C = 50$, which widens and shortens the damping factor range that provides the higher pressure amplitudes for the low and intermediate wave frequencies, accordingly.

The horizontal wave force (F_X) shown in Fig. 6b provides that over the whole tested damping factors (C), the maximum force occurs at the intermediate wavelength, and changing the damping factor does not affect the predicted force (variation within + 1.07 % to − 1.70 % off the mean value). Conversely, doubling the wave height significantly magnifies the force amplitude by almost two times. Results in Fig. 6c illustrate that the influences the damping factor and wave height have

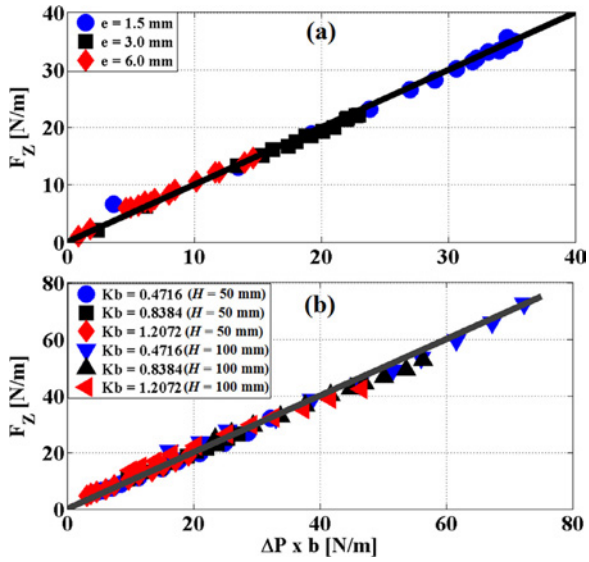

Fig. 7. Comparison between the hydrodynamic vertical wave force (F_Z) and the pneumatic force ($\Delta P\, x\, b$). (a) comparison for different wavelengths (Kb) and three damping (e) under a 50 mm wave height and (b) comparison for different wave heights ($H = 50$ and 100 mm) over different damping factors under three wavelengths (Kb).

on the vertical wave force (F_Z) are also similar to those on the chamber differential air pressure presented in Fig. 6a.

Considering the findings in Figs. 5 and 6, it seems that there is a good correlation between the chamber's differential air pressure (ΔP) and the hydrodynamic vertical force (F_Z). In order to discover this relation, Fig. 7 shows the hydrodynamic vertical wave force acting on the whole OWC structure (F_Z) in comparison with the pneumatic air (aerodynamic) force acting on the chamber's top plate that is defined as the product of the chamber's differential air pressure (ΔP) and the chamber's length (b). Fig. 7a demonstrates the forces resulting from Fig. 5b and d (i.e., the pneumatic and hydrodynamic vertical forces for the entire frequency range under three different damping of $e = 1.5$, 3.0 and 6.0 mm), while Fig. 7b compares the resulting pneumatic vertical forces (corresponding to air differential pressure amplitudes in Fig. 6a) and the hydrodynamic vertical forces (presented in Fig. 6c) over the whole studied 11 PTO damping factors (C) and two wave heights ($H = 50$ and 100 mm) for three wavelengths ($Kb = 0.4716$, 0.8384 and 1.2072). It is obvious from these results that the wave hydrodynamic vertical force is linearly proportional to the pneumatic differential air pressure force on OWC's top plate.

3.3. Horizontal versus vertical wave loads

The above discussed results show that the wave frequency (Kb) and damping factor (C) at which the maximum force occurs is different for the horizontal (F_X) and vertical (F_Z) wave forces. Also, the variation in each force is not synchronized with the each other. Accordingly, the ratio between these forces are studied in this section. Fig. 8 indicates that the horizontal force is always larger than the vertical force

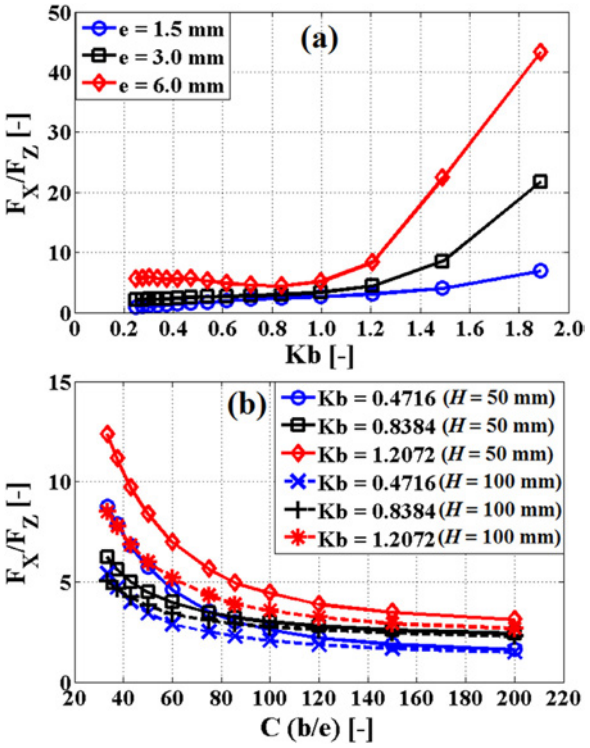

Fig. 8. Comparison between the horizontal (F_X) and vertical (F_Z) wave forces. (a) comparison for different wavelengths (Kb) and three PTO damping (e) under 50 mm wave height and (b) comparison for different wave heights (H = 50 and 100 mm) over different damping factors under three wavelengths (Kb).

for the whole tested wavelengths, damping factors and wave heights. The ratio between these forces (F_X/F_Z) is shown in Fig. 8a throughout the simulated wave frequencies for three PTO damping (e = 1.5, 3.0 and 6.0). The smaller damping (e = 6.0 mm) results in higher force ratios in comparison with the larger damping of e = 1.5 mm due to the smaller vertical forces induced by the larger damping (see Fig. 5d). Furthermore, as the wavelength decreases (Kb increases), the force ratio gradually increases from 1.0 at Kb = 0.2494 to 3.0 at Kb = 1.2072 and from 2.0 to 4.5 for e = 1.5 and 3.0 mm, respectively, whereas this ratio slightly declines for e = 6.0 mm from 5.5 at Kb = 0.2494 to 4.5 at Kb = 0.8384 (peak of F_X and F_Z in Fig. 5), before it also starts increasing. The increasing rate/slope of this ratio for the three damping values incredibly increases over the higher-frequency zone especially after Kb = 1.2072, which is more obvious for e = 3.0 and 6.0 mm. This can be assigned to the higher reduction rate in the vertical forces under higher frequencies (Fig. 5d) in comparison with the steady drop in the horizontal forces at high-frequency zone (Fig. 5c). For example, at the shortest (highest steep) wave of Kb = 1.886, the horizontal wave force (F_X) escalates up to 7.0, 22.0 and 43.0 times the vertical force (F_Z) under PTO damping e = 1.5, 3.0 and 6.0 mm, respectively.

At a given wavelength (Kb = 0.4716, 0.8384 or 1.2072), increasing the applied PTO damping factor from C = 33.33 (e = 9.0 mm) to 200 (e = 1.5 mm) results in reducing the force ratio as shown in Fig. 8b, which is a consequence of increasing the vertical forces with damping, whereas no effects on the horizontal forces (Fig. 6b and c). This reduction is more pronounced up to C = 120 where the force ratio drops from about 8.8, 6.2 and 12.4 at C = 33.22 for Kb = 0.4716, 0.8384 and 1.2072, respectively to almost 2.2, 2.8 and 3.9. Following this threshold (C = 120), the damping effect becomes little, which can be seen in the minor further reduction in the force ratio to 1.6, 2.4 and 3.1. Although increasing the wave height leads to increasing both the horizontal (Fig. 6b) and vertical (Fig. 6c) wave forces, the ratio between these forces (F_X/F_Z) is seen in Fig. 8b to decrease as the wave height increases to 100 mm, especially under small PTO damping, which in turn indicates that the vertical force is more sensitive to increasing the wave height than the horizontal force. For instance, at H = 100 mm, the force ratio drops to an average of 0.7, 0.9 and 0.75 times the ratios at H = 50 mm for Kb = 0.4716, 0.8384 and 1.2072, respectively that provides less effect on the intermediate wavelength. Having the correlation between the aerodynamic and hydrodynamic vertical wave forces (Fig. 7) together with the relation between the vertical and horizontal forces (Fig. 8), provides a possibility of utilizing the chamber's differential air pressure not only for estimating the device energy extraction efficiency, but also for predicting the loads acting on the device.

3.4. Nonlinear wave forces effect

The environmental conditions tested in this study provides a wide range of wave steepness 0.0075 ≤ H/L ≤ 0.064. Within this steepness range, the nonlinear effects change; therefore, its importance is discussed in this section. For each of the horizontal and vertical wave forces, time series data of five wave cycles are carefully selected. Fast Fourier Transform (FFT) is then used to resolve the energy contents in each frequency (fundamental wave frequency and its higher harmonics up to 3nd harmonic). Fig. 9 compares the contribution of the higher harmonics (2nd and 3rd) to the forces acting on the OWC as a percentage of the total force where E_X and E_Z represent the total energy content in the predicted horizontal and vertical force, accordingly, and the subscripts 2 and 3 refer to the energy concentrated in the and 2nd and 3rd harmonics, respectively. Fig. 9a shows that up to a Kb = 1.2072, the higher harmonics in the vertical force contribute up to about 10% of the total predicted vertical force, and this effect is almost the same for the three PTO damping of e = 6.0, 3.0 and 1.5 mm with only a slight increase for e = 6.0 mm at low frequency waves. Afterwards the Kb of 1.2072, incoming waves become more steep and nonlinear effects are more pronounced and progressively increases up to 24, 20 and 16% for e = 6.0, 3.0 and 1.5 mm, accordingly. In contrast, nonlinear effects are less than 5% for the horizontal wave force as given in Fig. 9c.

Impact of increasing the wave height to 100 mm and changing the PTO damping factor on the higher harmonics' contribution to the predicted vertical and horizontal forces are illustrated in Fig. 9b and d, respectively. Fig. 9b shows

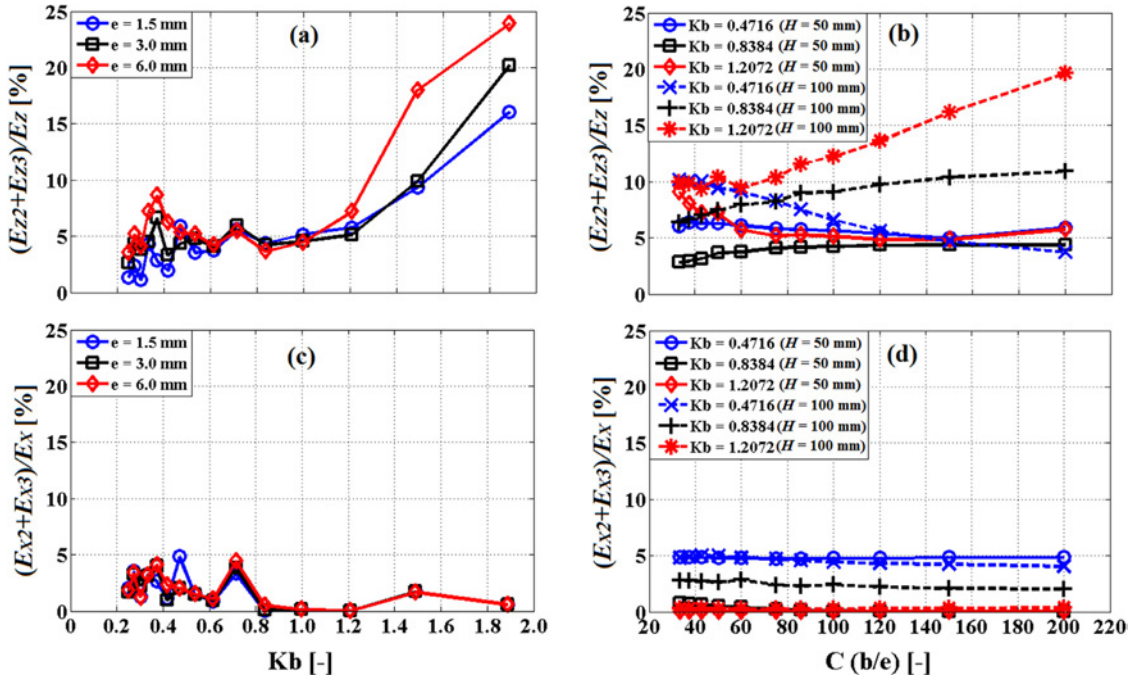

Fig. 9. Higher harmonics impacts on the predicted forces. (a and c) impacts of different wavelengths (*Kb*) and three PTO damping (*e*) under 50 mm wave height, (b and d) impacts of different PTO damping factors (*C*) and wave heights $H = 50$ and 100 mm for three wavelengths (*Kb*).

that as the damping factor (C) increases, nonlinear effects vary between 3.0 and 9.0% by either increasing from 3.0% at $C = 33.33$ to 4.5% at $C = 200$ for $Kb = 0.8384$ or decreasing from 9.0% to 6.0% for the shorter wavelength of $Kb = 1.2072$, where a slight variation of 5–6% is observed for the low frequency wave of $Kb = 0.4716$. Furthermore, after a damping factor (C) = 120, there is a little difference between the three tested wavelengths (Kb) that show almost a flat trend with a mean values of 5%. On the other side, increasing the wave height arises the nonlinear effects on the vertical wave forces (Fig. 9b), and these effects develop as the damping factor (C) escalates except for the longer waves where increasing the damping results in lesser nonlinear effects. For instance, under a short wavelength of $Kb = 1.2072$, nonlinear effects increase from 9% for $H = 50$ mm to 10% for $H = 100$ mm at $C = 33.33$ and from 6% to 19% at $C = 200$ for $H = 50$ mm and 100 mm, accordingly, while these effects are almost doubled throughout the whole damping range for the intermediate wavelength of $Kb = 0.8384$. For the horizontal (surge) force, nonlinear higher harmonics effects are seen to be insensitive to the damping factor. Also, increasing the wave height shows a little impact on the nonlinear contribution to the surging force, especially for the lower ($Kb = 0.4716$) and higher ($Kb = 1.2072$) wave steepness. However, for the intermediate wavelength ($Kb = 0.8384$), doubling the wave height escalates the nonlinear effect from only 0.35% to about 2.5%.

Time series data and corresponding FFT results are shown in Fig. 10 for a wavelength of $Kb = 1.2072$ under different wave heights and PTO damping. Fig. 10a and b confirm the results shown in Fig. 9d where a damping of $e = 1.5$ and 6.0 mm under wave heights of $H = 50$ and 100 mm result in a negligible nonlinear effect on the surging force with almost symmetric crest/trough time series data in Fig. 10a; accordingly, all energy (S_X) is concentrated in the fundamental incoming wave frequency of 1.0 Hz as shown in Fig. 10b. On the other side, nonlinear effects on the vertical forces are more obvious for a damping $e = 1.5$ mm and a wave height of 100 mm (see Fig. 9b) that is shown by the larger negative force (trough) in comparison with the positive value (crest) in Fig. 10c. This nonlinearity is represented by a second energy spike (S_Z) at the 2nd harmonic of 2.0 Hz in Fig. 10d, and represents about 17.5% of the total energy, while other analyzed conditions show only one peak value at the wave frequency with small/negligible second spike at the 2nd harmonic.

Similar to analyzing results for a short wavelength of $Kb = 1.2072$, time series data and FFT results for an intermediate wavelength of $Kb = 0.8384$ are shown in Fig. 11 with a damping $e = 1.5$ and 5.0 mm under wave heights of $H = 50$ and 100 mm. Fig. 11a and b illustrate the minor nonlinear effects on the horizontal surging force. Conversely, Fig. 11c and d highlight the nonlinear impacts on the predicted vertical force that are more clear under the larger wave height and PTO damping ($H = 100$ mm and $e = 1.5$ mm) with the second peak in FFT results representing about 9% of the total energy content in the predicted force.

3.5. 3D and PTO modeling effects

The above-discussed results are limited to 2D flow assumptions. In order to investigate the impacts the 3D modeling may have on the predicted hydrodynamic loads, the developed 2D CFD model in Section 2 is extended to 3D domain with boundary conditions as illustrated in Fig. 12a. Consid-

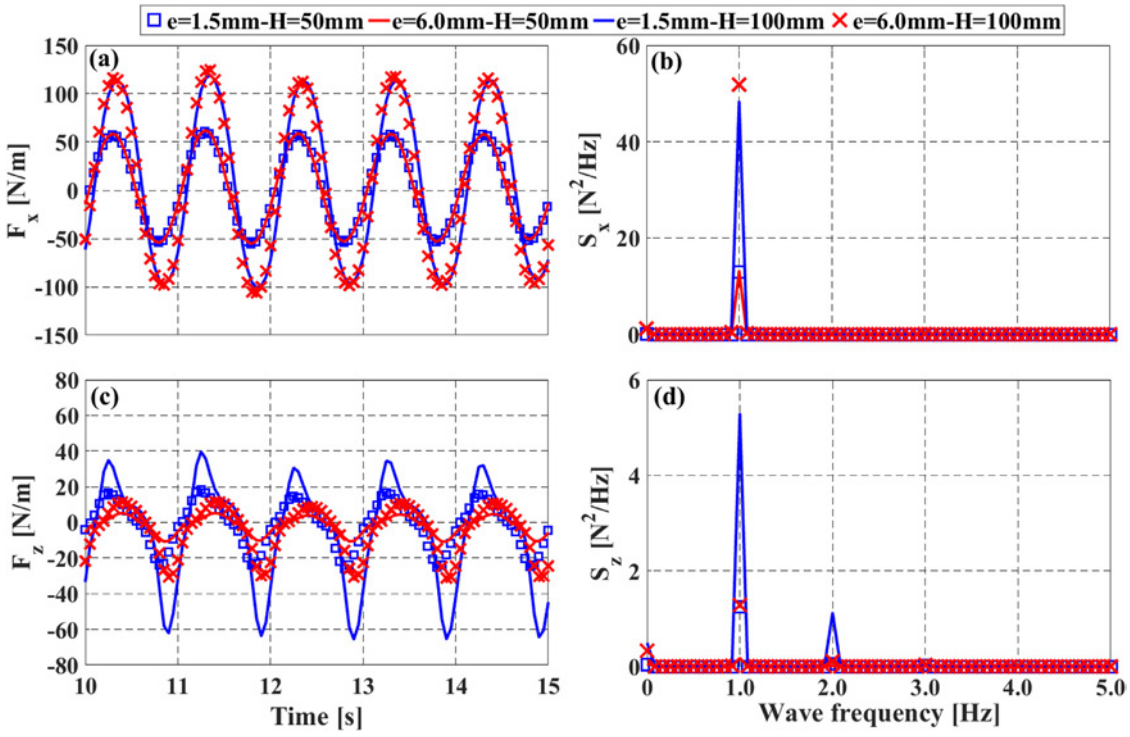

Fig. 10. Time series and FFT results of a damping $e = 1.5$ and 6.0 mm and a wave height $H = 50$ and 100 mm under a constant wavelength $Kb = 1.2072$. (a) horizontal force time series, (b) horizontal force FFT results, (c) vertical force time series, (d) vertical force FFT results.

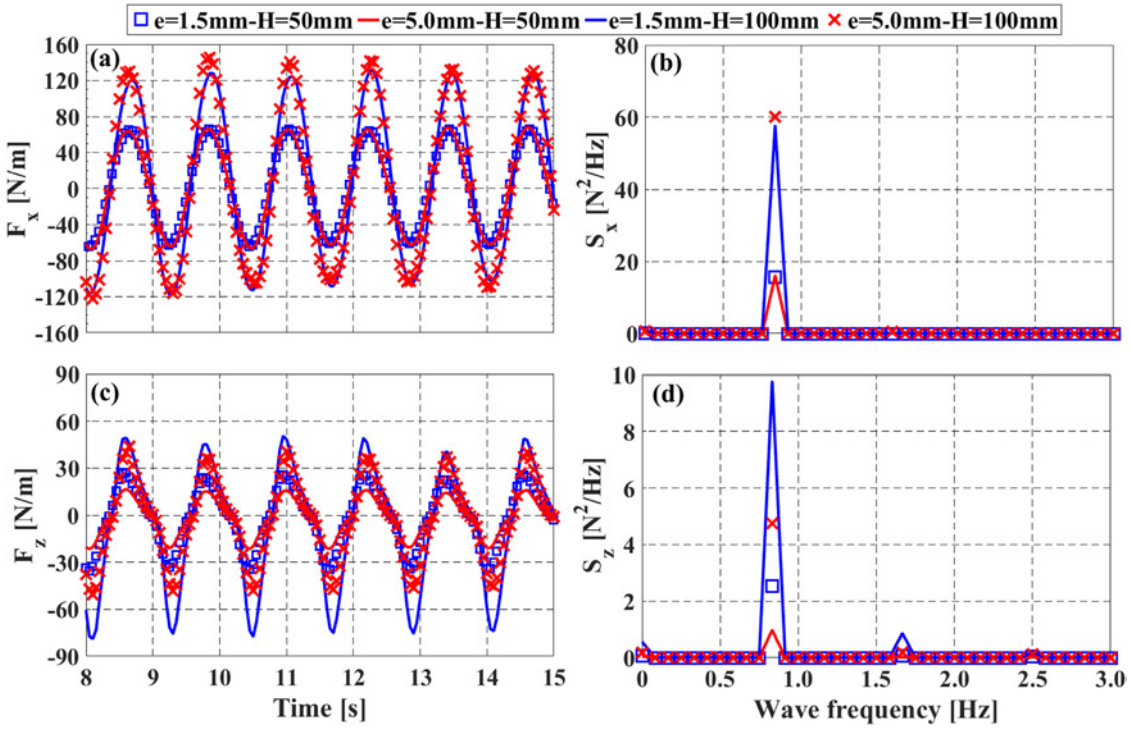

Fig. 11. Time series and FFT results of a damping $e = 1.5$ and 5.0 mm and a wave height $H = 50$ and 100 mm under a constant wavelength $Kb = 0.8384$. (a) horizontal force time series, (b) horizontal force FFT results, (c) vertical force time series, (d) vertical force FFT results.

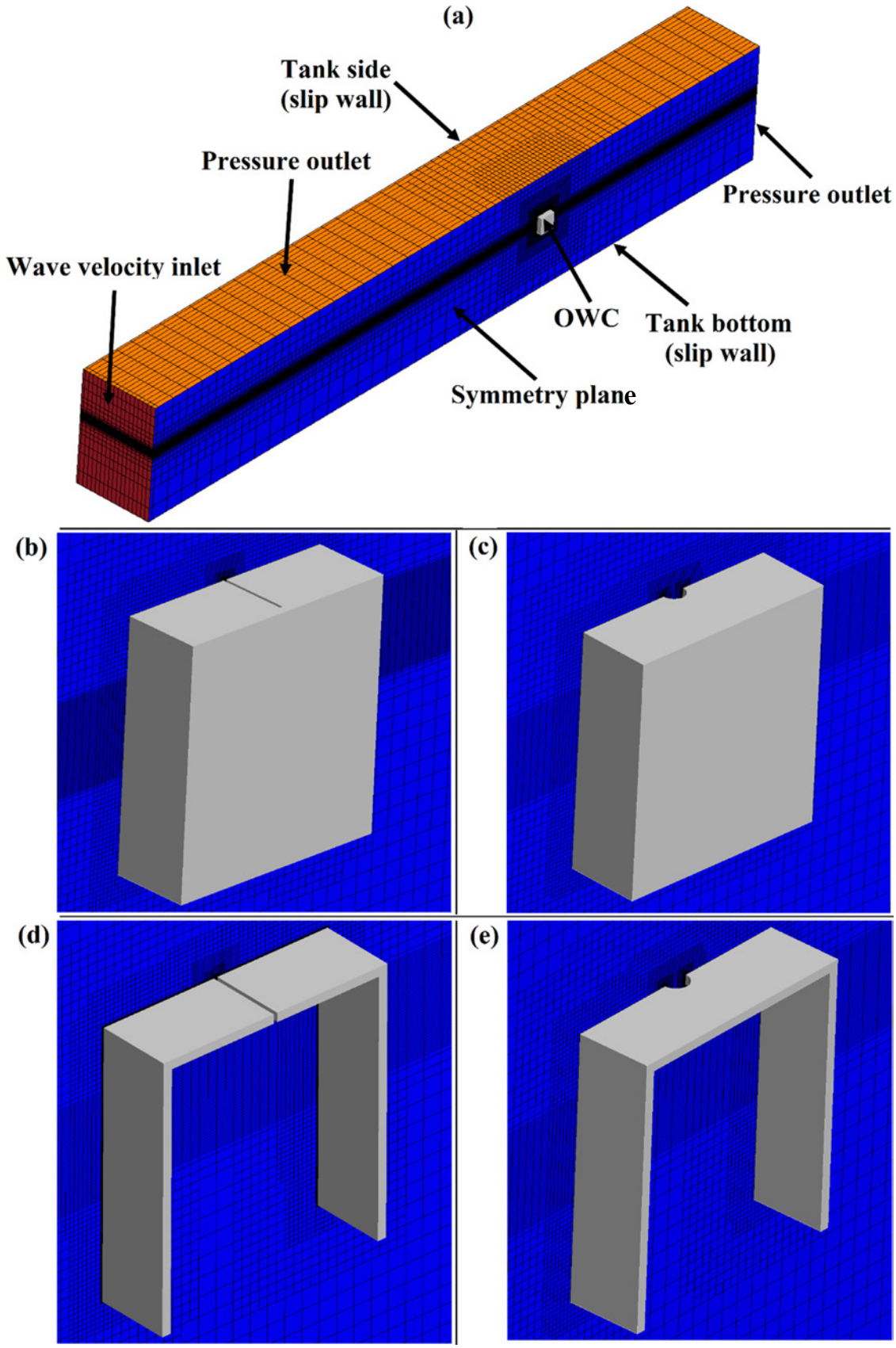

Fig. 12. 3D computational fluid domain. (a) Computational domain with mesh and boundary conditions, (b) 3D OWC with slot opening, (c) 3D OWC with orifice plate, (d) OWC with slot opening for flume tank and (e) OWC with orifice plate for flume tank.

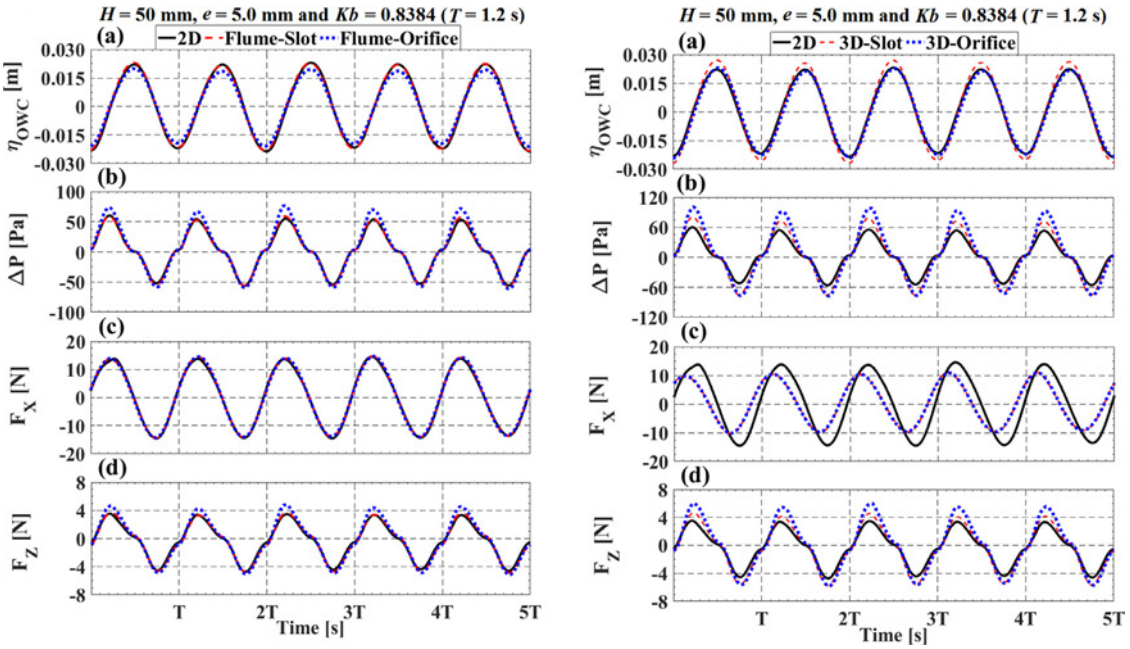

Fig. 13. 3D and PTO modeling effects on: (a) chamber's free surface oscillation (η_{OWC}), (b) chamber's differential air pressure (ΔP), (c) horizontal wave force (F_X) and (d) vertical wave force (F_Z). $H = 50$ mm, $e = 5.0$ mm and $Kb = 0.8384$ ($T = 1.2$ s).

ering that 3D modeling is time consuming, an intermediate stage between 2D and 3D modeling is investigated by testing the OWC in a numerical tank flume of breadth equal to the OWC's pneumatic chamber width of 100 mm with a symmetry plane. Results of this wave flume are compared with those from a fully 3D tank with breadth of 1750 mm (model's width is about 0.06 of the tank's breadth) that is enough to ignore the sidewall effects [40]. In addition, simulating the PTO damping via a slot opening restricts the flow to 2D; accordingly, a comparison between using a slot opening (2D) and an orifice plate (3D) with the same opening ratio (the ratio between the PTO opening and the chamber's waterplane area) is also included. All model's configurations are illustrated in Fig. 12b to e. To investigate all these parameters, testing conditions were limited to only one wave height of $H = 50$ mm, a slot opening $e = 5.0$ mm and three wave periods of $T = 1.0$ s ($Kb = 1.2072$), 1.2 s ($Kb = 0.8384$) and 1.6 s ($Kb = 0.4716$). Measurements include OWC's free surface oscillations (η_{OWC} that is based on an average of 25 numerical wave probes placed inside the pneumatic chamber), chamber's differential air pressure (average of 10 monitoring points) and the horizontal and vertical wave loads.

Starting with tank flume modeling and orifice plate effects on the predicted loads under a wave frequency of $Kb = 0.8384$, which results in the maximum loads under the considered PTO damping ($e = 5.0$ mm or $C = 60$, see Fig. 6), results in Fig. 13left illustrate that testing in tank flumes with PTO modeled with a slot opening provides almost the same results as 2D modeling for all measured parameters, except a slight increase of 4% in the vertical force. On the other hand, using an orifice plate (with a radius of 17.84 mm) instead of the slot opening induces higher air pressure (Fig. 13left-b) that in agreement with the experimental observations by He and Huang [41], which in turn reduces the chamber's free surface oscillation amplitude (Fig. 13left-a) and enlarges the hydrodynamic vertical forces (Fig. 13left-d) by 14.5% due to its coupling with the pneumatic force as discussed in Section 3.2. It is however, as discussed in Section 3.2, the horizontal forces (Fig. 13left-c) are independent of the applied damping that explains the identical results from PTO modeling with either a slot opening or an orifice plate.

In 3D modeling, not only wave scattering is considered, but also, removing the 2D flow restriction allows the water column to evacuate the chamber more easily, which in turn escalates the chamber's free surface oscillation amplitude as seen in Fig. 13right-a for OWC with 3D slot opening. In addition, for OWC with an orifice plate, the free surface oscillation amplitude increased in comparison with tank flume' results (Fig. 13left-a), but the oscillation is lower that the case with slot opening due to the higher damping induced by the orifice plate. This increase in the oscillation amplitude under a given wave period and PTO damping increases the oscillation rate (slope), which in turn escalates the air pressure amplitude (Fig. 13right-b) as well as the airflow rate through the PTO [29]. Similar to the tank flume, using the orifice plate improves the air pressure in comparison with the slot opening, and this effect is more obvious during the exhalation (pressurizing) stage. Having explained the increase in air pressure, it is expected that also the vertical wave forces in 3D modeling (Fig. 13right-d) are higher than those from flume tanks, and this increase found to be almost 20% for 3D with slot opening versus flume with slot opening, 20% for 3D with orifice plate versus flume with orifice plate and about 43% for 3D with orifice plate in comparison with 2D

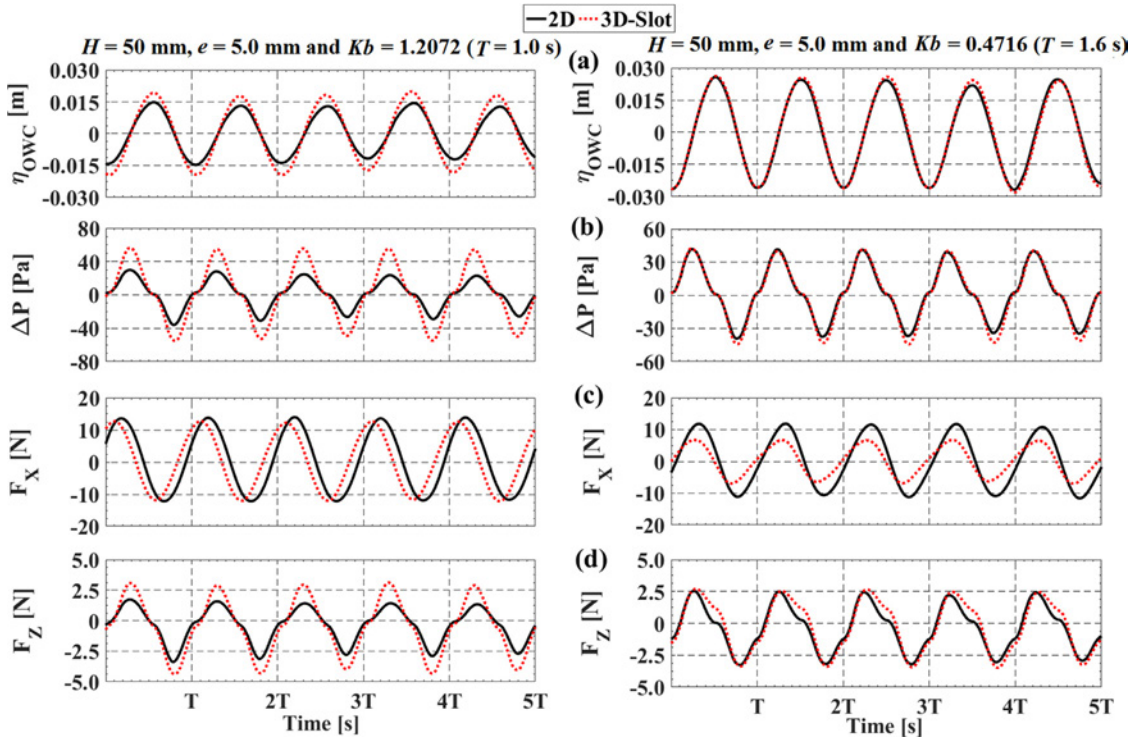

Fig. 14. 3D effects on: (a) chamber's free surface oscillation (η_{OWC}), (b) chamber's differential air pressure (ΔP), (c) horizontal wave force (F_X) and (d) vertical wave force (F_Z). H = 50 mm, e = 5.0 mm, Kb = 1.2072 (left) and Kb = 0.4716 (right).

modeling. Conversely, the horizontal wave loads in 3D modeling shown in Fig. 11right-c are lower that tank flume (or 2D) measurements. Further explanation regarding these reductions in surging forces is given later in this section.

Similar to the observations of 3D effects on the maximum measured forces under a wavelength of Kb = 0.8384, results for additional wave frequencies of Kb = 1.2072 (Fig. 14left) and Kb = 0.4716 (Fig. 14right) revealed the same impacts of 3D modeling. Additionally, these results illustrate that 3D modeling leads to a massive reduction and increase in the horizontal and vertical wave loads as the wavelength increases and decreases, respectively. For example, the reduction in horizontal loads (F_X) increases from 5% at Kb = 1.2072 (Fig. 14left-c) to 29% at Kb = 0.8384 (Fig. 13right-c) and then to 41% at Kb = 0.4716 (Fig. 14right-c). On the other hand, 3D simulations results in about 60% increase in the vertical wave force (F_Z) at Kb = 1.2072 (Fig. 14left-d) in comparison with 25% at Kb = 0.8384 (Fig. 13right-d, slot opening) and 7.5% at Kb = 0.4716 (Fig. 14right-d). Figs. 13 and 14 also highlight that 3D modeling not only affect the horizontal force amplitudes, but also, the frequency of the maximum force changes. For instance, the peak force was found at Kb = 0.8384 (Fig. 5c and time series data in Fig. 13c) in 2D modeling, but this peak seems to be shifted to a higher frequency of Kb = 1.2072 in 3D modeling (Fig. 14left-c).

As discussed in Section 3.1 the wave profile before and after the OWC is quite important for explaining the changes in the horizontal forces. For instance, results in Fig. 15 shows a comparison between 2D and 3D wave elevations for Kb = 0.8384 at four points along the tank on the symmetry plane (η_1 –η_3 are placed before OWC and η_4 is located behind OWC). Coordinates of these points are similar to the wave probes' locations described in Section 2.3. Results illustrate that 3D modeling allows most of the incoming waves

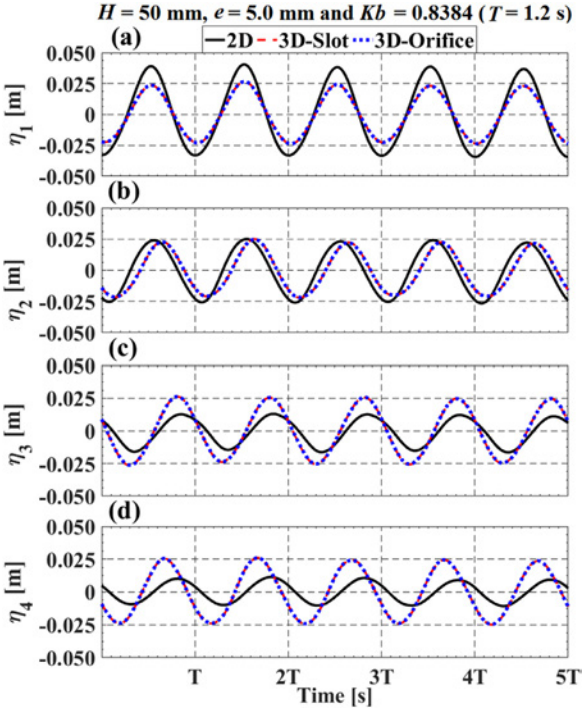

Fig. 15. 3D and PTO modeling effects on the wave envelope before and after OWC. H = 50 mm, e = 5.0 mm and Kb = 0.8384 (T = 1.2 s).

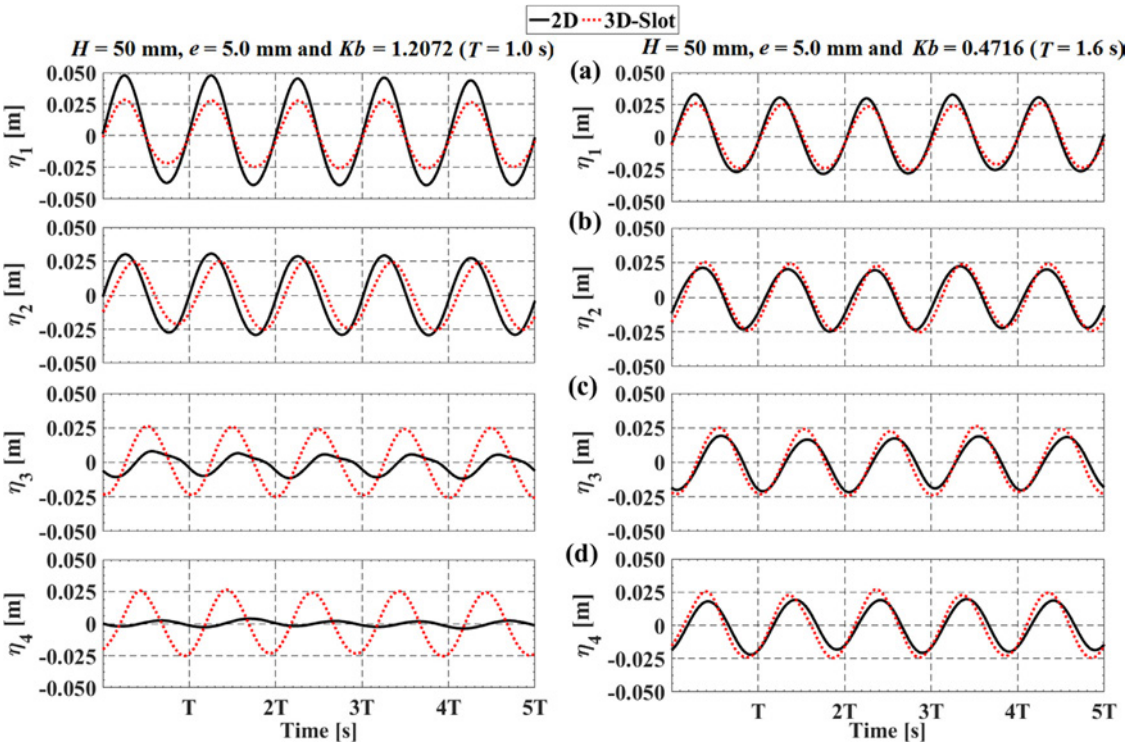

Fig. 16. 3D effects on the wave envelope before and after OWC. $H = 50$ mm, $e = 5.0$ mm, $Kb = 1.2702$ (left) and $Kb = 0.4716$ (right).

to be transmitted on the OWC's leeside, which can be seen in the consistency in the monitored wave amplitudes along the four points. Also, there is no visible impact of using an orifice plate rather than a slot opening. Furthermore, as reflection and transmission coefficients with 2D modeling are maximum and minimum respectively under short waves, it is expected that discrepancy with 3D modeling become more and less pronounced at high ($Kb = 1.2072$) and low ($Kb = 0.4716$) frequency waves as shown in Fig. 16left and right, respectively. These differences explain the overall reductions in the horizontal forces predicted with 3D modeling in comparison with 2D flow assumptions. However, to further clarify the escalation of these reductions with increasing the wavelength, the wave elevation is monitored and presented in Fig. 17 at two points closer to the OWC structure on each side: one at 50 mm in front of the OWC's seaward wall (Before OWC) and another one 50 mm behind the leeside (After OWC). It is clear that as the wavelength increases (Kb decreases), the wave amplitude after OWC with respect to the wave amplitude before OWC increases, while the phase shift between each wave trend diminishes (phase shift is $0.34T$ at $Kb = 1.2072$, $0.26T$ at $Kb = 0.8384$ and $0.16T$ at $Kb = 0.4716$). As a result, a large reduction in surging forces is more obvious under long waves in comparison with 2D results.

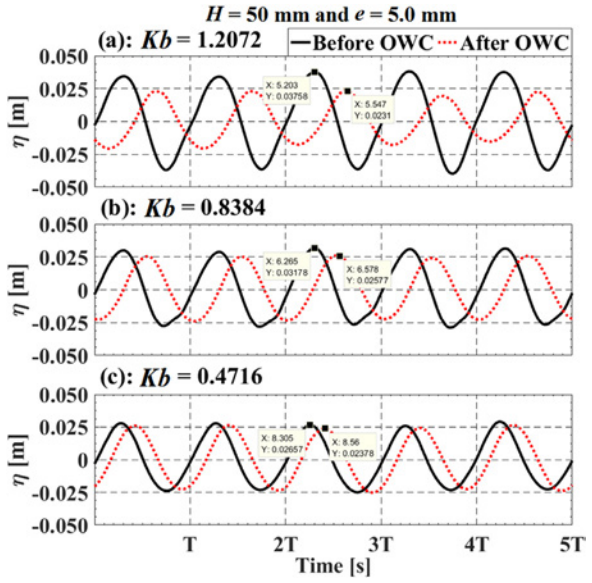

Fig. 17. 3D effects on the wave elevation at 50 mm before and after OWC. (a): $Kb = 1.2702$, (b): $Kb = 0.8384$ and (c): $Kb = 0.4716$. $H = 50$ mm, $e = 5.0$ mm.

4. Conclusions

2D and 3D CFD models based on RANS–VOF are implemented in this paper in order to study the hydrodynamic wave loads on an offshore-stationary OWC over a wide range of wave periods, wave heights and pneumatic damping. The model is validated in good agreement against nonlinear regular wave interactions with a surface-piercing fixed barge. From the investigations carried out of total 108 numerical tests, the following conclusions are drawn:

- The hydrodynamic horizontal wave load is independent of the applied PTO damping even with increasing the incoming wave height.
- Increasing the wave height by two times leads to almost doubling the surging wave force.
- The maximum horizontal force occurs at frequency bandwidth where reflection and transmission coefficients are almost the same.
- The predicted vertical hydrodynamic load is following the same variation of the chamber's differential air pressure with a peak value almost at the OWC natural frequency.
- The hydrodynamic vertical force is linearly proportional to the pneumatic air force acting on the chamber's top plate.
- Regardless of the incoming wave frequency, height and PTO damping, the hydrodynamic horizontal force is always larger than the vertical force.
- The ratio between the horizontal and vertical wave forces is higher for high frequency waves, smaller wave height and lower PTO damping.
- Nonlinear effects are more pronounced in the vertical force than the horizontal one.
- Nonlinearity contributes to about less than 5% of the total surging force energy, whereas this contribution can extend to 24% for the vertical force under high frequency waves.
- Testing offshore OWCs in tank flumes provides the same results as 2D modeling.
- Simulating the PTO damping with an orifice plate of the same opening ratio of a slot opening leads to high chamber's differential air pressure and in turn larger vertical wave force, whereas no impact on the horizontal force was found.
- 3D modeling results in reducing the horizontal wave forces, and this impact increases with increasing the wavelength.
- The maximum horizontal force in 3D modeling is shifted to a higher frequency in comparison with 2D modeling.
- 3D modeling leads to higher chamber's free surface oscillations, larger air pressure, and accordingly escalates the pneumatic and hydrodynamic vertical wave forces. These effects become more noticeable as the wavelength shortens.

Although the present work provided an overview on the hydrodynamic wave loads that an offshore OWC may experience during operational conditions (small waves), results were validated against two-dimensional model. Accordingly, as a continuation of this research, experiments will be performed to validate the numerical results not only for the 3D effects, but also under extreme environmental conditions representing survival events. Additionally, air compressibility may impact the predicted wave loads on the device, especially for large-scale prototypes [42], thus scaling effects with both incompressible and compressible airflow will be investigated.

Acknowledgement

The author is thankful to Associate Professor Gregor MacFarlane, Australian Maritime College, University of Tasmania, Australia for the preliminary review of this article. In addition, the author thanks the National Centre for Maritime Engineering and Hydrodynamics, Australian Maritime College, University of Tasmania, Australia for the financial support of his PhD.

References

[1] D. Evans, IMA J. Appl. Math. 22 (1978) 423–433.
[2] A.d.O. Falcão, A. Sarmento, in: 15th International Congress of Theoretical and Applied Mechanics, Toronto, Canada, 1980.
[3] D. Evans, J Fluid Mech. 114 (1982) 481–499.
[4] J. Falnes, P. McIver, Appl. Ocean Res. 7 (1985) 225–234.
[5] A.J. Sarmento, A.d.O. Falcão, J. Fluid Mech. 150 (1985) 467–485.
[6] A. Sarmento, Exp. Fluids 12 (1992) 286–292.
[7] M.T. Morris-Thomas, R.J. Irvin, K.P. Thiagarajan, J. Offshore Mech. Arct. Eng. 129 (2007) 273–278.
[8] D.-Z. Ning, R.-Q. Wang, Q.-P. Zou, B. Teng, Appl. Energy 168 (2016) 636–648.
[9] A. Brito-Melo, T. Hofmann, A. Sarmento, A. Clément, G. Delhommeau, Int. J. Offshore Polar Eng. 11 (2001).
[10] Y. Delauré, A. Lewis, Ocean Eng. 30 (2003) 309–330.
[11] C. Josset, A. Clément, Renew. Energy 32 (2007) 1379–1402.
[12] M. Lopes, P. Ricci, L. Gato, A.d.O. Falcão, in: Proceedings of the 7th European Wave and Tidal Energy Conference, Porto, Portugal, 2007.
[13] R. Sykes, A. Lewis, G. Thomas, in: Proceedings of the 7th European Wave and Tidal Energy Conference, Porto (Portugal), 2007.
[14] R. Sykes, A. Lewis, G. Thomas, in: Proceedings of the 8th European Wave & Tidal Energy Conference, Uppsala, Sweden, 2009.
[15] R. Gomes, J. Henriques, L. Gato, A. Falcao, Renew. Energy 44 (2012) 328–339.
[16] Y. Zhang, Q.-P. Zou, D. Greaves, Renew. Energy 41 (2012) 159–170.
[17] P.R. Teixeira, D.P. Davyt, E. Didier, R. Ramalhais, Energy 61 (2013) 513–530.
[18] I. López, B. Pereiras, F. Castro, G. Iglesias, Appl. Energy 127 (2014) 105–114.
[19] A. Kamath, H. Bihs, Ø.A. Arntsen, Int. J. Mar. Energy 10 (2015) 1–16.
[20] A. Kamath, H. Bihs, Ø.A. Arntsen, Ocean Eng. 102 (2015) 40–50.
[21] Y. Luo, J.-R. Nader, P. Cooper, S.-P. Zhu, Renew. Energy 64 (2014) 255–265.
[22] M. Anbarsooz, A. Faramarzi, A. Ghasemi, in: POWER & ENERGY Conference & Exhibition, Charlotte, USA, 2016.
[23] U. Şentürk, A. Özdamar, Prog. Comput. Fluid Dyn. Int. J. 13 (2013) 120–129.
[24] A. Elhanafi, A. Fleming, G. MacFarlane, Z. Leong, Energy (2016) (in press, doi:10.1016/j.energy.2016.09.118).
[25] A. Iturrioz, R. Guanche, J. Armesto, M. Alves, C. Vidal, I. Losada, Ocean Eng. 76 (2014) 65–74.
[26] A. Iturrioz, R. Guanche, J. Lara, C. Vidal, I. Losada, Ocean Eng. 107 (2015) 222–236.
[27] I. Crema, I. Simonetti, L. Cappietti, H. Oumeraci, in: 11 th European Wave and Tidal Energy Conference (EWTEC), Nantes, France, 2015.
[28] I. Simonetti, L. Cappietti, H. El Safti, H. Oumeraci, in: ASME 2015 34th International Conference on Ocean, Offshore and Arctic Engineering, Volume 9: Ocean Renewable Energy, American Society of Mechanical Engineers, St. John's, Newfoundland, Canada, 2015 (OMAE2015-42056).
[29] A. Elhanafi, A. Fleming, G. MacFarlane, Z. Leong, Int. J. Nav. Archit. Ocean Eng. (IJNAOE) (2016) (in press, doi:10.1016/j.ijnaoe.2016.08.002).
[30] A. Elhanafi, A. Fleming, G. MacFarlane, Z. Leong, Renew. Energy (2016) (provisionally accepted).

[31] V.S. Jayakumar, Wave force on oscillating water column type wave energy caisson: an experiment study, PhD Thesis in: Department of Ocean Engineering, Indian Institute of Technology Madras, India, 1994.
[32] S.J. Ashlin, S. Sannasiraj, V. Sundar, Procedia Eng. 116 (2015) 1019–1026.
[33] C.W. Hirt, B.D. Nichols, J. Comput. Phys. 39 (1981) 201–225.
[34] A. Elhanafi, A. Fleming, Z. Leong, G. Macfarlane, Prog. Comput. Fluid Dyn. (2016) (in press).
[35] N. Nojiri, K. Murayama, in: Transactions of the West-Japan Society of Naval Architects, 131, 1975, p. 152.
[36] K. Tanizawa, M. Minami, S. Naito, in: The Ninth International Offshore and Polar Engineering Conference, International Society of Offshore and Polar Engineers, 1999.
[37] E.P. Mansard, E. Funke, Coast. Eng. Proc. 1 (1980).
[38] Y. Goda, T. Suzuki, Coast. Eng. Proc. 1 (1976).
[39] D.-Z. Ning, J. Shi, Q.-P. Zou, B. Teng, Energy 83 (2015) 177–188.
[40] S.K. Chakrabarti, Offshore structure modeling, World Scientific Publishing, Singapore, 1994.
[41] F. He, Z. Huang, Ocean Eng. 88 (2014) 618–626.
[42] A.F. Falcão, J.C. Henriques, Int. J. Mar. Energy 6 (2014) 18–34.

Appendix L

Paper 12: Elhanafi A., Kim C.J. Experimental and numerical investigation on wave height and power take–off damping effects on the hydrodynamic performance of an offshore–stationary OWC wave energy converter. *Renewable Energy. Provisionally accepted, revised manuscript (2nd revision) submitted August 21, 2017*.

Experimental and numerical investigation on wave height and power take–off damping effects on the hydrodynamic performance of an offshore–stationary OWC wave energy converter

Ahmed Elhanafi[a,b], Chan Joo Kim[a]

a) National Centre for Maritime Engineering and Hydrodynamics, Australian Maritime College, University of Tasmania, Launceston, Tasmania 7250, Australia

b) Department of Naval Architecture and Marine Engineering, Alexandria University, Alexandria, Egypt

Abstract

Wave energy is a viable source of ocean renewable energy and research is being conducted worldwide. The Oscillating Water Column (OWC) device is recognised internationally as one of the most promising types of ocean Wave Energy Converters (WECs). To effectively utilize ocean waves for harvesting more energy, offshore OWC devices need to be deployed in deep–water where waves are more energetic. Therefore, the present paper experimentally investigated the hydrodynamic performance of a 3D offshore–stationary OWC device subjected to a wide range of regular wave conditions of different periods and heights and nonlinear power take–off (PTO) damping conditions simulated by an orifice. The experimental results were also employed to validate a 3D incompressible Computational Fluid Dynamics (CFD) model based on the RANS–VOF approach. It was found that device efficiency decreased as wave height increased, especially for wave frequencies higher than device resonance frequency. However, for low–frequency waves under small PTO damping, there was a noticeable improvement in device efficiency. More importantly, results of this study revealed that even with the changes in device efficiency as wave height doubled, the OWC device could extract more wave energy throughout the whole frequency range tested by a maximum of about 7.7 times, particularly for long waves under small PTO damping. Furthermore, the numerical results from the 3D CFD model were in good agreement with the experiments, while the 2D model provided misleading (overestimating) results for high–frequency waves.

Keywords: Wave energy; offshore oscillating water column device; OWC; 3D experiments and CFD; PTO damping effect; wave height effect.

* Corresponding author. Tel.: +61470352926

E-mail addresses: Ahmed.Elhanafi@utas.edu.au (A. Elhanafi)

1. Introduction

To cope with the increasing costs of fossil fuels as well as the environmental impacts due to the excessive use of these fuels, eco–friendly power from renewable energy sources has been under the spotlight and is believed to have an important role in resolving these effects. Ocean wave energy is considered to be one of the most promising renewable energy sources as it can provide noteworthy advantages when compared to other sources such as solar, wind and tidal. Wave energy offers the highest energy density and relatively small potential energy losses when travelling over long distance [1]. A key feature is that Wave Energy Converter (WEC) devices are able to produce power up to ninety percent of the time, whereas other types of renewable energy conversion devices such as solar energy converters and wind turbines can only generate power about twenty to thirty percent of the time [1]. The World Energy Council Report on World Energy Sources [2] estimated the total theoretical wave energy potential of 32,000 TWh/year. This value decreased to 16,000–18,500 TWh/year when the direction of the wave energy and the world coastline alignment were taken into account [3]; however, this is still comparable to the global electricity consumption (energy demand) of about 20,500 TWh in year 2015 [4]. Utilizing these advantages, several techniques have been proposed and developed to extract wave energy. These technologies can be categorised by deployment location (shoreline, nearshore and offshore), type (attenuator, point absorber and terminator) and mode of operation (submerged pressure differential, oscillating wave surge converter, oscillating water column and overtopping device) [1]. The wave energy electricity production by the current technologies and designs of devices when fully mature has been estimated to be 140–750 TWh/year; however, this figure could be increased to 2,000 TWh/year if all potential improvements to these devices are realised [5].

The Oscillating Water Column (OWC) device is a WEC that is based on wave–to–pneumatic energy conversion by utilizing ocean waves to drive the motion of a water column inside a pneumatic chamber that has an underwater opening to the ocean. The water column fluctuation (oscillation) compels the air inside being compressed and decompressed which creates a bidirectional airflow. The pneumatic energy is then converted into mechanical energy via forcing the air to flow through a turbine or a power take–off (PTO) system that is connected to a generator to transform the mechanical energy into electricity. Each phase of the energy conversion chain has its own importance in terms of overall performance. The significance of studying wave–to–pneumatic energy conversion stage (which is the focus of the present study) is that this is the primary stage where energy losses are expected to be high [6-9]. OWC devices

can be installed at different locations (shoreline, nearshore, and offshore) as either fixed or floating structures [10].

Investigating the hydrodynamic performance of OWC devices has been extensively performed by different means including analytical, experimental, numerical or in a combination of the aforementioned. Most if not all analytical studies such as McCormick [11], Falcão and Sarmento [12], Evans [13] and Falnes and McIver [14] are based on linear wave theory to model simple OWC device geometries like a thin–walled vertical tube and two parallel vertical thin walls. For complex geometries, the wave–OWC device interactions require numerical modelling that is usually solved using the Boundary Element Method (BEM) [15]. However, these methods are still based on the potential flow assumptions and cannot handle problems that require capturing detailed physics such as strong nonlinearity, complex viscous effects, turbulence and vortex shedding. For extensive reviews of utilizing analytical and potential flow models to study OWC devices, the reader is referred to Refs. [15, 16]. On the other hand, Numerical Wave Tanks (NWTs) based on the Reynolds–averaged Navier–Stokes (RANS) equations do not have the above–mentioned shortcomings. Accordingly, these advantages together with the increasing availability of computational power have made Computational Fluid Dynamics (CFD) more attractive and viable for researchers to study the hydrodynamic performance of OWC devices [9, 17-20]. However, CFD modelling of OWC devices has generally been restricted to 2D geometries and regular waves, and it still requires validation against physical model testing [15].

Over the past few decades, many physical scale model experiments have been performed to investigate the effects of different design parameters on the hydrodynamic performance of onshore OWC devices [21-25]. In comparison to the typical onshore and nearshore types of OWC devices, offshore OWC devices allow ocean waves to pass around and underneath the device, which in turn changes the hydrodynamic interactions and the energy balance of such devices [26]. However, there is a very limited number of experiments and/or numerical studies on offshore OWC devices. For example, Iturrioz et al. [27, 28] and Simonetti et al. [29, 30] developed open source CFD codes (IHFOAM) and (OpenFOAM) to model and investigate the hydrodynamic performance of a fixed detached OWC model and a three chamber OWC device, respectively after utilizing wave flume measurements to validate their numerical models. Elhanafi et al. [26] employed a 2D CFD model using a commercial code (STAR–CCM+) to study the relevance of incident wave amplitude, wave frequency and turbine damping to the energy balance of an offshore stationary OWC device. Recently, He et al. [31] experimentally investigated the importance of energy extraction and vortex–induced energy loss with respect to

energy dissipation for a pile–supported OWC model embedded breakwater. They discovered that the energy extraction and vortex–induced energy loss are closely related, and the pneumatic damping has a greater influence on the vortex–induced energy loss than the energy extraction. Although He et al. [31] achieved significant findings in their experimental investigation, it is worth noticing that the experiments were conducted in a 2D wave flume, which constrains wave diffraction and transmission around the device. In addition, the OWC model was subjected to a single small wave height representing weakly nonlinear waves of steepness 0.0123–0.0287, and only intermediate water depth conditions were tested based on the water depth and wave periods provided.

To complement previous studies, the main objective of this study is to experimentally investigate the hydrodynamic performance of a 3D offshore OWC device under the action of regular waves of different periods and heights including strong nonlinear waves in deep– and intermediate–water depth conditions. In addition, the effect of changing the PTO damping on device performance is studied. Finally, the capability of a 3D incompressible CFD model based RANS–VOF approach in predicting the device performance is discussed. Both experiments and CFD simulations were performed at a small scale model, and full–scale system dynamics inside the OWC chamber due to air compressibility effects [32] were not modeled in the present study.

2. Experimental set–up

2.1. Testing facility

The experimental campaigns were performed in the towing tank of the Australian Maritime College (AMC), University of Tasmania, Australia. The tank characteristics are 100 m long, 3.5 m width and a maximum water depth of 1.5 m. Waves are generated by means of a flap–type wavemaker installed at one end, whereas a wave–absorption beach is located at the other end.

2.2. Offshore OWC model

The 1:50 scale model offshore OWC device used in these experiments was manufactured of plywood with dimensions illustrated in Fig. 1–a, and it was positioned 15 m from the wavemaker (see Fig. 2). The model was scaled based on Froude's similitude law such that the water depth (1.5 m) of the towing tank represented 75 m at full–scale. The OWC model had an overall draught of 350 mm and a rectangular chamber (300 mm x 200 mm) with symmetric front and rear lips of 12 mm thickness and 200 mm submergence. Considering that the ratio of the tank width (W) to the model breadth (B) was 8.75 (i.e., $W/B > 5$), the tank sidewall effects could

be ignored [33]. The columns and pontoons attached to the chamber provide the required buoyancy to permit future experiments over a wider range of wave conditions on the same model, but as a floating OWC device which is tension moored using a similar concept to that proposed in Lye et al. [34].

The chamber top plate of 12 mm thick included a central opening to utilize testing different PTO damping conditions. To simulate the pneumatic damping induced by the PTO system during experiments of small scale models, it is common to use either an orifice (or a slot) to simulate an impulse turbine (nonlinear/quadratic pressure–flow rate characteristics) or a porous medium to mimic a Wells turbine (linear characteristics) [21, 32]. In the present study, an orifice of different diameters shown in Fig. 1–b was manufactured via a 3D printer and used to model nonlinear PTO damping. Each orifice was defined by its radius and opening ratio (the ratio between the orifice area and the chamber waterplane area (a x b) in percentage, %). Considering the 12 mm thickness of the chamber top plate and the orifice diameter, orifices R_2–R_5 were classified as thin–walled openings (i.e., the ratio between orifice thickness (12 mm) and orifice diameter is less than 0.5), while orifice R_1 was classified as a thick–walled opening [35].

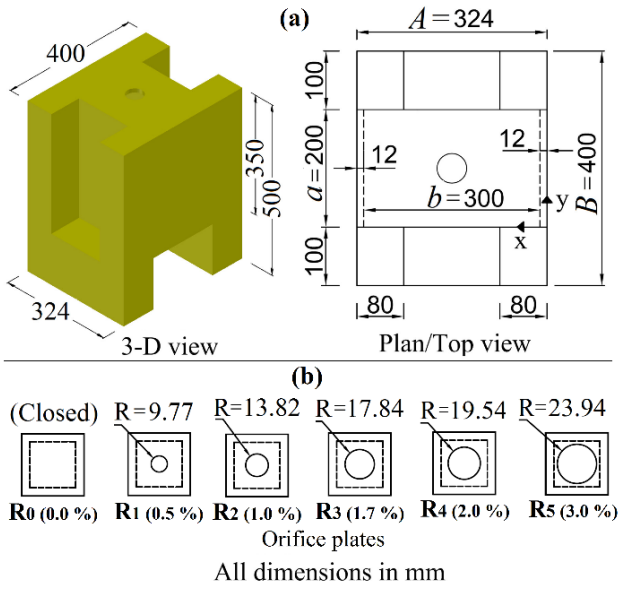

Fig. 1. 1:50 scale model of an offshore–stationary OWC device. (a): main dimensions and (b): orifice diameters

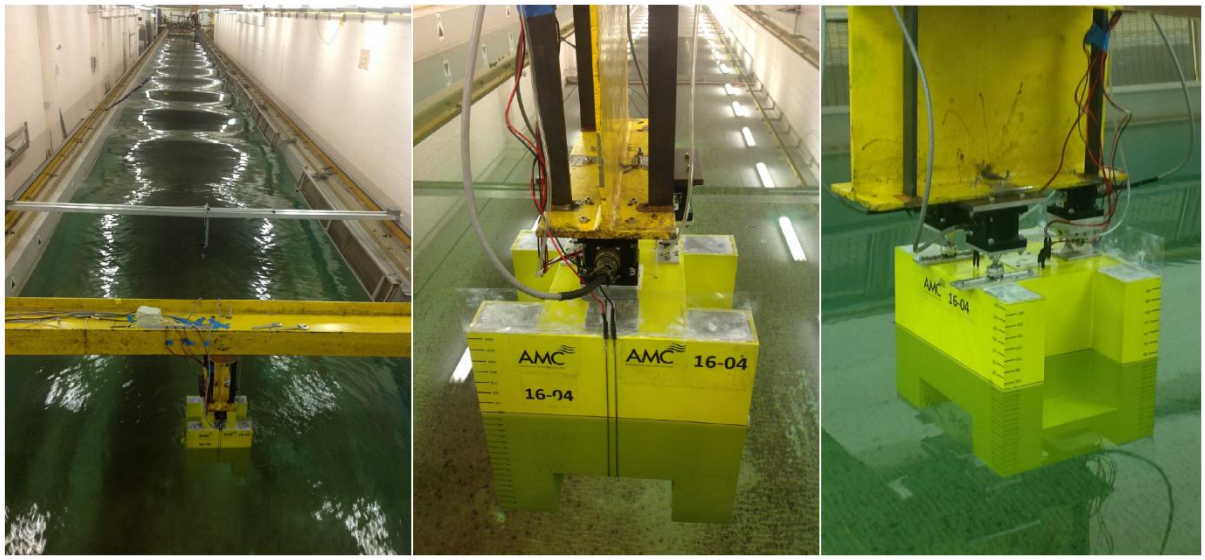

Fig. 2. Photographs showing the AMC towing tank with the OWC model, looking towards the beach (left) and test rig in–situ (centre: front view and right: back–side view)

2.3. Instrumentation and test conditions

In the experiments (see Fig.3 for experiment layout), three resistance–type wave gauges were used to measure the instantaneous free surface elevation in the tank and inside the OWC chamber. One wave gauge (G1) was positioned 6 m from the wavemaker to measure the free surface elevation of the incident wave. For rectangular shaped OWC devices like the model considered in this study, measurements of free surface motion inside the OWC chamber are usually carried out using one [36], two [31] or three [24] wave gauges. Herein, two wave gauges (G2 and G3) were situated inside the OWC chamber to spatially average the free surface elevation (η_{OWC}). To measure the differential air pressure between the OWC pneumatic chamber and exterior atmosphere, two pressure sensors (Honeywell–TruStability–001PD TSC Series) marked as P1 and P2 were installed on the top surface of the OWC chamber to average the measured pressure ($\Delta p(t)$). All measurements were sampled at 200Hz. During data processing, a low pass digital filter (Butterworth–filter [37]) with a 5 Hz cut–off frequency and 10^{th} order was applied using the Matlab function filtfilt [38].

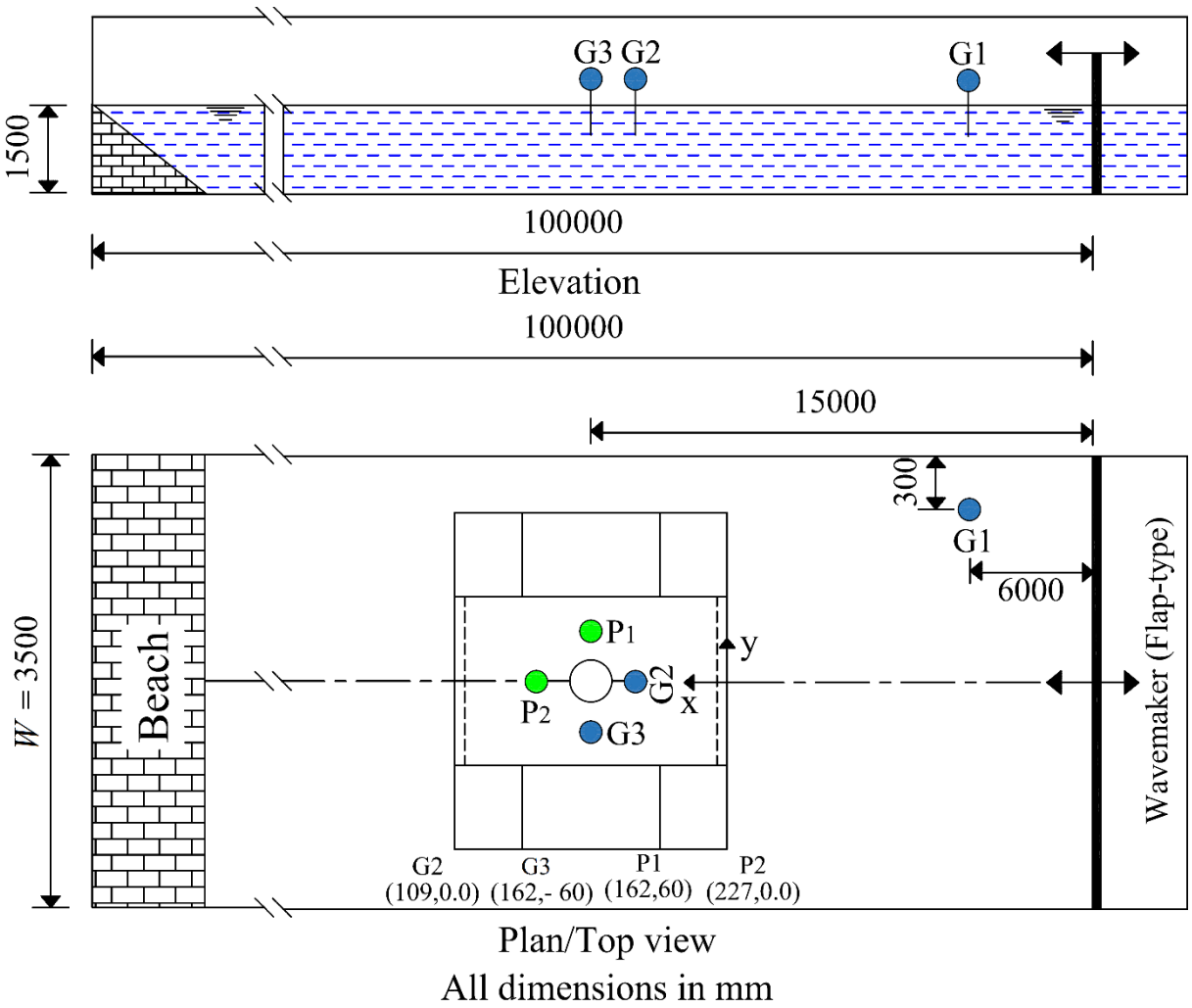

Fig. 3. Experiment layout (not to scale)

The physical measurements were designed to study the effect of incoming wave period, wave height and PTO damping on the hydrodynamic performance of the offshore OWC model described in Section 2.2. The experiments systematically investigated the following variables: two regular wave heights H = 50 and 100 mm, ten wave periods T = 0.9, 1.0, 1.1, 1.2, 1.3, 1.4, 1.5, 1.6, 1.8, 2.0 s and six orifice diameters: R_0 – R_5 (see Fig. 1–b). Within the range of wave conditions tested, wave steepness varied between 0.009 – 0.080 and both intermediate (T = 1.4–2.0 s) and deep–water (T = 0.9–1.3 s) conditions were covered.

2.4. Data analysis and OWC device performance

The overall hydrodynamic efficiency (ζ) that best represents the hydrodynamic performance of a WEC [39] is defined as in Eq. (1) for an OWC device [24]. The hydrodynamic

efficiency is also referred in the literature as capture width ratio [36, 39] or dimensionless capture width [40].

$$\zeta = P_E/(P_I a) \tag{1}$$

where P_I is the mean incident wave power (energy flux) per unit width, which is defined as the product of the wave energy (E_I) (potential and kinetic) per unit ocean surface area and the group velocity (C_g) [41] as given in Eqs. (2) and (3), while P_E is the time–averaged extracted pneumatic power determined as in Eq. (4) [7, 26, 42] and a is chamber width (Fig. 1–a).

$$P_I = \frac{1}{2}\rho g A^2 C_g \tag{2}$$

$$C_g = \begin{matrix} \frac{\omega}{2k}\left(1+\frac{2kh}{\sinh(2kh)}\right) & \text{for intermediate} - \text{water conditions } \left(\frac{L}{20} < h < \frac{L}{2}\right) \\ \frac{1}{2}\frac{L}{T} & \text{for deep} - \text{water conditions } \left(h > \frac{L}{2}\right) \end{matrix} \tag{3}$$

where A is incident wave amplitude (defined as half the measured wave height, H), ω is wave angular frequency, k is wave number given by the dispersion relationship $\frac{\omega^2}{g} = k\tanh(kh)$, L is incoming wavelength, T is wave period, h is still water depth, ρ is water density and g is gravitational acceleration.

$$P_E = \frac{1}{T}\int_0^T \Delta p(t)\, q(t)\, dt \tag{4}$$

where $q(t)$ is airflow rate through the orifice, which can be measured by two commonly accepted approaches: (1) using a pre–calibrated orifice together with the pressure measurement [43] and (2) by measuring the free surface elevation inside the OWC chamber [24, 31, 36, 42, 43] with incompressible flow assumption. The second approach was utilized in the present experiments as follows. Using the averaged chamber free surface oscillations (η_{OWC}), the free surface vertical velocity (V) was calculated by differentiating the measured time–series data (i.e., $V(t) = d\eta_{OWC}/dt$). Having defined the chamber free surface vertical velocity and assumed incompressible air for the small model–scale used in these experiments [44], airflow rate ($q(t)$) was calculated by Eq. (5). It is worth highlighting that air compressibility effects must be considered when scaling–up the results presented in this paper to assess device performance at full–scale.

$$q(t) = V(t)\, ba \tag{5}$$

where b and a are the chamber length and width, respectively (see Fig. 1–a).

3. Results and discussion

The hydrodynamic performance of the OWC device described in Section 2 was initially assessed when subjected to ten different wave periods and two wave heights H = 50 mm and 100 mm under three PTO damping conditions (R_2, R_4 and R_5). Fig. 4 illustrates the relevance of these variables to the amplification factor (η_{max}/A, defined as the ratio between the maximum free surface oscillation inside the chamber η_{max} and the incoming wave amplitude A), the pressure coefficient (C_P) given by Eq. (6) and the overall hydrodynamic efficiency (ζ). In this study, a dimensionless parameter Kb where $K = \omega^2/g$ was used to refer to the changes in wave period/frequency [26].

$$C_P = \frac{\Delta p_{\max}}{\rho g A} \tag{6}$$

where $\Delta p_{\max}$ is the differential air pressure amplitude defined as in Eq. (7)

$$\Delta p_{\max} = \left[\frac{\Delta p_{\max\,(\text{crest value},+\text{ve})} - \Delta p_{\min\,(\text{trough value},-\text{ve})}}{2}\right]_{\text{avg}-5\text{ cycles}} \tag{7}$$

Overall, both wave heights provided almost the same general trends for all assessed parameters as illustrated in Fig. 4. As wave frequency increased (Kb increased), the amplification factor (Fig. 4–a) gradually increased until peaked at a certain Kb value that increased as PTO damping decreased. Following this peak, a steep drop in η_{max}/A was observed as Kb further increased. This was in agreement with what has recently been reported experimentally for land–based OWC devices [24] and numerically with 2D CFD for offshore OWC devices [26]. Similar results were also found for the larger wave height, H = 100 mm (Fig. 4–d), except the peak value that was shifted to a lower frequency. This was more pronounced under PTO damping cases of R_2 and R_4 where maximum η_{max}/A was achieved under the longest wave tested of Kb = 0.30. Although the incident wave height increased twofold (i.e., H = 100 mm), the resulted amplification factors were smaller than those for H = 50 mm over the entire frequency range, which revealed a nonlinear relationship between chamber maximum free surface oscillation and incoming wave height. This could be attributed to the increase in chamber free surface deformation and water sloshing as wave height increased [26].

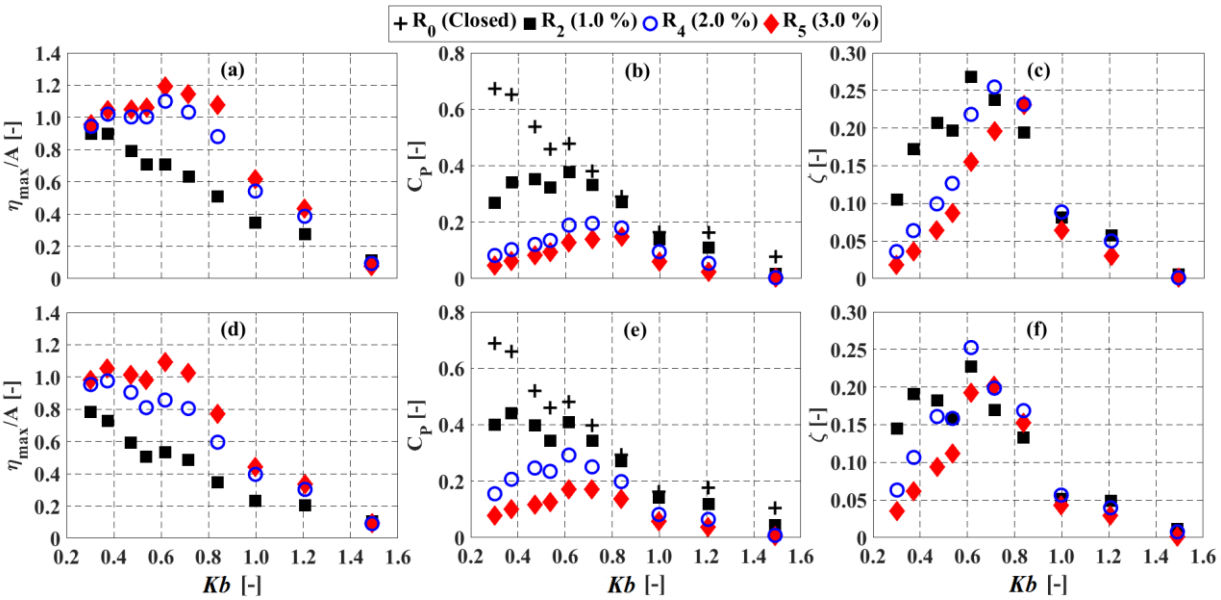

Fig. 4. Impact of wave height and frequency on the amplification factor (η_{max}/A), pressure coefficient (C_P) and device efficiency (ζ) under three damping conditions. (a), (b) and (c) for H = 50 mm and (d), (e) and (f) for H = 100 mm

The pressure coefficient (C_P) (Figs. 4–b and 4–e) increased as Kb increased, reached a maximum value at a certain frequency (Kb) representing (or close to) the chamber resonance frequency, and then declined with a further increase in Kb (i.e., wavelength shortened). The device resonance frequency was shifted to a lower value as PTO damping increased. This effect could obviously be seen in the case of the closed orifice (full–damping, R_0) where a maximum pressure coefficient of C_P = 0.68 for both H = 50 mm and H = 100 mm was found under the longest wave tested (Kb = 0.30). This was also observed by Iturrioz et al. [28] and He and Huang [35] for similar offshore OWC devices that have been tested in 2D wave flumes under a constant wave height.

Although Iturrioz et al. [28] did not present results for the amplification factor, it was stated that the maximum pressure happens close to the resonance period of the chamber, and at that period the chamber maximum free surface oscillation also occurs. Conversely, Simonetti et al. [29], Ning et al. [24] and Elhanafi et al. [26] found that the maximum pressure amplitude occurs at a frequency higher than that of the chamber maximum free surface oscillation for a given wave height, which is in line with the results presented in Figs. 4–a and 4–b of this study. However, Figs. 4–d and 4–e show that under the lowest damping tested (orifice R_5) the maximum pressure coefficient and amplification factor occurred nearly at the same frequency (Kb = 0.62), which supports the findings of Iturrioz et al. [28]. This contradiction can be explained by considering the fact that the chamber differential air pressure is related to the chamber free surface oscillation rate (slope) not to the oscillation amplitude solely [26]. For illustration, Fig.

5 shows the instantaneous variations (time–series results) of chamber free surface oscillation (η_{OWC}), chamber differential air pressure (Δp), airflow rate (q) and extracted pneumatic power (P_E) for a given PTO damping induced by orifice R4 under two wave heights H = 50 mm (Fig. 5–left) and H = 100 mm (Fig. 5–right) at different Kb values. Although low–frequency waves of Kb = 0.47 at H = 50 mm (Fig. 5–a) and Kb = 0.37 at H = 100 mm (Fig. 5–d) provided higher chamber free surface oscillation amplitudes (i.e., higher amplification factors considering a constant wave height of H = 50 or 100 mm), larger pressure amplitudes were found at a higher frequency of Kb = 0.84 for H = 50 mm (Fig. 5–b) and Kb = 0.62 for H = 100 mm (Fig. 5–e). This is because at these frequencies (i.e., Kb = 0.84 and 0.62), the smaller chamber free surface oscillation amplitudes were accompanied by shorter wave periods, which in turn resulted in a higher free surface oscillation rate inside the chamber (i.e., a higher slope with respect to time–axis) that are demonstrated by the higher airflow rate and pressure amplitudes shown in Figs. 5–b and 5–e. Except the closed orifice (R_0), increasing the wave height (Fig. 4–e) resulted in: (1) higher pressure coefficients throughout the whole Kb range tested, which further explains the associated reduction in the amplification factors and (2) a slight reduction in device resonance frequency that could be due to the coarse resolution of the Kb range tested (i.e., large wave period interval of 0.1 s, see Section 2.3).

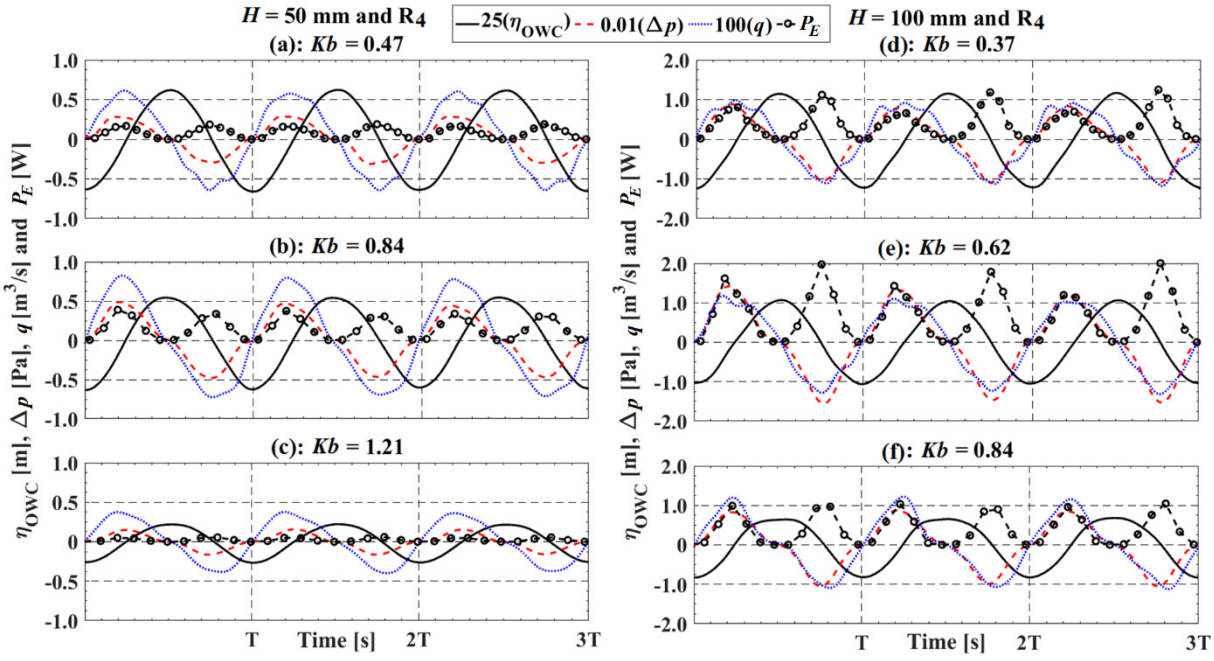

Fig. 5. Effects of wave frequency and wave height on the instantaneous chamber free surface oscillation (η_{OWC}), chamber differential air pressure (Δp), airflow rate (q) and extracted pneumatic power (P_E) at a constant PTO damping (R_4)

The overall hydrodynamic efficiency of the OWC model is illustrated in Figs. 4–c and 4–f for H = 50 mm and 100 mm, respectively. To explain the changes in device efficiency, it is

important to note that both the differential air pressure and the airflow rate are the governing parameters for the extracted pneumatic power as given in Eq. (4). Although the results of the airflow rate through the orifice are not presented in Fig. 4, it is expected the airflow rate to follow the same trend of the chamber differential air pressure at a given PTO damping [26]. This is because both parameters are related by a damping coefficient (C) as given in Eq. (8) for nonlinear PTO system [18] that was simulated by an orifice in the present study.

$$C = \frac{\Delta p^{\frac{1}{2}}}{q} \tag{8}$$

This correlation can also be seen in the results presented in Fig. 5. As a result, the extracted pneumatic power is also expected to have the same trend of the chamber differential air pressure (see Fig. 5) such that the maximum extracted pneumatic power was achieved at the same frequency of the maximum pressure. On the other side, as *Kb* increased the group velocity of the incoming wave decreased as given by Eq. (3), which in turn reduced the available incoming wave power as given by Eq. (2). Therefore, the device efficiency gradually increased according to Eq. (1) as *Kb* increased until peaked at a certain frequency of resonance (for example, at *Kb* = 0.71 and 0.62 for *H* = 50 mm and 100 mm respectively under a PTO damping of orifice R_4). Following that peak, the pneumatic power decreased due to the drop in the pressure and the airflow rate (see Figs. 5–c and 5–f); hence, the power extraction efficiency (ζ) decreased with a further increased in *Kb* (see Figs. 4–c and 4–f). For instance, considering the condition of *H* = 50 mm and orifice R_4 (Fig. 4–c), the overall efficiency (ζ) improved from 0.04 at *Kb* = 0.30 to a maximum of about 0.25 at *Kb* = 0.71, then dropped to 0.09 at *Kb* = 1.0 and diminished at the highest frequency tested of *Kb* = 1.5. A physical explanation for the low extracted pneumatic power at the high–frequency zone could be that the front lip draught (200 mm) did not provide a reasonable path for the small particles excursions under these short waves to smoothly enter the pneumatic chamber rather than formatting vortices at lips tip, breaking the rigid–piston like motion of the chamber free surface and/or reflecting [8, 45]. These effects can be seen in the small amplitudes of the chamber free surface oscillation, airflow rate and differential air pressure shown in Fig. 5–c for *Kb* = 1.21 and *H* = 50 mm.

Although the maximum efficiency reported in this paper (ζ_{max} = 0.26 for a PTO damping induced by orifices R_2 and R_3) is quite smaller than what was experimentally found for typical onshore OWC devices [24, 36], it is worth noting that Sarmento [21] predicted using linear theory [13] a maximum hydrodynamic efficiency of 0.5 for a two–dimensional chamber that had a vertical plane of symmetry (i.e., identical front and rear lips draught). In Sarmento's study, the

hydrodynamic efficiency was defined as the rest of the incoming wave energy that was not reflected and/or transmitted on the lee side of the chamber. This efficiency has recently been classified by Elhanafi et al. [26] in their energy balance model as the energy absorbed by the OWC structure, which represented the maximum available energy to be extracted for electricity generation. However, that maximum efficiency (0.5) was not achievable due to energy losses in terms of viscous, turbulence and vortex losses at chamber lips and PTO system [21, 26, 31]. Using 2D wave flume experiments, He et al. [31] reported a maximum efficiency of 0.25–0.37 (for different symmetrical lip draughts and PTO damping conditions, see Fig. 4 in He et al. [31]), which is slightly higher than the maximum efficiency presented in this paper. This difference could be related to the 2D behaviour of He et al.'s experiments that will be briefly discussed in Section 4.3 as well as to the different lip draughts tested. The relevance of chamber underwater geometry to the hydrodynamic efficiency of offshore OWC devices has found by Elhanafi et al. [8] to be significant. They tested several symmetrical and asymmetrical lips draught and thickness of a 2D OWC chamber with length (b) similar to that of the OWC model tested in this study (i.e., b = 300 mm, see Fig. 1–a), and reported a significant improvement in the efficiency up to 0.79, which is close to that of typical onshore OWC devices. This emphasises the importance of investigating the capability of CFD modelling (Section 4) in replicating the 3D physical measurements provided in this study so that it can be used for optimizing the underwater geometry of offshore OWC devices for a maximum efficiency.

Generally, Figs. 4–c and 4–f show that as wave height increased the maximum efficiency decreased. For instance, the maximum efficiency decreased from 0.26 for H = 50 mm at Kb = 0.62 and orifice R_2 to 0.23 for H = 100 mm at the same frequency (Kb = 0.62) and PTO damping. These results are in agreement with the CFD results of Luo et al. [19] and Kamath et al. [46] who found that the hydrodynamic efficiency of onshore OWC devices decreased as wave height increased. Ning et al. [24] concluded a negligible effect of wave height on device resonance under a PTO damping induced by an orifice with 0.66 % opening ratio. In the present study, similar results were observed only for the conditions with high PTO damping such as R_1 (0.5 %, not presented in Fig. 4) and R_2 (1.0 %), but for all other damping conditions (i.e., $R > R_2$), there was a slight reduction in the resonance frequency as wave height increased, which again could be attributed to the large wave period interval (0.1 s) used in this study. The effect of increasing the wave height on the device efficiency was influenced by the wave frequency and the PTO damping such that under high steepness waves (strongly nonlinear waves of high Kb) increasing the wave height decreased the efficiency, while at low–frequency waves (weakly nonlinear waves of low Kb), there was a noticeable improvement in device efficiency as wave height

increased, especially for low and intermediate PTO damping conditions. Similar observations were previously reported for 2D onshore and offshore OWC devices using numerical simulations [26, 47] and physical experiments [23, 24].

Previous experimental research on onshore OWC devices [23, 24] classified the pneumatic damping exerted by the turbine as the factor that most affects the device efficiency. Accordingly, the influence of the six orifices tested (see Fig. 1–b) on the amplification factor, the pressure coefficient and the overall efficiency is demonstrated by contour plots in Fig. 6 for all wave heights and *Kb* values tested in these experiments.

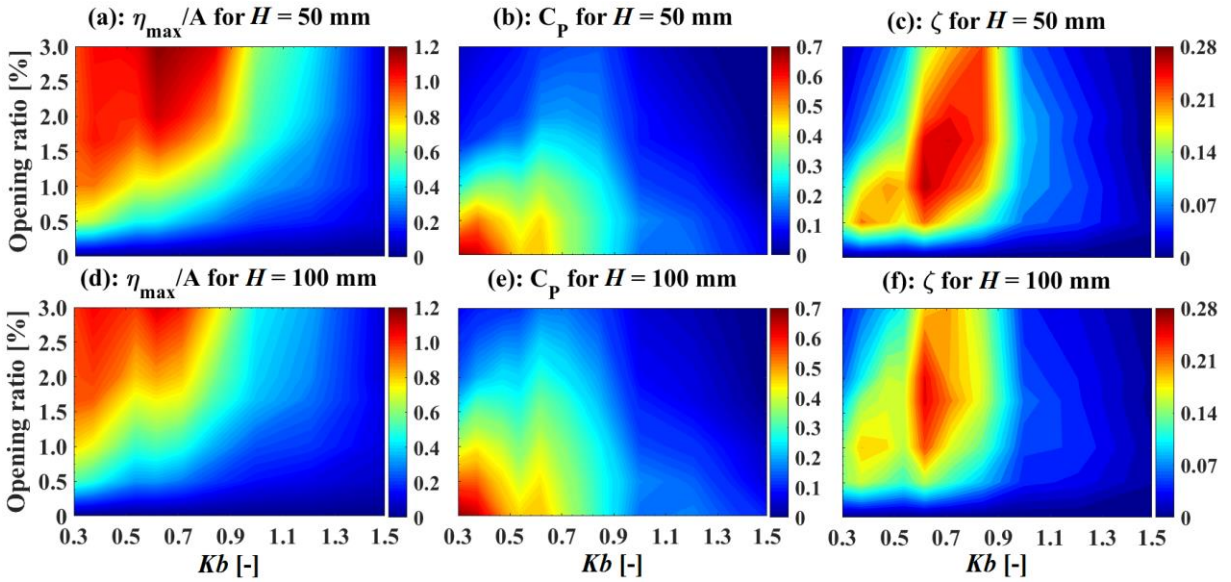

Fig. 6. PTO damping effects on the amplification factor (η_{max}/A), pressure coefficient (C_P) and device efficiency (ζ) for different wave conditions

Figs. 6–a and 6–d illustrate that the amplification factor for both wave heights increased as the opening ratio increased (i.e., PTO damping decreased). This in turn increased the free surface oscillation rate for each wave period (*Kb*), and hence the airflow rate also increased, especially for $Kb < 1.0$ under intermediate and large opening ratios (for example, see time–series results for $Kb = 0.71$, $H = 50$ mm in Fig. 7–left and $Kb = 0.62$, $H = 100$ mm in Fig. 7–right). Opposite trends were found for the chamber differential air pressure (Figs. 6–b, 6–e and Fig. 7). These contrary effects of the PTO damping on the variables (Δp and q) that control the extracted pneumatic power highlight the importance of selecting an optimum PTO damping to tune the device to a given frequency (*Kb*) range for maximizing the extracted power (see Fig. 7) and the device efficiency (see Figs. 6–c and 6–f). For each wave condition (period and height), there was an optimum opening ratio (damping) that provided a maximum efficiency. Reducing the PTO damping (increasing the opening ratio) shifted the maximum efficiency to a higher frequency

(Kb), but this effect was less pronounced for the larger wave height of H = 100 mm. Under the smaller wave height H = 50 mm, the device could efficiently extract wave energy over a broader frequency bandwidth (0.54 < Kb < 0.84) and opening ratios. For instance, Fig. 7–left shows that the device extracted almost the same power for a wave condition of H = 50 mm and Kb = 0.71 when applying different PTO damping conditions corresponding to opening ratios of 2 % (Fig. 7–b) and 3 % (Fig. 7–a). On the other hand, increasing the wave height reduced these frequency and opening ratio ranges, but under small PTO damping conditions (opening ratio > 1.0 %), the large wave height improved the device efficiency at the low–frequency zone (Kb < 0.62).

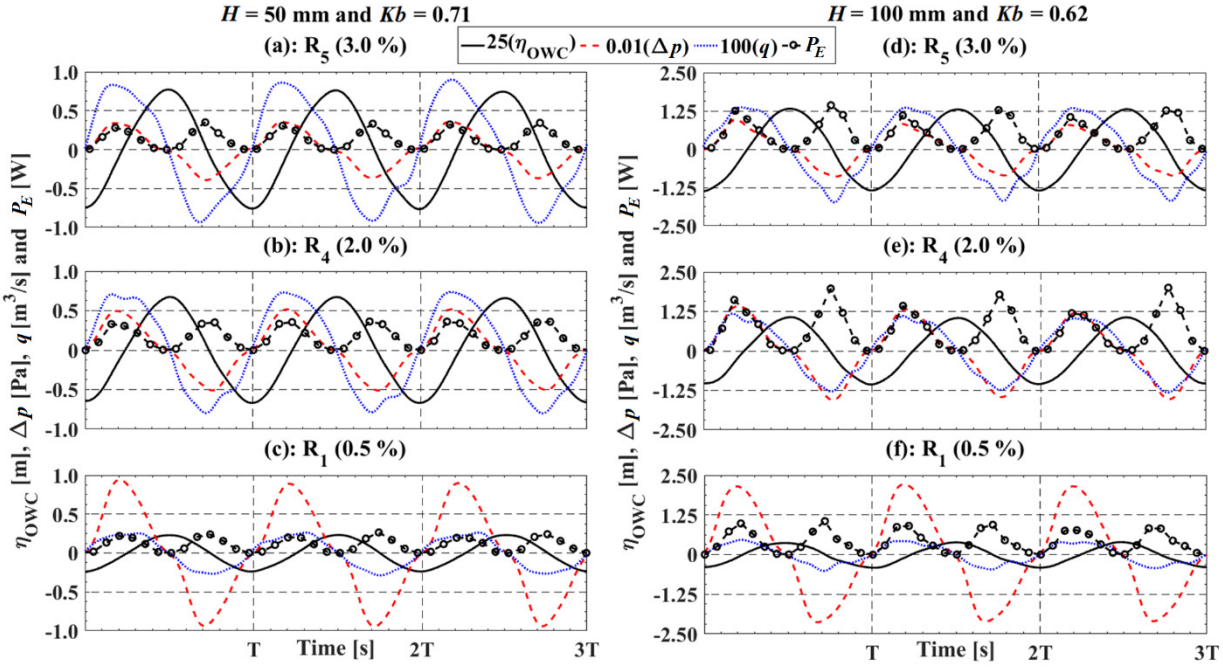

Fig. 7. Impact of PTO damping on the instantaneous chamber free surface oscillation (η_{OWC}), chamber differential air pressure (Δp), airflow rate (q) and extracted pneumatic power (P_E) at a two wave conditions. Left: H = 50 mm, Kb = 0.71 and right: H = 100 mm, Kb = 0.62

Elhanafi et al. [26] concluded that increasing the wave height not only increases the energy losses, but also the extracted pneumatic energy. Herein, regardless of the variations in the device efficiency due to changing the wave height, it was found that the extracted pneumatic energy given by Eq. (9) increased by 2.5–7.7 times as wave height doubled from H = 50 mm to 100 mm (i.e., the incident wave energy increased four times), which is demonstrated by the contour plot in Fig. 8. This effect was found to increase as wavelength increased (i.e., Kb decreased) and PTO damping decreased. This larger extracted energy highlights the effectiveness of deploying such offshore OWC devices in deep–water locations where waves are more energetic.

$$E_E = P_E\, T \tag{9}$$

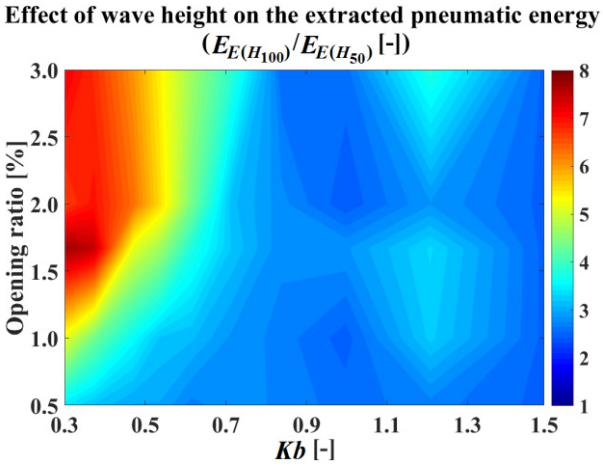

Fig. 8. Effect of increasing the wave height from H = 50 mm (H_{50}) to H = 100 mm (H_{100}) on the extracted pneumatic energy

4. CFD modelling and validation

As mentioned in the introduction (Section 1), CFD modelling became a viable tool that has previously been employed to investigate the hydrodynamic performance of 2D OWC devices. However, apart from being computationally expensive, CFD requires experimental validation [15]. Therefore, the above–described physical measurements are utilized in this section to validate the developed 3D CFD model. All numerical computations were performed using the RANS–VOF solver in the commercial CFD code STAR–CCM+ that utilizes a finite volume method and the integral formulation of the conservation equations for mass and momentum, while a predictor–corrector approach is used to link the continuity and momentum equations [48].

4.1. Governing equations and numerical settings

The CFD model developed in this section assumes incompressible flow since it has been found that air compressibility is negligible in small model–scale OWC devices such that tested in this study [28, 44]. The CFD model solves the continuity and RANS equations to describe the flow motion of the incompressible fluid. To solve the RANS equations, the instantaneous velocity and pressure fields in the Navier–Stokes equations are decomposed into mean value and fluctuating components, and then time–averaged. Consequently, additional unknowns called Reynolds stresses are introduced. To mathematically close the equations, a turbulence model must be utilized to relate Reynolds stresses to the mean flow variables. In this paper, the two–equation shear stress transport (SST) $k-\omega$ turbulence model was implemented since it has been found that $k-\omega$ (SST) provides superior results to k–ε in capturing detailed flow field (velocity

and vorticity) and estimating the energy losses in OWC devices when compared to experiments [9].

To model and track the free surface motion, the Volume of Fluid (VOF) method introduced by Hirt and Nichols [49] was used. The numerical settings of the CFD model were as follows. Time modelling: implicit unsteady with second–order temporal discretization scheme, flow modelling: segregated flow model with second–order upwind convection scheme (the segregated flow solver controls the solution update for the segregated flow model according to the SIMPLE algorithm) and multiphase model: VOF with segregated VOF solver that controls the solution update for the phase volume fractions (i.e. solve the discretized volume–fraction conservation equation for each phase present in the flow) with second–order convection scheme [48].

4.2. Computational domain, mesh, boundary and initial conditions

Ocean waves are the primary exciting source acting on offshore structures such as OWC devices; therefore, accurate modelling of these waves is crucial for providing a good estimation of the hydrodynamic loads and predicting the structure response and performance [50]. Referring to Fig. 9–a, the computational fluid domain of this study had an overall length (in x–direction) of 10L (L is wavelength) including 1L for the wave–damping zone at the end of the NWT, and the OWC model was positioned at a distance of 5L from the wave inlet boundary. This set–up was proven to be appropriate for capturing eight wave cycles up to a distance of 8L from inlet boundary without being influenced by waves reflected from the outlet boundary assigned at the end of the wave–damping zone [26]. To numerically mimic the width of AMC's physical towing tank without increasing the computation cost and time, the width of the NWT was set as half the width of the towing tank (i.e., $W/2$ = 1750 mm) with a symmetry plane. The assumption of using a symmetry plane and its impact on the numerical results was found to be negligible [44]. The domain height was fixed at 2500 mm including 1500 mm (still water depth) for the water phase and 1000 mm for the air phase. The tank side and bottom were defined as slip walls, while hydrostatic wave pressure was defined at the top and outlet boundaries.

Mesh generation was performed using the automatic meshing technique in STAR–CCM+ with a trimmed cell mesher. A base cell size of 400 mm was applied to the whole computational domain with progressive refinements at the free surface zone (the height of the free surface zone was set as 1.5 times the wave height) with at least 16 and 75 cells per wave height (z–direction) and wavelength (x–direction) respectively, which were close to what is recommended by the ITTC [51] and CD–Adapco [48]. The cell aspect ratio ($\Delta x/\Delta z$, the ratio between cell size in x

and z directions) at the free surface zone was set to be not more than 16 as recommended by Elhanafi et al. [26]. In the tank transverse (y) direction, a cell size of $\Delta y = 100$ mm was used as recommended by Elhanafi et al. [44] among the three different sizes tested. The time step (Δt) was carefully selected for each wave period (T) so that it satisfied the time step requirement ($\Delta t = T/2.4n$, where n is number of cells per wavelength) by CD–Adapco [48] with a second–order temporal discretization scheme. This resulted in a Courant number ($C = C_g.\Delta t/\Delta x$, where C_g is the wave group velocity) [48] smaller than 0.5; hence, the High–Resolution Interface Capturing (HRIC) scheme that is suited for tracking sharp interfaces [48] was guaranteed to be used during the simulations. The OWC non–slip surfaces were refined with 6.25 mm and 0.78125 mm cell surface size for the OWC walls and the PTO orifice opening, respectively as shown in Fig 9–b. For all non–slip walls (OWC and PTO), a first cell height equivalent to $y+ \cong 1$ was used with a growth rate of 1.5, ten prism layers and all y+ wall treatment. The initial conditions used in the present CFD model were set as follows (see Fig. 9–c). The water level was defined at the desired still water depth of $z = h = 1.5$ m, waves were prescribed by the velocity components at the wave velocity inlet boundary and were fully generated throughout the whole domain until the front lip of the OWC model by specifying that point on the water level (i.e., $x = 5L$).

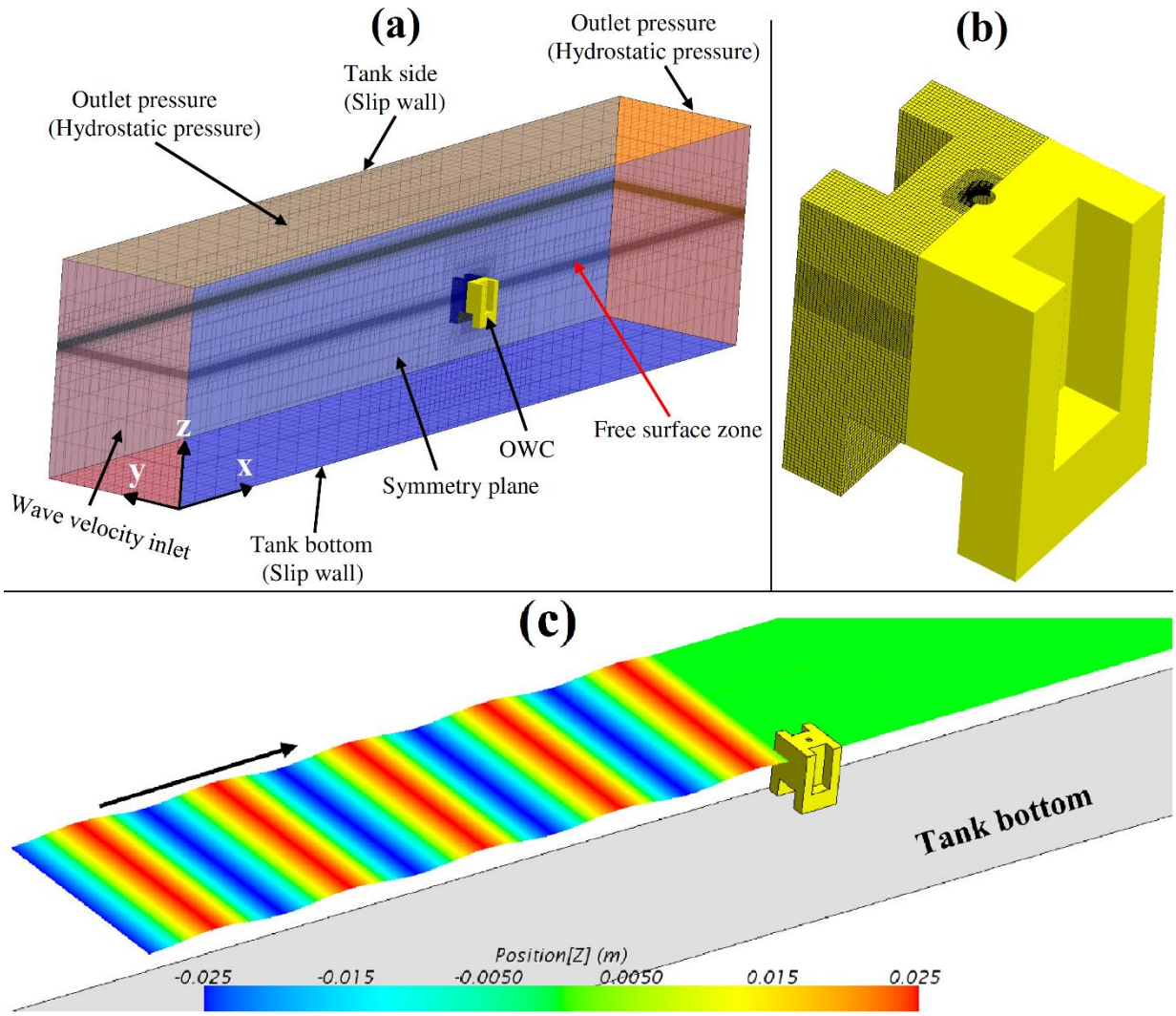

Fig. 9. Computational fluid domain (not to scale). (a): 3D mesh with boundary conditions, (b): OWC model surface mesh and (c): initial conditions

4.3. Comparison between CFD and experimental results

To validate the developed 3D CFD model, the overall efficiency curve from the CFD results shown Fig. 10 for a constant wave height H = 50 mm and PTO damping (R_3) was compared to the experimental results provided in Section 3. In this figure, 2D CFD results (with the same pneumatic chamber length (b) and a slot opening of the same opening ratio as R_3)[8] were included to highlight 3D effects. It can be seen that CFD results from the 3D model were in good agreement with the physical measurements, whereas the 2D model overestimated device efficiency for the high–frequency zone. These differences could be attributed to the constraints in the 2D modelling that did not let waves pass around the OWC device, especially for high–frequency (short) waves when wave diffraction was important [52]. This highlights the importance of using 3D CFD models in assessing the performance of offshore OWC devices.

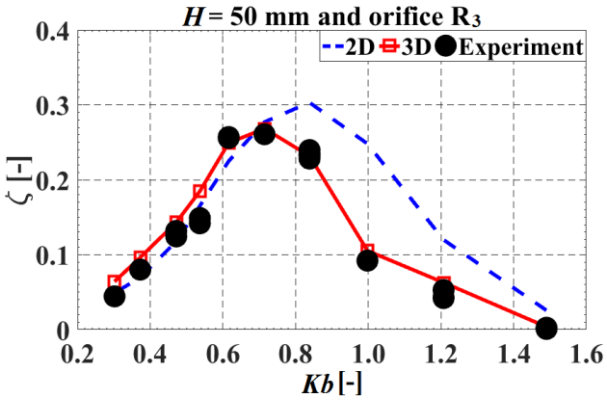

Fig. 10. Comparison between CFD (3D and 2D[8]) and experiments for device efficiency

Additional validations in time–series for incident wave elevation (η_1), average free surface elevation inside the chamber (η_{OWC}) and chamber differential air pressure (Δp) are shown in Fig. 11 for four different conditions. The normalized root mean square deviation (NRMSD) given by Eq. (10) was found to be in the range of 1.9–5.0 %, which further illustrates the good agreement between the 3D CFD results and the physical measurements.

$$\mathrm{NRMSD} = \frac{1}{x_{\max} - x_{\min}} \sqrt{\frac{1}{N}\sum_{i=1}^{N}(x_i - y_i)^2} \tag{10}$$

where x_i, y_i, are measured and estimated values form the experiment and the 3D CFD model, respectively, N is number of data point (here, data from five wave cycles were considered), $x_{\max}$, $x_{\min}$ are maximum and minimum measured values from the experiment, respectively.

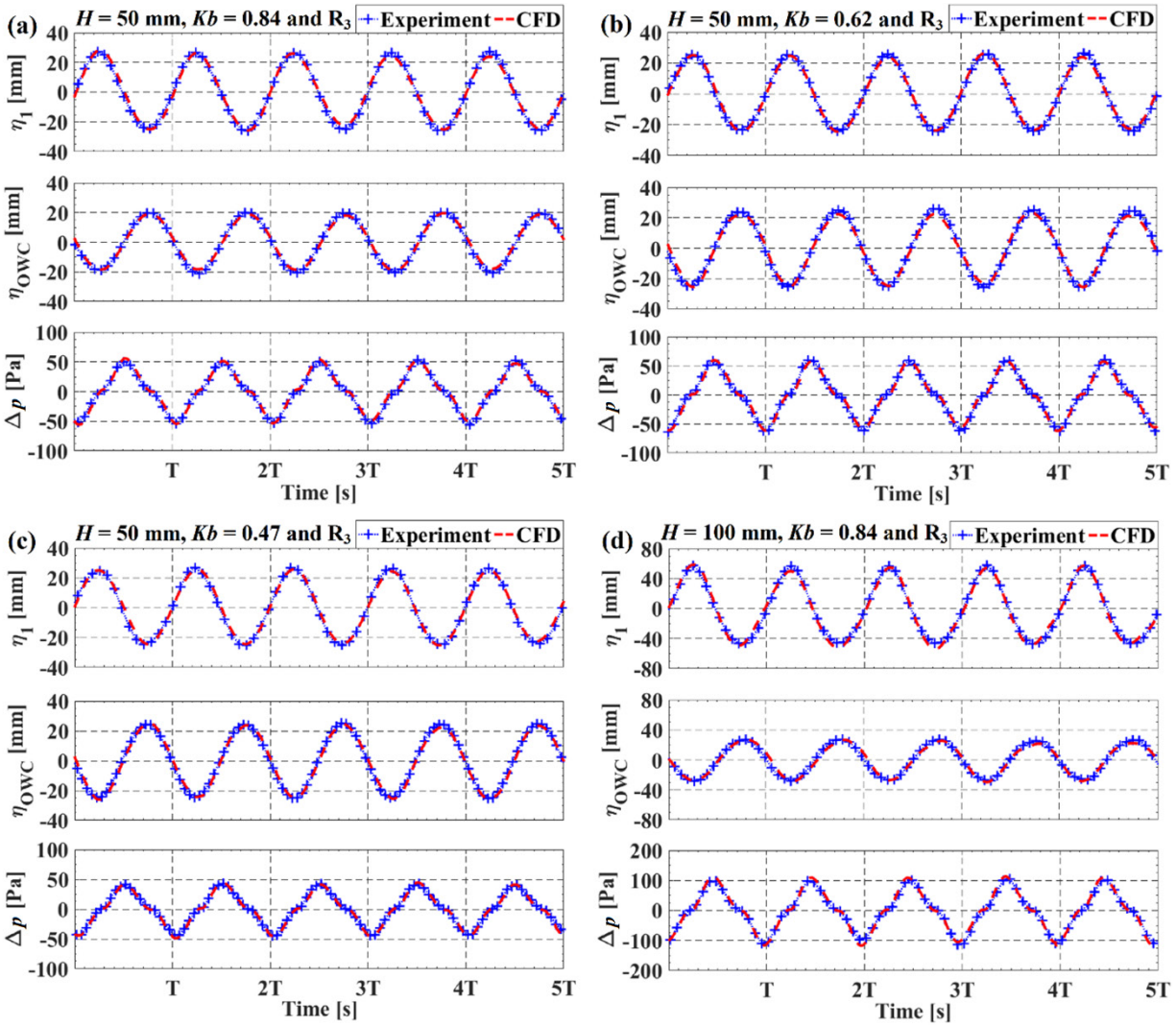

Fig. 11. 3D CFD results vs. time–series physical measurements for different wave conditions at a constant PTO damping (R_3). (a): H = 50 mm and Kb = 0.84 (T = 1.2 s), (b): H = 50 mm and Kb = 0.62 (T = 1.4 s), (c): H = 50 mm and Kb = 0.47 (T = 1.6 s) and (d): H = 100 mm and Kb = 0.84 (T = 1.2 s)

5. Conclusions

The hydrodynamic performance of a 1:50 scale offshore OWC model was experimentally investigated through 120 test conditions including different wave heights, wave periods and PTO damping. In addition, a fully nonlinear 3D incompressible CFD model based on the RANS–VOF approach was developed and validated against the physical measurements. The following main conclusions can be drawn from the present study based on the incompressible flow assumption at a small scale model and cannot be used at full–scale unless air compressibility effects are taken into account.

For a given wave height, the maximum free surface elevation inside the chamber did not occur at the resonance frequency of the OWC chamber but at a lower frequency. The relation

between chamber maximum free surface oscillation and incoming wave amplitude was nonlinear such that the amplification factor decreased as wave height increased.

The PTO damping provided an important parameter that could be adjusted to tune the OWC device to a given wave frequency range. As wave height increased, the overall hydrodynamic efficiency decreased and increased for wave frequencies higher and lower than the device resonance frequency, respectively. However, the differential air pressure as well as the airflow rate increased as wave height increased, which in turn increased the extracted pneumatic power. This proved the possibility of extracting more wave energy under large waves in offshore locations, especially for low–frequency waves under small PTO damping.

Utilizing 2D CFD models to investigate the hydrodynamic performance of offshore OWC devices could significantly overestimate the device efficiency, especially for the peak value and the high–frequency zone. In contrast, the numerical results from the 3D CFD model were in good agreement with physical measurements including incident wave elevation, chamber free surface elevation, chamber differential air pressure and device efficiency.

Acknowledgements

The authors would like to gratefully acknowledge the technical support during experiments from Associate Professor Gregor MacFarlane, Dr Alan Fleming, Dr Zhi Leong, Mr Tim Lilienthal and Mr Kirk Meyer, Australian Maritime College (AMC), University of Tasmania, Australia. In addition, the authors thank Mr Liam Honeychurch (AMC) for constructing the tested model. The financial support from the National Centre for Maritime Engineering and Hydrodynamics, Australian Maritime College, University of Tasmania, Australia is also acknowledged.

References

[1] B. Drew, A.R. Plummer, M.N. Sahinkaya, A review of wave energy converter technology, Proceedings of the Institution of Mechanical Engineers, Part A: Journal of Power and Energy, 223 (2009) 887-902.

[2] The World Energy Council. World Energy Resources, https://www.worldenergy.org/wp-content/uploads/2016/10/World-Energy-Resources-Full-report-2016.10.03.pdf [last accessed April 19, 2017].

[3] B.G. Reguero, I.J. Losada, F.J. Méndez, A global wave power resource and its seasonal, interannual and long-term variability, Applied Energy, 148 (2015) 366-380.

[4] Enerdata. Global Energy Statistical Yearbook 2016,

https://yearbook.enerdata.net/#electricity-domestic-consumption-data-by-region.html [Last accessed April 19. 2017].

[5] The World Energy Council. 2010 Survey of Energy Resources,

https://www.worldenergy.org/wp-content/uploads/2012/09/ser_2010_report_1.pdf [Last accessed April 19, 2017].

[6] R.-S. Tseng, R.-H. Wu, C.-C. Huang, Model study of a shoreline wave-power system, Ocean Engineering, 27 (2000) 801-821.

[7] A.C. Mendes, W.M.L. Monteiro, Performance analysis of a model of OWC energy converter in non-linear waves, in: Proceedings of the 7th European Wave and Tidal Energy Conference (EWTEC), September 11-13, Porto, Portugal, (2007).

[8] A. Elhanafi, A. Fleming, G. Macfarlane, Z. Leong, Underwater geometrical impact on the hydrodynamic performance of an offshore oscillating water column–wave energy converter, Renewable Energy, 105 (2017) 209-231.

[9] A. Elhanafi, A. Fleming, G. Macfarlane, Z. Leong, Numerical energy balance analysis for an onshore oscillating water column wave energy converter, Energy, 116 (2016) 539-557.

[10] T.V. Heath, A review of oscillating water columns, Phil. Trans. R. Soc. A, 370 (2012) 235-245.

[11] M.E. McCormick, A modified linear analysis of a wave-energy conversion buoy, Ocean Engineering, 3 (1976) 133-144.

[12] A.F. de O. Falcão, A.J.N.A. Sarmento, Wave generation by a periodic surface pressure and its application in wave-energy extraction, in: Proceedings of 15th International Congress of Theoritical and Applied Mechanics (ICTAM), August 17-23, Toronto, Canada, (1980).

[13] D.V. Evans, Wave-power absorption by systems of oscillating surface pressure distributions, Journal of Fluid Mechanics, 114 (1982) 481-499.

[14] J. Falnes, P. McIver, Surface wave interactions with systems of oscillating bodies and pressure distributions, Applied Ocean Research, 7 (1985) 225-234.

[15] A.F.O. Falcão, J.C.C. Henriques, Oscillating-water-column wave energy converters and air turbines: A review, Renewable Energy, 85 (2015) 1391-1424.

[16] V. Baudry, A. Babarit, A. Clement, An overview of analytical, numerical and experimental methods for modelling oscillating water columns, in: Proceedings of 10th European Wave and Tidal Energy Conference (EWTEC), September 2-5. Aalborg, Denmark, (2013).

[17] Y. Zhang, Q.-P. Zou, D. Greaves, Air–water two-phase flow modelling of hydrodynamic performance of an oscillating water column device, Renewable Energy, 41 (2012) 159-170.

[18] I. López, B. Pereiras, F. Castro, G. Iglesias, Optimisation of turbine-induced damping for an OWC wave energy converter using a RANS–VOF numerical model, Applied Energy, 127 (2014) 105-114.

[19] Y. Luo, J.-R. Nader, P. Cooper, S.-P. Zhu, Nonlinear 2D analysis of the efficiency of fixed Oscillating Water Column wave energy converters, Renewable Energy, 64 (2014) 255-265.

[20] T. Vyzikas, S. Deshoulières, O. Giroux, M. Barton, D. Greaves, Numerical study of fixed Oscillating Water Column with RANS-type two-phase CFD model, Renewable Energy, 102 (2017) 294-305.

[21] A.J.N.A. Sarmento, Wave flume experiments on two-dimensional oscillating water column wave energy devices, Experiments in fluids, 12 (1992) 286-292.

[22] F. Gouaud, V. Rey, J. Piazzola, R. Van Hooff, Experimental study of the hydrodynamic performance of an onshore wave power device in the presence of an underwater mound, Coastal Engineering, 57 (2010) 996-1005.

[23] I. López, B. Pereiras, F. Castro, G. Iglesias, Performance of OWC wave energy converters: influence of turbine damping and tidal variability, International Journal of Energy Research, 39 (2015) 472-483.

[24] D.-Z. Ning, R.-Q. Wang, Q.-P. Zou, B. Teng, An experimental investigation of hydrodynamics of a fixed OWC Wave Energy Converter, Applied Energy, 168 (2016) 636-648.

[25] T. Vyzikas, S. Deshoulières, M. Barton, O. Giroux, D. Greaves, D. Simmonds, Experimental investigation of different geometries of fixed oscillating water column devices, Renewable Energy, 104 (2017) 248-258.

[26] A. Elhanafi, A. Fleming, G. Macfarlane, Z. Leong, Numerical hydrodynamic analysis of an offshore stationary–floating oscillating water column–wave energy converter using CFD, International Journal of Naval Architecture and Ocean Engineering, 9 (2017) 77–99.

[27] A. Iturrioz, R. Guanche, J.A. Armesto, M.A. Alves, C. Vidal, I.J. Losada, Time-domain modeling of a fixed detached oscillating water column towards a floating multi-chamber device, Ocean Engineering, 76 (2014) 65-74.

[28] A. Iturrioz, R. Guanche, J.L. Lara, C. Vidal, I.J. Losada, Validation of OpenFOAM® for oscillating water column three-dimensional modeling, Ocean Engineering, 107 (2015) 222-236.

[29] I. Simonetti, L. Cappietti, H. El Safti, H. Oumeraci, Numerical modelling of fixed oscillating water column wave energy conversion devices: toward geometry hydraulic optimization, in: Proceedings of the 34th International Conference on Ocean, Offshore and Arctic Engineering, Volume 9: Ocean Renewable Energy, pp. (OMAE2015-42056), American Society of Mechanical Engineers (ASME), May 31–June 5, St. John's, Newfoundland, Canada, (2015).

[30] I. Simonetti, L. Cappietti, H. El Safti, H. Oumeraci, 3D numerical modelling of oscillating water column wave energy conversion devices: current knowledge and OpenFOAM® implementation, in: Proceedings of 1st International Conference on Renewable Energies Offshore, November 24-26, Lisbon, Portugal, (2015).

[31] F. He, M. Li, Z. Huang, An experimental study of pile-supported OWC-type breakwaters: energy extraction and vortex-induced energy loss, Energies, 9 (2016) 540.

[32] A.F.O. Falcão, J.C.C. Henriques, Model-prototype similarity of oscillating-water-column wave energy converters, International Journal of Marine Energy, 6 (2014) 18-34.

[33] S.K. Chakrabarti, Offshore structure modeling, World Scientific Publishing, Singapore, 1994.

[34] J.L. Lye, D.T. Brown, F. Johnson, An investigation into the non-linear effects resulting from air cushions in the Orecon oscillating water column (OWC) device, in: Proceedings of 28th International Conference on Ocean, Offshore and Arctic Engineering, American Society of Mechanical Engineers (ASME) May 31-June 5, 2009, Honolulu, Hawaii, USA.

[35] F. He, Z. Huang, Hydrodynamic performance of pile-supported OWC-type structures as breakwaters: An experimental study, Ocean Engineering, 88 (2014) 618-626.

[36] M.T. Morris-Thomas, R.J. Irvin, K.P. Thiagarajan, An investigation into the hydrodynamic efficiency of an oscillating water column, Journal of Offshore Mechanics and Arctic Engineering, 129 (2007) 273-278.

[37] The Mathworks, User Guide Matlab R2016a, Butterworth filter design, The Mathworks, Inc., Natick, Massachusetts, USA.

[38] The Mathworks, User Guide Matlab R2016a, Zero-phase digital filtering, The Mathworks, Inc., Natick, Massachusetts, USA.

[39] A. Babarit, A database of capture width ratio of wave energy converters, Renewable Energy, 80 (2015) 610-628.

[40] J.C.C. Henriques, L.M.C. Gato, A.F.O. Falcão, E. Robles, F.-X. Faÿ, Latching control of a floating oscillating-water-column wave energy converter, Renewable Energy, 90 (2016) 229-241.

[41] R.A. Dalrymple, R.G. Dean, Water wave mechanics for engineers and scientists, New Jersey: World Scientific Publishing Company, 1991.

[42] R. Pascal, G. Payne, C.M. Theobald, I. Bryden, Parametric models for the performance of wave energy converters, Applied Ocean Research, 38 (2012) 112-124.

[43] F. Thi´ebaut, R. Pascal, A.G. Andreu, Investigation into the calibration of orifices used in OWC tank testing, in: Proceedings of 11th European Wave and Tidal Energy Conference (EWTEC), September 6-11, Nantes, France, (2015).

[44] A. Elhanafi, G. Macfarlane, A. Fleming, Z. Leong, Scaling and air compressibility effects on a three-dimensional offshore stationary OWC wave energy converter, Applied Energy, 189 (2017) 1-20.

[45] A. Kamath, H. Bihs, Ø.A. Arntsen, Numerical investigations of the hydrodynamics of an oscillating water column device, Ocean Engineering, 102 (2015) 40-50.

[46] A. Kamath, H. Bihs, Ø.A. Arntsen, Numerical modeling of power take-off damping in an oscillating water column device, International Journal of Marine Energy, 10 (2015) 1-16.

[47] D.-Z. Ning, J. Shi, Q.-P. Zou, B. Teng, Investigation of hydrodynamic performance of an OWC (oscillating water column) wave energy device using a fully nonlinear HOBEM (higher-order boundary element method), Energy, 83 (2015) 177-188.

[48] CD-Adapco, User Guide STAR-CCM+ Version 10.02, (2015).

[49] C.W. Hirt, B.D. Nichols, Volume of fluid (VOF) method for the dynamics of free boundaries, Journal of computational physics, 39 (1981) 201-225.

[50] A. Elhanafi, A. Fleming, Z. Leong, G. Macfarlane, Effect of RANS-based turbulence models on nonlinear wave generation in a two-phase numerical wave tank, Progress in Computational Fluid Dynamics, 17 (2017) 141-158.

[51] ITTC, Recommended Procedures and Guidelines: Practical Guidelines for Ship CFD Applications, ITTC Report: 7.5-03 02-03, (2011).

[52] S.K. Chakrabarti, Hydrodynamics of offshore structures, WIT Press, Southampton, UK. (1987).